ABSTRACT

Title of dissertation: Characterization of Bending Magnetostriction in Iron-Gallium Alloys for Nanowire Sensor Applications

Patrick Ramon Downey
Doctor of Philosophy, 2008

Dissertation directed by: Professor Alison B. Flatau
Department of Aerospace Engineering

This research explores the possibility of using electrochemically deposited nanowires of magnetostrictive iron-gallium (Galfenol) to mimic the sensing capabilities of biological cilia. Sensor design calls for incorporating Galfenol nanowires cantilevered from a membrane and attached to a conventional magnetic field sensor. As the wires deflect in response to acoustic, airflow, or tactile excitation, the resultant bending stresses induce changes in magnetization that due to the scale of the nanowires offer the potential for excellent spatial resolution and frequency bandwidth. In order to determine the suitability for using Galfenol nanowires in this role, the first task was experimentally characterizing magnetostrictive transduction in bending beam structures, as this means of operation has been unattainable in previous materials research due to low tensile strengths in conventional alloys such as Terfenol-D. Results show that there is an appreciable sensing response from cantilevered Galfenol beams and that this phenomenon can be accurately modeled with an energy based formulation.

Report Documentation Page	Form Approved OMB No. 0704-0188

1. REPORT DATE **2008**	2. REPORT TYPE	3. DATES COVERED **00-00-2008 to 00-00-2008**	
4. TITLE AND SUBTITLE **Characterization of Bending Magnetostriction in Iron-Gallium Alloys for Nanowire Sensor Applications**		5a. CONTRACT NUMBER	
		5b. GRANT NUMBER	
		5c. PROGRAM ELEMENT NUMBER	
6. AUTHOR(S)		5d. PROJECT NUMBER	
		5e. TASK NUMBER	
		5f. WORK UNIT NUMBER	
7. PERFORMING ORGANIZATION NAME(S) AND ADDRESS(ES) **University of Maryland, College Park,Department of Aerospace Engineering,College Park,MD,20742**		8. PERFORMING ORGANIZATION REPORT NUMBER	
9. SPONSORING/MONITORING AGENCY NAME(S) AND ADDRESS(ES)		10. SPONSOR/MONITOR'S ACRONYM(S)	
		11. SPONSOR/MONITOR'S REPORT NUMBER(S)	

12. DISTRIBUTION/AVAILABILITY STATEMENT
Approved for public release; distribution unlimited

13. SUPPLEMENTARY NOTES

14. ABSTRACT

This research explores the possibility of using electrochemically deposited nanowires of magnetostrictive iron-gallium (Galfenol) to mimic the sensing capabilities of biological cilia. Sensor design calls for incorporating Galfenol nanowires cantilevered from a membrane and attached to a conventional magnetic eld sensor. As the wires de ect in response to acoustic, air ow, or tactile excitation, the resultant bending stresses induce changes in magnetization that due to the scale of the nanowires o er the potential for excellent spatial resolution and frequency bandwidth. In order to determine the suitability for using Galfenol nanowires in this role, the rst task was experimentally characterizing magnetostrictive transduction in bending beam structures, as this means of operation has been unattainable in previous materials research due to low tensile strengths in conventional alloys such as Terfenol-D. Results show that there is an appreciable sensing response from cantilevered Galfenol beams and that this phenomenon can be accurately modeled with an energy based formulation. For progressing experiments to the nanowire scale, a nanomanipulation instrument was designed and constructed that interfaces within a scanning electron microscope and allows for real time characterization of individual wires with diameters near 100 nm. The results of mechanical tensile testing and dynamic resonance identi cation reveal that the Galfenol nanowires behave similarly to the bulk material with the exception of a large increase in ultimate tensile strength. The magnetic domain structure of the nanowires was theoretically predicted and veri ed with magnetic force microscopy. An experimental methodology was developed to observe the coupling between bending stress and magnetization that is critical for accurate sensing and the key results indicate that speci c structural modi cations need to be made to reduce the anisotropy in the nanowires in order to improve the transduction capabilities. A solution to this problem is presented and nal experiments are performed.

15. SUBJECT TERMS

16. SECURITY CLASSIFICATION OF:			17. LIMITATION OF ABSTRACT	18. NUMBER OF PAGES	19a. NAME OF RESPONSIBLE PERSON
a. REPORT **unclassified**	b. ABSTRACT **unclassified**	c. THIS PAGE **unclassified**	**Same as Report (SAR)**	**299**	

For progressing experiments to the nanowire scale, a nanomanipulation instrument was designed and constructed that interfaces within a scanning electron microscope and allows for real time characterization of individual wires with diameters near 100 nm. The results of mechanical tensile testing and dynamic resonance identification reveal that the Galfenol nanowires behave similarly to the bulk material with the exception of a large increase in ultimate tensile strength. The magnetic domain structure of the nanowires was theoretically predicted and verified with magnetic force microscopy. An experimental methodology was developed to observe the coupling between bending stress and magnetization that is critical for accurate sensing, and the key results indicate that specific structural modifications need to be made to reduce the anisotropy in the nanowires in order to improve the transduction capabilities. A solution to this problem is presented and final experiments are performed.

Characterization of Bending Magnetostriction in
Iron-Gallium Alloys for Nanowire Sensor Applications

by

Patrick Ramon Downey

Dissertation submitted to the Faculty of the Graduate School of the
University of Maryland, College Park in partial fulfillment
of the requirements for the degree of
Doctor of Philosophy
2008

Advisory Committee:
Professor Alison B. Flatau, Chair/Advisor
Professor Inderjit Chopra
Professor Norman M. Wereley
Professor John P. Cumings
Professor Abhijit Dasgupta, Dean's Representative

To Logan.

Acknowledgments

This work could not have been accomplished without the help, guidance, and support of numerous people. My time spent working toward this degree has been memorable, challenging, and enjoyable, and I will forever appreciate everyone who has contributed to this chapter of my life.

My advisor, Professor Alison Flatau, deserves more thanks than I can properly express. She provided me with an incredible research opportunity that allowed me to greatly expand my knowledge and abilities. She showed far more patience than I deserved in getting this work underway, and then granted me the freedom to direct the course of the investigation. Dr. Flatau didn't even appear to mind my annoying habit of working for 72 straight hours and then disappearing for 4 days. She has always been understanding of my struggles, supportive of my decisions, trusting of my talents, and appreciative of my efforts. I'd like to apologize for every immature misstep along the way, and thank her for all that she has done. Under Dr. Flatau's tutelage I feel like I have grown and matured as a person as much as I have as a student, and for that I will always be grateful.

I would also like to thank my dissertation committee for their insight, advice, and time. Professor Inderjit Chopra has always been welcoming and helpful. Professor Norman Wereley has been exposed to numerous aspects of my research along the way, and has always provided useful comments with a funny, sharp, and down-to-earth demeanor. I had the privilege of taking a few courses with Professor Abhijit Dasgupta, and I thank him for his friendly and reassuring presence as

the committee's Dean's representative. I greatly appreciate all that Professor John Cumings has contributed to this work, which includes the donation of carbon nanotube samples and TEM grids, the time spent imaging nanowires with Lorentz TEM and EDS, and the various suggestions that resulted from data analysis. I still wish that there was something more than an acknowledgment and an author byline that I could have offered him in return.

This research was only made possible by the nanowire fabrication efforts of our collaborators at the University of Minnesota, Professor Bethanie Stadler and her students Patrick McGary and Liwen Tan. Dr. Stadler has worked very closely with us on handling and manipulating the nanowire arrays, and I thank her for being understanding of the feedback that we have provided. She has always been very kind and supportive and I sincerely hope that she knows how much I appreciate the contributions of her and her team. Patrick and Liwen have overcome numerous obstacles in order to successfully fabricate magnetic nanowires in well ordered arrays, and without their diligence and creativity my research would never have gotten off of the ground.

The design, construction, and integration of the nanomanipulator instrument is a testament to the openness and generosity of Professor Rodney Ruoff, formerly at Northwestern University, and his post-doctoral researcher Dmitriy Dikin. After a literature review identified their previous device as the perfect foundation for our intended machine, they were kind enough to host me for the day and answer every question that I had. We covered the key constraints to be wary of, the available means of data collection, some potential experimental pitfalls, even the most reliable

I would also like to thank Sean, my brother. He and I often see things in an uncannily similar manner, and so I know that he understands exactly what these past few years have entailed for me. I thank him not only for his empathy and advice during this time, but for inspiring me to achieve all that I could. I hope in return that I have spurred him on to go as far as his abilities may take him, as I am proud of the man that he has become. I additionally wish to thank my son, Logan, for although he is too young to appreciate it, his presence alone has made this accomplishment infinitely more satisfying than it would have been otherwise. The final and most important acknowledgment goes to Jen, as I am honored and privileged to have her by my side. I thank her for her patience and her unwavering support. I thank her for keeping me on track but recognizing when I truly needed a break. I thank her for the sacrifices that she has made in her own career. I thank her for shouldering all of the tasks that I have neglected recently, and for making sure that spending time with Logan wasn't one of them. But above all else, I thank her for injecting happiness into my life every single day.

Table of Contents

List of Tables

List of Figures

Chapter 1

Introduction

1.1   Magnetostrictive Materials

The phenomenon of magnetostriction can be summarized as a coupling between a material's magnetic and elastic states. This manifests as two primary responses: the direct effect where the sample strains as the magnetization changes, and the reciprocal effect where the magnetization varies with mechanical stress. As a result of these inherent properties, this class of materials is well suited for use in both actuator and sensor devices across a wide variety of technical disciplines. Although magnetostrictive alloys have been extensively researched, this dissertation aims to expand the state of the art by focusing on the unconventional transduction mechanism of beam bending and investigating magnetostriction on the scale of nanowires.

1.1.1   Background

Magnetostriction was first discovered in iron by Joule in 1842 [69], but the low strain magnitude of only 20×10^{-6} [58] initially limited its applications. Some early telephone receivers and hydrophones [62] made use of magnetostrictive materials, but it wasn't until the development of nickel sonar transducers in World War II that magnetostriction became a common and heavily studied transduction

mechanism. Clark [21, 116] led research on iron alloyed with rare earth elements to create the giant magnetostrictive Terfenol-D, which can attain saturation strains of up to 2000×10^{-6} and has become widespread in research, commercial, and naval transducers.

Some of the most common applications include sonar devices, active vibration control, and audio equipment, all of which take advantage of the large frequency bandwidth and high power density of the material [26]. Other applications make use of the small but precise displacements for positional control or automated machining [146]. Operating on the reciprocal effect, magnetostrictives make strong load cells, pressure sensors, and accelerometers [42, 80].

A simplified overview of the behavior of magnetostrictive materials is as follows. The material is composed of multiple magnetic domains, each of which has a uniform magnetization represented by the arrows in Figure 1.1. Their magnetic strength and orientation are tied to electron spins at the scale of the molecular lattice, details of which are expanded upon in the next section. When the sample is unmagnetized, minimization of the internal energy is achieved when these domains are equally distributed in the four directions of this simple square structure. If a magnetic field is applied to the material, a minimum energy state is achieved when the moments reorient into alignment with the direction of the field, resulting in an increase in length. As the strength is increased eventually the sample will "saturate," corresponding to the formation of a single magnetic domain oriented with the field, and no further length change is possible. As the field is cycled in the opposite direction, the magnetization vector is inverted but the sample itself will exhibit the

2
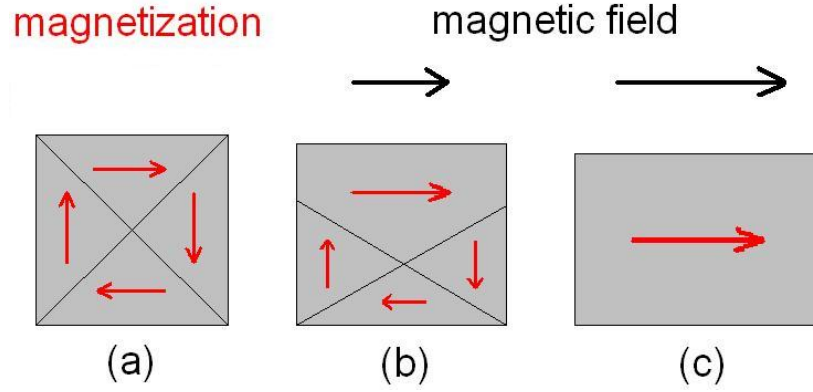
Figure 1.1: Simple cartoon of the magnetostrictive phenomenon. The undeformed sample begins at zero magnetization (a), and as a magnetic field is applied the magnetization becomes increasingly aligned (b) until saturation is reached (c). Due to the magnetostriction, this process induces a corresponding change in dimension.

same overall change in dimension. This creates the traditional "butterfly" curve plotted in Figure 1.2, showing the strain produced by the sample at all values of applied magnetic field.

The inverse phenomenon, known as the Villari effect, operates on the same fundamental principle. If the material begins at saturation such as in Figure 1.3, the application of a compressive stress will tend to orient the magnetization vectors along the short axis of the sample, perpendicular to the initial configuration. As a result, the magnetic domain structure changes and can be used as a measure of the net applied load. A more rigorous presentation of these concepts is provided in the next section.

Both the direct and reciprocal magnetostriction effects can be mathematically modeled as a set of linear coupled expressions often known as the constitutive mag-
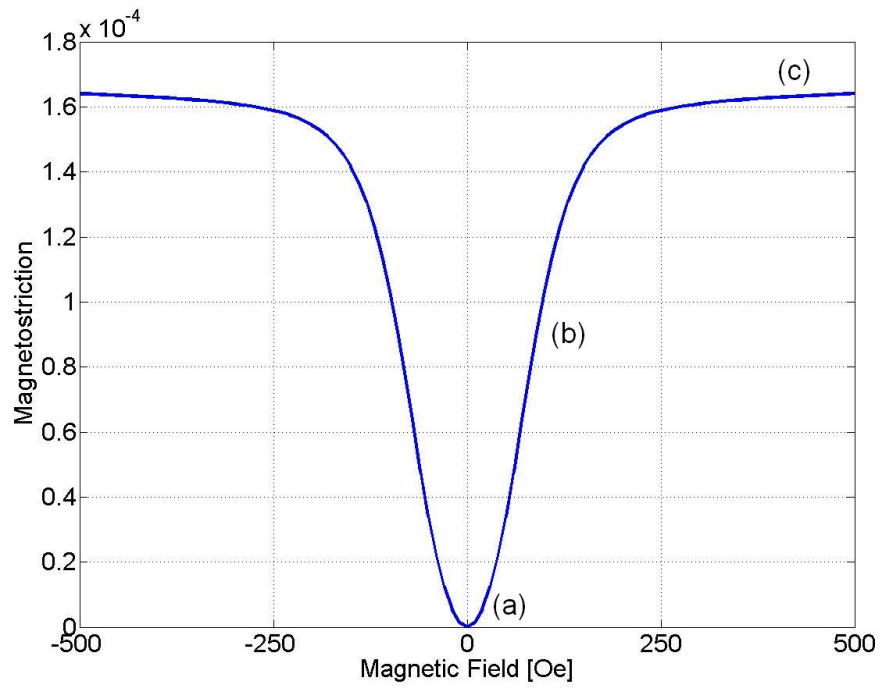
Figure 1.2: Plot of strain versus field for a typical magnetostrictive sample, revealing the key features of saturation and positive strain resulting from either field direction. Points (a)-(c) correspond to the states depicted in Figure 1.1.
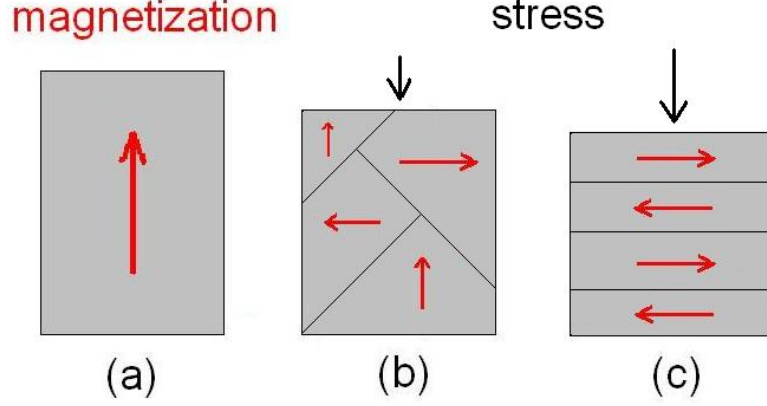
Figure 1.3: Simple cartoon of the sensing effect in magnetostrictive materials. Beginning with a magnetically saturated material (a), the application of an increasing compressive stress will tend to orient the magnetization vectors perpendicular to the load (b) until all of the moments are flat (c).

netostrictive equations or the piezomagnetic equations. While the inherent processes are highly nonlinear, these equations provide a reasonable means of modeling the coupling between the elastic and magnetic regimes over a limited range of small changes in strain ε, stress σ, magnetic field H, and magnetic induction B. The linearized 1-d form of these expressions are written as:

$$\varepsilon = \frac{\sigma}{E} + d_{33}H \tag{1.1}$$

$$B = d_{33}^*\sigma + \mu H, \tag{1.2}$$

where E is the Young's modulus, μ is the magnetic permeability, and d_{33} and d_{33}^* are the linearized coupling coefficients. In a material with zero coupling, these equations reduce to Hooke's law for elastic materials and the fundamental magnetic law $B = \mu H$. The constitutive equations capture the basic transduction mechanisms described previously, where an increase in the field directly produces a strain pro-

portional to d_{33}, and conversely the application of a stress changes the magnetic induction.

1.1.2 Origin of Magnetostriction

Magnetism is an inherent property at the atomic scale. The electron configuration, consisting of both orbital motion and spin, is analogous to a small current loop that creates an overall atomic magnetic dipole $\boldsymbol{m}$ [75, 7]. The magnetization $\hat{\boldsymbol{M}}$ is the volume density of magnetic moments, and is often expressed normalized to the saturation value $\boldsymbol{M} = \hat{\boldsymbol{M}}/M_s$. The magnetization referred to throughout the remainder of this dissertation is this normalized vector quantity, such that when a material becomes saturated in a given direction, $M_x = 1$ for example, the value in the other coordinates is zero. When a sample is demagnetized it has a purely random distribution of magnetic moments that average to a zero magnetization in all directions.

In materials that exhibit net magnetic moments there is a tendency for them to locally align with an external field, a phenomenon known as paramagnetism. When the field is removed, there is no coupling force acting to keep the moments aligned and they return to a random configuration with zero magnetization. Magnetostriction is observed in a more select class of materials known as ferromagnets (including ferrimagnets and antiferromagnets), which are so named due to iron being the archetype rather than being a necessary element in the composition. In ferromagnetic alloys there is spontaneous magnetization in the absence of an exter-

nal field, and conversely if a field is applied and then removed the sample will retain some remanent magnetization. These effects are due to an exchange coupling caused by the Weiss mean field [154, 75, 72] between nearby atomic moments that tends to align adjacent dipoles in parallel. As a result, this exchange coupling will force some volume of moments to align and create a domain of non-zero magnetization even in the absence of an applied field. Although the exchange energy tries to enforce all of the moments in a body to be parallel, there are competing energies that can make this configuration unfavorable. In practice, neighboring moments align over a short range of uniform magnetization known as a magnetic domain, and the entire material is often broken up into several domains of random orientation separated by distinct boundaries. Note that all ferromagnets revert to a pure paramagnetic state above a certain temperature known as the Curie point, which can vary substantially between materials but is typically several hundred °C for common magnetostrictive alloys.

The magnetization curve of a ferromagnetic sample will generally take the form of Figure 1.4, where at zero field there is still the remanent magnetization and as field is increased this value grows until saturation is reached. Physically, the increase in magnetization consists of two mechanisms, domain wall motion and domain rotation. The former constitutes those domains that begin favorably aligned with the field growing at the expense of the others, which has the apparent effect of the domain walls moving within the material as depicted in Figure 1.5(b). Assuming the presence of pinning sites associated with common material defects, domain wall motion will eventually be inhibited. Figure 1.5(c) depicts that at higher levels of
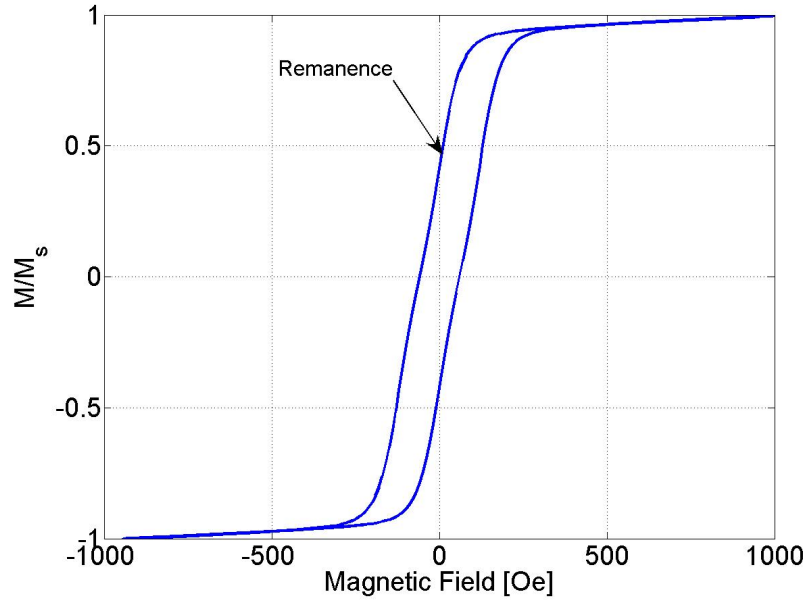
Figure 1.4: Representative plot of the magnetization versus applied field for a ferromagnetic material, revealing the remanence at zero field that occurs during cycling.

applied field the pinned domains themselves will begin to rotate into the preferred direction. Domain wall motion is largely reversible, whereas domain rotation is an irreversible process and the primary source of the hysteresis observed in these materials, as shown in Figure 1.4 [31, 66, 32].

Ferromagnetic crystals generally have substantial anisotropy, which is the directional dependence of material properties. A primary source of this is the magnetocrystalline anisotropy, other key contributors include the magnetoelastic and magnetostatic energy that are introduced as needed in the relevant sections of this dissertation. The magnetocrystalline anisotropy represents the preference of the magnetic moments to align with certain crystallographic directions in the lattice.
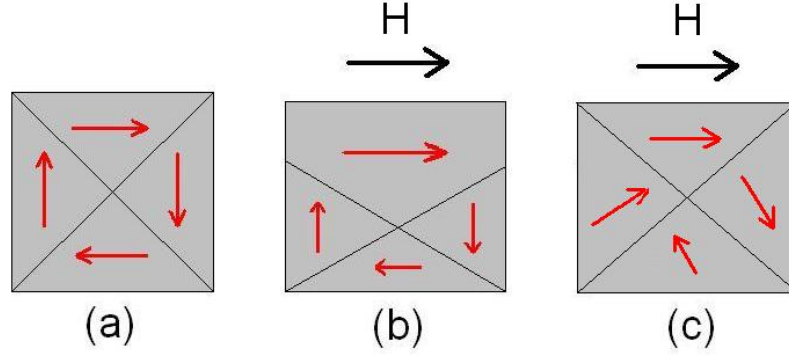
Figure 1.5: Magnetization processes from an unmagnetized state (a) generally consist of domain wall motion (b), where the favorable domain grows as the walls appear to shift downward, and domain rotation (c), where each domain tries to rotate into the preferred alignment.

The exact origin of this energy is believed to be the interaction between the magnetization of an atomic dipole and the electrostatic charge of the nearby ions. Because the magnetization "sees" [75] the crystal lattice through the orbital motion of the electrons, there will be particular orientations that are energetically favorable for the overlapping wave functions. The result of this phenomenon is that a ferromagnetic material will have "easy" and "hard" axes, and cubic crystals in particular will have an additional "medium" direction. This simply implies that when magnetizing the material, the processes of domain wall motion and domain rotation will be far easier when trying to align them into a crystallographic easy axis rather than a hard axis. Figure 1.6 depicts this effect graphically, where significantly more field needs to be applied along the hard axis in order to saturate the material.

The critical process for magnetostriction is that the state of strain of the material is dependent on the magnetization. The origin of this coupling is that a
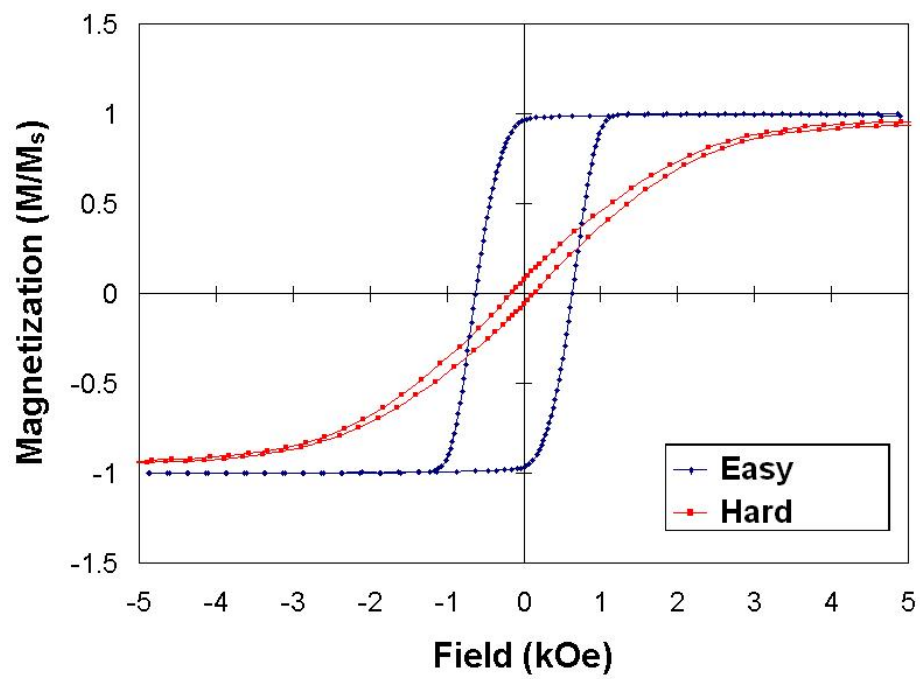
Figure 1.6: Magnetization data from a nickel nanowire array highlighting the difference between saturating the sample along the easy and hard axes [97].

change in the magnetic state causes the stable structure of the crystal to deform away from the original lattice. As a consequence, there is a shift in inter-atomic distances as the lattice deforms in order to reduce the anisotropy energy, resulting in magnetostrictive strain. The reciprocal Villari effect is largely due to stress induced anisotropy, where the forced elastic deformation of the crystal lattice causes the magnetization to rotate into the nearest preferred configuration, directly altering the net magnetization of the material that can be measured in sensor applications.

1.1.3 Iron-gallium Alloys

Magnetostrictive materials have historically been organized into two classes. The first includes common elements such as iron, nickel, and cobalt, which while possessing strong metallurgical properties have maximum magnetostrictive strains on the order of 10×10^{-6}. The second group is made up of the "giant" magnetostrictive materials such as Terfenol-D that exhibit up to 200 times the strain capability but are incredibly brittle, with tensile strengths of only 28 MPa. For actuator and sensor design, the material selection reduces to either using Terfenol-D in limited uniaxial devices while under constant compressive loading or using a mechanically tougher metal and substantially sacrificing transduction. Various alloys and additions have somewhat managed to bridge the gap between these extremes, but there is still a clear niche for a magnetostrictive material that exhibits a compromise of large magnetostriction and strong mechanical properties.

Iron-gallium alloys, known as Galfenol, were developed fairly recently by Clark

et al. [25] to fill this void. Galfenol appears to hold substantial promise for use in a variety of smart structure applications, and is currently the focus of extensive research into the growth procedures [132], alloying additions [59, 23], deformation processing [102], and enhancing anisotropy [115, 163]. Although the exact mechanism of magnetostriction is still not fully understood in this material [159, 73, 74], the behavior of the alloy across a wide spectrum of compositions has been characterized in detail [7, 72, 22].

Crystallographically, Galfenol consists of b.c.c α-iron with a random substitution of gallium atoms. Cullen and Wuttig [161, 30] have proposed a model that suggests pairs of neighboring Ga atoms displace the lattice and create anisotropy that leads to magnetostriction. As the probability of Ga-Ga pairs increases with gallium content in the solid solution, the magnetostriction increases as shown in the first peak of Figure 1.7. The data reveals that above 17 at. % Ga, the strain output decreases due to the formation of a $D0_3$ phase that is highly ordered and not as conducive to magnetostriction. This theory is supported by the increasing complexity near 20 at. % Ga in the phase diagram of Figure 1.8, and the fact that quenching samples from high temperature extends the magnetostrictive peak to 19 at. % Ga by locking in the disordered b.c.c. structure. More specific data relating the formation of $D0_3$ to composition, heat treatment, and cooling rate have been presented in the literature [85, 35]. Clark et al. [22] have explained the origin of the second peak in Figure 1.7 as a drastic softening of the material that outpaces the diminishing magneto-mechanical coupling.

The primary advantages of Galfenol are that it generates large magnetostric-
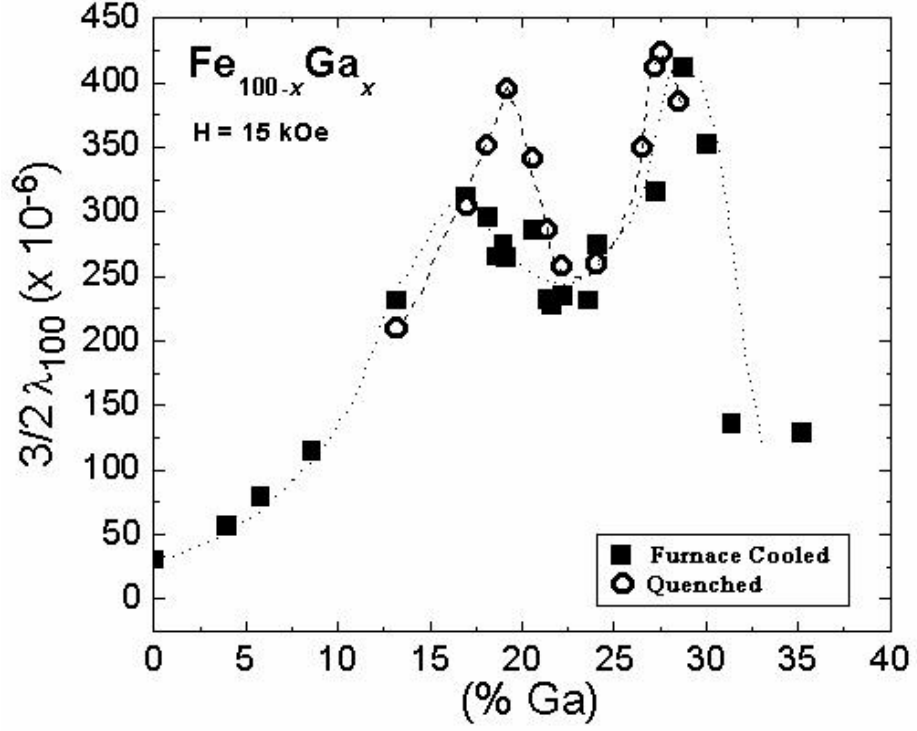
Figure 1.7: Measured saturation magnetostriction versus composition for a mix of slow cooled and quenched Galfenol samples. Quenching appears to suppress the formation of the $D0_3$ phase and extend the first peak closer to 20 at. % Ga. The second peak is likely due to a softening of the crystal lattice [22].
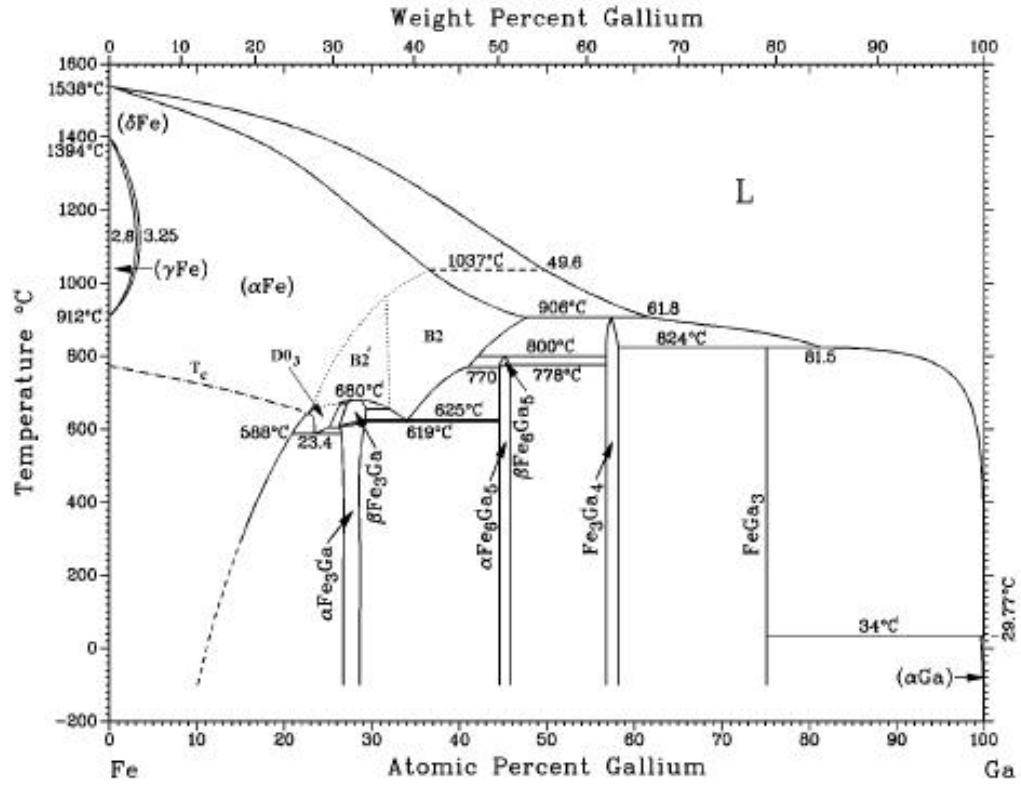
Figure 1.8: Phase diagram of the Fe-Ga binary system showing the multitude of ordered structures that form above 20 at. % Ga [78, 91].

14

tive strains up to 400×10^{-6} [27] while having a tensile strength of 500 MPa [71]. While these values have been observed in ideal single crystal samples, properties of the same order are universal throughout polycrystalline samples [132] that are easier and less expensive to fabricate. Other desirable metallurgical properties of iron-gallium alloys are that they are machinable [147], weldable, partially ductile [71], and can withstand shock loads [155]. In terms of utilizing Galfenol samples in devices, they have the added benefits of saturating at relatively low magnetic fields, displaying little temperature dependence, and having low hysteresis. These traits allow for the use of smaller solenoids, expand the operational environment, and decrease losses. Research on potential applications include torque sensors [107], gyroscopes [164], dynamic actuators [145], morphing plate mechanics [34], and MEMS devices [63, 89].

The unique properties of iron-gallium alloys greatly expand the design possibilities for magnetostrictive materials. This includes not only filling the operational gaps of conventional transducer applications, but more importantly opening the door for novel devices and implementations. The mechanical strength of the alloy allows for structural members to be built entirely out of Galfenol, incorporating load bearing, actuation, and sensing into a single component. Custom smart material drivers can be created in arbitrary configurations through conventional machining and joining processes. The impact toughness and shock tolerance could be an asset in underwater explosive applications where most active materials cannot be used. Galfenol also provides a means of obtaining large magnetostriction in flexible thin films for an array of microscale transducers. With regards to this project,

iron-gallium alloys present the possibility of harnessing magnetostriction in bending beam structures that has been unattainable in previous materials research.

1.2 Biological Inspiration

1.2.1 Cilia Transduction in Nature

Cilia are organelles extending from cells in nearly all biological species, and are primarily used as either motion sources or sensory devices. As sensors, these tiny hair-like formations fill a wide variety of an organism's detection needs, including vibration and touch along the legs of insects [4, 10], hydrodynamic imaging via the lateral lines of fish [29, 28, 19, 162] for tracking obstacles and prey, and acoustic transduction in the cochlea of reptiles, birds, and mammals [48, 88, 153, 108]. Figure 1.9 shows some images of cilia from the inner ear.

The transduction mechanism of cilia has evolved to become a versatile and efficient process. Mechanical deflection of the cilium opens an ion channel, inducing a chemical potential that effectively stimulates the attached neuron as pictured in Figure 1.10. The membrane to which the cilium is cantilevered has been found to decouple beyond a certain point, allowing for the cilium to bend independently once saturated [11]. While the dimensions of the cilia vary significantly with the particular location and function, the diameters typically range from hundreds of nanometers to tens of microns, with lengths of up to a millimeter.

A recent trend in sensor development is biomimetic design, where the well adapted operation of biological constructs are mimicked at the engineering level.
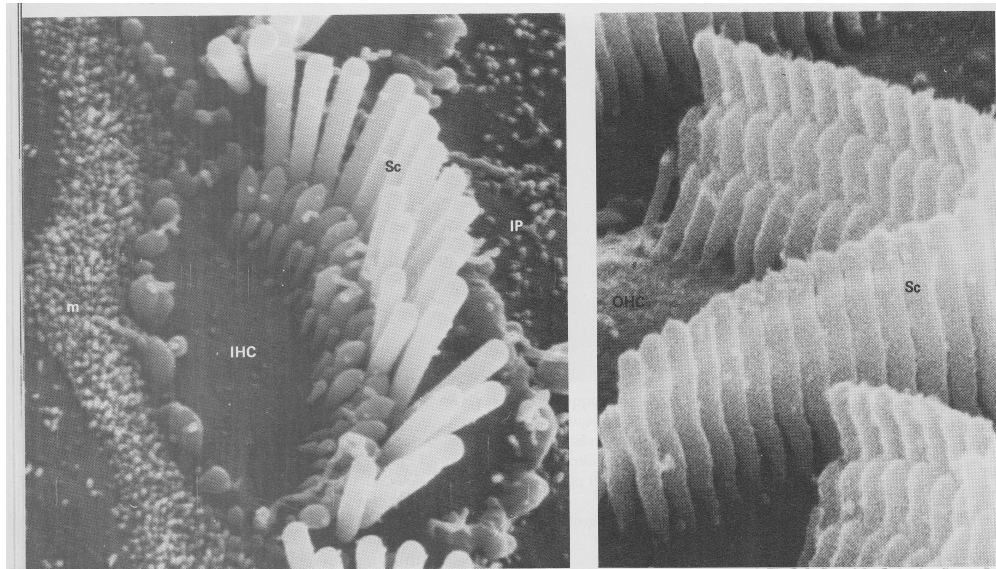
Figure 1.9: Images of the cilia from inner (left) and outer (right) hair cells within the human cochlea [165].
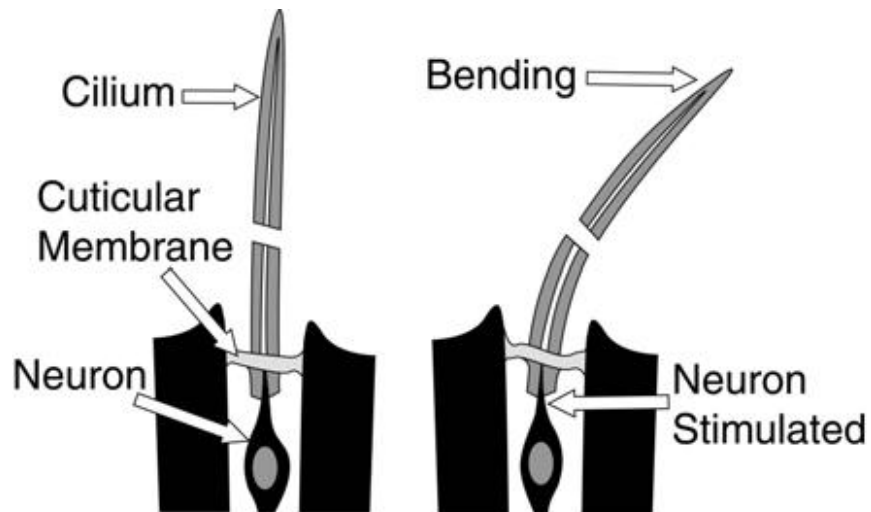
Figure 1.10: Cartoon of a bending cilium that is attached to a neuron [20].

Advances in MEMS fabrication techniques have greatly aided this approach, and several researchers have begun fabricating artificial cilia devices for technological solutions to challenging sensor problems [106, 148, 20, 46, 144]. These systems currently focus on air flow measurements that could prove useful in micro air vehicle control, but the foremost motivation for this research is mimicking the acoustic transduction of cilia within the human cochlea [157] with the intention to deploy sensors for underwater acoustic measurements.

1.2.2 Details of the Human Cochlea

The ear is composed of outer, middle, and inner sections as presented in Figure 1.11. The purpose of the outer ear is to focus sound waves onto the tympanic membrane and amplify those frequencies in the human audible range (approximately 20 - 20000 Hz). The middle ear consists of three tiny bones that are responsible for transferring sound waves into the inner ear. As the tympanic membrane vibrates, the bones provide a mechanical advantage such that the pressure transmitted to the oval window of the cochlea is 22 times greater than the pressure at the tympanic membrane [15]. The middle ear also serves as an impedance match between the air cavity of the outer ear and the fluid filled inner ear, minimizing reflections and data loss.

The inner ear is composed of the vestibular system that controls balance and the cochlea that transduces sound waves into brain impulses. A typical human cochlea is a fluid filled chamber that is approximately 1 cm wide and 35 mm long [48]

vestibular
system

footplate of stapes
in oval window

cochlear nerve

scala tympani

scala media

scala vestibuli

helicotrema (scala
vestibuli joins
scala tympani)

outer ear
canal

tympanic
membrane

round
window

organ of Corti
in scala media
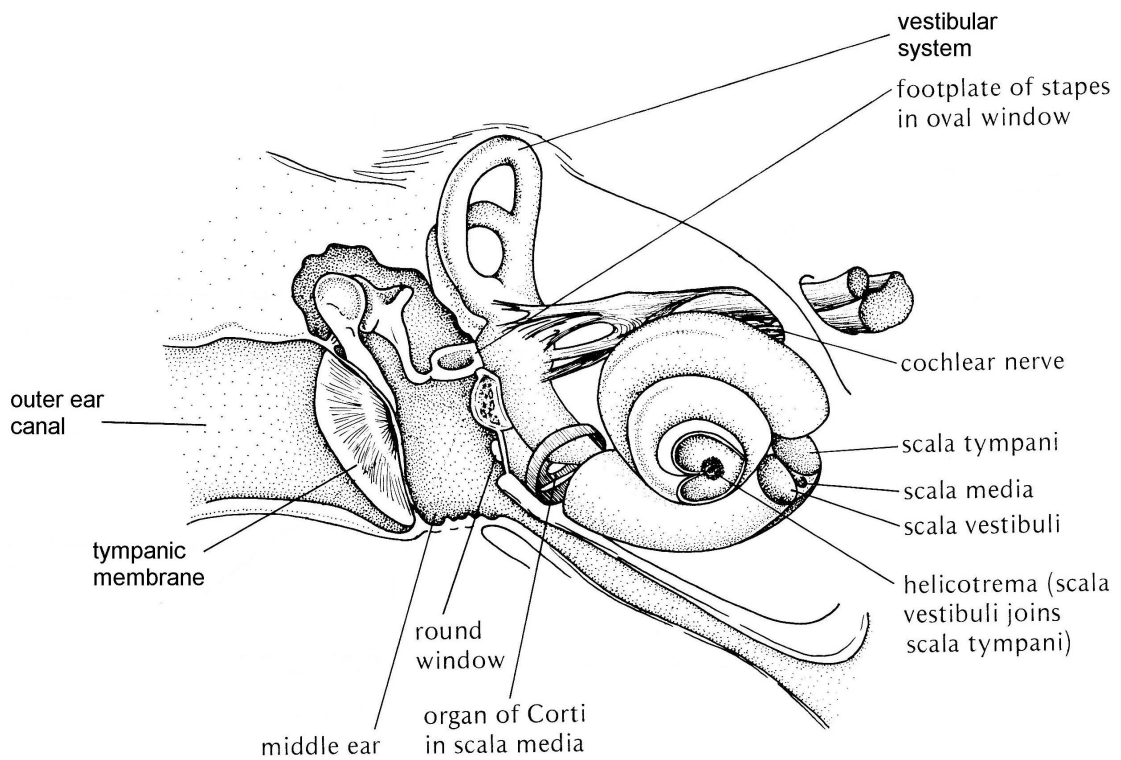
middle ear

Figure 1.11: Schematic of the primary features of the human ear. The outer ear canal focuses sound waves onto the tympanic membrane, which are then amplified and matched to the impedance of the cochlea by the middle ear. The cochlea itself consists of several fluid filled chambers wherein the organ of Corti transduces sound into nerve signals [165].

and coiled upon itself to reduce the total volume required to attain high frequency resolution. Pressure waves enter from the vibrations of the oval window connected to the middle ear, and induce acoustic waves in the perilymph fluid of the scala vestibuli, the cochlea's upper chamber. These waves propagate outward toward the helicotrema opening at the end of the chamber, and then return within the scala tympani, or lower chamber, until terminating at the round window [165].

The membrane that divides the scala vestibuli from the scala tympani is itself a fluid filled chamber known as the scala media. Within this region is the organ of Corti, an assembly of membranes, cilia, and cells that perform the actual coupling between sound waves and electrical impulses. Figure 1.12 displays a cross-section of this organ, which sits along the basilar membrane. The principal component of interest are the clusters of cilia that sit atop hair cells and are tethered to the tectorial membrane, as shown in Figure 1.13. As sound waves propagate in the cochlea, the motion induces relative displacements between the basilar and tectorial membrane that create a shearing force on the cilia as depicted in Figure 1.14. This deflection triggers the neurons attached to each hair cell and transmits the impulses to be interpreted by the brain.

In order to process frequency information, the location of the stimulated neurons, rather than their firing rate, provides the most information. The spatial dependence is made possible by the low pass filtering in the elastic vibrations of the basilar membrane, which grows in width and decreases in mechanical stiffness from the base to the end at the helicotrema. As a result, sound waves at different frequencies excite motion over only a narrow region of the organ of Corti, with lower
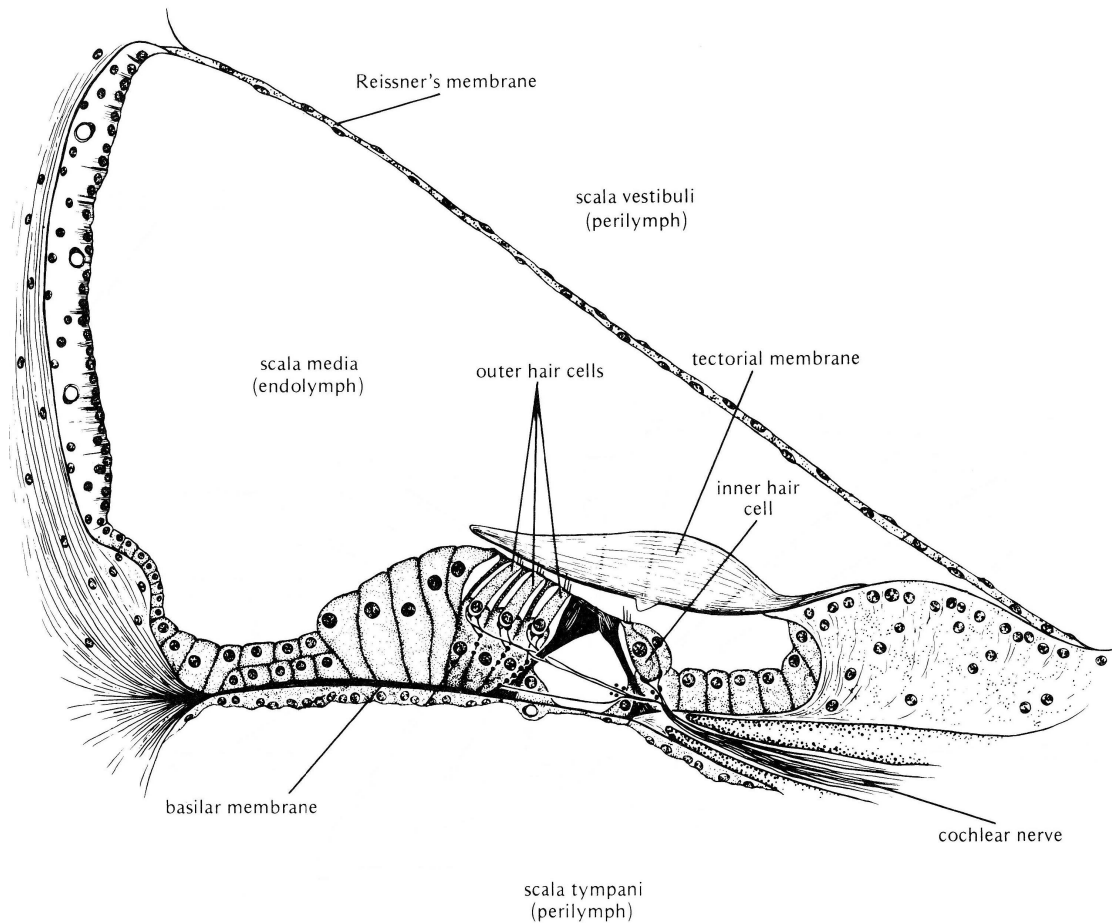
Figure 1.12: Cross-sectional view of the human cochlea, revealing the fluid filled chambers of the scalae vestibuli, media, and tympani. The organ of Corti is composed of outer and inner hair cells sitting atop the basilar membrane, each with a cluster of cilia tethered to the tectorial membrane [165].
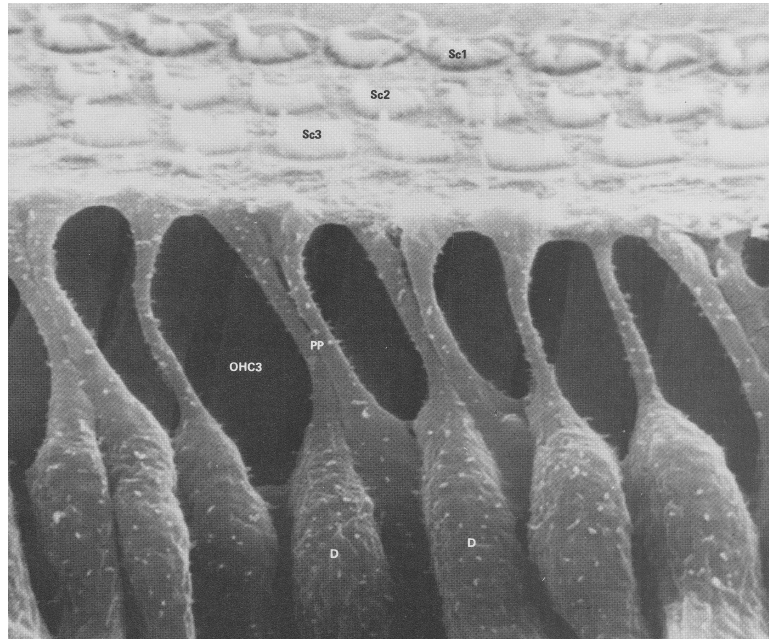
Figure 1.13: Image of several dense clusters of cilia protruding from outer hair cells [165].
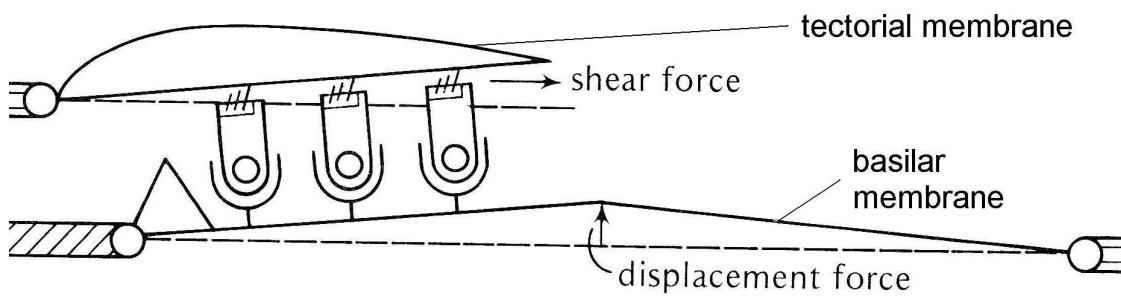
Figure 1.14: Schematic of how motion of the basilar membrane induces deflection in the cilia due to the attachment of the tectorial membrane [165].
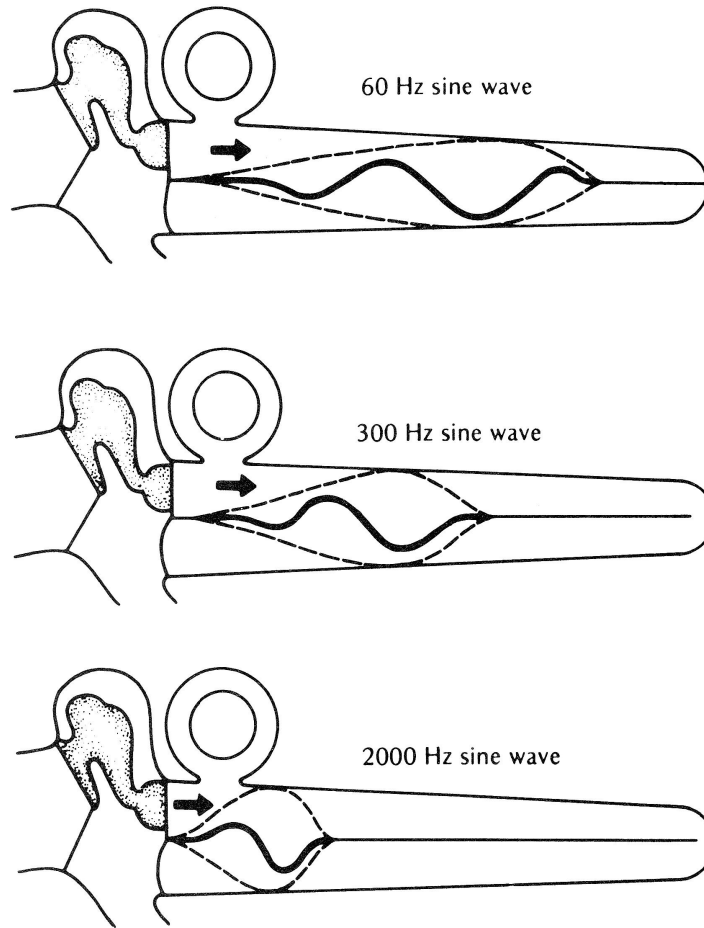
Figure 1.15: Diagram of sound waves of different frequency attenuating at various locations along the basilar membrane [165].

frequencies propagating further along the membrane as shown in Figure 1.15. This function is evolutionarily rather young, as non-mammalian species have only a weak cochlear attenuation [88].

1.3   Galfenol Nanowire Sensors

1.3.1   Proposed Design

The overall motivation for this project is to develop a novel sensor device that combines the universal applicability and sensitivity of cilia detection with the magnetostrictive transduction of Galfenol. It is proposed that Galfenol nanowires have the unique capability of being mechanically flexible and robust while still displaying appreciable coupling between the elastic and magnetic regimes. This research explores the operation and behavior of Galfenol nanowires in order to establish their suitability for use in this role.

Based off of the typical cilia configuration found in nature, the nanowires will have a large aspect ratio and be cantilevered from the sensor base. In this setup, they can easily deflect in response to acoustic signals, fluid flow, ground vibration, tactile loading, etc. The actual sensing mechanism relies on the iron-gallium alloy mechanically withstanding large bending stresses caused by cantilever vibration, where the stress induces a change in magnetization due to Villari effect magnetostriction. The unique material properties of Galfenol allow for each nanowire beam to dually act as the vibrating structural member and sensing material without the need for a unimorph or bimorph design [127, 83, 34].

The general sensor design is sketched in Figure 1.16, where nanowires are cantilevered from a substrate layer in a dense array. There are two broad concepts for this sensor, the first of which calls for nanowires to be uniform to create a very high mechanical quality factor Q that is precisely tuned to the resonance frequency

of that beam geometry. This system would also likely perform ideally for fluid flow measurement where the wire deflection maps directly to the velocity. The alternate approach in Figure 1.16(b) would create a broadband device, taking greater inspiration from the human cochlea. Here a membrane layer with varying width and/or thickness would provide acoustic attenuation similar to that of the basilar membrane and allow wires at different locations to measure distinct frequencies, with the bandwidth being tailored by the chosen geometry of the nanowires and membrane.

Due to the miniaturization of these beams, it is believed that the Galfenol nanowire sensors can obtain a significant increase in sensitivity and resolution compared to conventional devices. If, for example, a row of nanowires is excited by an ultrasonic wave at 500 MHz in air, the nanowire spacing is small enough to sample five discrete points in one wavelength [48]. When placed in a 2-d array, the complex response of each oscillating beam provides data that can be used to recreate underwater images with excellent pixel resolution [13]. Additionally, the flexibility and sensitivity of these nanowires should allow for a measurable change in magnetization from tactile forces down to the order of 1 nN. A serious challenge arises when trying to measure the magnetization change from each of these beam elements. Not only does the scale prevent traditional magnetic field measurement, but there is a critical limit on the number of data input channels that would be available for signal processing. Treating each nanowire as an individual sensor element would have enormous wiring and data acquisition requirements as the array density can roughly be estimated to be 25×10^6 nanowires/mm^2. In order to alleviate this

(a)

(b)
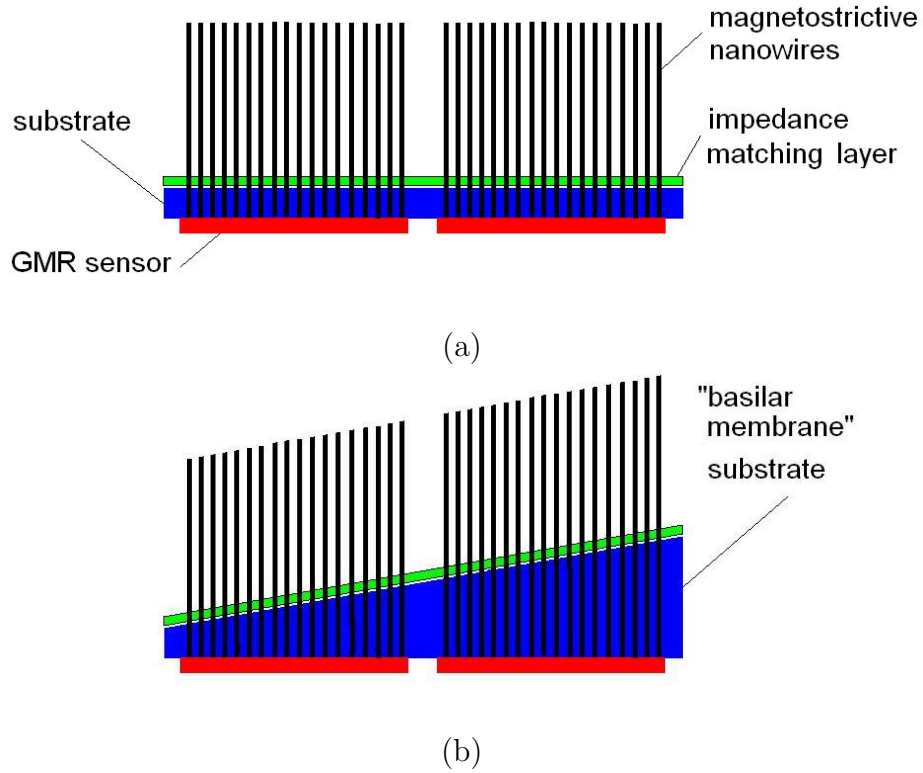
Figure 1.16: Proposed designs for Galfenol nanowire sensors. Cantilevered wires act as cilia that deflect in response to excitation, and the resultant change in magnetization can be detected with magnetic field sensors. A high Q device would employ numerous wires of equal dimension to be precisely tuned to a specific frequency (a), whereas a broadband device could make use of the spatial attenuation properties of the basilar membrane to measure a wide range of acoustic signals (b).

problem the entire nanowire array can be attached to a single sensor, such as the giant magnetoresistance (GMR) sensor shown in Figure 1.16, and the data from the entire array collected at once. This approach will certainly increase the complexity of deconvoluting the GMR voltage into a replicate of the excitation, but it allows for a manageable number of wire leads and input channels.

The GMR sensor is tentatively selected as the primary measurement device due to its position as the leading option for miniaturized magnetic field detection in applications such as hard drive read heads [143], microfluidics [140], and encoders [123]. The operation of this sensor is roughly as follows. Two ferromagnetic electrodes are separated by a thin layer of a nonmagnetic material, with common materials including cobalt, permalloy, or nickel sandwiched around copper or aluminum oxide. One of the two layers has its magnetization fixed in a given direction by an antiferromagnetic pinning layer and is invariant to an applied field. The magnetization of the other layer is free to rotate in order to align with the orientation of the external field, as demonstrated in Figure 1.17. Due to the electronic structure of the materials the resistance felt by a current passed between the two magnetic electrodes changes with the alignment of the magnetization vectors. This relationship follows the first order approximation of $R \propto \sin \theta$, where R is the resistance and θ is the angle between the two ferromagnetic layers as depicted in Figure 1.17(b). When these magnetoresistance elements are wired in a Wheatstone bridge, an output voltage develops in direct proportion to the external magnetic field. The sensitivity profile for an example GMR sensor from NVE, Inc. is shown in Figure 1.18.
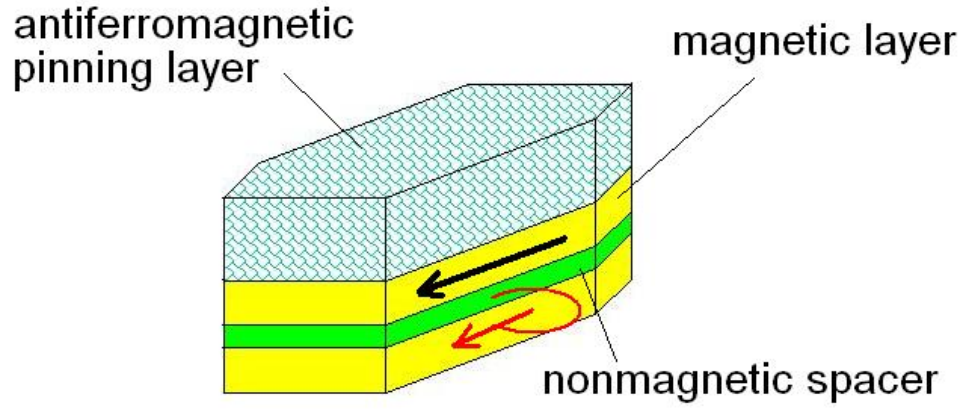
(a)
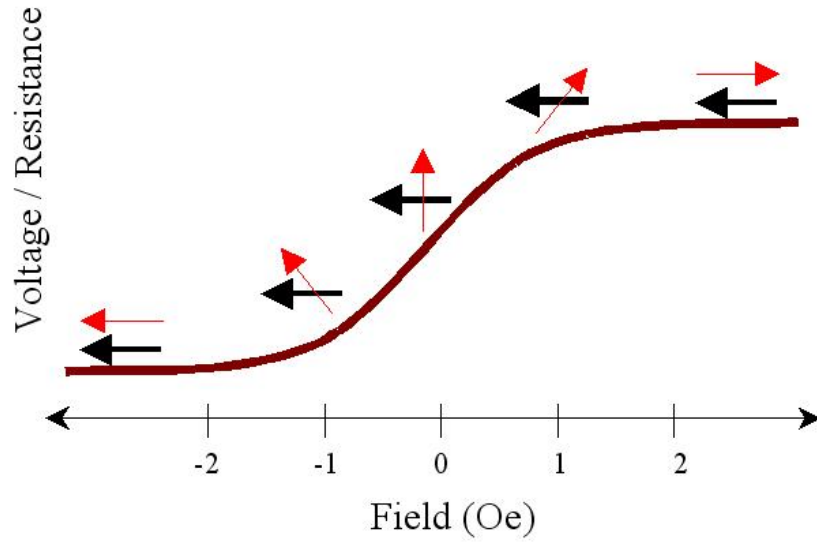
(b)

Figure 1.17: The construction of a GMR sensor consists of two ferro-magnetic electrodes sandwiched around a nonmagnetic layer, with the top electrode magnetically pinned due to the exchange coupling of the antiferromagnetic layer (a). The sensor operates on the principle that the electrical resistance of the structure varies with the angle between the pinned and free magnetizations (b) [140].

AA002-02 Sensor Characteristic, 5V Supply
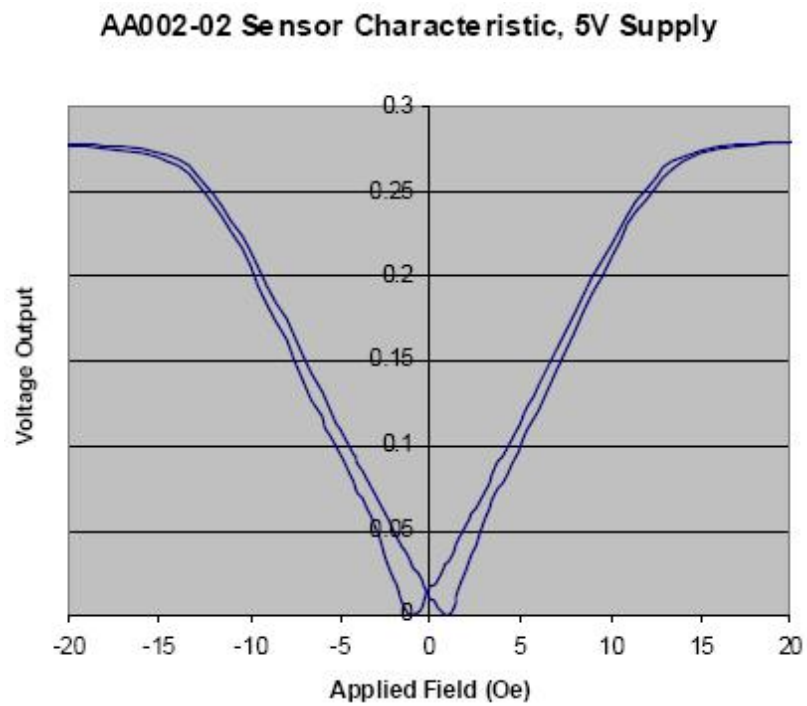
Figure 1.18: Plot of the voltage response of a typical GMR sensor from NVE, Inc. to various magnetic fields in air [139].

1.3.2   Nanowire Array Fabrication

Fabrication of nanowire arrays is typically done with a template method, where wires are formed within the spaces of a host material [158, 150]. This method is generally inexpensive and easy to carry out in bulk when compared to alternative approaches that use different lithography techniques [87]. The basic premise is to start with a porous template of alumina, electrochemically deposit the iron-gallium alloy within the pores, and then remove the alumina matrix with select chemical etchants. The properties of the wires can be specifically controlled via the pore sizes in the original template, the deposition time, the applied voltage, and the electrolyte solutions. The entirety of this process has thus far taken place in the lab of our collaborator Dr. Stadler at the University of Minnesota, primarily by Patrick McGary [97] with contributions from Liwen Tan [96].

The process begins by anodizing aluminum [92, 82] to produce porous templates into which the nanowires can be grown. There are many recipes for the anodization procedure in the literature [93, 137, 65, 9], but the basic method consists of exposing an aluminum film to an acidic solution in the presence of an applied voltage. The pores that self assemble in a typical commercial batch of anodized aluminum oxide (AAO) have only short range order and diameters that often vary significantly, as shown in Figure 1.19. For the purposes of the artificial cilia sensors, it is preferable to have nanowires with more uniform size and spacing, reducing the complexity of both the experimental characterization and the necessary modeling assumptions. To this end, alumina is first indented with a nanoimprint formed from
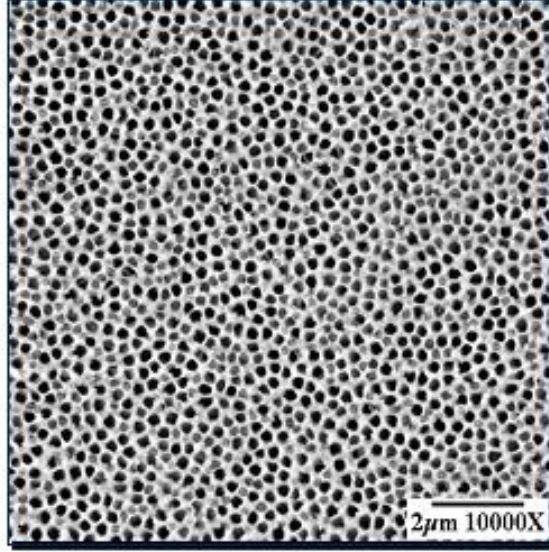
Figure 1.19: Micrograph of the self-assembled pores from a commercial AAO template [130].

a nitride stamp made via lithography [96]. This initial conditioning helps force the pores to form in the valleys that result from the stamping, which greatly improves the long range order as shown in Figure 1.20.

The next step in readying the AAO templates is to remove the insulating barrier layer present during anodization. After etching with phosphoric acid, a 30 nm copper film is sputtered onto the back side of the alumina matrix to provide a counter electrode for use during deposition. A final step calls for dipping the sample in 0.1 vol. % of Triton-X 100 to wet the pores, the application of which has been found to greatly improve the fill rate of the pores during deposition [97].

Once the templates are prepared, electrochemical deposition of Galfenol is performed. This technique has many variations [95, 103, 125, 109], but in this work [41] positive metal ions are reduced within the pores from an aqueous solution

Figure 1.20: AFM image of the nitride stamp used for imprinting (left) and the resultant improvement in long range order (right) after stamping [130].
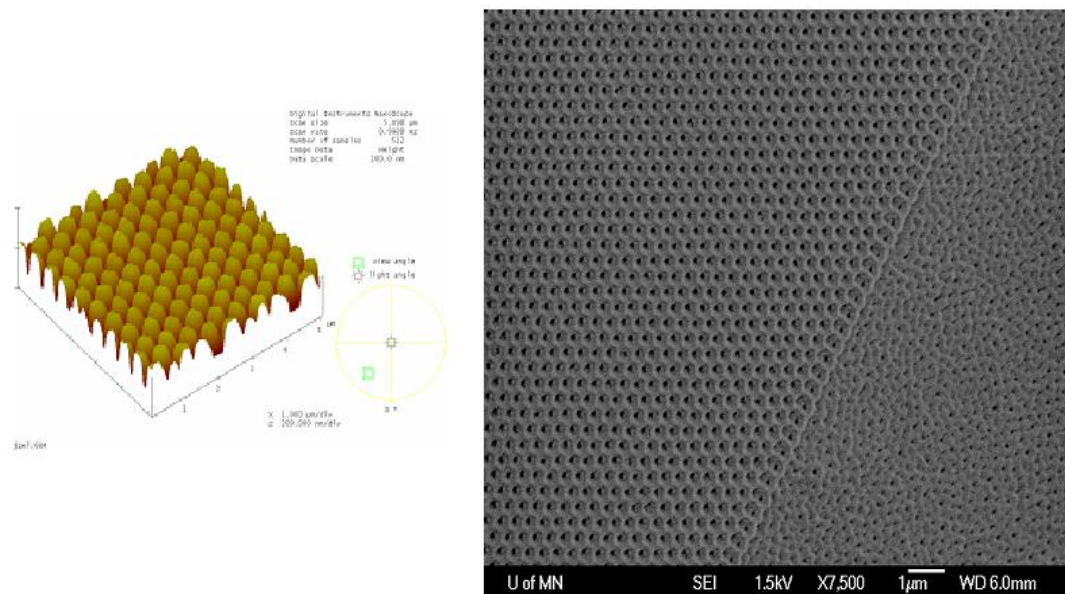
of 0.025 M gallium(III) sulfate, 0.01 M iron(II) sulfate, and 0.05 M sodium citrate using static potentials of -1.25 to -1.375 V. The deposition of single elements proved to be straightforward, but getting a binary composition to grow correctly required characterizing the deposition rate versus the electric potential. A Hull cell was employed (see Figure 1.21) where the current distribution varies spatially with the distance between the electrodes. By depositing simple thin films of Galfenol with this Hull cell and then analyzing the resultant stoichiometry with distance, the optimum growth potential for the alloy could be determined.

The result of this process is an AAO matrix filled with cylindrical metal nanowires that is subsequently etched away with chromic acid to reveal the cantilevered wire array used for testing. Handling of the array is performed by using

32
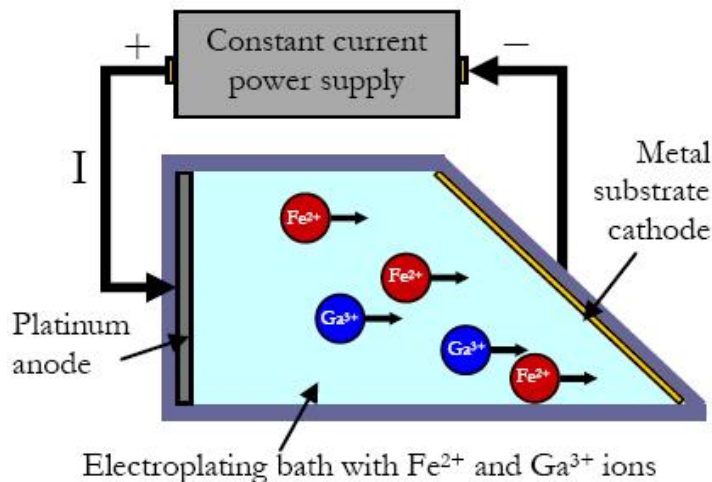
Figure 1.21: Diagram of the Hull cell used to create a spatial distribution of current density during electrochemical deposition [97].

tweezers to carefully grasp a small tag of copper foil that has been affixed to the AAO and placing it where desired. In some cases the matrix is completely etched away, so rather than wires being cantilevered they are entirely free and kept suspended in isopropanol. In this case they are typically collected with an eye dropper and deposited onto a silicon wafer or other substrate material, and are ready for use once the alcohol evaporates.

The overall nanowire fabrication has been a parallel process [97] to the characterization studies of this research, and as such many challenges have arisen along the way and some intriguing features have resulted. In the interests of better understanding the nanowire manipulations and testing discussed in this dissertation, a collection of images of various nanowire structures are presented in Figures 1.22 through 1.27.
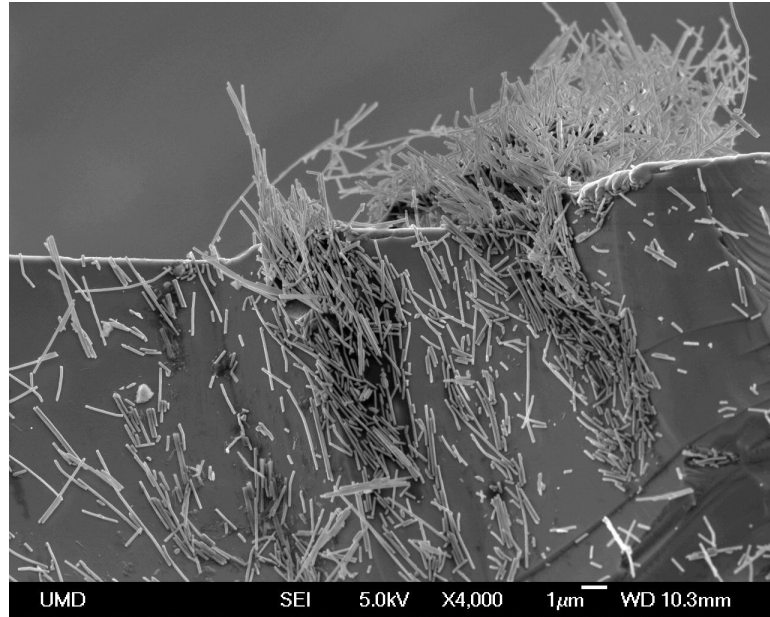
Figure 1.22: Image of numerous fragments of Galfenol nanowires clinging to the edge of a silicon wafer.
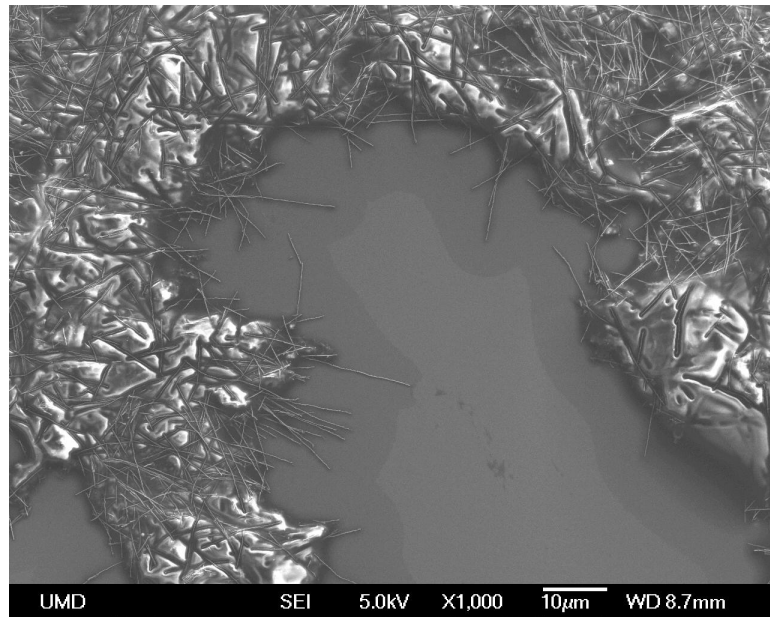
Figure 1.23: Image of loose Galfenol nanowires clustered together on a silicon wafer and coated in a polymer layer.
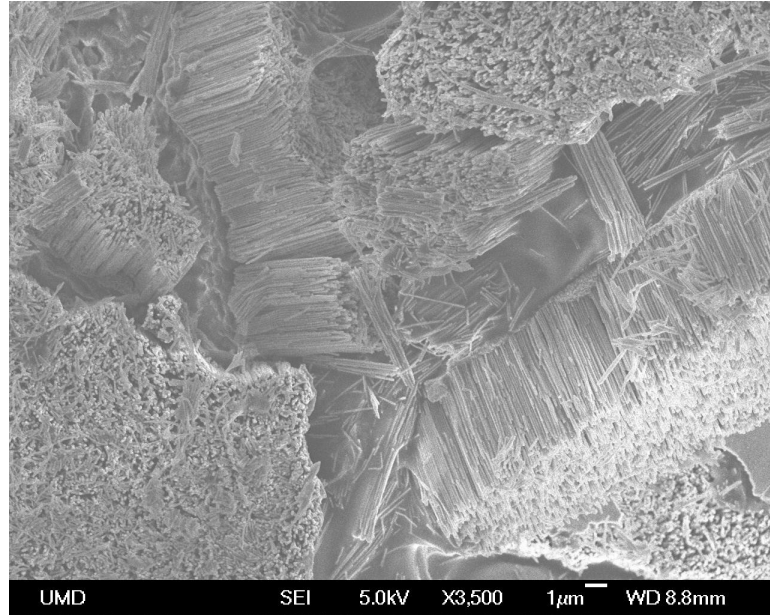
Figure 1.24: Image of several cantilevered nanowire arrays in different orientations, with a fair number of loosely scattered wires adhered throughout.
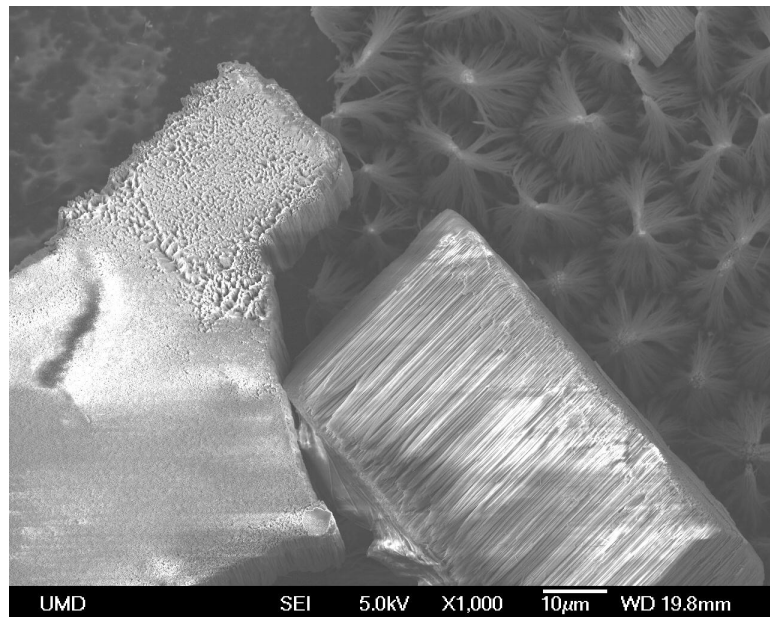
Figure 1.25: Image of two nanowire arrays laying normal to each other, both displaying excellent nanowire density and uniformity in length.
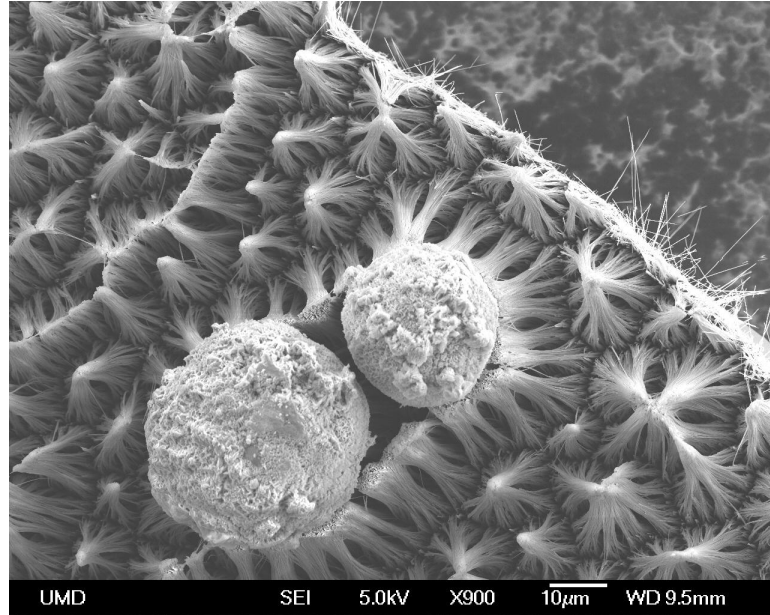
Figure 1.26: Image of nanowires that naturally adhered to each other at the tips to form conical structures. The large spheres are remnants of the fabrication process.
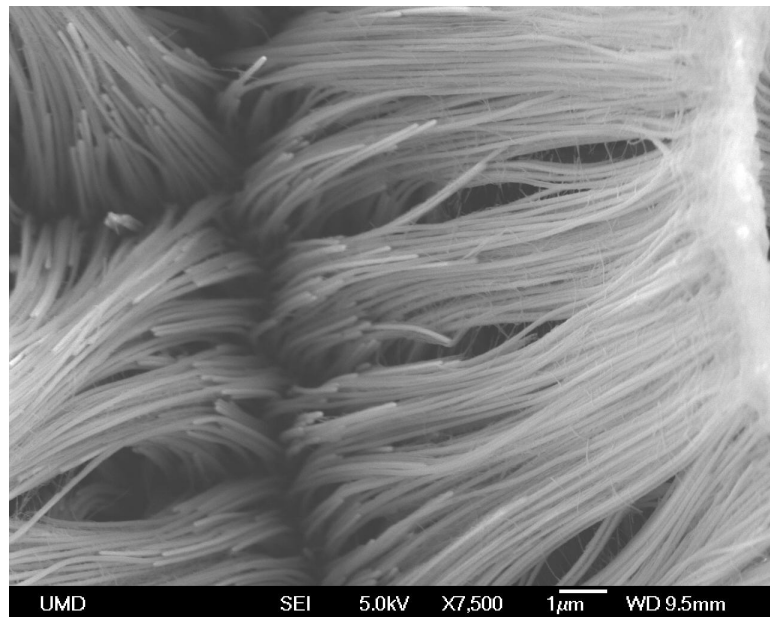
Figure 1.27: Zoomed image of the conical structures, revealing very fine fibers tangled throughout.

1.4 Research Objectives

The primary objective of this research is to investigate the hypothesis that magnetostrictive iron-gallium nanowires can be used to mimic the transduction of biological cilia in aeronautical and aerospace applications such as underwater acoustic sensors. The various steps taken toward this goal are organized as follows.

Before commencing studies on the Galfenol nanowires themselves, the transduction mechanism of a magnetostrictive beam in pure bending must first be validated. Chapter 2 details the experimental procedure carried out on bulk Galfenol beams that verifies the appreciable sensing response and confirms that this effect can be measured with traditional techniques. In addition, the fundamental mechanism of the bending behavior is explained and accurately simulated using a magneto-mechanical model that is described in Chapter 3.

Another significant goal of this dissertation is to develop a means by which the Galfenol nanowires can be observed and interacted with in order to allow for the direct characterization of their properties. This task calls for becoming fully proficient in several microscopy techniques and constructing an instrument with capabilities for locating, grasping, and manipulating individual nanowires. Chapter 4 reviews the highlights of this work and leads directly into the nanowire characterization.

In order to sufficiently understand the differences between the bulk Galfenol alloy and the nanowire structures, several key mechanical properties are measured in Chapter 5. Using the aforementioned nanomanipulator instrument, the elastic modulus, ultimate tensile strength, and failure mode of individual nanowires are

measured through a combination of quasi-static tensile testing and dynamic resonance identification. Perhaps more important than the data itself, a key objective of this work is to identify and correct sources of error in the testing procedure in order to outline a straightforward experimental approach to nanowire mechanical characterization that can easily be adopted in future studies.

An additional goal of this research is to adapt the analytical model of magnetostriction to accommodate for the unique scale of the Galfenol nanowires. Chapter 6 details the predicted nanowire magnetic domain structure and the various experimental observations that validate this result. Chapter 7 focuses on the final research objective of investigating the coupling between bending stress and magnetization in the nanowire samples. This work covers the original experimental methodology used to measure this transduction, makes recommendations for improving the proposed nanowire sensor design, and enacts initial modifications. Future work suggestions are specific to invoking additional changes to the system such that the operable use of Galfenol nanowires as artificial cilia is firmly established.

Chapter 2

Experimental Verification of Bending Magnetostriction

2.1 Overview

The critical assumption in using iron-gallium nanowires as artificial cilia is that the magnetostrictive transduction is still observable when the material is loaded in pure bending. Considering the volume of research done on magnetic materials and their applications, there are very few studies that touch upon this configuration [61, 119, 53, 156] due to it being mechanically impractical in conventional magnetostrictives such as Terfenol-D. While the advantages of iron-gallium alloys now make it feasible to load a sample into bending, the question remains of whether or not there is an appreciable Villari effect response.

The primary concern stems from the stress distribution in a bent beam, where according to continuum mechanics there are equal yet opposite axial stresses on the top and bottom surface. This can be derived from Euler-Bernoulli beam theory [98], where the bending moment is related to the displacement as

$$M(x,t) = EI(x)\,\frac{\partial^2 w(x,t)}{\partial x^2},\tag{2.1}$$

where M is the moment, w is the beam deflection, E is the elastic modulus, and I is the area moment of inertia. The $\frac{\partial^2 w(x,t)}{\partial x^2}$ term is often called the curvature of the

beam, and is connected to the strain ε through the thickness coordinate z,

$$\varepsilon = z \, \frac{\partial^2 w(x,t)}{\partial x^2}. \tag{2.2}$$

In the ideal case of a cantilevered beam of length L with a force F applied at the tip, the moment can be expressed as

$$M(x,t) = F(t) \, (x - L). \tag{2.3}$$

Finally, assuming linear elastic material behavior, $\sigma = \varepsilon E$, equations (2.1 - 2.3) can be combined to write the beam stress distribution as

$$\sigma(x,z,t) = \frac{F(t)}{I(x)} \, (x - L) \, z, \tag{2.4}$$

which is antisymmetric due to the dependence on z, as depicted in Figure 2.1. Therefore, as the positive and negative stresses throughout the material sum to a zero net stress for the bulk sample, a number of questions arise about the validity of measuring any change in magnetic induction from a beam loaded in bending.

In the subsequent sections of this chapter this phenomenon is investigated experimentally on a number of macroscale iron-gallium beams in a cantilevered configuration, with the intent to verify that bending magnetostriction can result in a non-zero transduction. The applicability of measuring the output using GMR sensors, as in the proposed nanowire device, rather than the conventional pickup coil is also studied. Results show that there is a significant change in magnetic induction of the material due to bending stress, that the bending transduction tends to follow known trends for iron-gallium alloys, and that the GMR sensors are capable measurement devices when used in proper configurations.

40
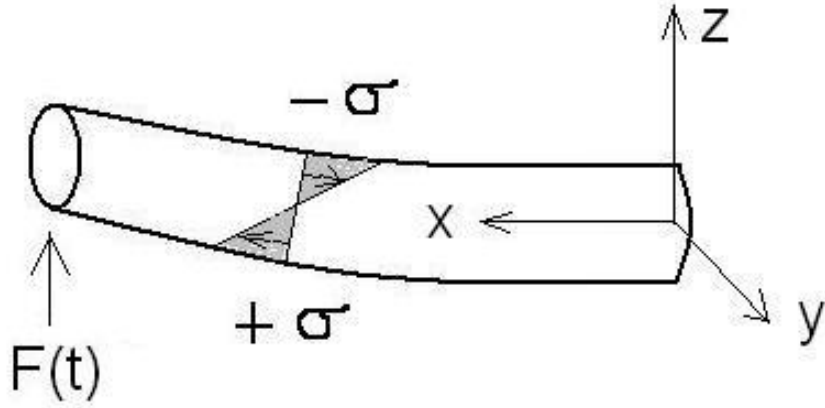
Figure 2.1: Antisymmetric axial stress distribution in a beam loaded in pure bending due to tip load $F(t)$.

2.2 Experiment

2.2.1 Proof of Concept Testing

Initial experiments are conducted for the purpose of verifying the existence of sensing magnetostriction before progressing to a more thorough characterization. The first sample studied is a thin plate of single crystal $Fe_{79}Ga_{21}$ with dimensions of 7.2 mm x 2.1 mm x 0.3 mm, with a [100] texture along the length. Two small brass cylinders 2 mm in diameter are placed in a vise and used to clamp one end of the Galfenol plate, resulting in a cantilevered beam. Figure 2.2 shows this setup prior to testing. In order to measure any change in magnetization of the sample, a commercially available GMR sensor from NVE Corporation is placed behind the brass clamps and level with the back of the beam. This sensor is a model AA002-02 powered with +5 V dc excitation, producing a linear sensing range up to 10 Oe with
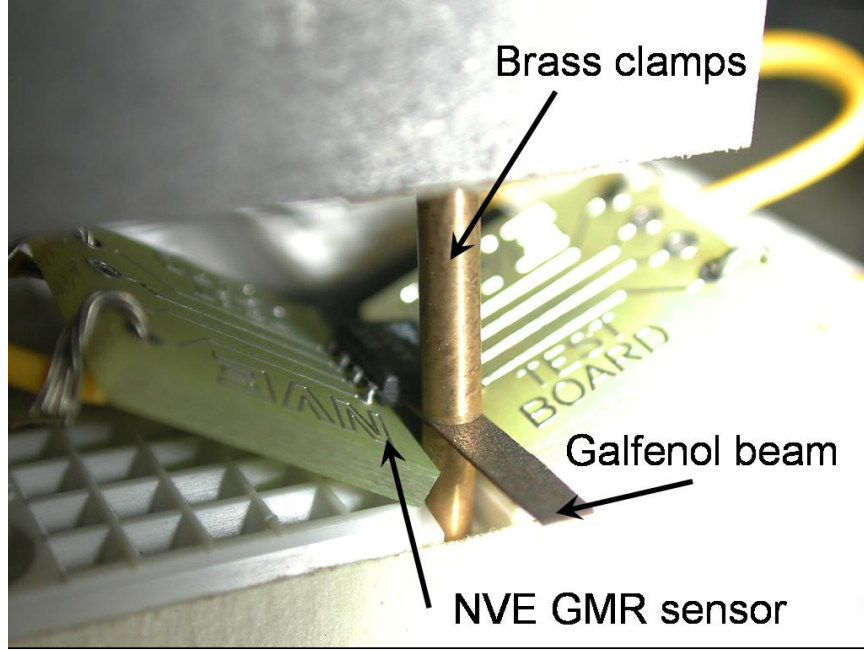
Figure 2.2: Photograph of the proof of concept experiment, showing the $Fe_{79}Ga_{21}$ plate cantilevered by brass clamps, with a GMR sensor located at the back for measuring the change in magnetization.

a sensitivity of 20 mV/Oe.

The simplest experiment consists of manually deflecting the beam tip and measuring the GMR output. Figure 2.3 shows the result from four consecutive downward loads on the beam, where the GMR detects a drop in magnetization due to each bend, albeit with a very small magnitude, i.e. less than 0.03 Oe. The weakness of this signal is due to the lack of an applied magnetic bias field, leaving the material in its state of magnetic remanence, known to be quite small due to the inherently low hysteresis in iron-gallium alloys. The second test attempts to identify how the beam responds under the application of loads of varying strength. Figure 2.4 reveals the GMR data from a set of alternating "weak" then "strong"

42

deflections applied to the beam tip, again with no bias field. The magnetic signal clearly distinguishes between the two loads, but the basic proof-of-concept nature of these experiments prohibits quantitatively characterizing the magnitude of these forces. There is a slight bump in the response of both of these figures approximately one second after the loading is completed, but as it went unnoticed at the time of the experiment it can only retrospectively be attributed to a minor repetitive error during the procedure.

Experiments are repeated in the presence of a permanent magnet placed above the beam, with the hope that beginning from a state closer to magnetic saturation will enhance the amount of stress-induced domain rotation and provide a larger amplitude output. The actual field from the permanent magnet will be far from uniform along the length of the beam, but each test is performed with a -2.6 Oe dc reading at the GMR sensor location. Similar to the previous trials, the beam is first loaded with a series of unidirectional deflections. The results in Figure 2.5 reveal that the GMR data now measures an amplitude of 0.4 Oe, much larger than that obtained in the absence of the bias field. As expected, the signal to noise ratio has improved as well. Results from the final test conducted on this sample are shown in Figure 2.6, where the beam is now excited with a manual sinusoidal-like tip loading. The most important feature of this data is the revelation that bending in both directions produces the same decrease in magnetization, resulting in a GMR signal that appears as a rectified version of the beam motion. The small variation in amplitude on alternating half-cycles is presumably due to a combination of unequal loading and nonuniform bias conditions caused by the permanent magnet position.
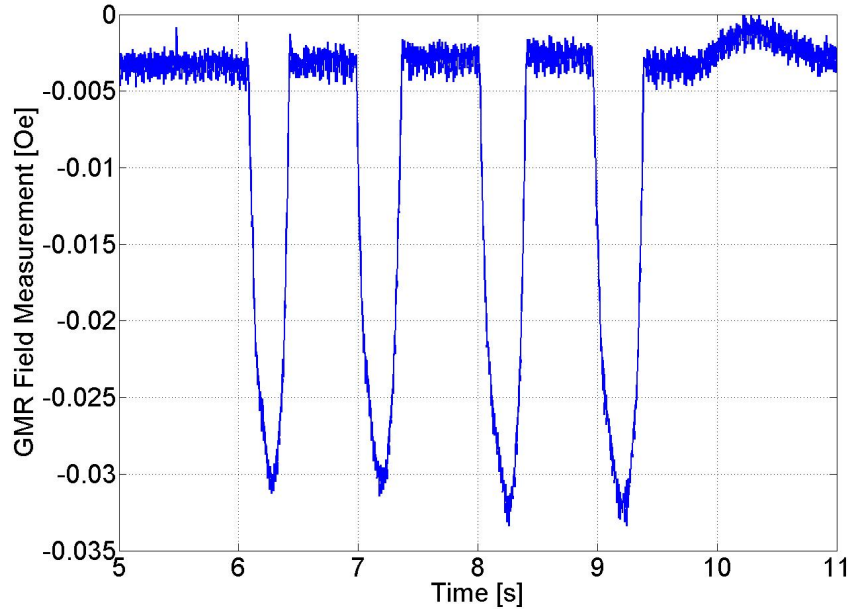
Figure 2.3: Magnetic field measured by the GMR sensor in response to four consecutive downward loads applied manually to the tip of the Galfenol beam.
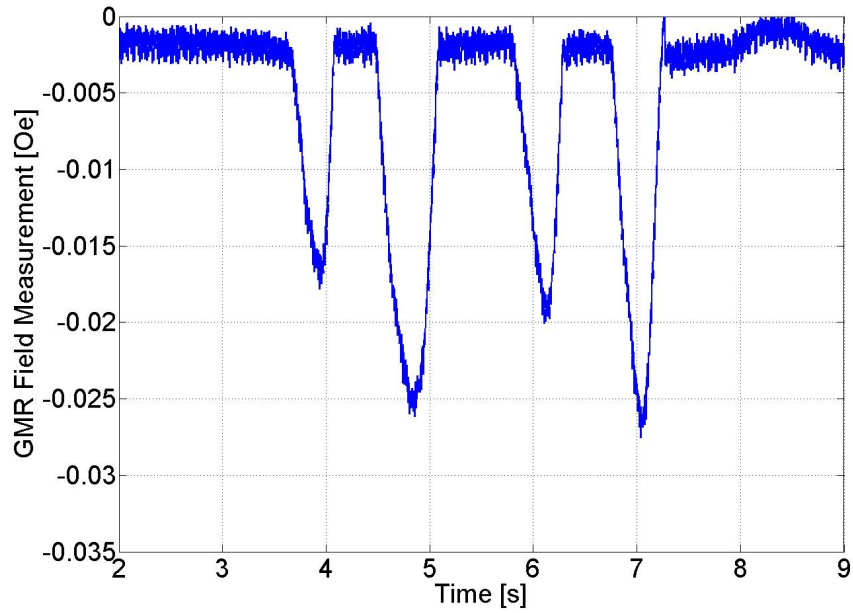
Figure 2.4: Magnetic field measured by the GMR sensor in response to alternating "weak" then "strong" loads.
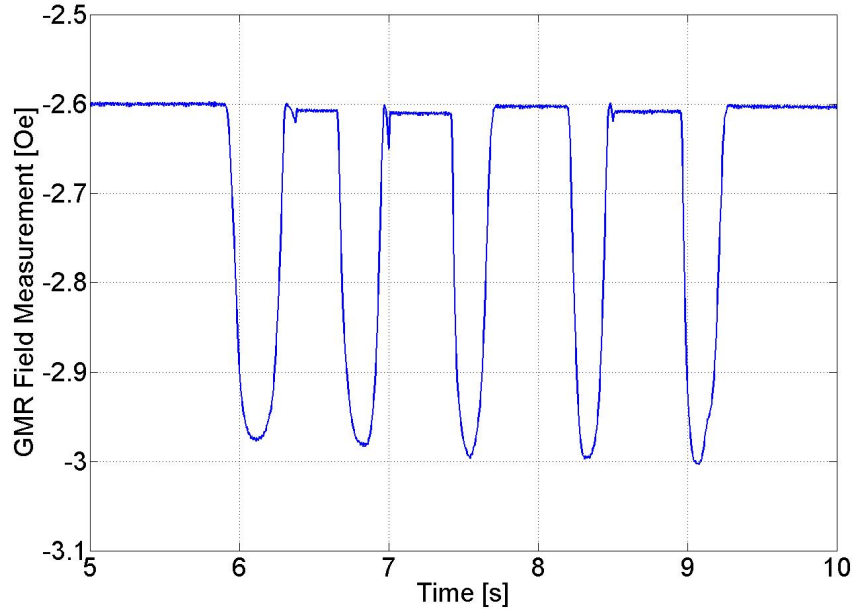
Figure 2.5: Beam response to tip loading with magnetic bias field. The amplitude of the signal has increased by an order of magnitude.
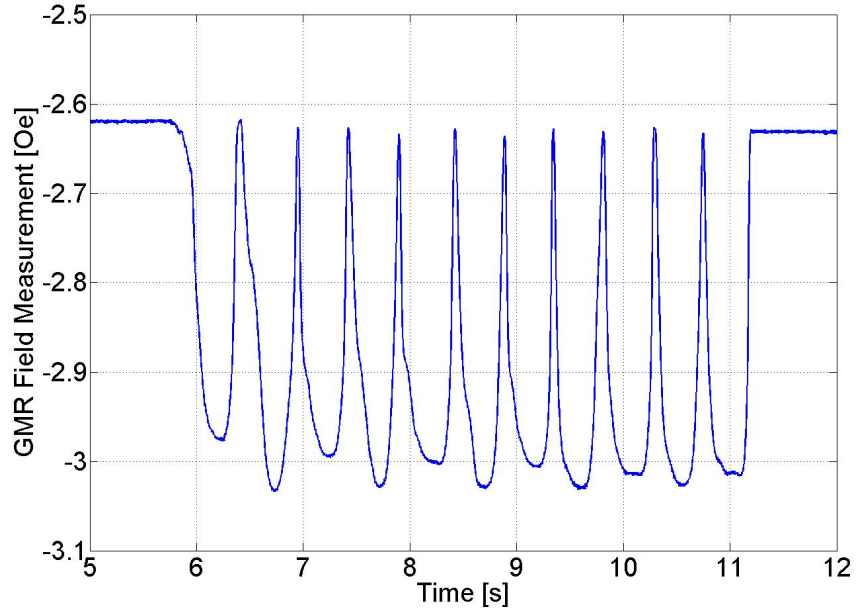
Figure 2.6: GMR signal when the Galfenol is bent with a sinusoidal tip load, revealing that the sample magnetization decreases uniformly regardless of the direction of beam motion.

2.2.2 Detailed Characterization of Galfenol Beam Bending

The initial proof of concept results were promising enough to warrant a more thorough investigation into the magnetic response of bending Galfenol beams. Several new samples were obtained, consisting of two single crystal rods grown with the modified Bridgman technique from Ames Laboratory and two production grade polycrystalline rods produced by the free stand zone melt method at Etrema Products, Inc. Each single crystal sample is extracted from the length of a [100] ingot, while the machined polycrystalline materials maintain a [100] grain orientation over only 44% of the cross section and have an average grain size of 630 μm. The specific properties of these samples are listed in Table 2.1 below.

The experimental setup for these four samples is simply a more refined version of the one used for the initial trials. New brass clamps were machined to fix the last 6.4 mm of each rod, creating a more reliable cantilevered configuration when placed in the vise. To measure the magnetic response of the samples, an AA002-02 GMR sensor is placed directly behind the rod centerline, attached to an optical positioning stage that allows manual control of the z coordinate at the back of the beam. In

Table 2.1: Specifications of the Galfenol samples used in bending experiments.

Sample	Crystallography	Composition	Dimensions
1	Single	$Fe_{84}Ga_{16}$	1.58 mm diameter, 32.7 mm long
2	Single	$Fe_{79}Ga_{21}$	1.58 mm diameter, 24.8 mm long
3	Poly	$Fe_{81.6}Ga_{18.4}$	3.18 mm diameter, 57.3 mm long
4	Poly	$Fe_{80.5}Ga_{19.5}$	3.18 mm diameter, 49.3 mm long

addition, the GMR data is corroborated by the use of conventional pickup coils of 26

AWG (for the polycrystalline samples) and 34 AWG (for the single crystal samples)

wire wound directly on each sample centered at the midlength. A Walker Scientific

MF-5D integrating magnetic fluxmeter is used to convert the voltage V induced in

each coil into a magnetic induction value according to the equation

$$B(t) = -\frac{1}{NA} \int V \, dt, \qquad (2.5)$$

where A is the area enclosed by the coil and N represents the number of turns.

A picture of this setup is presented in Figure 2.7. Another solenoid 34.7 mm in

diameter and 33.6 mm long is placed surrounding the entire configuration and used

to provide dc magnetic fields to bias the rods with a field of up to 10 Oe. The

diameter of this solenoid is considered sufficient for a uniform field throughout the

range of beam motion. Some additional tests call for replacing the large solenoid with

cylindrical permanent magnets 25.4 mm in diameter in order to increase the strength

of the bias field beyond what can safely be generated with the coil. Mechanical

excitation is provided by a dynamic shaker attached to the tip of each beam, with a

load cell and accelerometer placed at the shaker armature in order to measure both

the input load and the beam motion. Due to the shaker armature being magnetically

driven, the stray magnetic field from the shaker corrupted the pickup coil and GMR

signals at higher drive levels. As a result, in many such cases the beam vibration

was manually excited with approximate sinusoidal loading.

With this setup in place, the first thing to investigate was what effect the

various compositions and crystal structures of the four samples had on the sensing
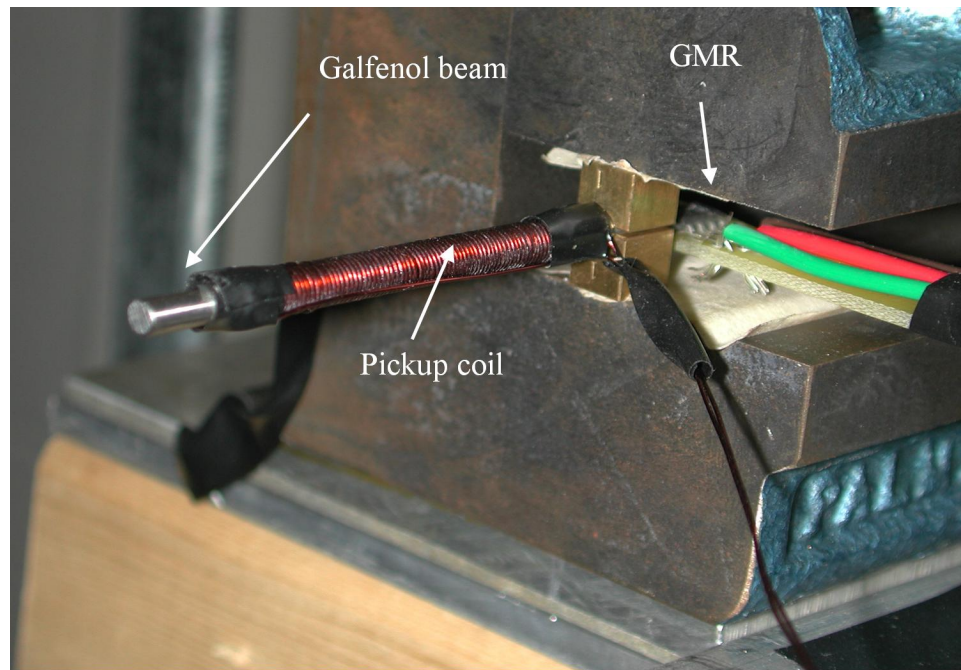
Figure 2.7: Photograph of the experimental setup used to test the four Galfenol rods. Not shown are the cylindrical magnets that would surround the entire beam and the dynamic shaker typically mounted to the beam tip.

behavior. Each beam was driven with a 10 Hz signal to the shaker, with the load applied varying with each sample in order to normalize the maximum stress at 85 MPa despite the different beam dimensions. The amplitude of magnetic induction change measured with the pickup coils is plotted versus bias field in Figure 2.9. These results agree with two known trends of the iron-gallium alloy. First, by comparison with Figure 2.8, it is clear that sample #1 has the best composition for maximizing magnetostrictive transduction, with sample #3 following closely behind and the other two being worse off. The other notable trend [7] is that due to the large variation in texture of the polycrystalline samples, they are outperformed in terms of strain and sensitivity compared with single crystal materials. This combination leads to the single crystal $Fe_{84}Ga_{16}$ sample being the optimum of the four with regards to bending sensor performance, and as such this composition is used exclusively in all subsequent macroscale tests.

Characterization of the GMR sensor voltage is done by direct comparison with the pickup coil integrated magnetic induction signal. The data presented in Figure 2.10 shows that qualitatively the GMR appears identical to the pickup coil, including increasing with applied field and detecting the significant 60 Hz noise in the data. The amplitude of the GMR measurements is over an order of magnitude lower than the coil however, due primarily to measuring the stray field in the small air gap between the back of the rod and the actual sensor element. As the pickup coil wound directly on the sample provides a more accurate measurement of the net internal magnetization in the rod, it will be relied upon for validating the magneto-mechanical model presented in Chapter 3.
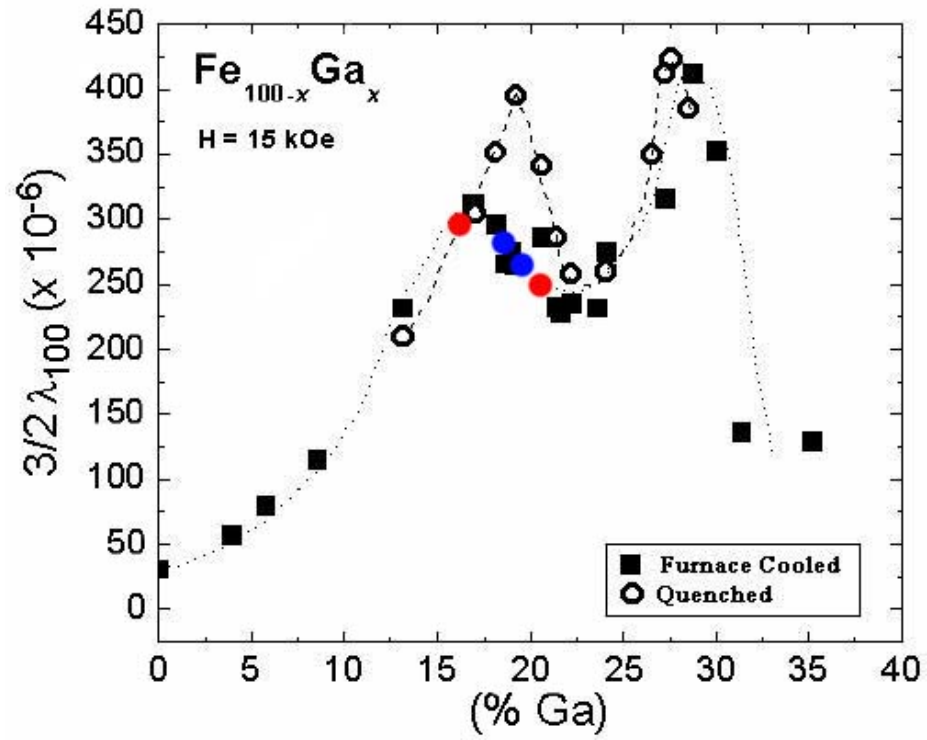
Figure 2.8: Measured magnetostriction $(3/2\lambda_{100})$ versus gallium content [22], highlighting the compositions of the four samples used for bending experiments (red are single crystal, blue are polycrystalline).
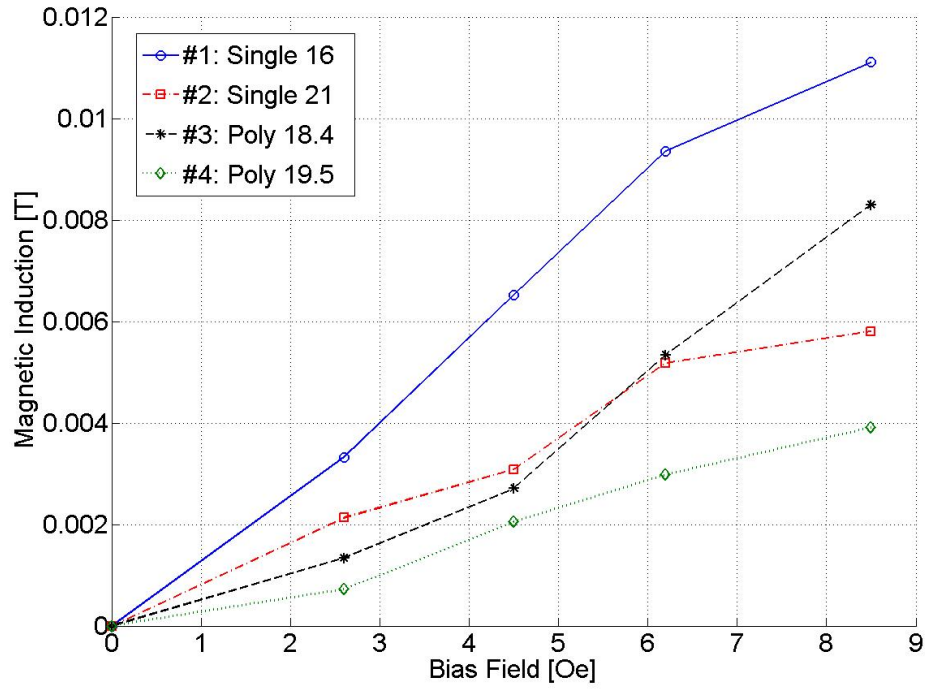
Figure 2.9: Amplitude of magnetic induction change to a normalized load of 85 MPa as measured with the pickup coil for each of the four Galfenol samples, and the effect of incremental increases in applied bias field.
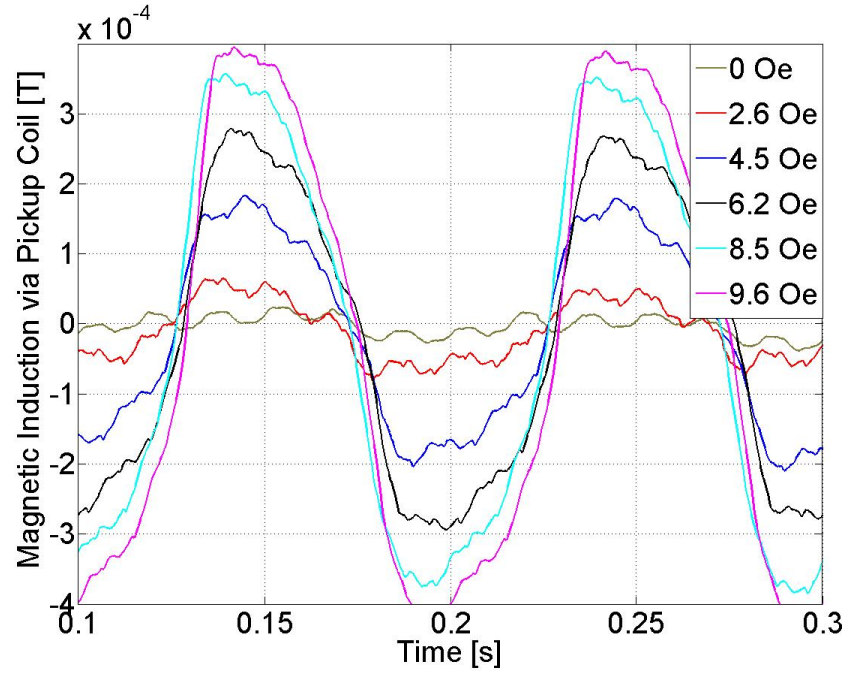
(a)
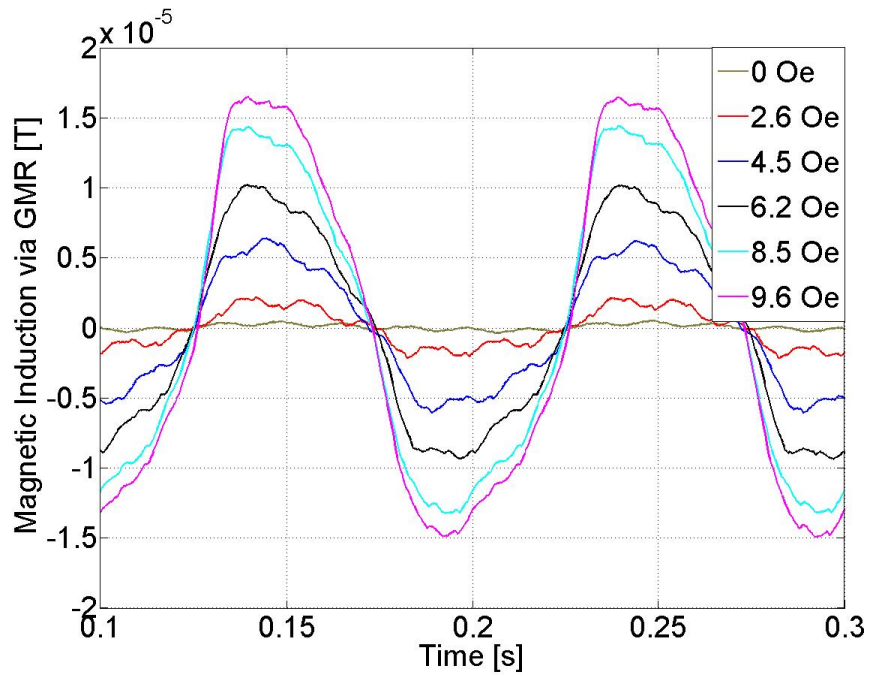
(b)

Figure 2.10: Measured induction with increasing dc bias from pickup coil (a) and GMR sensor (b), showing that the signals are a match with the exception of the amplitude, where the GMR output is over an order of magnitude smaller due to its position at the rear of the sample.

The other concern about using the GMR to measure the magnetic induction is whether or not the specific placement of the sensor has an effect on the detected signal. As the actual magnetoresistance elements are located on a thin layer of silicon, it is conceivable that they may be more sensitive to the magnetization of the particular beam plane that they are adjacent to. In most conventional magnetostrictive applications this would not be a concern, but because in this case the beam stress (equation (2.4)) directly varies with the height coordinate z, it may prove to be critical in the discussion of Galfenol beam bending. To this end, the GMR signal in response to tip excitation with a 4.5 Oe bias is measured at five different heights behind the beam: slightly above the top surface of the beam, below the top surface, at the center, above the bottom surface, and slightly below the bottom surface (see Figure 2.11). If the sensor detected the stress induced magnetization specifically from each plane, one would expect maximum transduction near the top and bottom surfaces and no significant output at the beam neutral axis. Instead, it is observed in Figure 2.12 that an equivalent periodic signal is measured at each point, indicating that what is being measured is the intended volume average induction for the sample. The diminished amplitudes at the points above and below the actual cross section of the rod indicate that less flux diverges out to these positions, and the fact that they are unequal suggests that they are not equidistant from their respective surfaces, which is easily possible due to experimental error. The additional spikes in the one measurement were alleviated in all further tests by tightening the beam-shaker connection, but unfortunately this data was not recollected.

Another approach to this is to look at the effect of bending the beam in
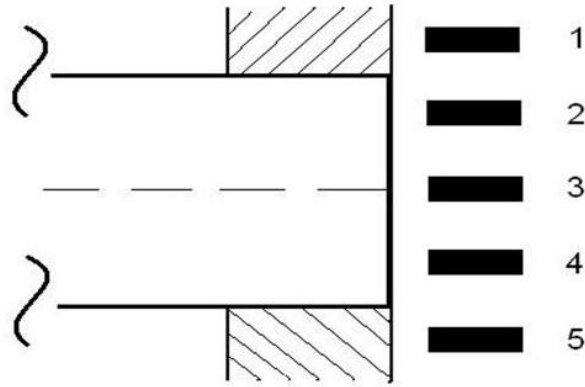
Figure 2.11: Diagram of the five different planes at which the GMR data was measured.
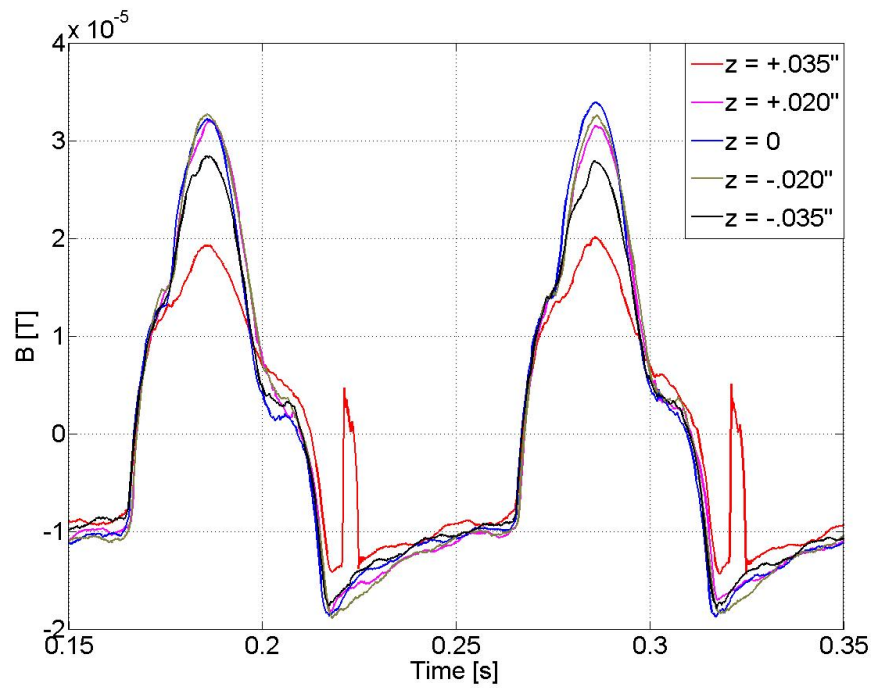
Figure 2.12: Measured data from the GMR sensor at the five positions behind the beam, showing a decrease in signal only when the sensor is placed outside of the cross section of the rod.

different directions. The previous experiment bent the beam in the vertical plane, but considering the circular cross section of the sample it could just as easily be bent in any direction. The advantage this simple test provides is that by deflecting the rod perpendicular to its original orientation the stresses now arise along the sides of the beam rather than on the top and bottom. If there is still any chance that the GMR measurement is weighted heavily toward the local stress effects, this loading configuration should look dramatically different. Fortunately, the data in Figure 2.13 reveals this not to be the case, as bending in different directions produces the same GMR signal and strongly corroborates the previous data that the measurement is the volumetric average of magnetic induction. The significance of this result is that for use in applications such as the proposed nanowire sensor devices, GMR sensors can detect the net induction from an active material regardless of exact position or excitation direction.

With a thorough understanding of the sensing mechanism, some final data is collected from the vibrating $Fe_{84}Ga_{16}$ rod that more accurately characterizes the response first observed in the initial thin plate samples of Figure 2.6. The result of primary interest is that with a surrounding permanent magnet providing a bias field of 67 Oe, a 4 N force applied manually to the beam causes a very large magnetic induction change of 0.3 T, as measured by the pickup coil. Figure 2.14 shows that this signal also still appears as a rectified sinusoid, a phenomenon more fully discussed in Section 2.3.

Early results, like those in Figure 2.9, suggested an increase in magnetic output with stronger bias fields. The use of permanent magnets allows for much larger
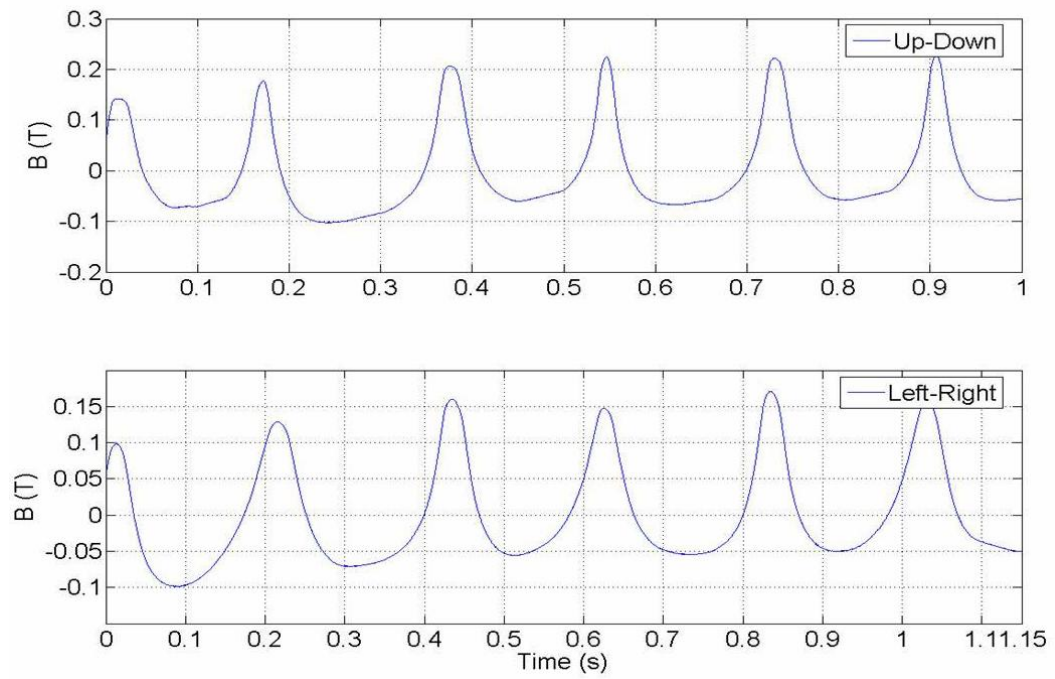
Figure 2.13: Measured GMR response to bending the beam in different directions relative to the sensor plane.
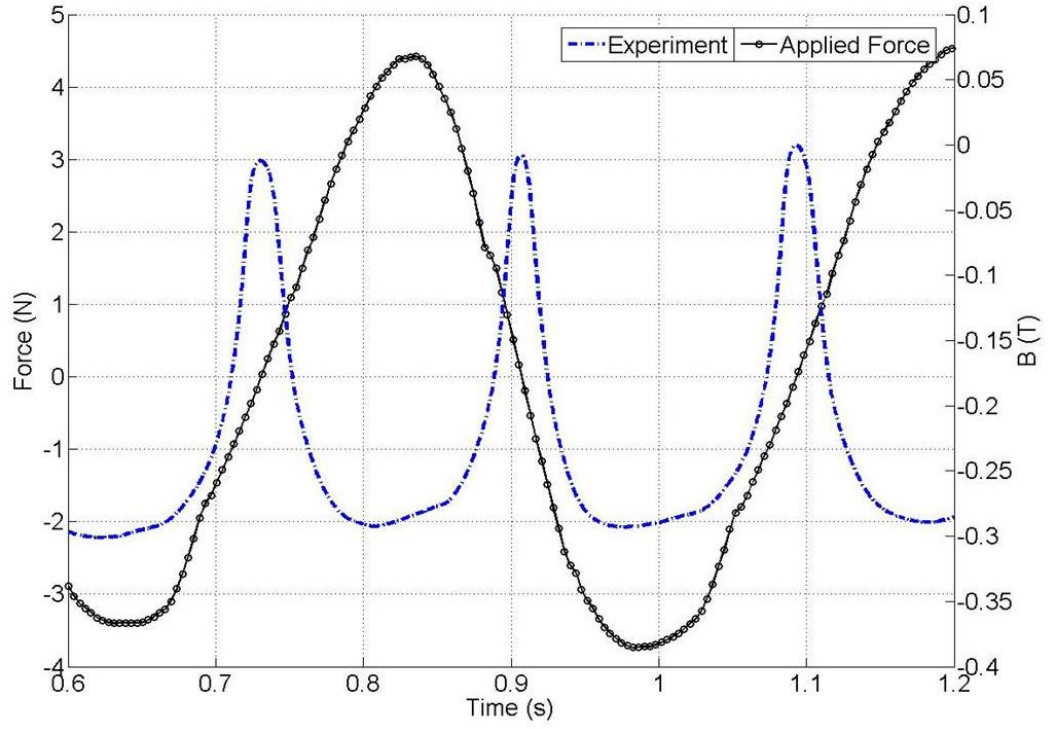
Figure 2.14: Experimental 0.3 T variation in magnetic induction measured with a pickup coil of the single crystal $Fe_{84}Ga_{16}$ beam with a 67 Oe bias field subjected to manual sinusoidal-like force input of 4 N.
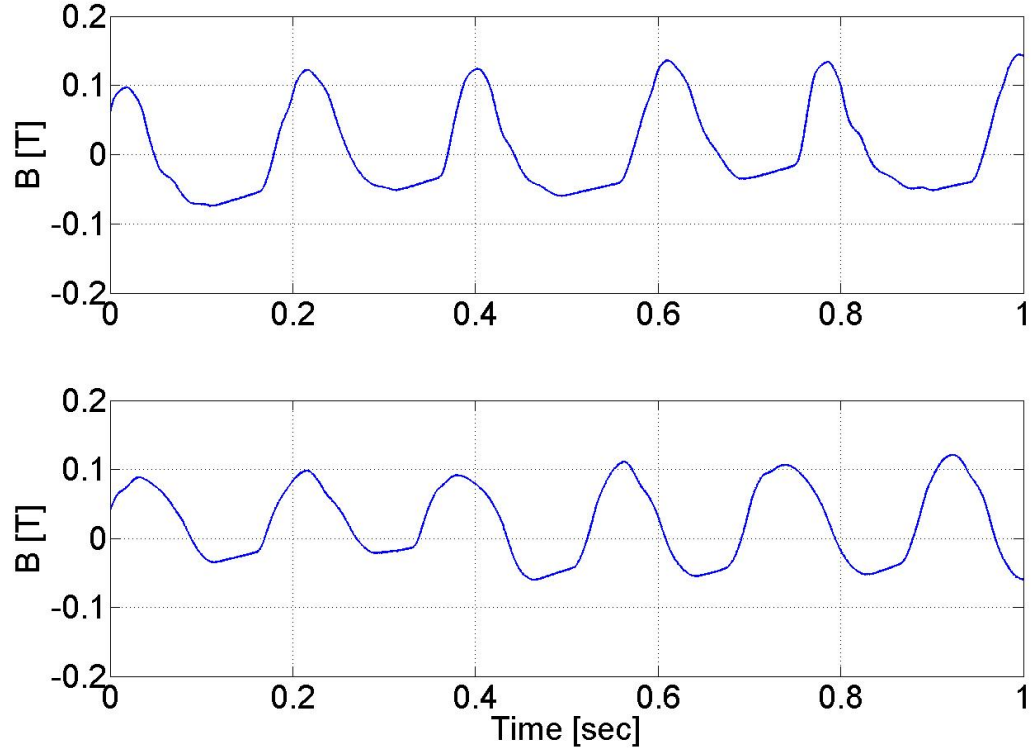
Figure 2.15: Measured change in magnetic induction from the Galfenol beam in the presence of 22 Oe (top) and 89 Oe (bottom) of magnetic bias field. While there is some minor variation in amplitude due to discrepancies in the manual loading, the sample behaves consistently across this large range of fields simplifying potential sensor design.

bias fields to be generated than was practical with the solenoid. Results in Figure 2.15 reveal that there is very little variation in measured induction for bias fields ranging from approximately 20 - 90 Oe. The very low bias fields used during the initial testing were clearly insufficient to saturate the sample, but once saturation is reached the beam behaves rather consistently. This result bodes well for deploying Galfenol beams as robust bending sensors because it implies moderate perturbations in applied field will not be detrimental to the signal quality, eliminating one possible design constraint.

2.2.3 Testing of Rolled Galfenol Sheet

A large volume of Galfenol research focuses on deformation processing to optimize and control specific magnetic and metallurgical properties. Much of this has dealt specifically with hot rolling Galfenol sheets [102] for the purpose of generating thin laminae of active material that can be used in both actuator and sensor applications. The material that results from the hot rolling procedure typically has a very large aspect ratio and excellent flexibility, and therefore was tested in a similar manner to the Galfenol rods in order to further the understanding of not only the beam bending magnetostriction but also the behavior of the rolled material in general.

The sheet originated as a polycrystalline $Fe_{81.3}Ga_{18.7}$ button that was doped with the addition of 2 at.% molybdenum to facilitate ductility and grain boundary cohesion throughout the rolling process. Succesive passes in the mill were conducted from 900 °C down to 600 °C, resulting in a sheet that is 216 mm long, 29.2 mm wide, and 0.18 mm thick. The beam was clamped in a vise and placed on its edge to prevent it from sagging under its own weight. The AA002-02 GMR sensor was once again positioned at the base of the material, and an accelerometer was attached to one face of the beam at the middle of the free length, as shown in Figure 2.16. The first resonance frequency of this beam was experimentally measured to be only 3.1 Hz. Excitation was provided by plucking the sample and measuring both the transient vibration and the fluctuating magnetic field caused by the changing magnetic induction.
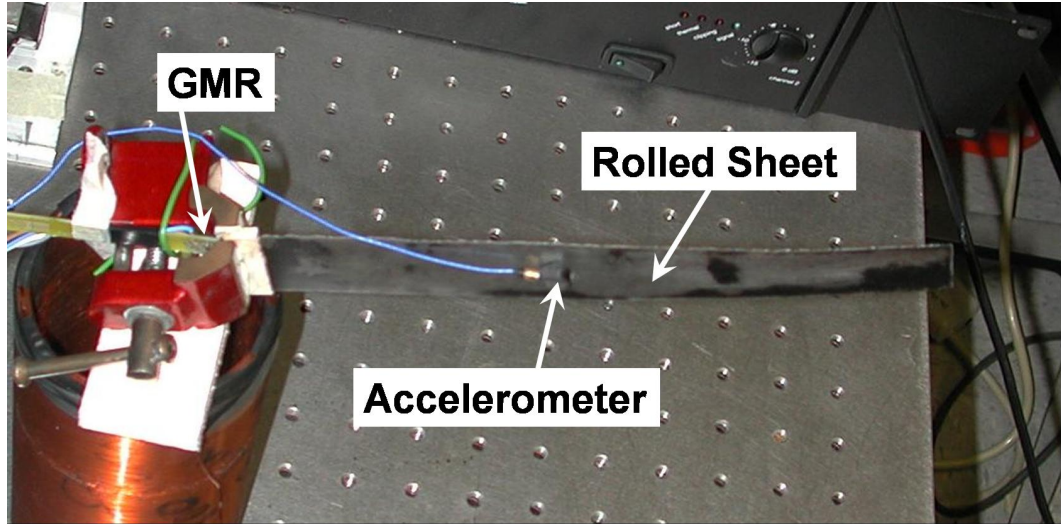
Figure 2.16: Photograph of the 0.18-mm thick rolled polycrystalline sheet that has been cantilevered in a vise for dynamic testing. The GMR sensor at the base measures changes in magnetization and the accelerometer records the beam motion.

Results from this test are plotted in Figure 2.17. The top graph shows beam displacement (from integrating the accelerometer signal twice) and magnetic field change from the GMR. Note that as both signals damp out the magnetic field remains at twice the frequency of vibration, in agreement with the previous experiments. The bottom graph depicts the Fourier transform of each signal, where the GMR data is primarily at 6.2 Hz but does contain some component of the natural frequency of 3.1 Hz. This is most likely due to the fact that the GMR sensor will inherently measure some magnetic field change attributed solely to the motion of the magnetic material in front of it. The earlier results from the Galfenol rods do not exhibit this phenomenon because the stiffer beams had much lower amplitudes of vibration and the amplitude of the bending induced signal was improved due to
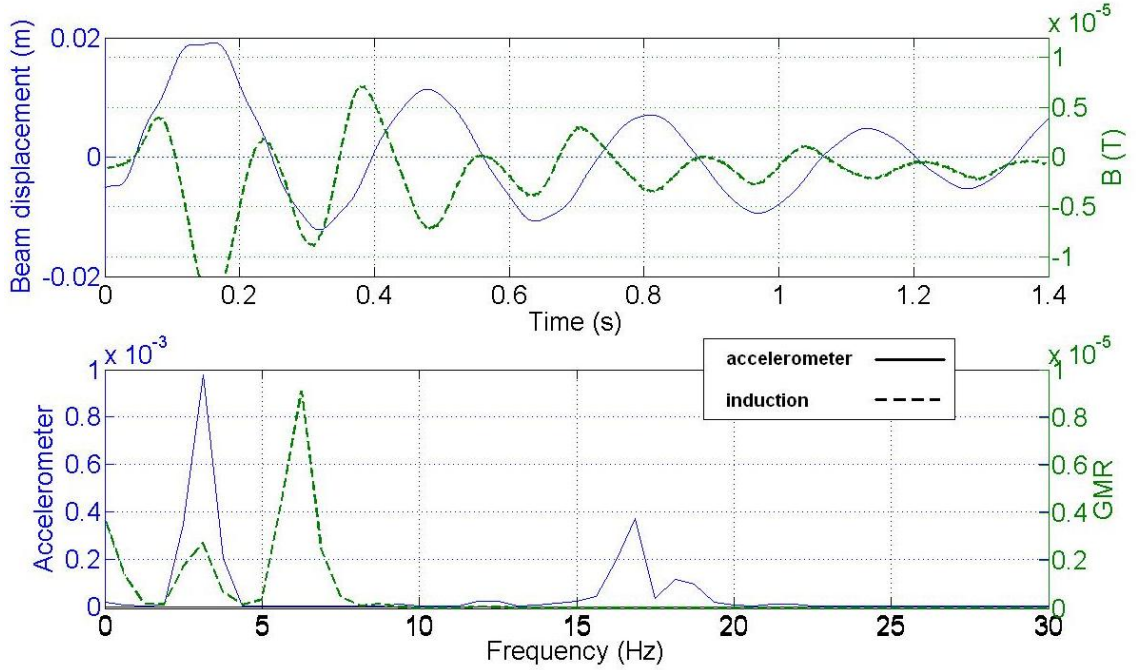
Figure 2.17: Measured time signals from the accelerometer and GMR (top) in response to plucking the the rolled Galfenol beam. The Fourier transform of these signals (bottom) shows that while the magnetization still appears predominately at twice the frequency of beam vibration, there is some purely motional component as well.

the application of a magnetic bias field.

There are a few key points to take away from this data. The first is that the as-rolled material maintains a useful level of magnetostriction, despite the lack of optimization via atmospheric annealing and further additives that have since been discovered. This offers strong potential for using rolled sheets in applications ranging from single thin film sensors up to bulk structures produced by joining multiple laminae. The second thing to note is that the presence of multiple harmonics in the GMR output must be considered in the structural design and signal processing algorithms of the nanowire sensors.

2.3 Discussion

The origin of the magnetic induction change occurring at twice the frequency of excitation is best explained by looking at the schematic in Figure 2.18. This diagram shows that when the material starts in an axially magnetized state and is subjected to pure bending loads, the tensile side of the beam has an insignificant effect on the magnetization as the moments are already aligned in the preferred direction. In contrast, the compressive stresses want to orient the moments perpendicular to the beam axis, and as such can cause a full 90° of rotation resulting in a net decrease in sample magnetization. Because the compressive loads peak during each half cycle of beam oscillation, the magnetic signal appears as the rectified sinusoid observed in the data. This fundamental result supports using the magnetostrictive sensing properties of Galfenol in bending applications despite the antisymmetric stress distribution.

Some additional results can be explained by examining the curves in Figure 2.19. This data [7] shows that when a modest bias field is applied to the material it easily reaches its magnetic saturation, but that the application of compressive stress shears the curves downward, reducing the magnetization and requiring additional field H in order to return to saturation. While the data does not explicitly show the effect of tensile stress it is known to cause the opposite shift, namely forcing the curves upwards until they reach the theoretical limit of a horizontal line at saturation across all positive fields. The close proximity of the unstressed condition to this limiting state clearly demonstrates how the tensile stresses will have only a

trivial effect on the magnetization.

The implications for this with regards to corroborating the data are as follows. First, it is clear from the magnetic softness of the material that small increases in applied bias field will greatly improve the initial magnetization, and therefore the magnitude of the drop in B when stress is applied, reaching a maximum when the material has been saturated. This explains the increasing effect that small bias fields had on the sensing response in Figure 2.9. In addition, once saturation is reached at approximately 15 Oe, additional field has no dramatic effect on the initial unstressed state, in agreement with the observation in Figure 2.15. Finally, the magnetic induction curves in Figure 2.19 also reveal that while achieving a stress-induced decrease in B is not dependent on field, the actual compressive stress that causes the maximum drop certainly is. For example, with an applied field of 100 Oe, the magnetic induction is essentially unaffected by stresses up to 30 MPa, but above 30 MPa it changes sharply. With a field of only 20 Oe however, the first 15 MPa of compression cause a larger drop in induction than any higher increment. Therefore, this suggests that while the beam magnetization is most sensitive to only a narrow range of stresses depending upon the applied field, so long as these stress levels occur somewhere in the beam (recall the spatial variation in equation (2.4)) then a consistent magnetic induction measurement will occur. This verifies the critical assumption that the GMR sensors detect the volume average of magnetization rather than only local fluctuations. This concept will be expanded upon further using the analytical model developed in Chapter 3.
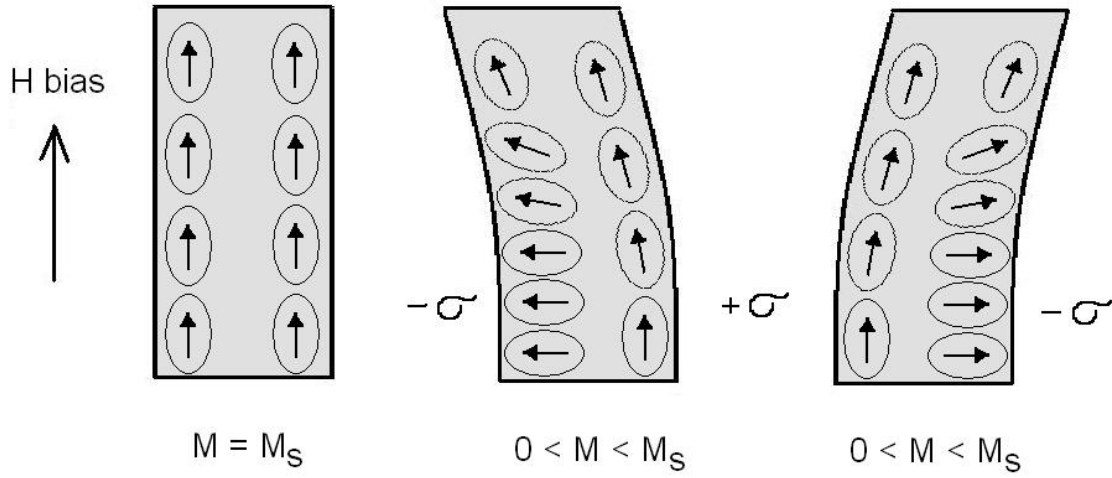
Figure 2.18: Schematic of the sensing mechanism in bending magnetostrictive materials.
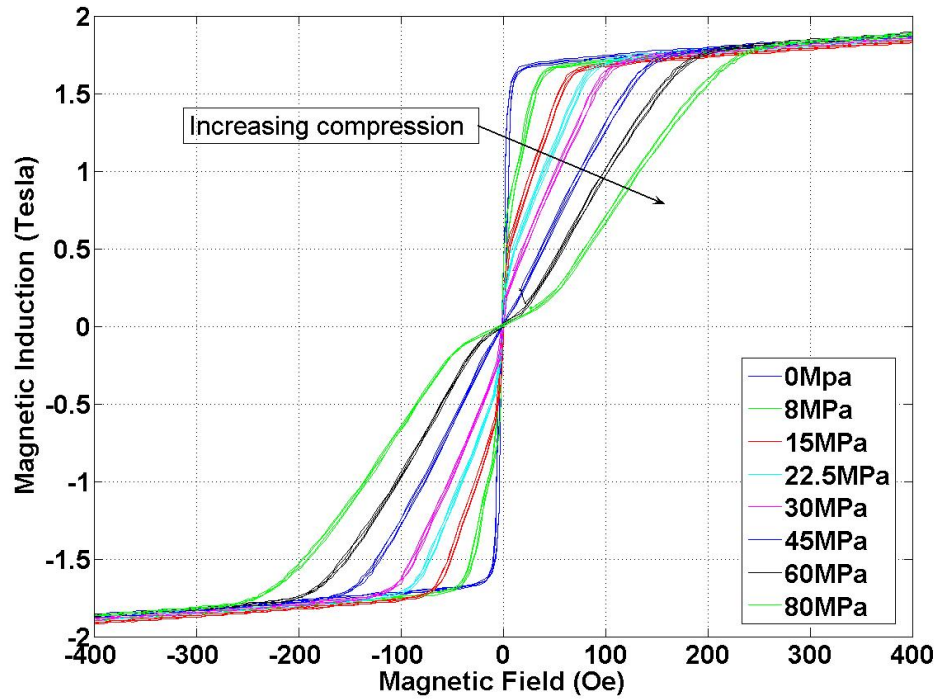
Figure 2.19: Experimental induction vs. field curves for single crystal Fe$_{84}$Ga$_{16}$ with increasing compressive stress [7].

Chapter 3

Magneto-mechanical Modeling of Bending Behavior

3.1   Modeling Introduction

This chapter outlines the development of a coupled magneto-mechanical model that can simulate the sensing behavior of magnetostrictive beams subjected to various magnetic fields and bending loads. The purpose of this model is to have a means of verifying the experimental data and predicting the output from arbitrary structures. One critical goal of the model is to accurately capture the rectified magnetic induction response of the beam in bending, and to do so in a manner that extends naturally from existing magnetostriction models that have been presented in the literature.

The most straightforward approach relies on the constitutive piezomagnetic expressions coupling stress and strain to the magnetic field and induction. While these equations are inherently limited to narrow regions of linear transduction, the nonlinear magnetostriction can be simulated with the use non-constant coefficients and several simplifying assumptions. Although this technique works quite well, it is entirely empirical and lacks the elegance and flexibility of a more thorough nonlinear model.

A number of advanced approaches have been taken in the past for simulating the magnetoelastic effects in magnetostrictive alloys. As Terfenol-D was the primary

material of interest, these models generally focused on accurately capturing the one-dimensional actuation strain and the significant hysteretic losses. Perhaps the most widely regarded of these is the Jiles-Atherton model [66, 67, 68], which considers magnetization processes through both reversible domain rotation and irreversible domain wall motion pinned by defect sites. The coupling with stress is incorporated via a magnetic field component that depends on magnetoelastic interactions, H_σ, that is added to the effective field H_e. One potential advantage of using this model for iron-gallium alloys is that the hysteresis can be reasonably ignored, which reduces the complexity and computation time by focusing solely on the anhysteretic magnetization $M_{an} = M_s \left(\coth \left(H_e/a \right) - a/H_e \right)$ described by the Langevin function of the effective field and an empirical constant a. Even with this simplification, the model still needs to be solved iteratively, models magnetostriction phenomenologically, and is inherently limited to one dimension. Dapino [32, 33] advanced the model by including the dynamics of the active material, but the above limitations still hold.

An energy based method for modeling smart materials was developed by Smith [128, 129] that applies Boltzmann statistics to the Gibbs free energy to construct a hysteresis kernel. One of the most prominent characteristics of this approach is that it is universally applicable to any hysteretic ferroic material typically used in smart structures because of the analogous energy expressions for the magnetic and electric regimes. While this model has the same overall drawbacks as the Jiles-Atherton method, its inclusion of stress effects by the simple addition of an appropriate energy term is a preferred feature.

The most appropriate energy model for capturing the unique behavior of iron-gallium alloys appears to be the Armstrong method [5]. It was originally conceived for modeling Terfenol-D, but its suitability for simulating Galfenol actuation performance became readily apparent over the past few years [115, 101, 47]. The model sums energy terms for the magnetocrystalline anisotropy, magnetoelastic coupling, and externally applied field, the minimization of which gives the probability of the magnetization aligning in any given direction. By performing a weighted summation over the volume, this model provides the average bulk property of the sample. The largest advantages of this method are that it (1) accounts for crystallographic effects; (2) is formulated in three dimensions; and (3) is computationally straightforward. Recent extensions [7] have further improved upon the model by modifying the original energy terms to more accurately capture the physics of the material.

Regardless of the model used to calculate the magnetization, the stress variable needs to reflect that the Galfenol samples in this application are bending beams rather than axial rods. Because the bending sensor operation makes use of well defined beams that exhibit linear elastic deformations, the Euler-Bernoulli beam equation provides a direct means of calculating the mechanical loads in the sample in both static and dynamic applications. Therefore, the overall model relies on beam theory to determine the stress distribution throughout the material and inputs that value as a parameter in the Armstrong magnetization model, the result of which is converted into the bulk magnetic induction change. This in turn is comparable with experiment for model validation.

3.2 Beam Mechanics

The vibration of bending beams is mathematically represented by a fourth order partial differential equation with respect to the transverse deflection $w(x, t)$. The most common model, known as the Euler-Bernoulli beam theory, involves the critical assumption that planes normal to the neutral axis remain straight and normal during the deformation. As a result, the rotation of a differential beam element is considered negligible compared to the vertical translation and the shear deformation is ignored. These assumptions are particularly valid for thin beams with an aspect ratio of greater than 10, suitable for both the bulk samples in Chapter 2 as well as the Galfenol nanowires.

The Euler-Bernoulli equation can be derived by a simple force balance performed on an arbitrary differential beam element of length dx such as that sketched in Figure 3.1. The inertial force $m\ \partial^2 w / \partial t^2$ must be balanced by the tension T, shear S, moment M, and distributed loading $f(x, t)$. The summation is

$$\sum F = (T + \frac{\partial T}{\partial x}dx)\ \sin(\frac{\partial w}{\partial x} + \frac{\partial^2 w}{\partial x^2}dx) - T\ \sin(\frac{\partial w}{\partial x}) + S\ \cos(\frac{\partial w}{\partial x}) \tag{3.1}$$
$$-(S + \frac{\partial S}{\partial x}dx)\ \cos(\frac{\partial w}{\partial x} + \frac{\partial^2 w}{\partial x^2}dx) - m\frac{\partial^2 w}{\partial t^2}dx + f(x, t)\ dx,$$

which with the use of the small angle assumptions

$$\cos(\frac{\partial w}{\partial x}) \quad \approx \quad 1 \tag{3.2}$$

$$\sin(\frac{\partial w}{\partial x}) \quad \approx \quad \frac{\partial w}{\partial x}, \tag{3.3}$$

can be reduced to

$$f(x, t) - m\frac{\partial^2 w}{\partial t^2} - \frac{\partial S}{\partial x} + \frac{\partial}{\partial x}(T\ \frac{\partial w}{\partial x}) = 0. \tag{3.4}$$

The sum of the moments in the system can be done in a similar manner to reveal that

$$\frac{\partial M}{\partial x} = S, \tag{3.5}$$

and from mechanics of materials [111] it is known that

$$M = EI \frac{\partial^2 w}{\partial x^2}. \tag{3.6}$$

Substituting equations (3.5)-(3.6) into equation (3.4) yields the standard form of the Euler-Bernoulli beam equation,

$$-\frac{\partial^2}{\partial x^2}(EI(x) \frac{\partial^2 w}{\partial x^2}) + \frac{\partial}{\partial x}(T \frac{\partial w}{\partial x}) + f(x,t) = m \frac{\partial^2 w}{\partial t^2}. \tag{3.7}$$

This equation can alternatively be derived via an energy method such as Hamilton's principle. The potential energy V_{pe} includes the strain energy of a bending beam

$$V_{pe} = \frac{1}{2} \int_0^L EI(x) \, (\frac{\partial^2 w}{\partial x^2})^2 dx, \tag{3.8}$$

and the kinetic energy T_{ke} has the conventional form

$$T_{ke} = \frac{1}{2} \int_0^L m(x) \, (\frac{\partial w}{\partial t})^2 dx. \tag{3.9}$$

Setting the variation of the Lagrangian $L_e = T_{ke} - V_{pe}$ equal to zero and integrating by parts yields the correct differential equation (3.7) with the boundary conditions properly included.

The resultant expression is a separable partial differential equation of the fourth order that can be solved by assuming a response $w(x,t) = W(x)Y(t)$. Solving the spatial equation for $W(x)$ requires four known boundary conditions, typically
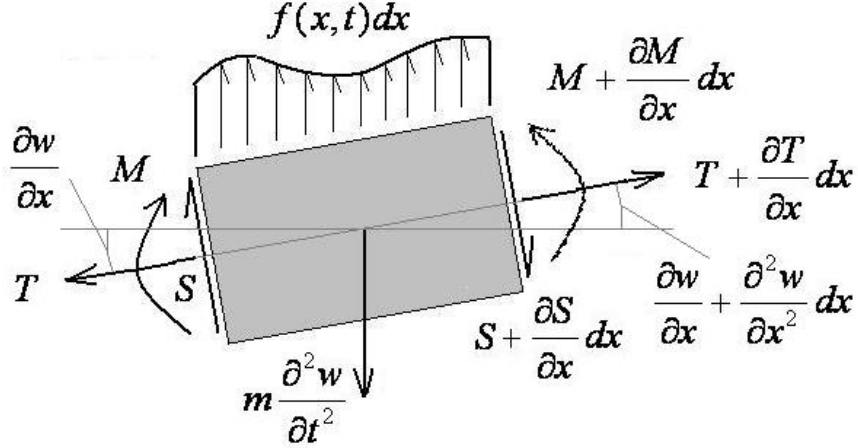
Figure 3.1: Free body diagram of a beam element in pure bending.

chosen from a list of known entities including fixed, free, pinned, and spring supported ends [98]. The result is a characteristic equation for that particular beam configuration that represents the shape of the deflected beam. Section 5.3 provides a thorough analysis of this procedure for a cantilevered beam.

The amplitude of vibration takes the form of this shape function modulated by the periodic signal $Y(t)$ that is dependent on the forcing function. For comparison with the experimental data in Chapter 2, the beam is considered cantilevered with an applied tip load of $F(t)$ that is input directly from the measured load cell data. This results in a total beam deflection and curvature of

$$w(x,t) = F(t)/2 \left(\sin(px) - \sinh(px) - C' \left(\cos(px) - \cosh(px) \right) \right), \quad (3.10)$$

$$w''(x,t) = F(t)\, p^2/2 \left(-\sin(px) - \sinh(px) - C' \left(-\cos(px) - \cosh(px) \right) \right), \quad (3.11)$$

$$C' = \frac{\sin(pL) + \sinh(pL)}{\cos(pL) + \cosh(pL)}, \quad (3.12)$$

where $p = (m\omega^2/EI)^{1/4}$. With the assumption of linear elastic behavior, the bending

70

stress in the material can be written with the modified Hooke's Law presented in equation (1.1),

$$\sigma = E(\varepsilon - d_{33}H_0), \tag{3.13}$$

assuming a constant applied bias field H_0. Mechanics of materials relates the strain in a bending beam with the curvature as $\varepsilon = w''(x,t)\,z$, yielding the total stress distribution throughout the material:

$$\sigma(x,z,t) = E\left(\frac{\partial^2 w(x,t)}{\partial x^2}\,z - d_{33}H_0\right). \tag{3.14}$$

These values of stress are used as an input variable to the magnetic coupling models discussed in the following sections. It is noted that in many cases magnetostrictives require bi-directional coupling [101] in the model, iterating the effects of the stress on the field and vice versa. Due to having a free end condition however, the beam is able to extend as field and stress fluctuate and no internal stresses are developed due to a blocked condition. As such, the errors due to using only uni-directional coupling are minimized.

3.3 Constitutive Model

3.3.1 Implementation

The most direct way of modeling the magneto-mechanical coupling is with the linear constitutive piezomagnetic equations, which have the drawback of being valid only over small operating ranges of applied field or stress. Specifically, equation

(1.2) is rewritten here for the magnetic induction B,

$$B = d_{33}^*\sigma + \mu H, \tag{3.15}$$

which is the sum of the magnetic effects of the material permeability μ multiplied by the magnetic field H and the stress coupling via the coefficient d_{33}^*. As mentioned in the motivation for the macroscale experiments, it is the product of this constant and the antisymmetric stress that caused the original doubts about the validity of a bending mode sensor. As such, the performance of this model hinges entirely on the formulation of the d_{33}^* coefficient. Early experimental evidence [8] revealed that this sensitivity parameter does in fact vary substantially as a function of both stress and field, as shown in Figure 3.2. Incorporating these effects with a non-constant $d_{33}^*(\sigma, H)$ coefficient in equation (3.15) better captures the physics of the problem and produces the anticipated non-zero output.

Implementing this requires fitting a high order polynomial P_H to each data curve presented in Figure 3.2, focusing on the peak range of -6 to -100 MPa. Above and below this range, the apparent asymptotic value of 2 T/GPa from beyond -100 MPa is assumed. Given a magnetic bias field between the experimental limits of 22 and 111 Oe, the $d_{33}^*(\sigma, H_0)$ curve for an arbitrary field is generated by the linearly weighted combination of the two bounding reference polynomials. For example, if modeling an applied bias field of 50 Oe, the data used would be

$$d_{33}^*(\sigma, 50) = \frac{50 - 45}{67 - 45} P_{67} + \frac{67 - 50}{67 - 45} P_{45}. \tag{3.16}$$

With this resultant function, the coupling coefficient can be interpolated at any field and stress combination.
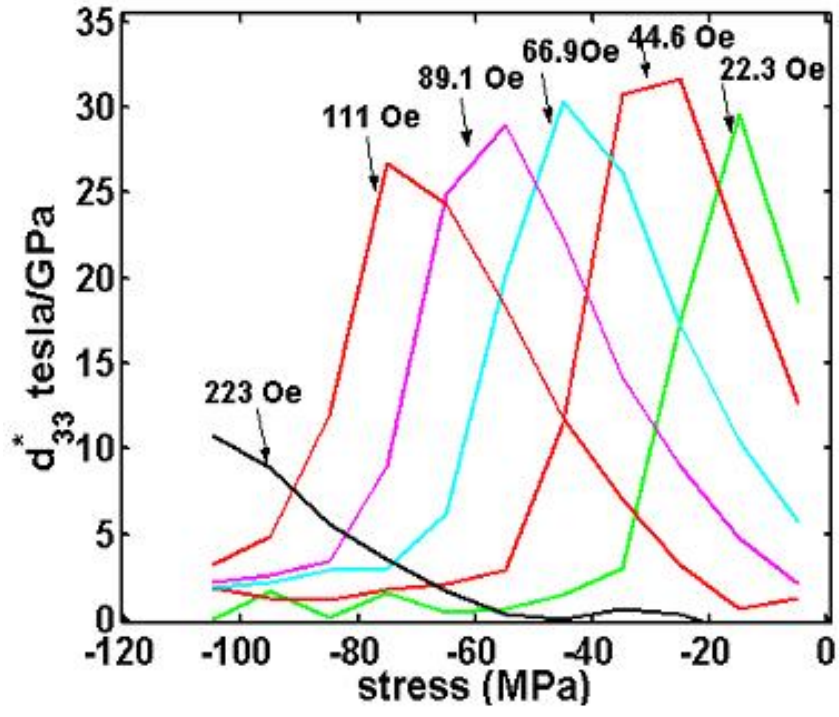
Figure 3.2: Experimentally measured dependence of the sensing coupling coefficient d_{33}^* on compressive stress and magnetic bias field [8].

The model operates by identifying the d_{33}^* for each point in the stress distribution $\sigma(x, z, t)$, then substituting both of these terms into equation (3.15). The result is the magnetic induction $B(x, z, t)$ at each point within the material. From the experiments in Chapter 2 it was theorized that both the pickup coil and the GMR sensor were measuring only a time dependent signal $B(t)$ from the net average of the induction throughout the sample. Therefore, the mean value of induction is computed by taking the integral average over the cylindrical volume V with diameter d and length L,

$$B(t) = \frac{1}{V} \int_0^L \int_{-d/2}^{d/2} 2\sqrt{(d/2)^2 - z^2} \, B(x, z, t) \, dz \, dx. \tag{3.17}$$

3.3.2 Acquisition of Tensile Data

The d_{33}^* data used for interpolation was originally limited to compressive stresses, as it was collected from existing test fixtures that were intended for this traditional magnetostrictive operating regime. Experience strongly suggests that the coupling coefficient is quite small over the tensile range, and that the presumed 2 T/GPa value used across the board is reasonable, but in order to be thorough this data was experimentally collected in tension as well.

The experiments were performed on an Etrema Products, Inc. production grade polycrystalline dogbone of $Fe_{81.6}Ga_{18.4}$, with a gage area 6.35 mm in diameter and 25.4 mm long. The ends were threaded for convenient loading in the custom housing apparatus that had been previously constructed for tensile testing in the MTS machine. A solenoid that had been calibrated to produce axial field at 300

Oe/A surrounded the entire structure. The measured data included applied force from the load cell in the MTS system, strain from a gage placed directly on the side of the sample, and induction from a pickup coil wound around the rod. In each test, the specimen was loaded in tension with a prescribed strain rate of 0.0035 mm/s that ramped to a limit of 0.07 mm and back down. During testing, the solenoid was used to provide magnetic bias fields to the rod between 0 and 39 Oe dc.

A resultant plot of induction vs. the applied stress at different levels of bias is presented in Figure 3.3. There are several key features of note. The primary observation is that the effect of tensile stress is greatly diminished as even low to moderate magnetic fields are applied. This agrees with the understanding of the material behavior, as the applied field and the tensile stresses both act to align the magnetic moments axially along the rod, leaving little for the stress to do when the sample begins near saturation. A more interesting characteristic is that the first increment of field at 4.5 Oe actually improves upon the zero field condition before decreasing at 9 Oe and above. A likely explanation for this is that with both the stress and field magnitudes being rather low, the small amount of field actually helps the stress to rotate any moments that were otherwise trapped at pinning sites, which should be quite numerous as defects and grain boundaries are plentiful in polycrystalline samples. It is only closer to saturation that the two energies become redundant rather than additive.

Each set of data also appeared very hysteretic, especially for a Galfenol alloy. Some of these losses can be attributed to the aforementioned polycrystallinity, but the largest sources are probably the threaded sample attachment and the magnetic

75
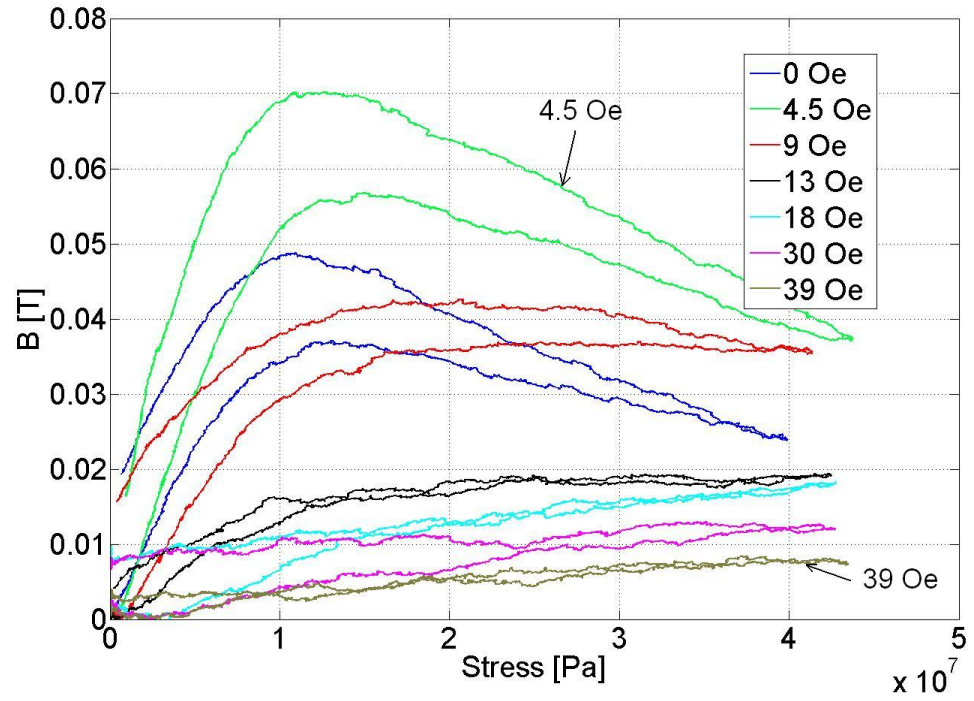
Figure 3.3: Measured magnetic induction vs. tensile stress with increasing magnetic field for the polycrystalline $Fe_{81.6}Ga_{18.4}$ dogbone. Results follow the expected trends, as small tensile stresses increase B but the effect quickly drops off as stronger fields are applied.

circuit. The last unexpected trend is that after peaking, the magnetic induction measured from the 0 and 4.5 Oe cases actually decreases. Conceptually, once the moments are aligned axially it is difficult to picture additional tensile stresses rotating them out of this configuration. It is conjectured that this can be linked to the poor grain alignment in the production grade rods, which on average have only 44% of the grains in the desired [100] texture. Drawing any specific conclusions about the origin of this phenomenon would require additional dedicated testing.

Using this B vs. σ data requires fitting an anhysteretic curve to the induction and differentiating with regards to stress to yield the desired d_{33}^* coefficient. This is done at each level of applied bias field to generate a set of reference polynomials just as was done with the compression data. The two sets of data are combined to generate plots of the variation in sensitivity with stress at any applied magnetic field, as demonstrated in Figure 3.4. The far greater amplitude of d_{33}^* in compression rather than tension confirms how the compressive side of the beam dominates the sensing response as first observed in the macroscale proof of concept experiments.

A final interesting result from this tensile characterization was the stress vs. strain data with no applied field plotted in Figure 3.5. The overlapping minor loops nicely show the hysteresis losses that accrue when moving from the loading (upper) and unloading (lower) lines. This data also is a good example of the delta-E effect common in mechanical loading of magnetostrictive alloys. There is a distinct decrease in slope in the loading curve over the range of 6 - 12 MPa that occurs due to softening by magnetoelastic strain. This phenomena is a useful property of magnetostrictive materials that offers potential for unique actuator and sensor
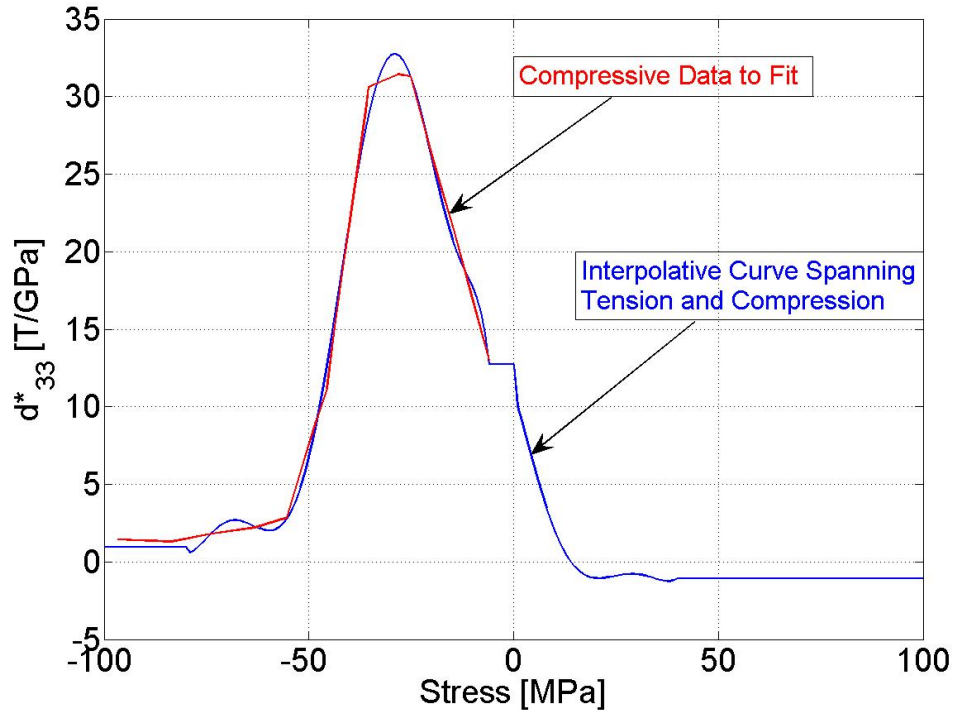
Figure 3.4: Interpolative curve of d^*_{33} at 22 Oe fit to both the compression and tension data. The coefficient, and thus the bending stress sensitivity, is heavily weighted to the compressive side of the beam.
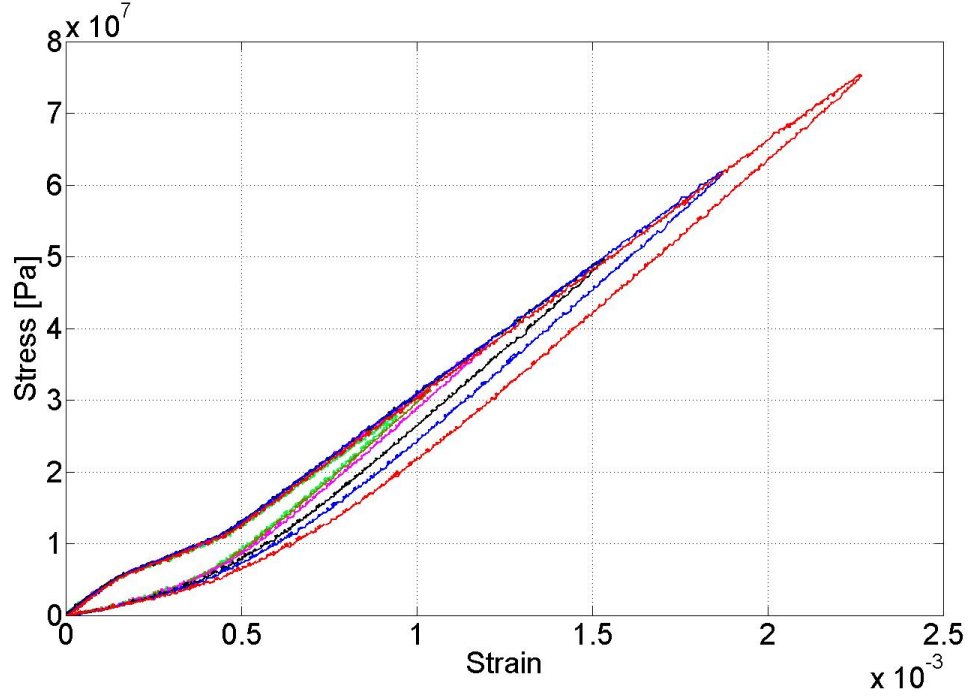
Figure 3.5: Stress vs. strain minor loops from the dogbone sample loaded and unloaded in tension with ramp functions of increasing strength. These loops show the delta-E effect as the slope of the upper loading line decreases over the 6 - 12 MPa range before returning to the original value.

devices [81, 24].

3.3.3 Results

With the coupling coefficient explicitly defined at all values of stress and field, the magnetic induction of the beam is calculated with equations (3.14), (3.15), and (3.17). The response to a sinusoidal input load is plotted in Figure 3.6, where the modeled magnetic induction accurately captures the rectified behavior expected. The amplitude of the response is of the appropriate magnitude as anticipated from the experimental results, which made use of manual loading that approached 4 N
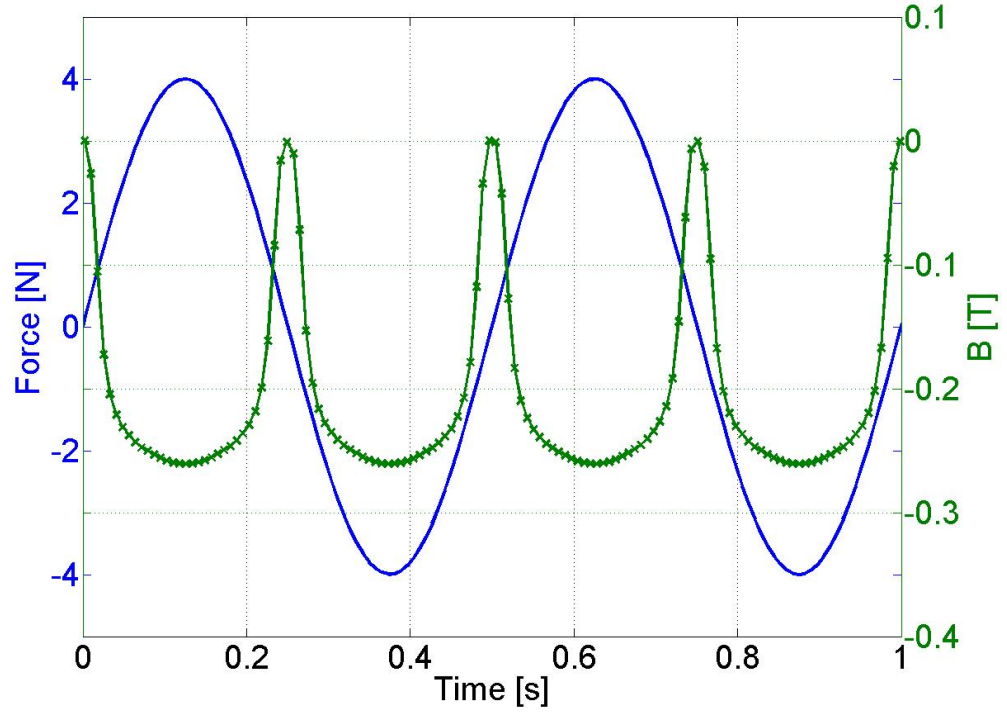
Figure 3.6: Constitutive model induction response to a 4 N sinusoidal force at the beam tip.

according to the attached load cell.

Another characteristic of the data that the model verifies is the minor variation in B with increasing bias field, as discussed in Section 2.3. The key assumption was that although the actual stress level that causes the primary change in B varies with applied field, so long as this combination occurs somewhere in the beam then the average induction measurement will be reasonably consistent. Essentially, the region within the sample that has the maximum d_{33}^* will be a surface of equal stress that shifts during the beam deformation. Figure 3.7 shows the model prediction for these different surfaces (projected in two dimensions) throughout the beam, revealing that

the bias field and the stress affect the distribution of B more than the maximum value.

A ramification of this is that once the beam deformation is large enough to induce a significant stress, the amplitude of the induction response is no longer directly comparable to the strength of the input. Instead, for a given bias field H_0, additional load will only make the reduction in B sharper, as the full effect is felt before the peak in the sinusoidal stress, as demonstrated in Figure 3.8. In fact, at some point increasing stress becomes detrimental and the induction increases slightly, due to the optimum plane of sensitivity being pushed to the bounds of the material and the minor contributions of tension. Figure 3.9 shows a related consequence, that a beam with a low bias field will undergo the same stress distribution but have a stronger induction response than a beam with a higher applied field, but this manifests in the sharpness of the response more than in the amplitude. This correlates well with the data originally presented in Figure 2.15.

The model also works quite well when given the imperfect forcing function from the actual data. Figure 3.10 shows the experimental induction measured from sample #1 of Table 2.1 overlaid with the prediction of the constitutive model. There clearly is a strong correlation, and the most important aspects are well captured. Numerically, the error can be estimated by the mean absolute error percentage, written as

$$\text{error} = \frac{1}{N} \sum_{i=1}^{N} \left| \frac{B_i^{exp} - B_i^{model}}{B_i^{exp}} \right|, \tag{3.18}$$

which is computed to be 9.7% between the constitutive model and the experiment.
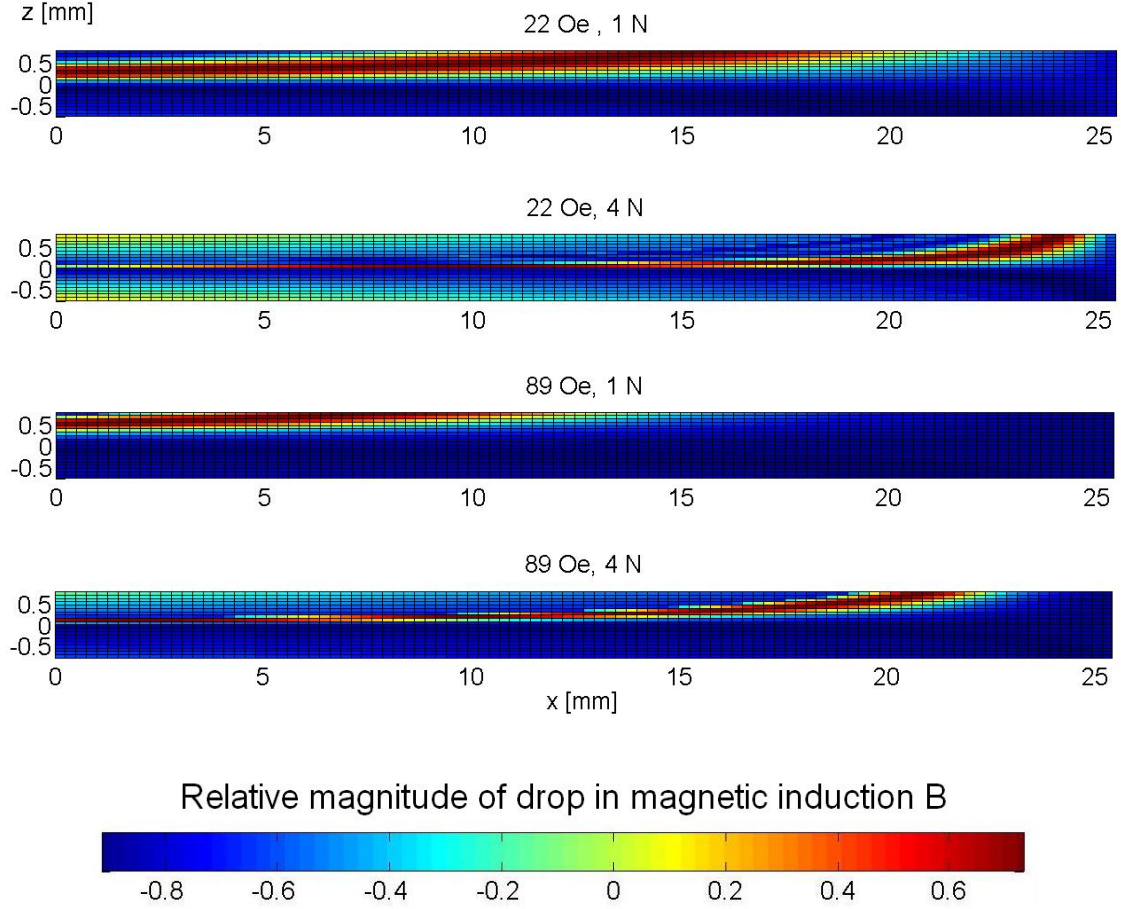
Figure 3.7: Simulation of the magnetic induction distribution in the x/z plane within beams with various bias field and loading conditions. Higher loads push the surface of maximum (negative) induction downward to the center of the beam and outward to the right, but the red color representative of the greatest magnitude does not get appreciably darker. Increasing the magnetic bias field simply changes the value of compression that creates the largest drop in B, shifting the surface up and to the left. Although the higher load plots in general have a thinner red area, they are weighted more heavily due to being much closer to the center of the beam where the width is maximum.
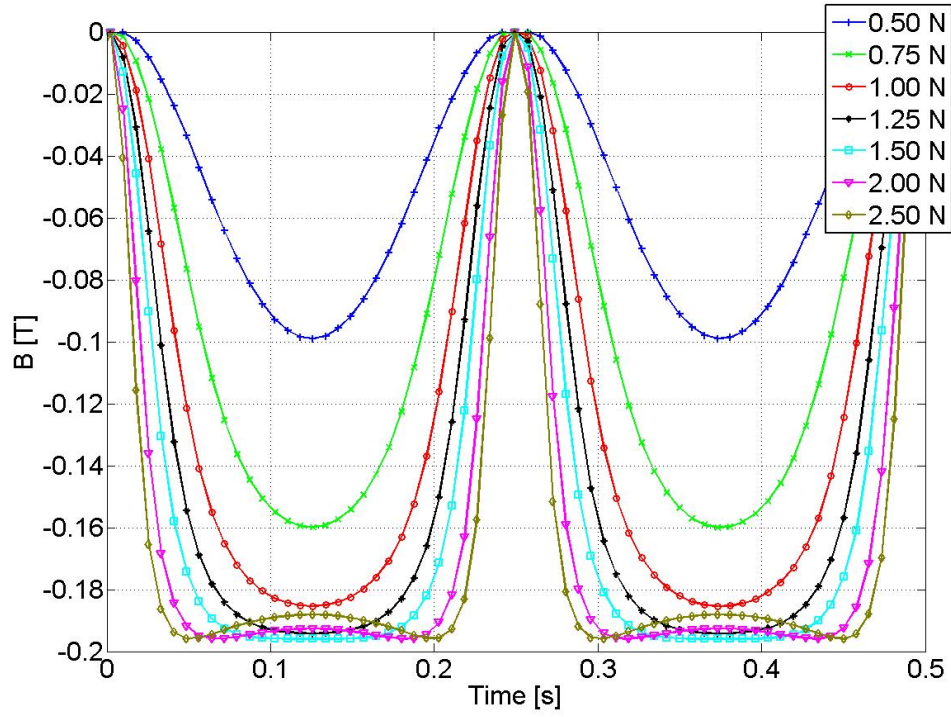
Figure 3.8: Simulated magnetic induction response to a 2 Hz sinusoidal force of increasing amplitude. The change in B grows quickly with higher force until the amount of stress generated is sufficient to envelope the peak in the d_{33}^* coefficient. From that point on, additional load widens the induction well but has little effect on the magnitude. Eventually the center begins to increase again due to the less optimal position of the maximum B surface and the minor contributions of tension.
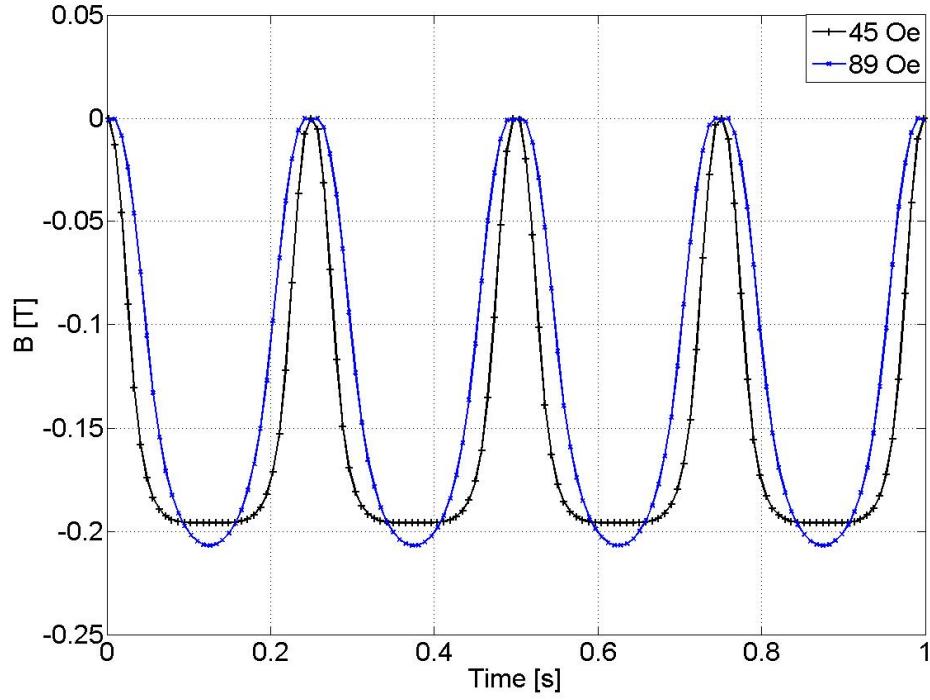
Figure 3.9: Predicted magnetic induction response of a sinusoidal bending beam with different bias fields applied, revealing similar magnitudes but wider B wells for the lower bias state, similar to the data observed in Figure 2.15.
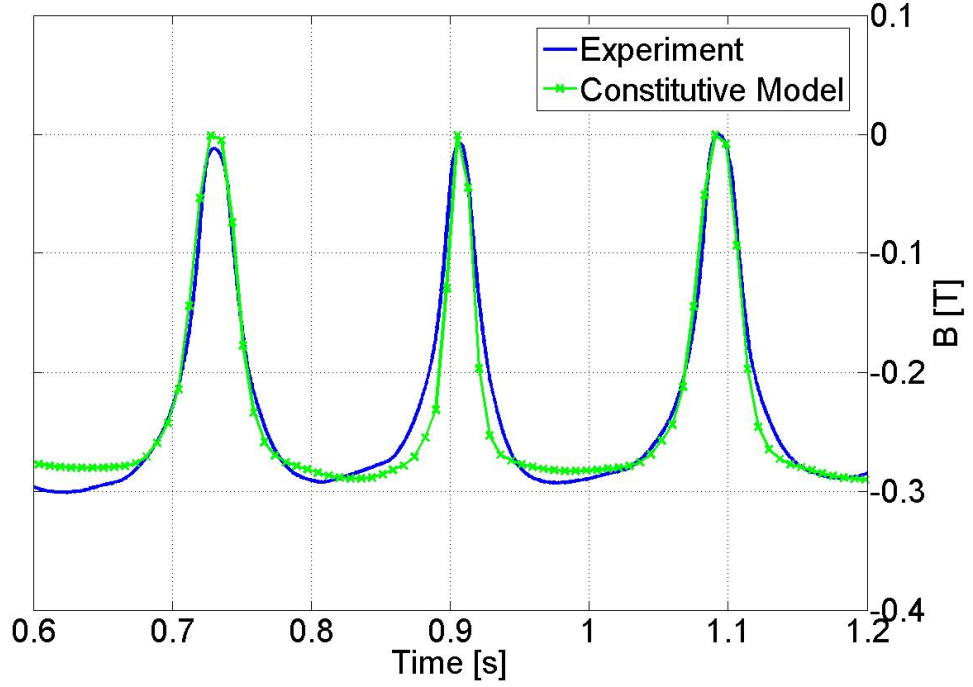
Figure 3.10: Comparison of the constitutive model using the experimental force input and the measured induction data from Figure 2.14.

This value is reasonably large given how well the model mimics the dominant features of the data, but clearly the less than perfect matches along the minima quickly add up. Nonetheless, the model appears to serve its primary purposes of verifying the conclusions drawn from the raw data and providing a means of predicting results.

The reason that this model works as well as it does relying on the constitutive magnetostriction equations is of course the non-constant d_{33}^* coefficient. Because the variation of this parameter with stress and field was taken directly from the data, it easily overcomes the traditional weaknesses of the linear equations and matches

the experiments well. This inherently limits the model however, to samples from which this data is readily provided. While most material models rely to some degree on experimental values, there is a large advantage to having these parameters be few in number and universal in availability. Unfortunately, neither d_{33}^* nor the B vs. σ curves from which it is derived are standard data for magnetostrictive alloys, which typically would be λ vs. H and B vs. H curves taken under conditions of no external stress.

3.4   Energy Model

The motivation for switching to an energy based model is primarily the greater flexibility. The constitutive model is limited to specific compositions previously characterized, does not accept conventional material parameters, is clunky due to the need for multiple interpolative curves, poorly handles the near-zero field range, and certainly cannot be expected to work well for Galfenol nanowires. The nonlinear energy based approach should not only be easier to implement, but also adaptable enough to properly model any magnetostrictive bending beam down to the nanoscale.

3.4.1   Included Terms

The Armstrong model was originally constructed as the sum of the magnetic field, magnetocrystalline, and magnetoelastic energies [5]. The total free energy can be used to calculate the energy cost associated with a magnetization vector pointing

in any direction, and the minimization of this energy yields the magnetization profile for an arbitrary body. This modeling approach, often with additional terms, has been used for analyzing magnetic domain structures [75, 31] for many decades; the specific application to bending Galfenol beams is discussed below.

The magnetic energy, sometimes known as the Zeeman energy, is the energy associated with a magnetic moment oriented in an external field. Physically, this energy is minimal (maximally negative by convention) when the moment and the field are parallel and zero when they are perpendicular. Mathematically this is typically written as

$$E_H = -\mu_0 \, \boldsymbol{M} \cdot \boldsymbol{H} = -\mu_0 \, M_s \, H \, \alpha_1, \tag{3.19}$$

where E_H is the magnetic energy, μ_0 is the permeability of free space, and $\boldsymbol{M}$ and $\boldsymbol{H}$ are the magnetization and magnetic field vectors, respectively. In the simple case where the applied field is parallel to the beam axis, this reduces to the scalar expression relating saturation magnetization M_s, field magnitude H, and the direction cosine of the magnetization relative to the beam axis α_1.

Magnetocrystalline anisotropy energy represents the tendency for magnetic moments to align along certain crystallographic directions in the lattice. In cubic Galfenol, the preferred "easy" axes are $< 100 >$, while the $< 110 >$ are "medium" and the $< 111 >$ are "hard". The anisotropy arises from the excess energy required to align the moments in the undesirable hard axes, and traditionally is written as

$$E_{an} = K_0 + K_1(\alpha_1^2\alpha_2^2 + \alpha_1^2\alpha_3^2 + \alpha_2^2\alpha_3^2) + K_2(\alpha_1^2\alpha_2^2\alpha_3^2) + \ldots \tag{3.20}$$

for cubic crystals, where E_{an} is the anisotropy energy, the K's are material and

temperature dependent anisotropy constants, and the α's are again the direction cosines of magnetization. The fourth order K_1 term is occasionally [115] written as $K_{cubic}(\alpha_1^4 + \alpha_2^4 + \alpha_3^4)$, but the equivalence of the terms can easily be shown [75]. The form of this expression varies for other crystal structures, with the general result being that lattices of low symmetry have high magnetocrystalline anisotropy, and vice versa [75]. For the case of beam bending, the K_0 term is dropped because it is independent of magnetization and only the difference in energy between directions is of interest. In addition, the axial symmetry of the beam allows for the problem to be treated in only two dimensions by setting $\alpha_2 = 0$.

The magnetoelastic energy relates the influence of stress and strain on the magnetization. The anisotropy energy expression represents an unstrained lattice but can be expanded about equilibrium due to small strains, and will be balanced by the elastic energy due to deformation of the crystal. Minimization of this sum yields the magnetoelastic energy equation

$$E_{me} = -\frac{3}{2}\lambda_{100}\,\sigma\,(\alpha_1^2\beta_1^2 + \alpha_2^2\beta_2^2 + \alpha_3^2\beta_3^2) - 3\lambda_{111}\,\sigma\,(\alpha_1\alpha_2\beta_1\beta_2 + \alpha_1\alpha_3\beta_1\beta_3 + \alpha_2\alpha_3\beta_2\beta_3),$$

$$(3.21)$$

where E_{me} is the energy, λ_{100} and λ_{111} are the material specific magnetostriction coefficients, and the applied stress vector is represented as $\sigma\,[\beta_1, \beta_2, \beta_3]$. In the ideal case of uniform beam bending the stresses are applied only along the axis $[1, 0, 0]$. As a result, the stress is coupled to the magnetization via $E_{me} = -\frac{3}{2}\lambda_{100}\,\sigma\,\alpha_1^2$.

Another energy often included in models of ferromagnetic materials is the exchange coupling between neighboring electron spins. The exchange energy E_{ex}

introduces magnetic order and can be expressed as

$$E_{ex} = -2 \sum_{i>j} J_{ij} \left(\boldsymbol{S}_i \cdot \boldsymbol{S}_j \right) = -2 \, J \, S^2 \sum_{i>j} \cos \theta_{ij}, \qquad (3.22)$$

where J_{ij} is the exchange integral and $\boldsymbol{S}$ is the spin angular momentum associated with each atom. Assuming only nearest neighbor interactions, the exchange strengths are all equal to J and can be factored out of the summation. For ferromagnetic materials, J is positive and therefore the energy is minimum when the spins are aligned ($\theta_{ij} = 0$). This coupling causes neighboring spins to stay parallel even in the absence of an applied magnetic field, and contributes to the uniform spontaneous magnetization that forms domains.

The exchange energy is often written in a different form with respect to an exchange stiffness constant A, which can be thought of as the force acting to keep moments parallel. This derivation [75] arises from the manipulation of equation (3.22) by expanding the direction cosines of the adjacent lattice point in a Taylor series. The result is that the exchange energy for a body-centered cubic material may also take the form

$$E_{ex} = A \left((\nabla \alpha_1)^2 + (\nabla \alpha_2)^2 + (\nabla \alpha_3)^2 \right), \qquad (3.23)$$

where $A = 2 \, J \, S^2 \, / \, a_0$ and a_0 is the lattice parameter. Experimental evidence has shown that for most magnetostrictive alloys A has a magnitude between 1×10^{-11} and 2×10^{-11} J/m.

The exchange term is not included in the total free energy summation of the Armstrong model because the energy cost due to neighboring misalignment only manifests significantly at domain walls, which make up a very small volume fraction

89

of the material. The Armstrong model represents the bulk magnetization response of the single crystal sample, and can tacitly ignore the exchange energy due to its diminutive magnitude and the lack of interest in domain boundary formation. The inclusion of this term will be reexamined when adapting the model for the Galfenol nanowires.

Therefore, the sum of the magnetic, anisotropy, and magnetoelastic energies constitutes the total free energy of the system,

$$E_{total} = E_H + E_{an} + E_{me}. \tag{3.24}$$

The parameters required to numerically implement the energy are the anisotropy constant K_1, the applied external field H, the saturation magnetization M_s, the magnetostriction constant λ_{100}, and the axial stress σ. Each of these can be either directly measured from experiment, taken from available literature, or designated as a prescribed input such as the stress. Knowing these coefficients, the energy cost associated with a given magnetization direction $[\alpha_1, \alpha_3]$ can be easily calculated, and the directions at which this energy is minimized are the most likely orientations for the magnetization vectors to align. However, simply using the α's that minimize the energy results in very sharp non-physical features in the magnetization response, so the model utilizes an energy weighted average

$$M(\sigma, H) = \frac{\sum\limits_i M_s \, \alpha_{1,i} \, e^{\frac{-E_{total,i}}{\Omega}}}{\sum\limits_i e^{\frac{-E_{total,i}}{\Omega}}} \tag{3.25}$$

over all i possible configurations for α. Armstrong introduced a factor Ω that accounts for the number of imperfections in the material and has the effect of smooth-

90

ing the magnetization curves but leaving the position of features unchanged [5, 115]. A critical assumption in this approach is that the predicted magnetization is wholly independent of the previous magnetic state, yielding an anhysteretic output. In the case of modeling Galfenol this is generally acceptable, but for some applications capturing the hysteresis may be of importance.

An example of the energy cost associated with the magnetization direction is presented in Figure 3.11. The first plot shows the preferred orientations within a [100] oriented beam with a small 5 Oe field applied axially and zero stress. In this case, the 0° direction along the axis is the minimum as it corresponds to both a crystallographic easy axis and aligns with the external field. The 90°, 180°, and 270° orientations have local minima due to also being easy axes of the cubic crystal (the magnetocrystalline anisotropy causes the lobes at 45°), but are in opposition of the magnetic field energy that unbalances the figure toward 180°. The calculated average magnetization is $M/M_s = 0.94$, revealing that the sample is near saturation due to being primarily oriented at 0° but some portion of the moments are still lying within the other local minima. Once a 15 MPa compressive stress is added in the lower graph, the magnetoelastic energy term strongly favors the directions perpendicular to the beam at $\pm$ 90°, and each of these becomes equally preferred. The energy weighted average now predicts $M/M_s = 0.02$ as very little of the sample will be magnetized axially.
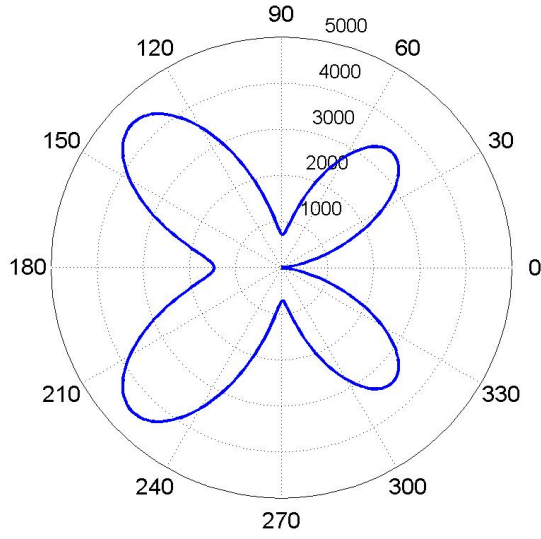
(a)
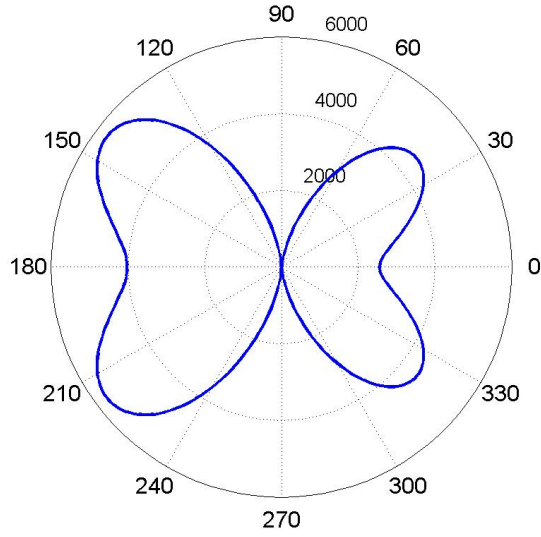
(b)

Figure 3.11: Energy cost in J/m³ associated with all possible magnetization directions α, where 0° is along the beam axis. When there is a 5 Oe field applied axially (a), the magnetization aligns predominantly with this orientation. With the addition of 15 MPa of compression (b), the preferred alignment becomes perpendicular to the beam.

3.4.2 Results

The model is first validated by generating static B vs. H curves at constant stress, as this data is measured for most magnetostrictive samples. The model parameters were fit to the data from a single crystal $Fe_{84}Ga_{16}$ sample [7] that was originally plotted in Figure 2.19, and are tabulated in Table 3.1. The stress in the model was fixed at the levels used during the experiments, and the field cycled from -500 to 500 Oe. Conversion of the model output M to the induction was done with the typical relation $B = \mu_0 (M + H)$. Figure 3.12 shows the output induction curves from the model overlaid on the original data, and the fit is quite good. As this composition was similarly used for the majority of the bending sensor experiments, these model parameters are carried through for the remainder of the calculations.

Using the model for vibrating Galfenol beams follows the same overall procedure as used for the constitutive model. A fixed bias field and the bending stress distribution $\sigma(x, z, t)$ from equation (3.14) are input to the free energy terms and the magnetization $M(x, z, t)$ is calculated from equation (3.25). This is converted to magnetic induction once again with $B = \mu_0 (M + H)$ and then reduced to the

Table 3.1: Coefficients used in the Armstrong model for fitting B vs. H data of single crystal $Fe_{84}Ga_{16}$.

Parameter	Value
λ_{100}	167×10^{-6}
K_1	13×10^3 J/m^3
M_s	1432 kA/m
Ω	200 J/m^3
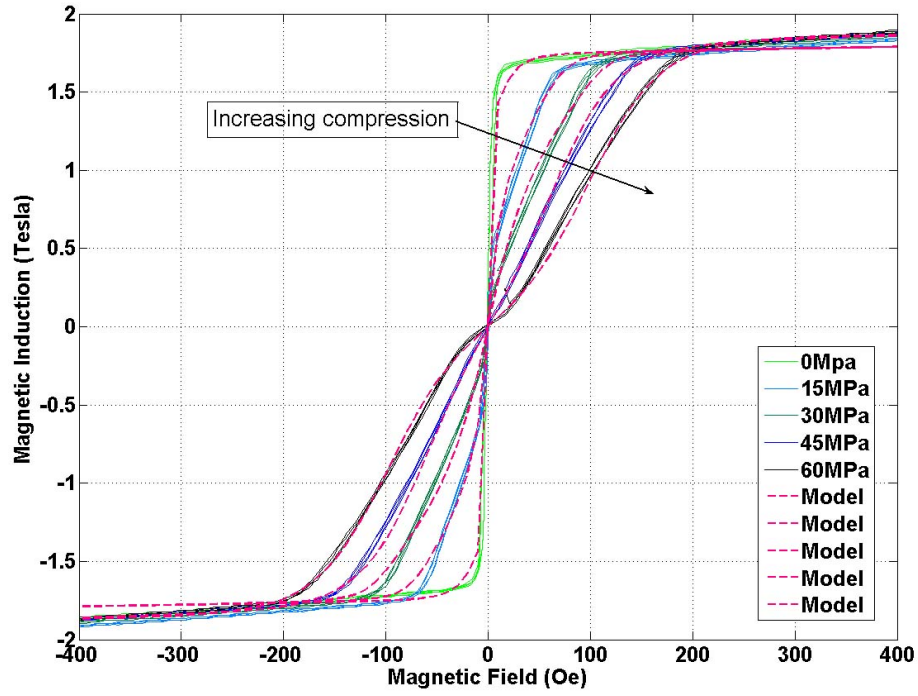
Figure 3.12: Armstrong model simulations using the parameters from Table 3.1 of B vs. H curves at various levels of compression, overlaid with the $Fe_{84}Ga_{16}$ single crystal experimental data [7] from Figure 2.19.

average $B(t)$ with equation (3.17).

The model is compared with the measurement from the bending experiments just as was done with the constitutive method, using the imperfect force input from the data. The comparison is shown in Figure 3.13, where once again all of the key characteristics are well represented. Equation (3.18) is used to determine the mean absolute error at 10.2%, which is nearly identical to the error of the constitutive model. While the free energy method doesn't necessarily provide better accuracy it required far less parameter fitting to begin with, and it still holds the distinct advantage of being applicable for any stress and field condition. Figure 3.14 shows the Armstrong model prediction and the experimentally measured induction from two cases near zero field that were given offbeat manual loading. Using the experimental load cell signal as an input, the model matches rather well even at these operating points, at which the constitutive model cannot technically even be implemented.

3.4.3   Adaptability for Modeling Nanowires

The Armstrong model performs up to expectations for capturing the behavior of the macroscale Galfenol beams, but questions arise about the validity of directly using it for nanowire structures. The formulation of the included terms will not change, but the relative strengths of the terms could be quite different. The magnetic energy will often be ignored because the application of field should prove to be challenging in the context of nanowire experiments. The magnetocrystalline
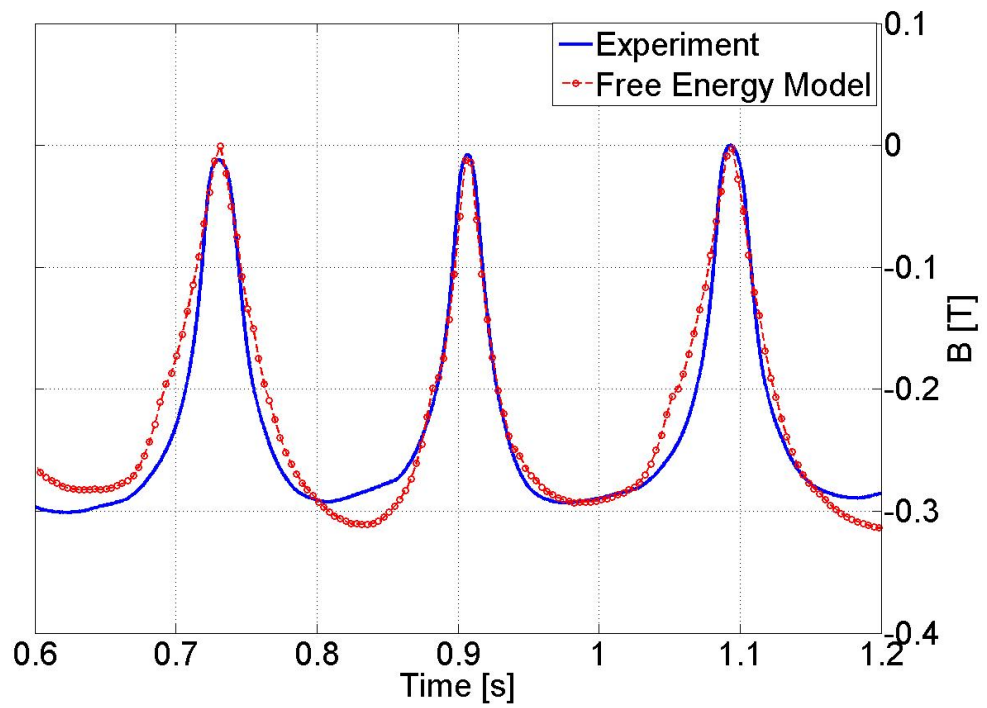
Figure 3.13: Comparison of the free energy model using the experimental force input and the measured induction data from Figure 2.14. As with the constitutive model, the dominant experimental characteristics are well captured.
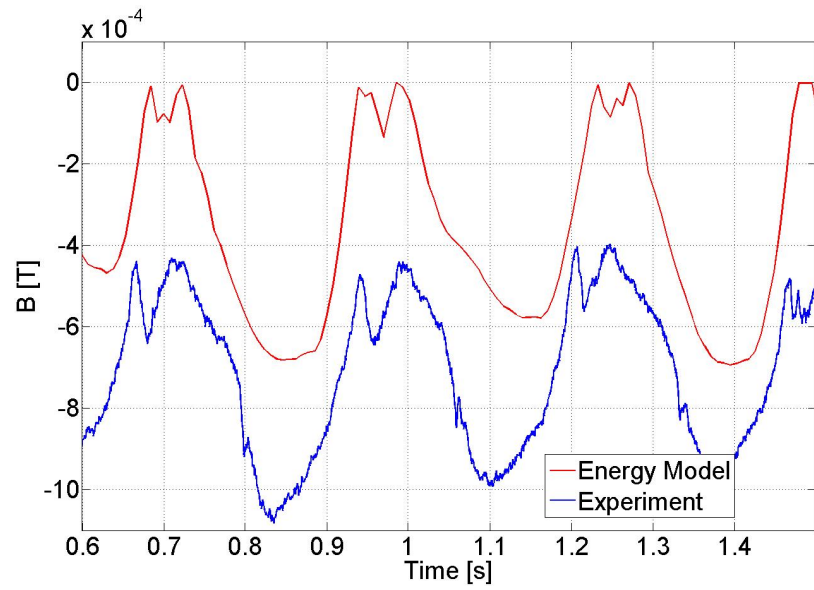
(a)
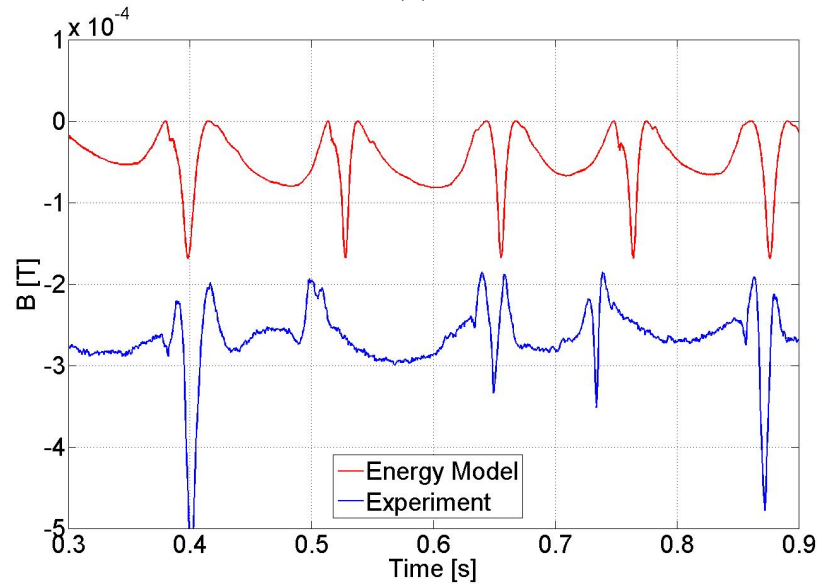
(b)

Figure 3.14: Comparison of the free energy model and experimental induction from a bending Galfenol beam. In each case the sample was near remanence, with the model using only 0.2 Oe (a) and 0.1 Oe (b) of bias field in the simulations, and the loading was less uniform than usual. The dc offset between traces is added for viewing clarity.

anisotropy will have the same form but the angles of minimization should be different, as the nanowire axis is expected to be a [110] texture rather than the [100] of the bulk samples [64]. The magnetoelastic term should be unaffected, although the use of a macroscale λ_{100} might not be particularly accurate. In addition, the exchange coupling will definitely be incorporated as it limits the formation of multiple domains in sufficiently small structures. Finally, a shape anisotropy term should be included due to the small diameter and high aspect ratio of the Galfenol nanowires.

Mechanically, the wires in this research are large enough for continuum mechanics to still apply, so the Euler-Bernoulli derivation for the stress distribution will be used as is. Enrichment of the material model is a future work possibility if there is an observed need. Overall, the modified Armstrong model should be able to predict the change in magnetic induction of every bending nanowire in an array and thus determine the output of an attached GMR sensor.

Chapter 4

Design and Construction of the Nanomanipulator

4.1   Intentions for Nanowire Characterization

Implementing iron-gallium nanowires as artificial cilia requires characterizing their properties in detail. It is possible that there are some differences between the nanowires and bulk material that would directly alter their sensing behavior and thus the accuracy of the corresponding model. In addition, the nanowires could display unique advantageous characteristics that have not yet been predicted by theory.

The techniques available for studying nanoscale materials are incredibly diverse, but commonly rely on spectroscopy to produce averaged data from an entire batch of individual structures, and often look only into the properties of samples in their equilibrium state. In order to approach the nanowire characterization in a familiar manner akin to that performed at the macroscale, this work requires a means of manipulating elements and applying mechanical forces in a controllable way to samples that include individual Galfenol nanowires and close packed arrays, as shown in Figure 4.1. This chapter describes the design, construction, and operation of a custom nanomanipulator device built to achieve this goal.
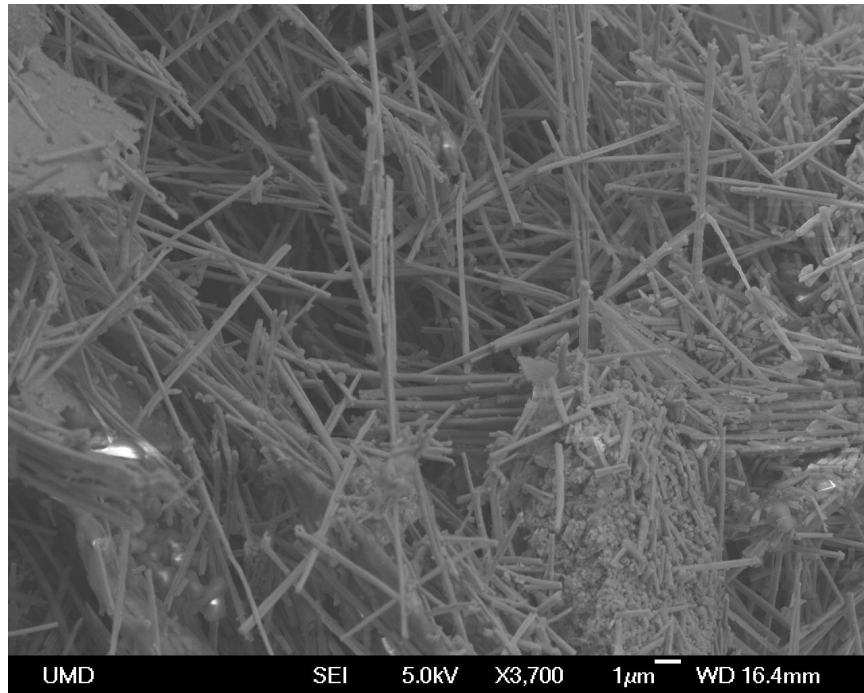
(a)
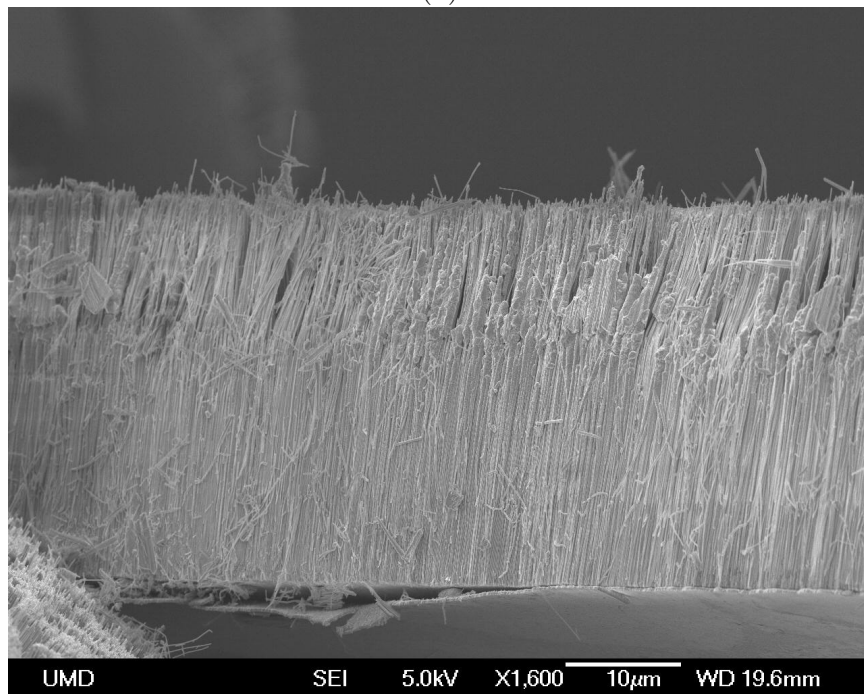
(b)

Figure 4.1: Micrograph of Galfenol nanowires that have been freed from the matrix (a) and as grown in a close packed cantilevered array (b).

4.1.1 Desired Capabilities

There are a number of attributes that need to be considered in order to design an apparatus with sufficient capability and flexibility for reliable nanowire characterization. The most important of these is to incorporate a positioning system that has both fine resolution and precise control. A small step size is imperative for manipulating wires with movements small enough to deflect but not break them, and having accurate control will allow the isolation and attachment of a single ideal wire while minimizing missteps. In addition to having quasi-static positioning, the system needs to include a means of dynamically exciting the samples for validating high bandwidth sensor applications.

This device should allow for real time visualization so that the exact geometry and orientation of each nanowire can be accurately measured before, during, and after experiments. The manipulator should provide a means of collecting quantifiable data in addition to qualitative images, with force and deflection information being of highest priority as they can directly translate into the mechanical stresses and strains of interest. The machine must have flexible configurations for performing multiple experiments depending upon the constraints of each sample, and be versatile enough to handle materials ranging from loose nanowires up to fully packaged artificial cilia devices. Finally, it is desirable to have a customizable system that can be modified for experiments on any other nanomaterials that may be developed in the future.

Figure 4.2: The Zyvex S100 nanomanipulation system that incorporates most of the desired features [3].

4.2   Device Design

There are several commercial options that fulfill most of the manipulator requirements, particularly from Zyvex Instruments with whom detailed discussions took place. The S100 system shown in Figure 4.2, for example, has up to four sharp probes each with a three-directional resolution of approximately 5 nm, all positioned around a separate stage holding the sample. Although it lacks dynamic capabilities, these are certainly the types of features that are desired. Due to several constraints however, including cost, it was decided that a custom solution would be a better use of resources, not to mention an excellent component of this dissertation.

A literature survey uncovered research by a group headed by Rodney Ruoff then at Northwestern University. They had constructed a device that sat within a

scanning electron microscope (SEM) and was used to perform mechanical testing on individual multi-wall carbon nanotubes (MWCNT) [166]. Because this machine appeared to be the perfect prototype for the manipulator, a meeting was arranged with Dmitriy Dikin, a post doctoral member of the group. He was extremely open to sharing information, and described the key components of their device, the critical challenges of integrating it within the SEM, and the data analysis used for actual experiments. He cannot be thanked enough. After returning from this invaluable visit, the manipulator design was formalized and construction was pending the installation of the SEM.

4.2.1 Components and Construction

The foundation of the device consists of two opposed optical stages from OptoSigma, each with a footprint of 25 mm square. One stage has linear translation in both the x and y directions with a maximum travel of $\pm$ 6 mm, controlled manually with standard micrometer drivers. The other stage provides motion in the z direction, but uses a pivot mechanism to limit the maximum height to 25 mm, as this is a critical design constraint for the safety of the electron gun. Each stage is manufactured from stainless steel, uses non-silicone bearing grease, and is fabricated with no blind holes, all in order to reduce outgassing and ensure vacuum compatibility within the SEM.

In order to achieve precise motions from each stage, the micrometer drivers are replaced with vacuum compatible Picomotor actuators from New Focus that

operate by driving a high pitch screw with a set of jaws connected to a piezoelectric transducer. This method of operation takes advantage of static friction in the threads to hold a fixed position and bypass the drift that typically occurs when driving a piezoelectric material with a dc signal. While the specific performance of these actuators will be calibrated in conjunction with the optical stages, they are rated to have a resolution of under 30 nm and exert 5 lb of force. While acquiring closed loop actuators was contemplated, both the additional size from incorporating encoders and the higher cost were seen as prohibitive.

For dynamic characterization, a Q220-A3NM-103XB piezoelectric bending actuator from Piezo Systems is mounted onto the x/y stage, providing additional deflection in the y direction. This bimorph uses non-magnetic shim material, is suitable for vacuum use, and is 31.8-mm long, 3.2-mm tall, and 0.51-mm thick. The maximum tip deflection is rated at 237 μm in response to 180 V, with a block force of 0.06 N, but for most nanowire experiments it will be driven far below these limits. The frequency bandwidth of operation will be capped by the available electronics, but typical usage will range from tens of kHz to a few MHz.

The manipulator components are assembled onto a plate machined from 304 stainless steel that is designed to fit within the 4″ wafer holder included with the JEOL JSM-6500F SEM. This allows the entire device to make use of the dovetail and grippers built into the microscope's sample stage for optimum security and alignment. By strictly limiting the overall height of the manipulator device, lowering the stage's manual working distance position to the lower limit of 40 mm still provides at least 15 mm of clearance from the electron gun. Figure 4.3 is a photo-
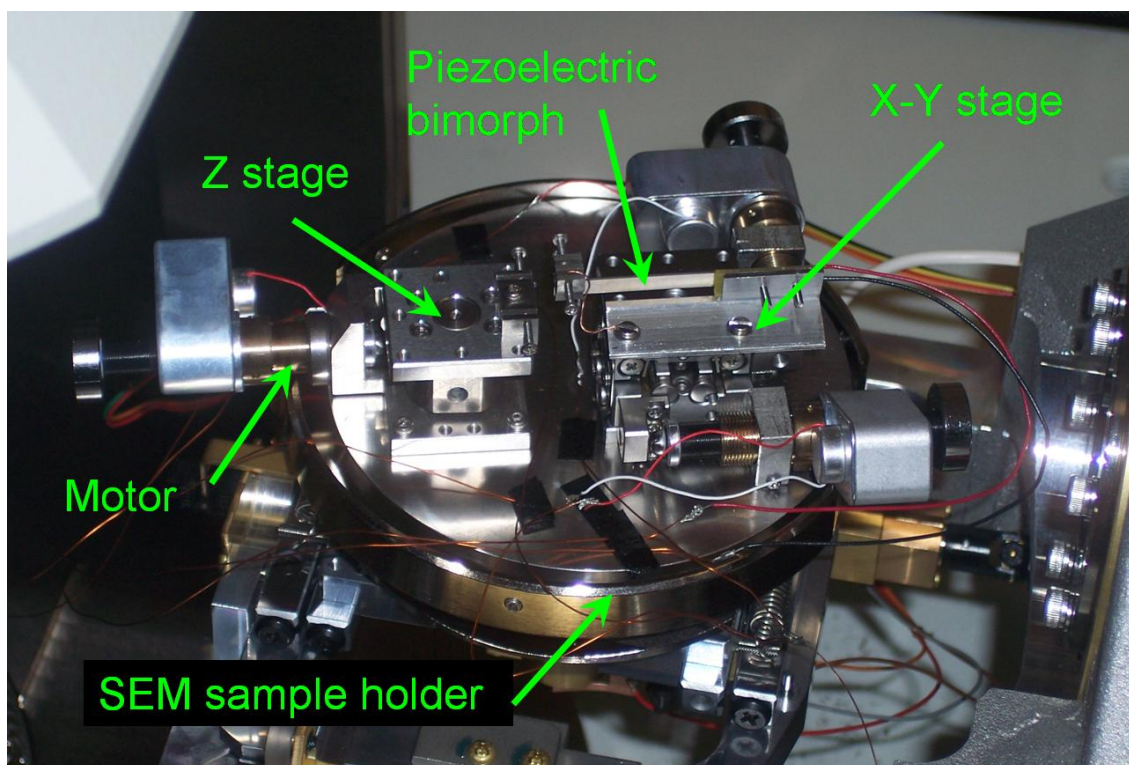
Figure 4.3: Photograph highlighting the key components of the assembled nanomanipulator device attached to the SEM sample stage.

graph showing the completed device attached to the sample stage prior to closing the SEM door. Evacuation of the chamber takes anywhere from 4 to 24 hours, but is far more dependent on the nanowire samples than the manipulator itself, as the nanowires often have insulating polymer layers and chemical etchant residues with poor vacuum properties.

The last requirement of the device is a means to translate the motion capabilities into actual manipulations of Galfenol nanowires. For this task, atomic force microscopy (AFM) probes are to be placed on the two optical stages to utilize the relative motion between them to interact with attached nanowire samples. These
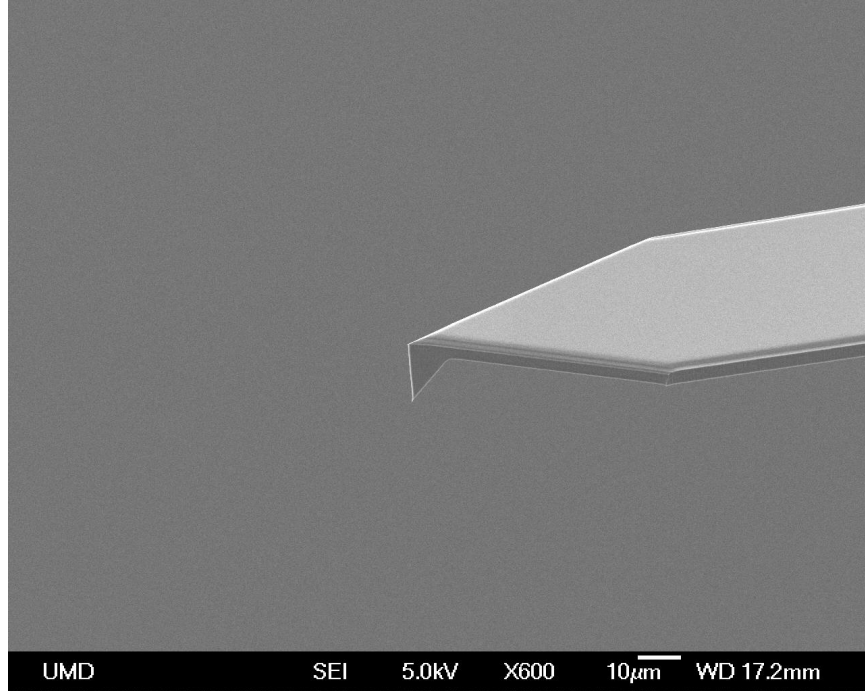
Figure 4.4: Micrograph of an OTESPA model AFM cantilever mounted onto the manipulator for use in nanowire characterization.

probes are an ideal choice for manipulating the nanowires as they feature sharp tips intended for nanostructure characterization, are available in a wide variety of geometries, and are inherently interchangeable. A discussion of their intended use in force microscopy can be found in Chapter 6. In order to incorporate the AFM cantilevers, one mounting block is built into the edge of the z stage and another is affixed to the free end of the piezoelectric bimorph, each containing several narrow slots into which probes can be held with 0-80 set screws in a few select orientations. Figure 4.4 is an SEM image of an OTESPA model probe from Veeco Instruments to be used in the manipulator.

4.2.2   Electrical System

Each component of the manipulator device must be wired within the SEM chamber in order to eliminate potential arcing and to ensure proper operation. The three Picomotor actuators and the piezoelectric bimorph each use polyimide coated wire to reduce outgassing, with the positive leads attached to the electrical feedthrough in the wall and the negative terminals grounded to the chamber itself. On the exterior side, the actuators are connected to their controller box and can then be completely operated with the accompanying keypad terminal shown in Figure 4.5. This device allows for real time user inputs as well as the programming of scripts for specific repeated commands. The bimorph is driven by a 20 MHz Agilent function generator without the need for a power amplifier due to the very small deflections desired. Internally, the SEM operation requires the sample stage to be biased at a constant 0.6 V dc, so all potential sources for a floating ground are hard wired back to the base plate of the manipulator, especially the AFM holder on the end of the bimorph. To accommodate conductivity, the nanowire samples themselves are also always mounted on an appropriate piece of copper or silicon before being placed in the device. Even with all of these precautions it is still not uncommon to observe charging effects in the SEM display, but they are at most a minor hindrance rather than a credible threat to the instrument.

Some characterization experiments attempt to measure the magnetic fields produced from the nanowires, and as such require additional electrical considerations. GMR sensors have been acquired from NVE Inc. that consist of unpackaged
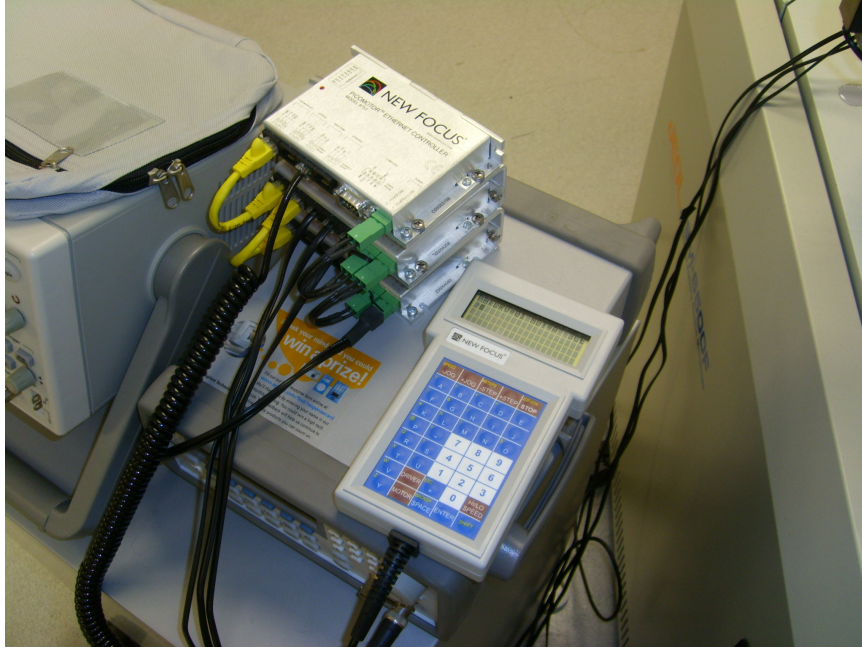
Figure 4.5: Handheld input terminal for controlling the three Picomotor actuators that drive the manipulator stages.

resistors laid out on a printed circuit board, as displayed in Figure 4.6. These exposed resistors allow for nanowire samples to be placed as closely as possible to the sensing elements, which are then wired in a Wheatstone bridge configuration with a pair of reference resistors to measure the changes in magnetic field, as depicted in Figure 4.7. The inclusion of the GMR sensors requires three additional channels in the electrical feedthrough, with the bridge excitation and output measurement being provided by a Vishay 2310A signal conditioning amplifier originally designed for strain gages.

A final consideration is the inclusion of permanent magnets within the SEM chamber to provide magnetic bias fields to the various nanowire arrays of interest. As magnetic fields deflect the electron beam needed for observation, it was discov-
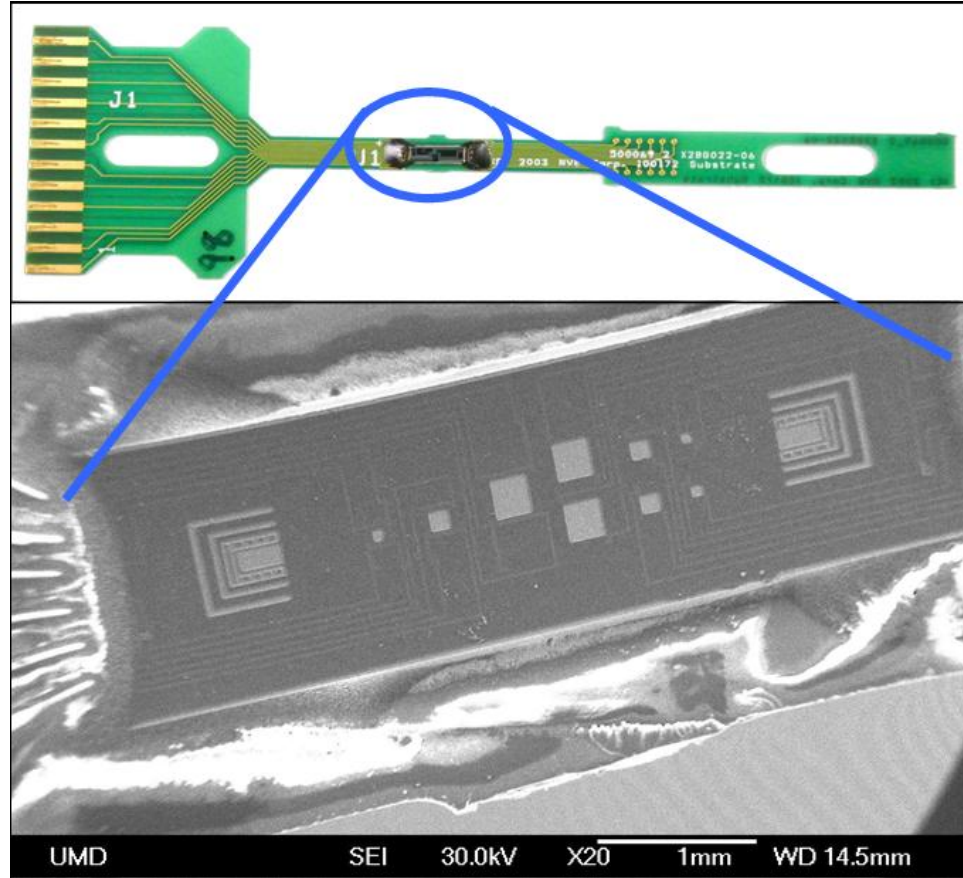
Figure 4.6: Unpackaged GMR sensor from NVE [140] that consists of several sensing resistors laid out on a printed circuit board for potential measurement of nanowire magnetic fields. The light colored squares are 50, 100, and 200 μm square areas of exposed resistor elements.
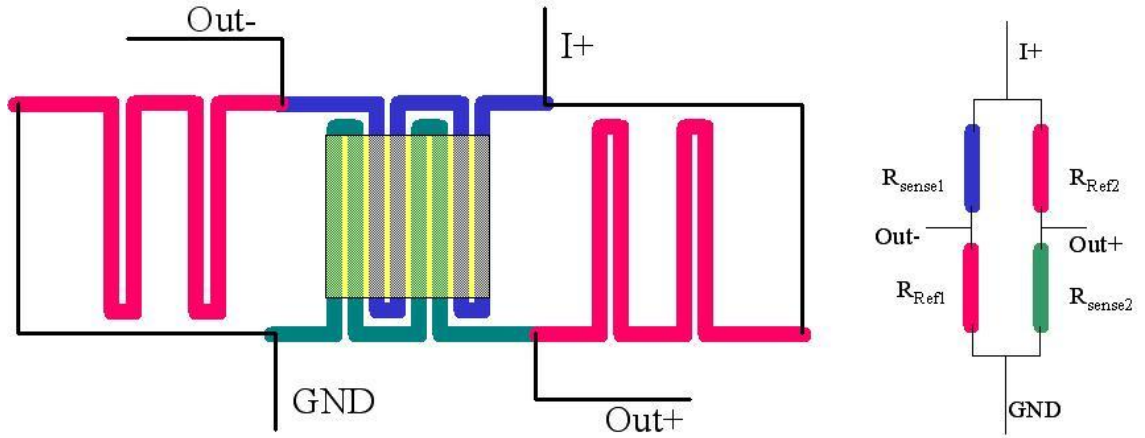
Figure 4.7: Diagram of the GMR Wheatstone bridge layout [140], where the yellow area corresponds to the exposed resistors in Figure 4.6.

ered through trial and error that maintaining accurate imaging required placing the magnets far off of the beam path, which as a result could provide a maximum of only 20 Oe to the samples. An amusing result of placing a strong magnet directly in the beam path can be seen in Figure 4.8.

4.3 Functionality

The first operation conducted with the finished manipulator was the calibration of the positional resolution of the optical stages driven with the Picomotor actuators. The stages were moved into a position such that an AFM probe tip attached to each stage could be imaged simultaneously. As the tip on the z stage is not being driven, it provides a fixed frame of reference to eliminate natural image drift between successive frames. Using the single step function on the controlling keypad, both the x and y motors were given twenty individual pulses in both the
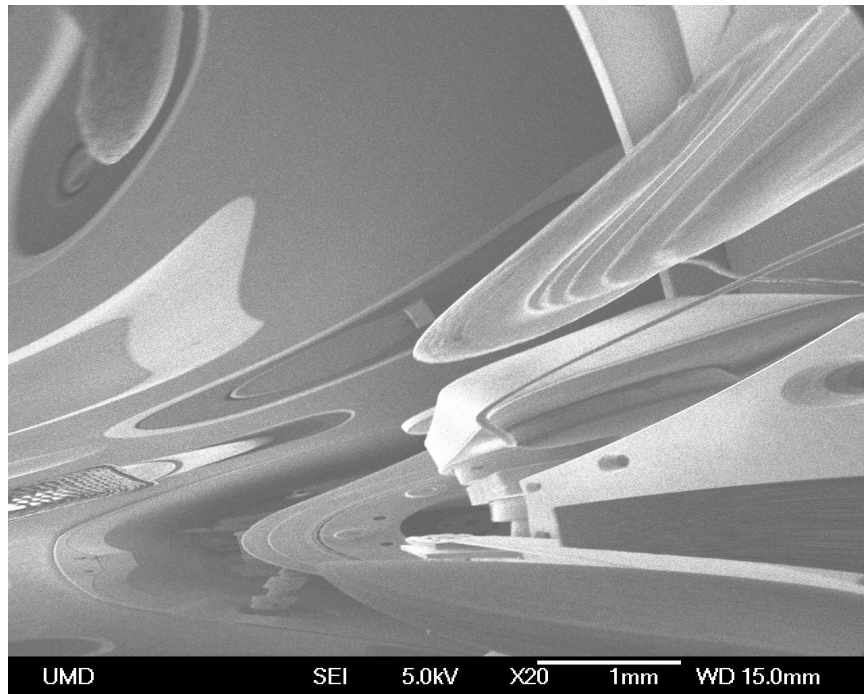
Figure 4.8: Heavily distorted SEM image taken with a permanent magnet placed within the beam path. The magnetic field deflects the electrons in such a way to allow visualization of the roof and side walls of the chamber but not the magnet itself.

Table 4.1: Measured position resolution of the x/y manipulator stage (in nm).

Direction	# of Steps	X motor	Y motor
Positive	1	23.2	10.0
	20	11.6	11.5
Negative	1	5.5	13.9
	20	12.3	13.7

positive and negative directions in order to determine any difference due to bearing friction or return springs. In addition, they were also driven by a single twenty-step pulse for comparison.

Results are presented in Table 4.1, where it is clear that the x motor has a large directional variance when being driven with single steps, most likely due to the forces of the stage's spring mechanism. When driven at the larger step size these forces are overcome and the positional resolution is roughly uniform. The y motor showed little variation with step size and only a minor increase in motion when moving in the negative direction. Data from the z stage is unattainable due to the movement occurring parallel to the electron beam, so proper depth alignment relies on matching the focus of two planar objects.

The capability of the piezoelectric bimorph was verified with the SEM raster scanning at an appropriately quick rate, causing the displayed image to be updated in essentially real time. When a dc voltage is switched on from the function generator, the beam deflection in y is clearly visible. The voltage amplitude can be decreased until the motion of the bimorph is indiscernable, implying that this can
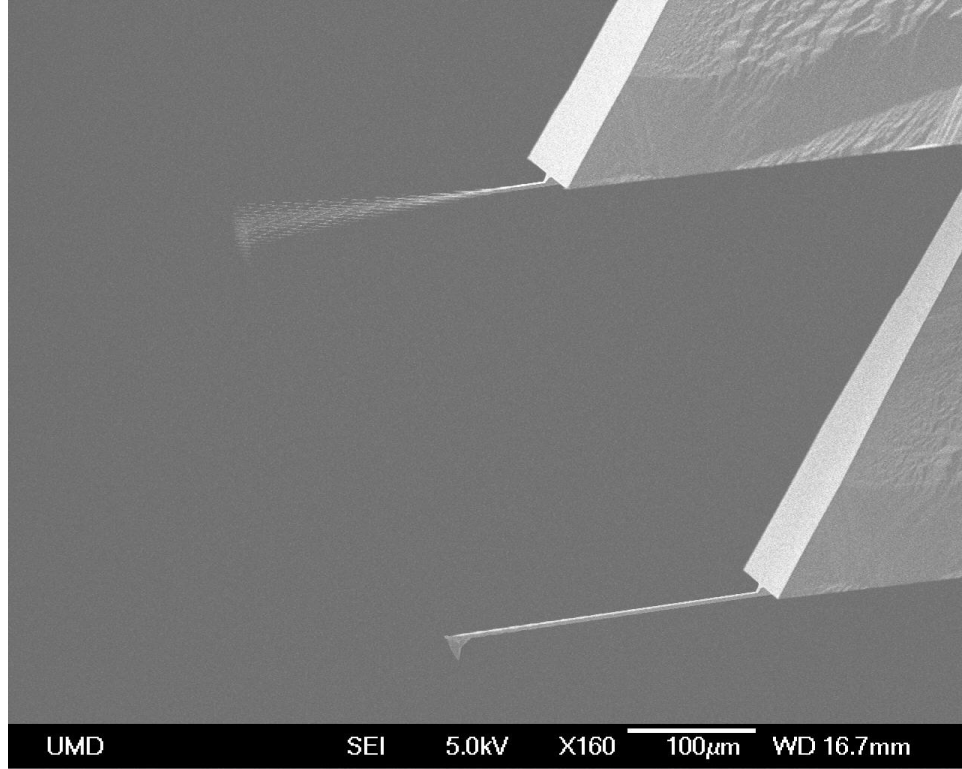
Figure 4.9: SEM image of two FESP model AFM probes mounted onto the end of the piezoelectric bimorph. When driven at 71.344 kHz the top cantilever is excited into resonance, and appears as a blurred cone due to the frequency of vibration being much greater than the raster scan rate of the microscope.

be used for fine motion control inside of the resolution of the step actuator. The ability to excite mechanical resonance in cantilevered structures was verified on an FESP model AFM probe shown in Figure 4.9, where the beam is vibrating at 71.344 kHz. The second FESP tip in the image remains still, evidence that the oscillation is confined solely to the intended cantilever and is not motion of the entire bimorph nor electrical interference. The dynamic actuation can also be used to simulate shock or fatigue loading on nanowire arrays.

Galfenol nanowires can be firmly attached to AFM probes inside of the SEM

through a technique known as electron beam induced deposition (EBID) [77, 100], often referred to as "nano-welding." This procedure consists of decomposing hydrocarbon molecules via high energy irradiation, which effectively results in the adsorption of the carbonaceous material wherever the electron beam is focused. Typically the source of the residual organic molecules is the oil used by the vacuum pump that persists even at pressures down to 10^{-6} Pa, although in some instances paraffin wax is included in the SEM solely for enhancing these deposition rates [167]. Once the AFM probe is positioned in contact with the target nanowire, the SEM accelerating voltage is increased to the maximum 30 kV, and the beam is placed in spot mode rather than raster scanning. The time required for deposition varies heavily with the cleanliness of the chamber, the contamination of the surface, and the beam parameters, but typically within a few minutes a blob of glue will form at the interface and securely affix the wire to the probe tip, an example of which can be seen in Figure 4.10. Once the wire is attached it can be extracted from the array by simply withdrawing the manipulator motors, although in many cases this can result in an unintentionally broken wire or even the removal of an entire cluster of adhered wires, as shown in Figure 4.11.

Using this rather odd arrangement of wires secured to the AFM tip, an initial attempt was made to visualize the mechanical behavior of the iron-gallium nanowires. The sequence of images in Figures 4.12, 4.13, and 4.14 demonstrate nanowire bending using the manipulator device, revealing large elastic deflections and adhesion between wires. These capabilities will be put to use during the more rigorous mechanical testing described in the following chapters.
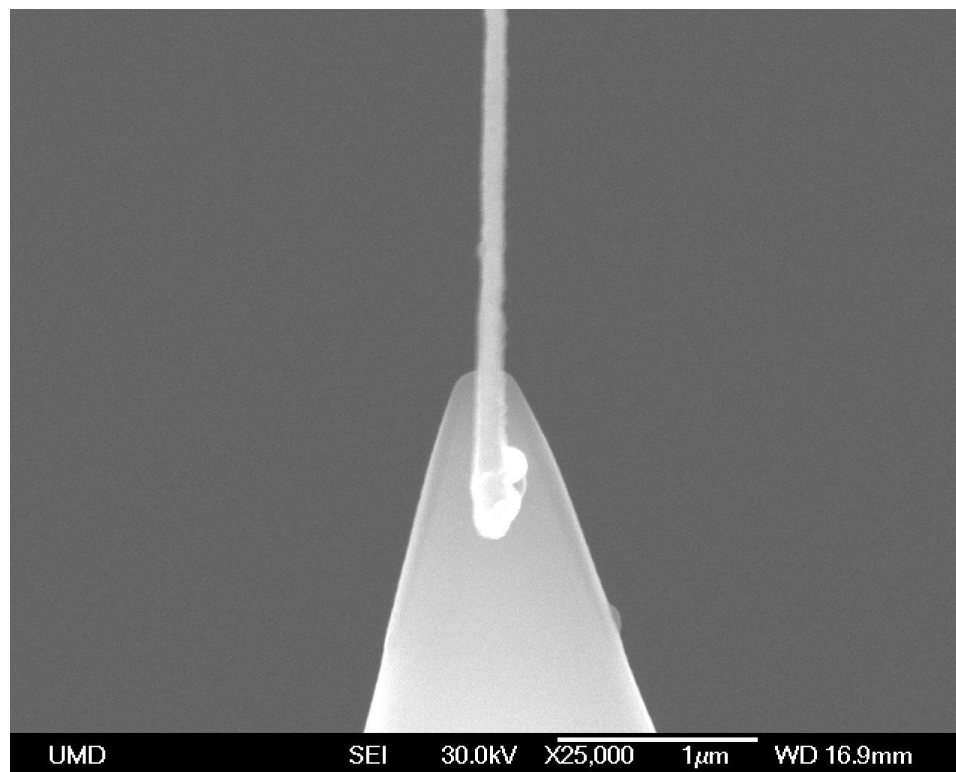
Figure 4.10: A 125 nm diameter Galfenol nanowire securely attached to an AFM tip with an EBID clamp of deposited carbonaceous material.
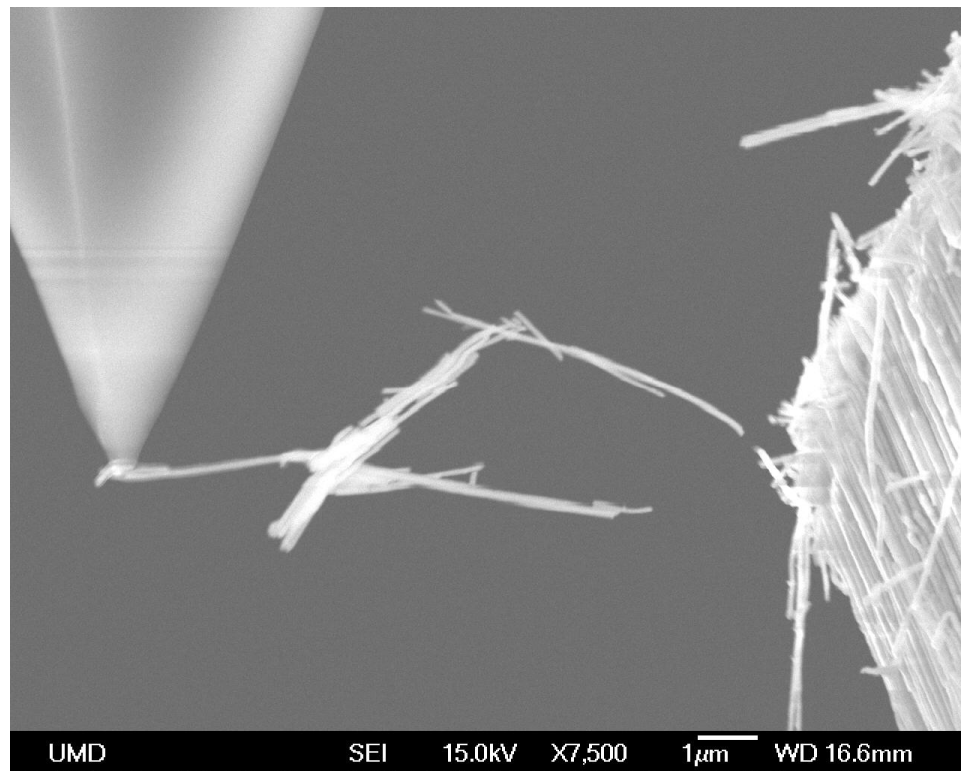
Figure 4.11: Micrograph showing an entire group of nanowires that have been pulled off of the array. The one free end was attached via EBID to the AFM tip, and the remaining wires came along due entirely to adhesive forces between them. This haphazard structure provides a good example of the stiffness in both the clamp and the original nanowire.
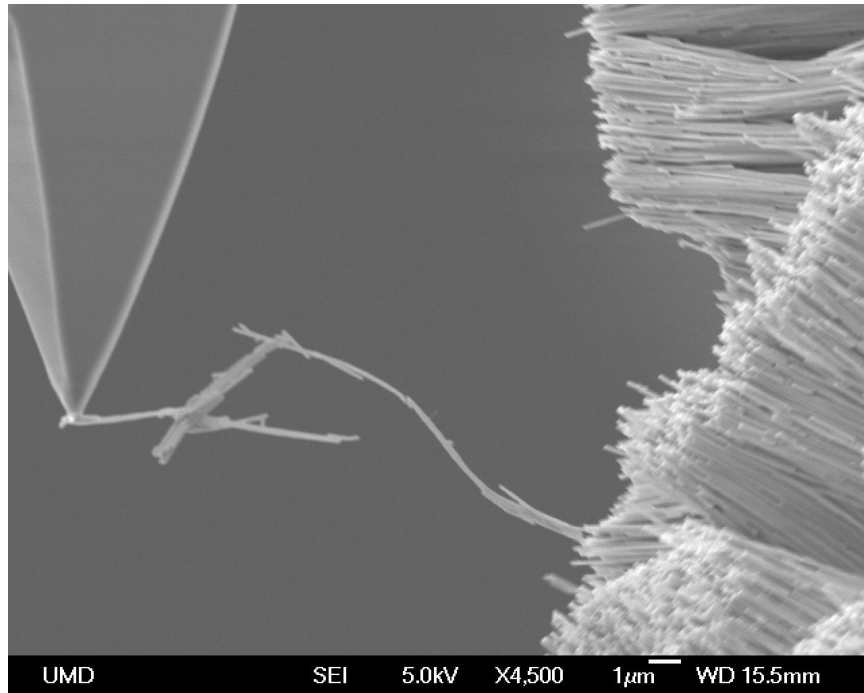
(a)
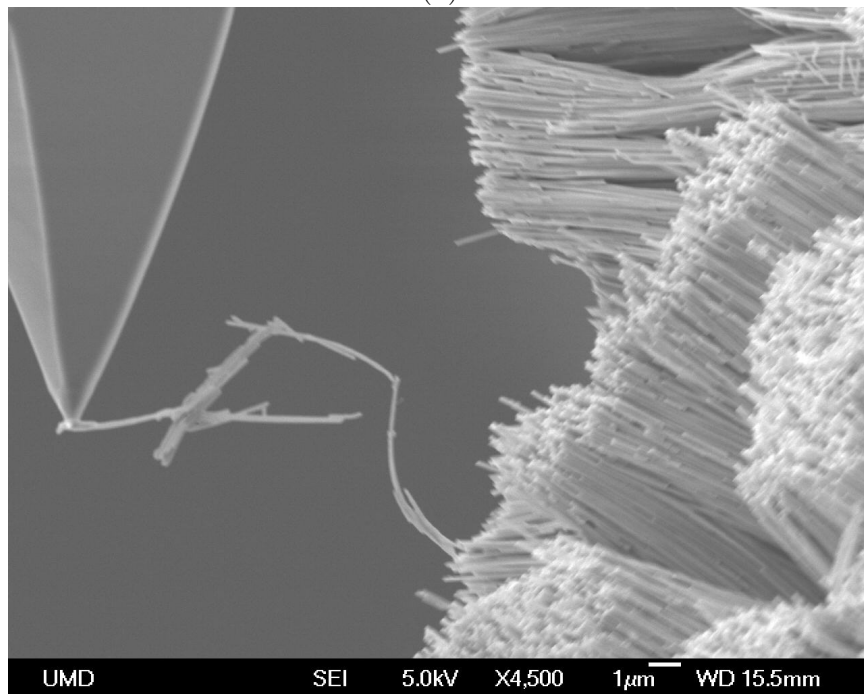
(b)

Figure 4.12: Sequence of micrographs demonstrating the bending of Galfenol nanowires using the manipulator device. The end of the wire cluster makes contact with the tip of another wire still in the array (a), and both are deflected as they are pushed closer together (b).

117
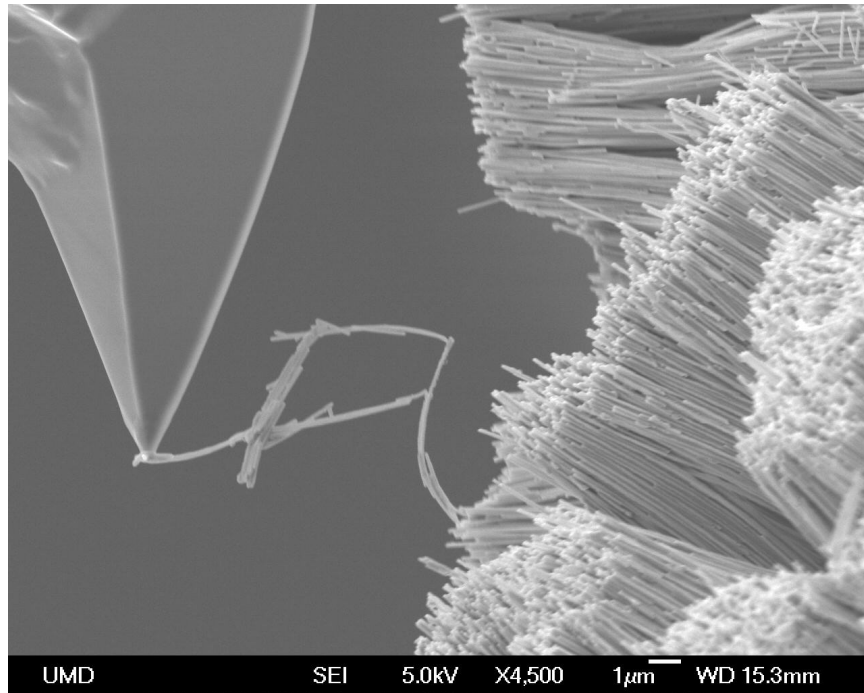
(a)
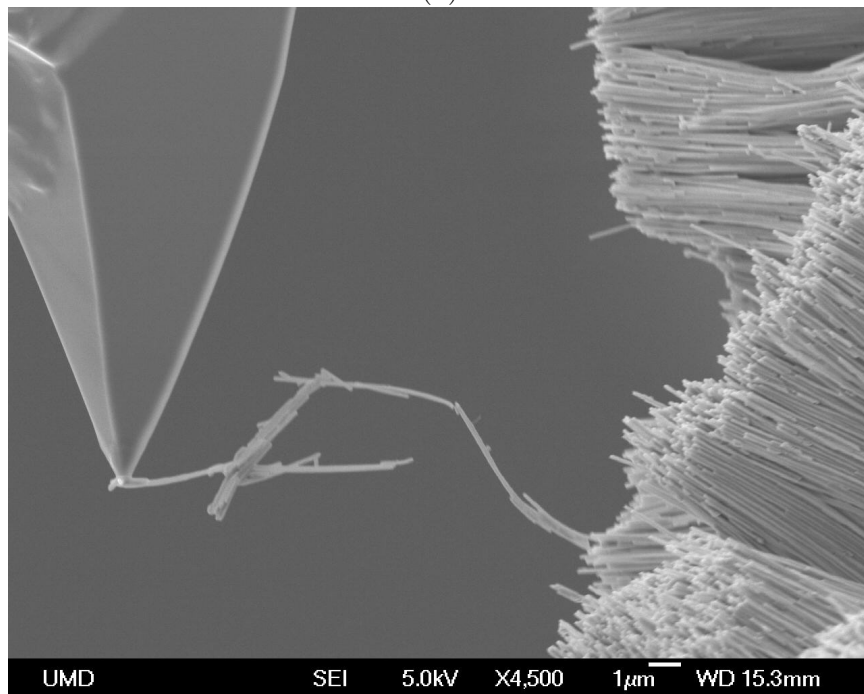
(b)

Figure 4.13: As the manipulator stages are pushed even closer together the wires bend very sharply (a), and elastically return to form as the stages are retracted (b).
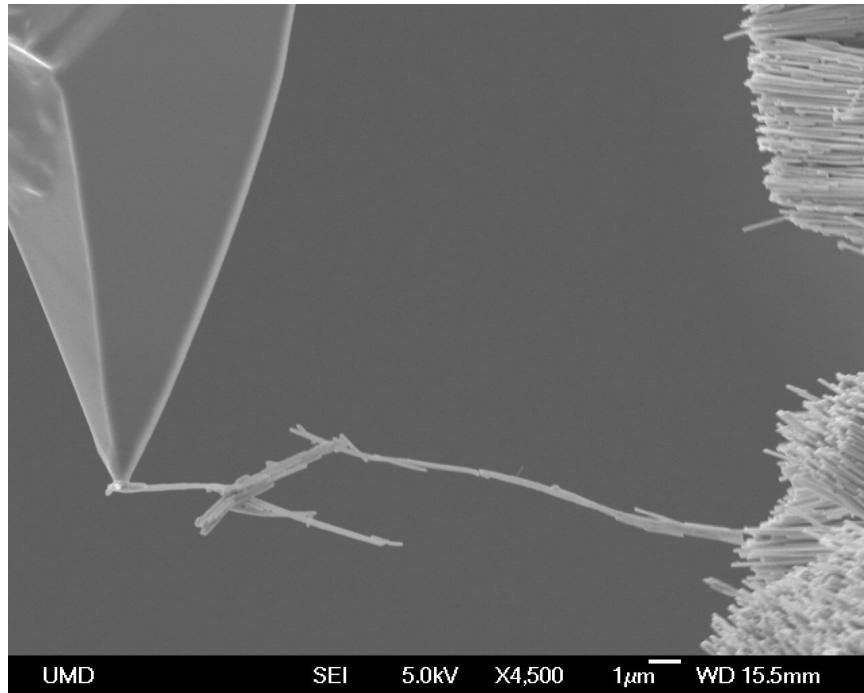
(a)
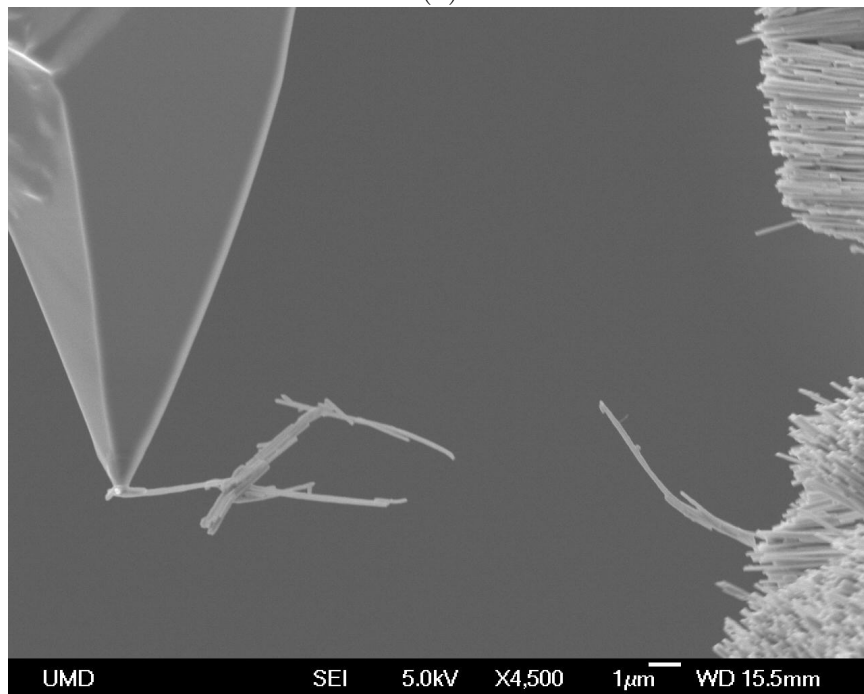
(b)

Figure 4.14: Upon withdrawal, attractive forces hold the wires together beyond the point of original contact (a), before finally snapping apart with no sign of permanent deformation (b).

Chapter 5

Characterization of Nanowire Mechanical Properties

5.1   Objectives

This chapter details the investigation into the mechanical behavior of iron-gallium nanowires. In order to facilitate the design of artificial cilia sensors, several key properties need to be measured in order to verify the assumption that the ordinary continuum theory utilized in Chapter 3 is valid for structures of this size. Therefore, the primary goal of this investigation is the identification of Young's modulus, linear elastic behavior, ultimate tensile strength, and failure mode using the nanomanipulator device discussed in Chapter 4.

The conducted experiments emulate procedures performed at the macroscale for directly measuring these properties, namely quasi-static tensile testing and mechanical resonance identification. Due to the inherent challenges in studying nanomaterials however, these tests contain a larger level of uncertainty than one would expect during a typical evaluation on an ideal bulk sample. As such, this work is intended more as verification that the Galfenol nanowires are sufficiently robust for handling the deformations expected in a cilia sensor device, rather than as a comprehensive study of mechanical parameters.

5.2 Tensile Testing

5.2.1 Experimental Method

The first and often most challenging step in performing a tensile test is locating a suitable nanowire sample. Ideally, the wire needs to be aligned perfectly vertical in the SEM field of view in order to maintain this orientation during the tensile loading. Unfortunately, the often random arrangement of the cantilevered nanowire arrays depicted in Figure 5.1 make it difficult to locate nanowires that meet this criterion. In many cases even if a section of an array is well aligned, it is so densely packed that isolating a single wire proves impossible.

One workaround to these issues is to use loose wires dropped onto a silicon wafer, which provide a much larger range of possible orientations as shown in Figure 5.2. This also reduces the odds of the selected wire being still firmly attached at the base of the array. The deposition of the wires onto silicon does introduces some other concerns however, including: wires being much shorter due to breakage, neighboring fragments adhering to the sides, and the loss of knowledge about alignment in the z direction. In practice, the identification of tensile samples makes heavy use of the nanomanipulator capabilities, trial and error, and experience.

In any regard, after selecting a usable wire the AFM probe attached to the x/y stage is moved into position directly behind the nanowire. Getting the correct z depth is first approximated by making sure the wire and the probe tip are at the same working distance, then fine tuned by simply moving the tip past the nanowire and adjusting until the two make noticeable contact. At this point, an EBID weld
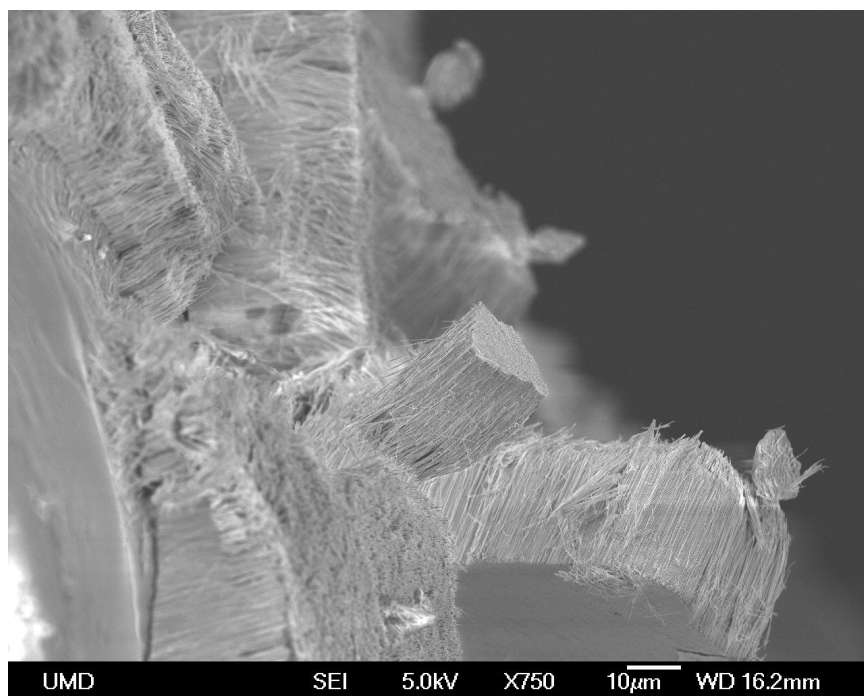
Figure 5.1: Galfenol nanowire cantilevered arrays in various orientations attached to the nanomanipulator stage.
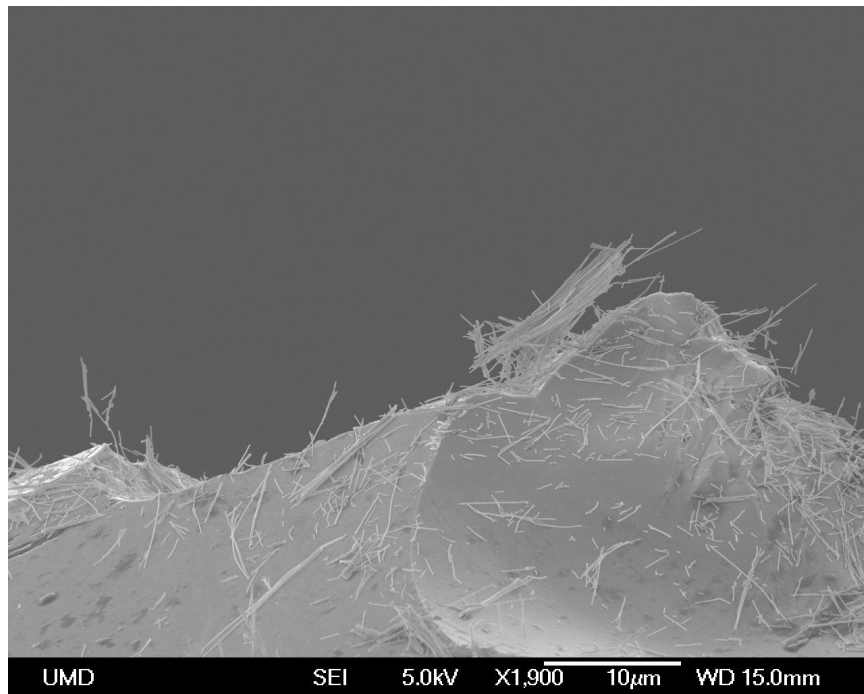
Figure 5.2: Loose Galfenol nanowires scattered along the edge of a silicon wafer for easier extraction for mechanical testing.
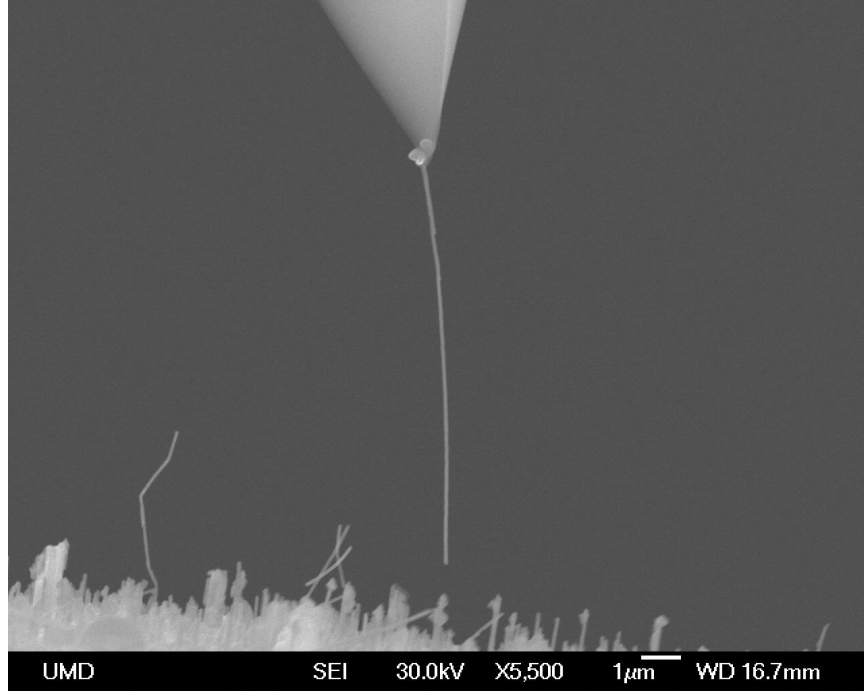
Figure 5.3: Nanowire welded onto the AFM tip and successfully removed from the array with the manipulator.

is applied to the top of the wire to create a rigid attachment between the two, and then using the motors of the manipulator the wire is fully extracted as in Figure 5.3.

Once the nanowire is securely removed, it is moved into position such that the free end is in contact with the tip of a second AFM probe mounted on the z stage. Once again the exact position is fine tuned, and then another EBID clamp is formed at the base of the wire to hold it in suspension between the opposing AFM probes, as shown in Figure 5.4. The resultant structure is essentially a set of three mechanical springs arranged in series, the two cantilever AFM springs and the extensional stiffness of the nanowire. Experimentally this allows for controlling the
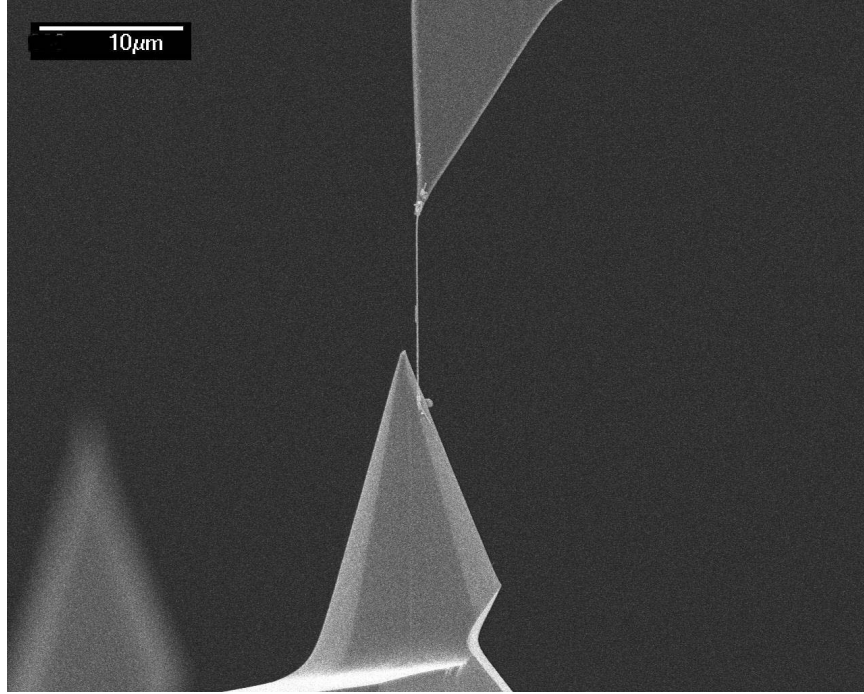
Figure 5.4: Nanowire firmly attached to opposing AFM probes for tensile testing. As the two tips are pulled apart with the manipulator motors, the sample is loaded in tension and stress and strain data are recorded.

load applied to the Galfenol, as the force applied to all three spring components is equivalent.

To this end, the spring stiffness coefficient of each AFM cantilever is experimentally calibrated prior to use in the SEM. While each commercial batch of probes has a rated stiffness, it is estimated from a nominal cantilever geometry that is known to vary by as much as 20% across a silicon wafer from which the probes are manufactured [142]. This is exemplified by a box of FESP model probes, for example, listing a resonance frequency somewhere between 60 and 100 kHz. Given this uncertainty, the exact spring constant can be more accurately determined by comparison with reference cantilevers of known stiffness. These reference canitlevers are specially

125

fabricated and tested for this purpose by Veeco Instruments, Inc.

The calibration procedure is as follows. First, the cantilever to be calibrated is mounted in the AFM instrument and moved downward a set distance into contact with a solid material assumed to be infinitely stiff. The deflection of the cantilever δ_0 is recorded with the standard AFM software. Next, the cantilever is placed above the free end of one of the known reference cantilevers, and moved downward the same distance while recording the new deflection δ_{test}. By assuming that the solid material does not deform at all, the deflection of the reference probe will be the relative difference, $\delta_{ref} = \delta_0 - \delta_{test}$. The calculation of the spring constant k_{test} of the desired probe simply follows from a force balance of the two springs:

$$ k_{test} = k_{ref} \, \frac{\delta_{ref}}{\delta_{test} \, \cos \theta}, \tag{5.1} $$

where k_{ref} is the known stiffness of the reference cantilever and θ represents the slight angle of inclination introduced by mounting the test cantilever on the standard AFM probe holder [142].

For tensile testing, the two AFM probes between which the nanowire is suspended are chosen to have widely different spring constants. It is desirable to have one of the probes be far stiffer than the other and act as a fixed boundary, resulting in only the softer cantilever noticeably deflecting. This greatly improves the ease with which measurements are made. For achieving this condition during a typical tensile test, the top probe is usually an OTESPA model with a stiffness at least 40 times greater than the general purpose FESP model bottom cantilever.

With the nanowire suspended between the two AFM probes with accurately

known spring constants, the actual tensile experiment is conducted by slowly pulling the tips apart with the manipulator motors. Typically, the first few steps simply remove any slack in the system, but subsequent pulling nicely loads the wire into tension. The exact strain rate is difficult to estimate, but typically appeared to be on the order of 5 nm/s. Every few seconds the pulling ceased, and a series of micrographs were taken for data analysis. Because the nanowire and AFM tips are in series, the force throughout the structure can be directly measured from the deflection of the soft AFM cantilever with known spring constant. Throughout the test this deflection x_{afm} is readily apparent within the SEM, as shown in Figure 5.5. The distance that the tip has moved is measured from the backside of the bent cantilever at the position of the nanowire to the plane of the fixed base on the left of the image. This value is simply multiplied by the spring constant to provide the applied force F. Close examination of the nanowire diameter d allows the cross-sectional area $A = \pi d^2/4$ to be measured, and the wire tension σ is simply F/A.

The strain data comes from directly measuring the length of the nanowire during loading. As the pixel resolution of the SEM images is greatly reduced at lower magnification, it is often necessary to divide the sample into several smaller lengths that can be zoomed in upon and more accurately measured. The presence of attached fragments or noticeable defects in the wire surface make for useful landmarks during this process. Once the total wire length L is summed up, the strain ε is calculated by $\varepsilon = (L - L_0)/L_0$.

Both the stress and strain measurements clearly include some uncertainty,
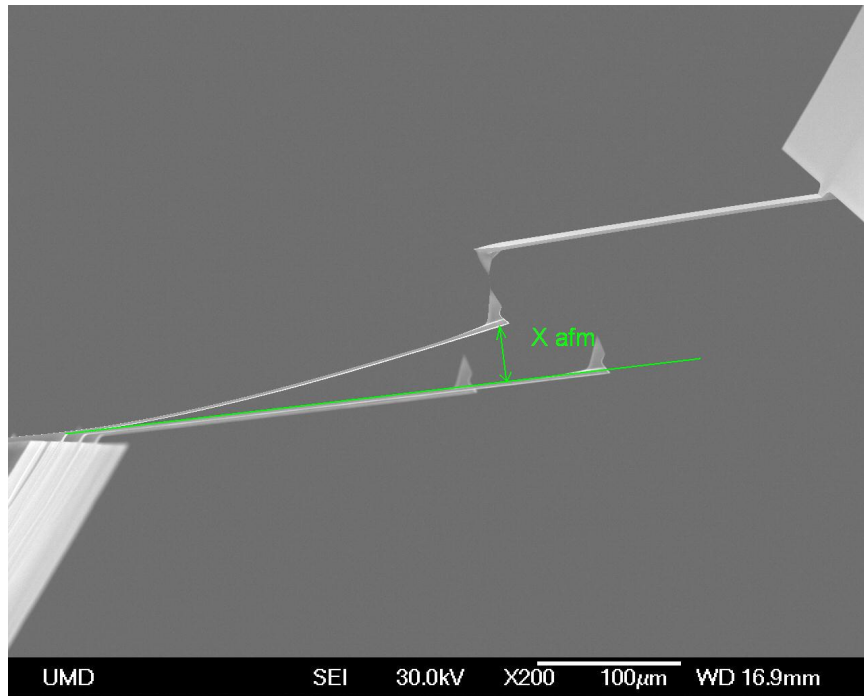
Figure 5.5: During tensile testing, the deflection x_{afm} of the soft lower cantilever is readily apparent, and is used to calculate the stress applied to the nanowire.

which based on the resolution of each individual measurement can turn out to be rather significant. Specifically, the stress value σ is calculated from

$$\sigma = \frac{k_{test}\, x_{afm}}{\pi\, d^2/4}, \tag{5.2}$$

which implies that the total uncertainty is

$$err_\sigma = \sqrt{\left(\frac{\partial \sigma}{\partial k_{test}}\, err_k\right)^2 + \left(\frac{\partial \sigma}{\partial x_{afm}}\, err_x\right)^2 + \left(\frac{\partial \sigma}{\partial d}\, err_d\right)^2}, \tag{5.3}$$

where the errors associated with each measurement are $err_k = 0.1 \times k_{test}$ N/m, $err_x = 3$ μm, and $err_d = 5$ nm. Similarly, the error in the strain is computed from

$$err_\varepsilon = \sqrt{\left(\frac{\partial \varepsilon}{\partial L}\, err_L\right)^2 + \left(\frac{\partial \varepsilon}{\partial L_0}\, err_L\right)^2}, \tag{5.4}$$

where the wire length error is a constant $err_L = 10$ nm.

5.2.2   Results and Error Analysis

The initial tension tests were performed on samples from the earliest batch of Galfenol nanowires received from the University of Minnesota, with the intent to become familiar with the technique and to identify any blatant sources of error. As a result, the first data collected was a check of the linearity of the cantilever spring constant. As the manipulator motors pulled the stages apart, the load in the structures as calculated from the bottom cantilever deflection was plotted against the current relative distance between the top and bottom cantilever bases. The data in Figure 5.6 shows that the applied force behaves very linearly when compared with the distance traveled, validating the linear spring model assumption for the AFM probe.
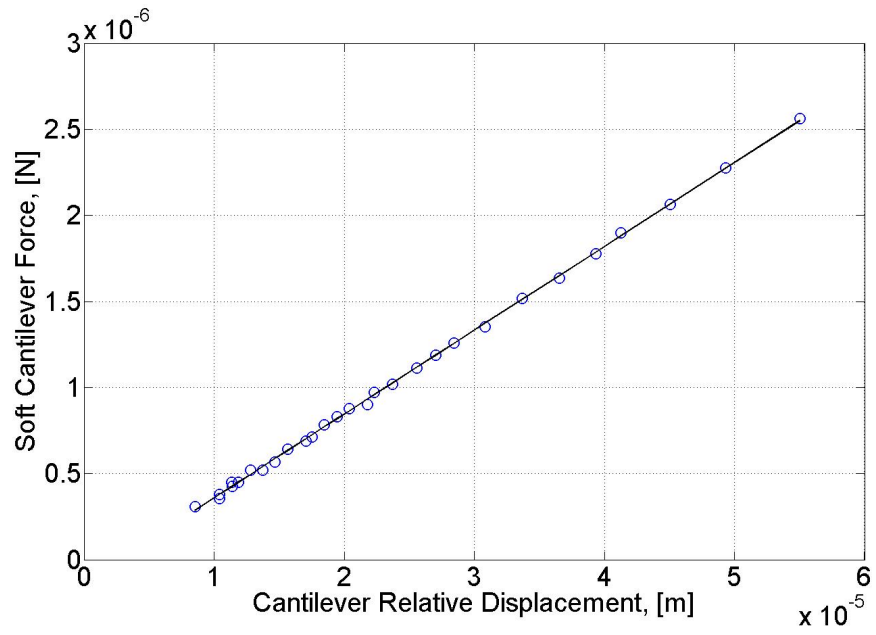
Figure 5.6: Plot of the force applied by the soft bottom cantilever as calculated by its deflection, versus the total relative displacement between the fixed bases of the two AFM cantilevers. This data confirms that the bottom cantilever deflects linearly with the manipulator motor spacing.

An example of the stress vs. strain data collected from an iron-gallium nanowire is plotted in Figure 5.7. The nanowire specimen was observed in the SEM to be 13.8 μm long and 135 nm in diameter, clamped between a rigid OTESPA model cantilever and a MikroMasch CSC37 probe with calibrated stiffness of $k_{test} = 1.42$ N/m. The sample was loaded in increasing tension until failure, which occurred just above the last presented data point, near 1200 MPa. The wire fracture occurred approximately 1 μm below the upper weld joint and appeared to be entirely brittle in nature, as evidenced by Figure 5.8 and supported by the lack of apparent plastic deformation in the stress vs. strain curve. Attempts to more clearly image the fracture surface were unsuccessful. The data also reveals good linear elastic behavior with a slope that implies a Young's modulus $E = 60 \pm 7$ GPa. While this value is strongly suggestive of the [100] modulus of 65 GPa measured in bulk $Fe_{83}Ga_{17}$ [71], the 1200 MPa ultimate strength is more than double the maximum macroscale value of 500 MPa. As will be discussed in Section 5.4 however, the modulus similarity is likely an erroneous comparison due to the difference in composition. It is postulated that the root cause of the drastic improvement in strength can be traced to the nanowire fabrication process outlined in Section 1.3.2, where the electrochemical deposition produces material with numerous dislocations that are effectively work hardened within the AAO pores. The result of this would be an improvement in strength at the cost of ductility, in agreement with the presented data.

During the course of the initial testing a number of potential sources of systematic error were identified, beyond the aforementioned measurement uncertainties. The first of these is the nanowire alignment, as any deviation from the perfectly
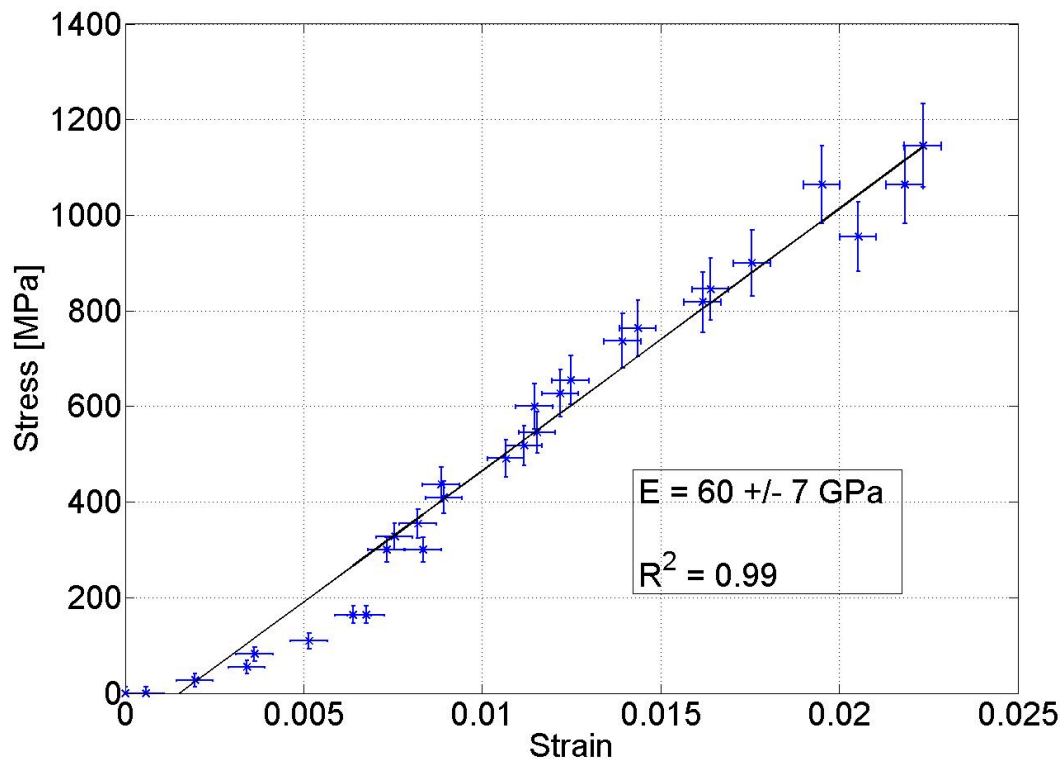
Figure 5.7: Stress vs. strain data from a tensile test performed on a 135 nm diameter, 13.8 μm long Galfenol nanowire. The sample had a Young's modulus of approximately 60 GPa, an ultimate tensile strength of 1200 MPa, and no plastic deformation.
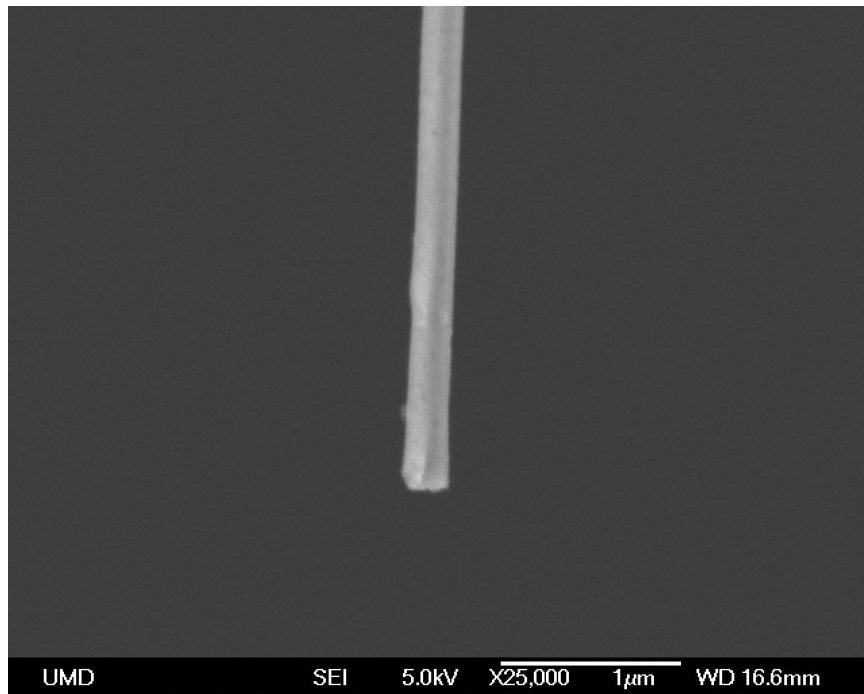
Figure 5.8: Micrograph at the point of nanowire tensile failure showing a brittle fracture mode.

Figure 5.9: Error analysis considered in [39], where the wire has pinned boundary conditions resulting in misalignment angles α in the x/y plane and β in the y/z plane. While α can be monitored within the SEM, β is very difficult to detect.

vertical condition will result in applied force inaccuracies. Ding et al. [39] provides a thorough discussion of these effects, where the misalignment angle α in the x/y plane is readily apparent and correctable in the SEM (see Figure 5.9), but a height mismatch β is difficult to detect due to the z depth information being done entirely by eye. Often this error is only detectable after wire failure when the opposing fracture surfaces do not line up. This reference formulates that the error due to this effect decreases the measured force by a factor of $(1 - cos\beta)$ and results in the calculated ultimate strength and modulus values to be lower bounds.

There is of course an additional source of error caused by this misalignment that is not touched upon in the literature, namely that the EBID clamps at the wire ends do not behave as simple supports but rather as fixed boundary conditions. The result is that misalignment during the tensile test will introduce bending loads in addition to the uniaxial tension. Starting from the Euler-Bernoulli beam equation for a sample with uniform bending stiffness EI, deflection w, and no distributed

loading:

$$EI\,w'''' = 0, \tag{5.5}$$

the beam deflection $w(x)$ will be of the form

$$w(x) = \frac{1}{EI}\left(\frac{C_1}{6}\,x^3 + \frac{C_2}{2}\,x^2 + C_3\,x + C_4\right). \tag{5.6}$$

The four coefficients can be solved for by using the boundary conditions for a fixed-fixed beam,

$$w'(0) = 0 \tag{5.7}$$

$$w'(L) = 0 \tag{5.8}$$

$$w(0) = 0 \tag{5.9}$$

$$w(L) = \Delta \tag{5.10}$$

where L is the beam length and Δ is the misalignment distance between the AFM probe tips in either the x/y or y/z planes, as depicted in Figure 5.10. The result is a bending moment at each end of the wire with magnitude of

$$M(0) = -M(L) = EI\,w'' = \frac{6\,EI\,\Delta}{L^2}, \tag{5.11}$$

causing a maximum axial stress of

$$\sigma = \frac{3\,E\,d\,\Delta}{L^2}, \tag{5.12}$$

with d representing the wire diameter. This bending stress and the pure tension are combined through superposition, resulting in larger actual stresses than what is calculated via $\sigma = F/A$. Using typical material properties, this underestimation can be as much as 10% for a Δ of 1 μm.

Figure 5.10: Misalignment error considering fixed-fixed boundary conditions. Any offset Δ will add bending stresses to the sample in addition to the tension, and result in an underestimation of stress by up to 10%.

In addition to the alignment issues, there are concerns that the actual stiffness of the bottom AFM cantilever can skew the results. The impetus for this reasoning was that initial data suggested a lower Galfenol Young's modulus when tested on a softer probe. In order to diagnose this, a set of tensile tests were conducted on incrementally stiffer cantilevers available in the lab. Table 5.1 shows that while there certainly is a trend between AFM stiffness and measured modulus at low values of k_{test}, above a minimum threshold of approximately 1.4 N/m the data is consistently within the experimental uncertainty. The explanation for this is that if the AFM cantilever is overly soft it can bend beyond the range where deflections are assumed vertical and start to move radially about its fixed end. Not only does this decrease the accuracy of the linear spring model, it clearly enhances the misalignment errors and accentuates the underestimation of stress and the overestimation of strain. Once the tip is stiff enough to remain well behaved, further increases have no effect on the nanowire data.

Another potential problem in accurately measuring tensile data is the assump-

tion that the EBID welds are fixed. Clearly the quality of the boundary condition is dependent on the deposition time, but previous research [39] has shown that it asymptotes with incremental deposits of carbonaceous material. In light of this information, each EBID joint was deposited for approximately 30 minutes to firmly attach the AFM tip and nanowire, but it is acknowledged that other variables such as vacuum pressure and electron beam current also play a role. With regards specifically to the tensile testing, there is also the potential problem of the weld material itself straining during application of stress. Any strain in the EBID joint would not alter the force applied to the nanowire due to it being mechanically in series, but it can lead to incorrect strain data if the measurements are made between points on the weld rather than on the wire itself. As the deposited clamp often has unique topographic features (see Figure 5.11) between which length measurements are more convenient, this error can occur frequently.

As a result of identifying these sources of error in the tension experiments, a few modifications were implemented to the testing procedure. First, it was decided that the large measurement uncertainty of the stress made the data unreliable. The primary culprit in this was the uncertainty of the AFM tip deflection err_x in equation (5.3), which is very high due to imaging at a sufficiently low magnification to see both the bent probe and the fixed cantilever end in the field of view. To

Table 5.1: Effect of AFM cantilever stiffness on the modulus of Galfenol nanowires.

k_{test} [N/m]	0.05	0.97	1.42	3.60	23.2
E [GPa]	7	46	60	58	59
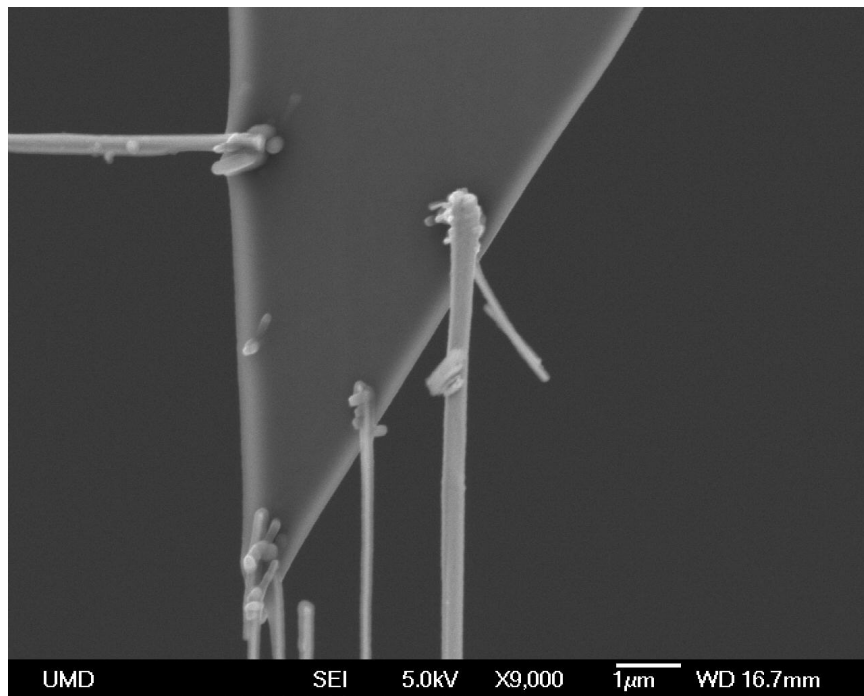
Figure 5.11: Image revealing the unique surface features of the deposited carbonaceous weld material. Slight variations in deposition settings result in numerous different growth shapes and sizes.

improve this, an alternate measurement technique was used that relies on the angle of deflection of the AFM tip rather than its absolute position. Beginning once again with equation (5.5) for a bending beam with small displacements, the boundary conditions now take the form of

$$w(0) = 0 \tag{5.13}$$

$$w'(0) = 0 \tag{5.14}$$

$$w''(L) = 0 \tag{5.15}$$

$$w'''(L) = F \tag{5.16}$$

for a fixed end at $x = 0$ and a free end with point load F at the tip. As a result, the deflection $w(x)$ and slope $\theta(x)$ of the beam are

$$w(x) = \frac{F}{EI} \left(\frac{1}{6} x^3 - \frac{L}{2} x^2\right) \tag{5.17}$$

$$\theta(x) = w'(x) = \frac{F}{EI} \left(\frac{1}{2} x^2 - L x\right), \tag{5.18}$$

which implies that the desired deflection at the tip is related to the angle via

$$w(L) = \frac{F L^3}{3 EI} = \frac{2}{3} L \cdot \frac{F L^2}{2 EI} = \frac{2}{3} L \cdot \theta(L). \tag{5.19}$$

As the angle that the AFM tip makes with the plane can be measured at much higher magnification within the SEM, the angular uncertainty is $\pm 0.1°$ and results in an overall reduction in stress data error. Another minor change that was made to the overall experimental method was the exclusive use of cantilevers with a stiffness above 3 N/m in response to the data in Table 5.1. A final consideration was that in order to minimize the potential effect of EBID weld stretching on the recorded strain

data, it was ensured that the nanowire length measurements were taken between points on the wire itself and not convenient landmarks on the deposited material.

Tensile tests were conducted on several more nanowires from the same fabrication batch. The use of commercial AAO templates results in some variation in size between samples, but nonetheless all four wires presented in Table 5.2 appear to have similar mechanical properties. It must be noted that these samples were later found to have very poor stoichiometry (see Section 5.4), and as such the data is more useful for validating the experimental procedure than comparing to literature values. Figure 5.12 shows wire 3 in testing position, with the remnants of wire 1 directly to its left. In each case, the stress vs. strain data originally presented in Figure 5.7 exemplifies the result from every wire, as there was a large improvement in tensile strength and brittle failure near one end. While this data attests that the nanowires are capable of the large elastic deflections desired for artificial cilia applications, and is adequate for modeling the mechanical behavior, the similarity in moduli and the uncertain composition still raise the question of whether the values are actually from the nanowires or if the procedure systematically measures ≈ 60 GPa for any arbitrary sample. In order to alleviate this final doubt, it was decided to perform tensile tests on a suitable benchmark material.

5.2.3   MWCNT Validation

Multi-wall carbon nanotubes (MWCNT's) represent an ideal choice for comparison with the iron-gallium nanowires primarily because they are readily available

Table 5.2: Tensile testing results from nanowire samples that were found to contain on average only 3 at. % Ga and excessive levels of O.

Wire No.	Diameter [nm]	Length [μm]	Ultimate Strength [MPa]	Young's Modulus [GPa]
1	105±5	9.80±0.01	1230±170	58±9
2	135±5	13.8±0.01	1200±150	60±7
3	225±5	36.8±0.01	1080±120	55±8
4	130±5	7.55±0.01	1050±150	59±10
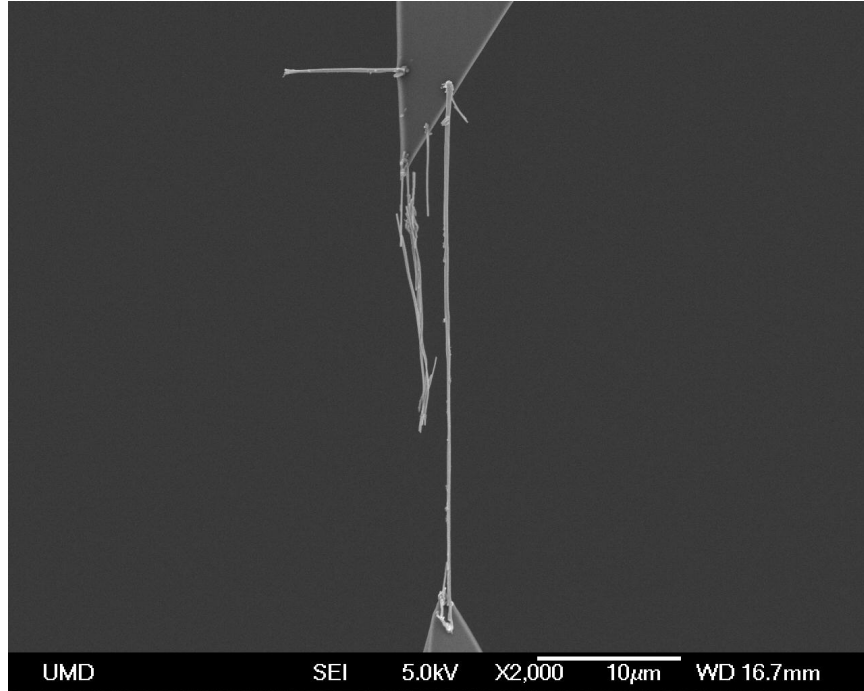
Figure 5.12: Tensile wire 3 attached to opposing AFM probes prior to loading. This image is a lower magnification version of Figure 5.11, revealing the fractured remnant of wire 1 immediately to the left of the wider wire 3. Additional things of interest are an extraction attempt foiled by adhered neighbors and a cantilevered wire intended for resonance testing.

and have been intensely studied. In fact, the machine built by Professor Ruoff's group that strongly influenced the nanomanipulator design was originally used to investigate tensile failure in CNT's [167]. As such, tensile test results can be compared with both the Galfenol data and published values in the literature.

Dr. Cumings kindly provided arc-grown MWCNT samples [44, 70] that were placed onto a silicon wafer in a similar manner to the Galfenol nanowires. The manipulator device was used to extract a few nanotubes from the overall cluster shown in Figure 5.13, and then attached as before between an OTESPA and an FESP model AFM cantilever. Manipulating the CNT's provided a different set of challenges, as while they were easier to extract and weld than the Galfenol nanowires, they also were much harder to align and tended to permanently kink in a frustrating manner.

Nonetheless, the tensile experiment was carried out in exactly the same manner used previously, where Figure 5.14 shows one example of a MWCNT attached at both ends. The only difference from the previous Galfenol testing was that the area A used for the calculation of stress is taken to be the space between adjacent layers with outer diameter OD and inner diameter ID, separated by a small distance δ. The area expression is derived from

$$A = \frac{\pi}{4}\left(OD^2 - ID^2\right) \tag{5.20}$$

$$A = \frac{\pi}{4}\left(OD + ID\right)(OD - ID) \tag{5.21}$$

$$A = \frac{\pi}{4}\left(OD + OD - 2\delta\right)(2\delta) \tag{5.22}$$

$$A \approx \pi\, OD\, \delta, \tag{5.23}$$
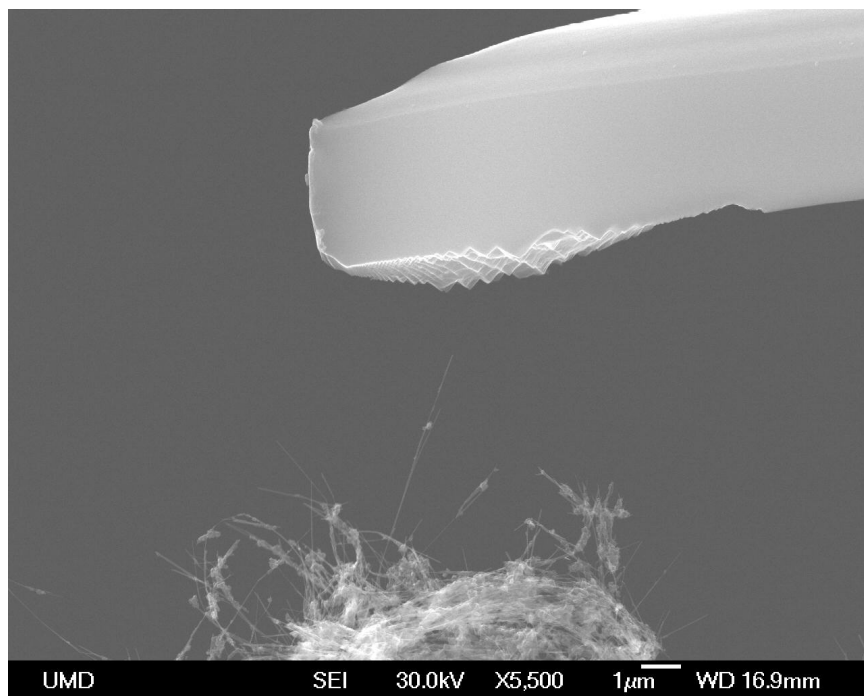
Figure 5.13: Cluster of MWCNT's from which the tensile samples are extracted. It was discovered that the AFM probe tip had broken off of the cantilever prior to installation in the manipulator, but the jagged Si fracture surface made a suitable replacement.
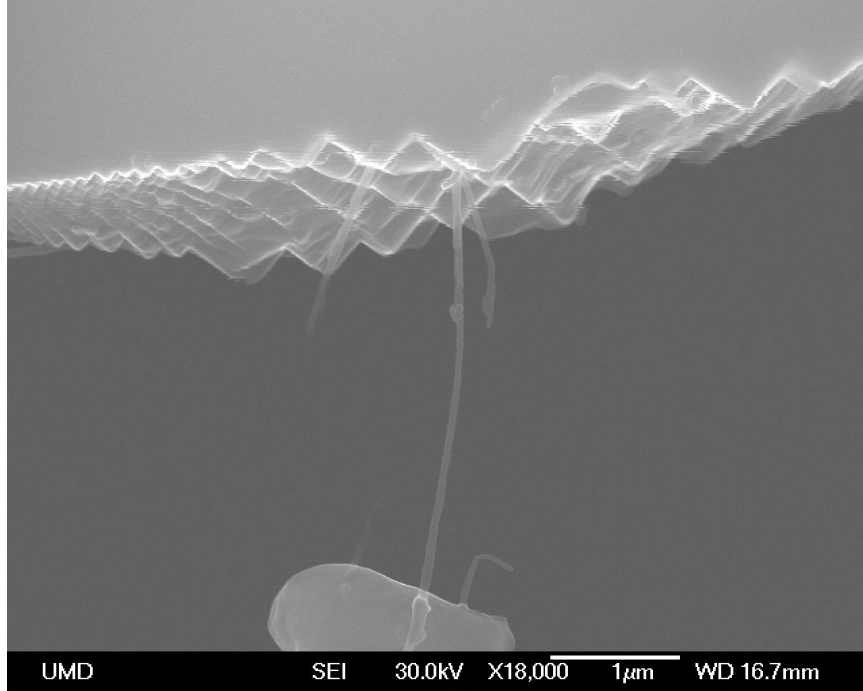
Figure 5.14: MWCNT with outer diameter of 110 nm loaded in tension. The various crooked ends demonstrate failed attempts at properly aligning and attaching tensile specimens.

which matches Yu et al. [167] when using an interlayer separation of $\delta = 0.34$ nm. Certainly there are other nominal area calculations that can be used, but this approach was taken to make the results most comparable with the literature.

Looking at the stress vs. strain data plotted in Figure 5.15, it is clear that the stresses and strains experienced by the MWCNT are significantly greater than those observed in the Galfenol nanowires. This nanotube with outer diameter of 110 nm had a tensile strength of nearly 90 GPa, a maximum elongation of over 13%, and a measured Young's modulus of 650 GPa. Upon failure, the inner layers that pulled out were tested again, now with a diameter of 60 nm, and were found to have a 60 GPa strength, 8% strain, and a 680 GPa modulus. All of these numbers

144
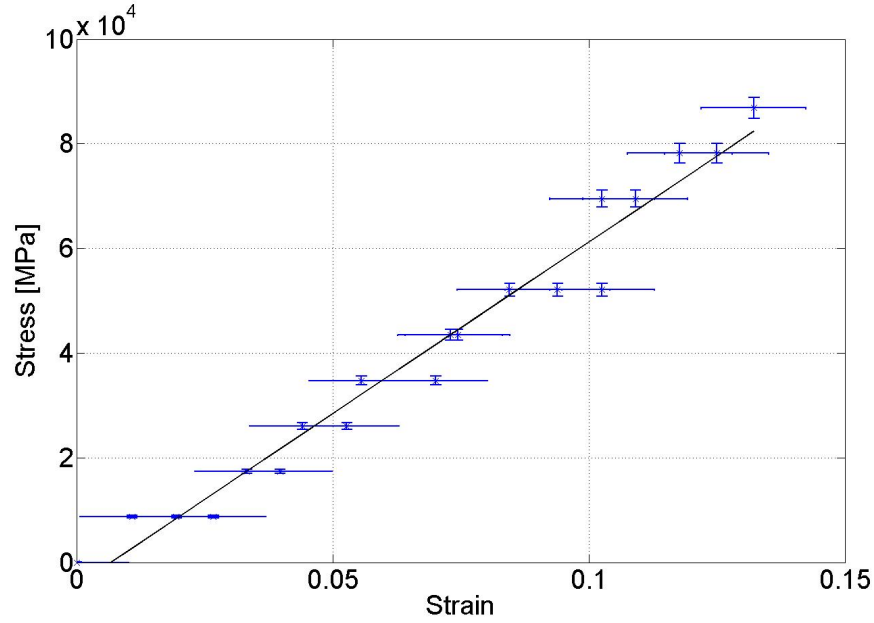
Figure 5.15: Stress vs. strain data gathered from the tensile testing of an arc-grown MWCNT with outer layer diameter of 110 nm. The tensile strength is nearly 90 GPa at a maximum strain of 13%, resulting in a modulus of 650 GPa, far above what was measured for the Galfenol samples.

agree well with the referenced study, which found strengths ranging from 11 to 63 GPa, strains of up to 12%, and moduli from 270 to 950 GPa. Because the measured moduli values were repeatable and clearly not $\approx$ 60 GPa, it is reasoned that the values obtained during tensile testing on the Galfenol nanowires are in fact a solid representation of the material properties.

A final note about the MWCNT testing is that the failure mechanism is quite different from the iron-gallium specimens. The layered nature of the nanotubes often results in a 'sword-in-sheath' failure mode, where the outermost layer fractures and the inner ones are free to pull out of the remaining shell. Figure 5.16 displays a few examples of this observed within the SEM, where in one instance the result is

a significant decrease in nanotube diameter and in another it manifests as a large length change with a region of slightly smaller diameter.

5.2.4   Effect of Magnetic Field

It is common for magnetostrictive devices to operate in the presence of a magnetic bias field in order to linearize behavior or improve performance. The results in Chapter 2 demonstrate the advantages of having axially magnetized beams used as bending mode sensors, and as such the effect of an applied field on the mechanical properties was also investigated. It is known that the magnetoelastic strain softens the material within a prescribed stress region, as it is easier to rotate the magnetization than to elastically strain the aligned lattice. This effect, commonly referred to as 'delta-E,' has been observed in several magnetostrictive materials [81, 24] and appears to exist in the nanowire data of Figure 5.7 as well, where the slope of the curve is flatter over the low stress region but becomes uniform once the tensile loads have aligned the magnetization to saturation.

To determine the exact effects of an applied magnetic field on these results, tensile experiments are conducted with a small permanent magnet placed inside of the manipulator. The placement of the magnet was such that it did not noticeably interfere with the SEM imaging, but as a result the strength of the field at the sample position was only 20 Oe as measured with a Hall probe. While the stray field from the magnet obviously has a large spatial variation it was assumed uniform over the small length of the nanowires being tested.

146
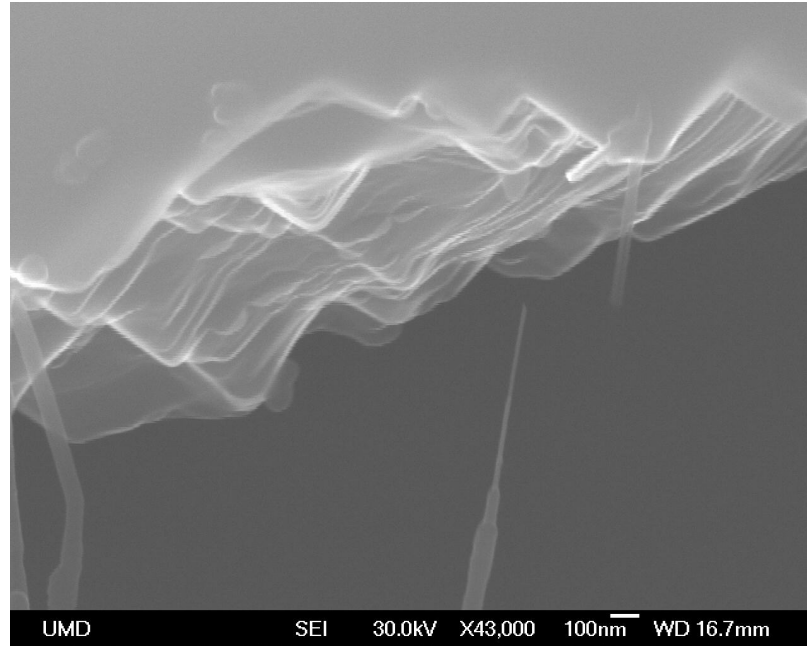
(a)
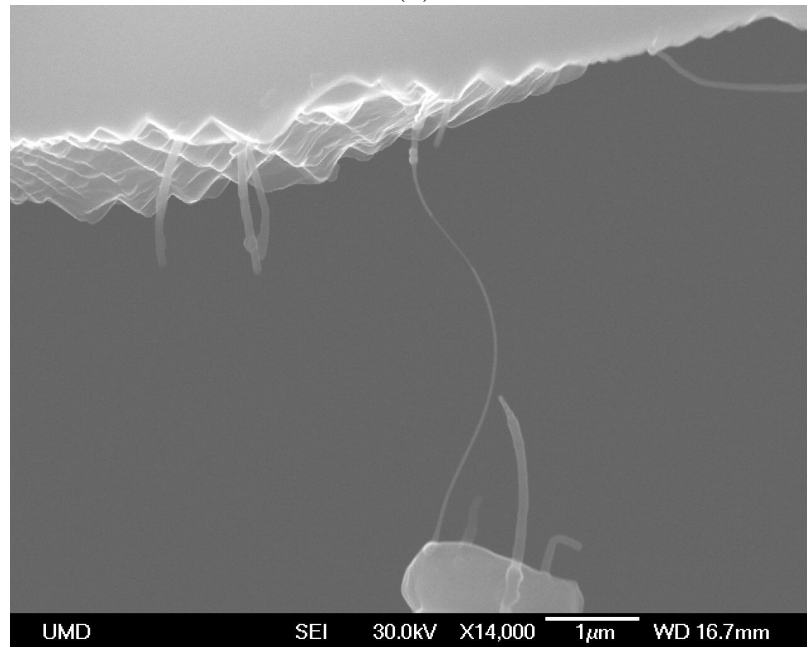
(b)

Figure 5.16: Observations of failure in the MWCNT tensile testing. Failure in 'sword-in-sheath' mode reveals several narrower sections of inner layers that pull out from the outermost layer (a). When the outer layer fails the inner portion slides within, resulting in a large increase in length that bends the sample into a curve (b).

The effects of magnetic field were found to be very minor, in agreement with expectations. Figure 5.17 compares data from tests with and without the bias field applied. By comparison, the only potential difference is the removal of the apparent lower slope region due to the lack of magnetostrictive strain in the saturated sample. However, considering the dominance of the magnetic shape anisotropy to be discussed in Chapter 6, this trend is most likely due to initial slack in the system or simple measurement error. The modulus of elasticity of 55 GPa is well within the range of uncertainty from the 53 GPa measured without the field applied, and considered unaffected. As the wire was needed for further testing it was not loaded to failure, so the maximum stress in the plots is substantially below the failure strength. The positive implication of this result is that even moderate fluctuations in field experienced by a nanowire sensor should have a negligible effect on performance.

5.3 Resonance Testing

5.3.1 Experimental Method

The alternate method of measuring the elastic moduli of Galfenol nanowires is a resonance test [38], where the material properties are directly related to the resonance frequencies of cantilevered nanowire beams. As the dynamic excitation for this procedure is provided by the piezoelectric bimorph vibrating in the y direction of the SEM image, the first step in performing this task is the EBID attachment and subsequent extraction of a nanowire aligned roughly parallel to the AFM cantilever.
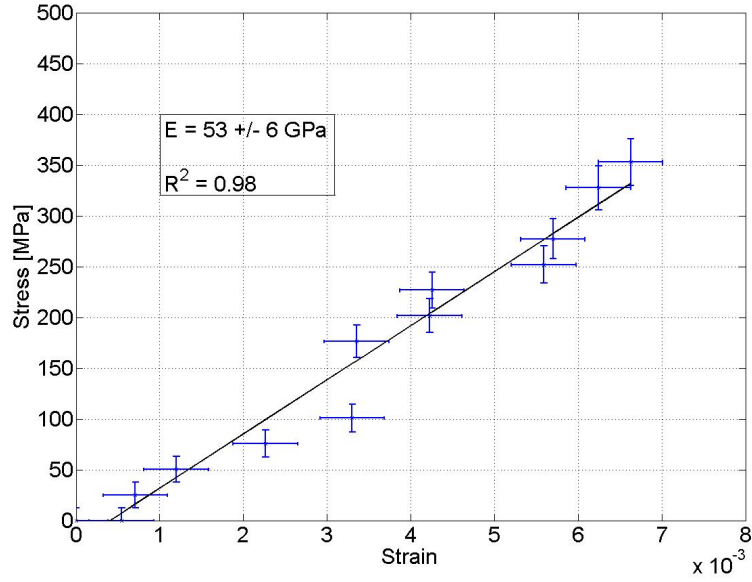
(a)
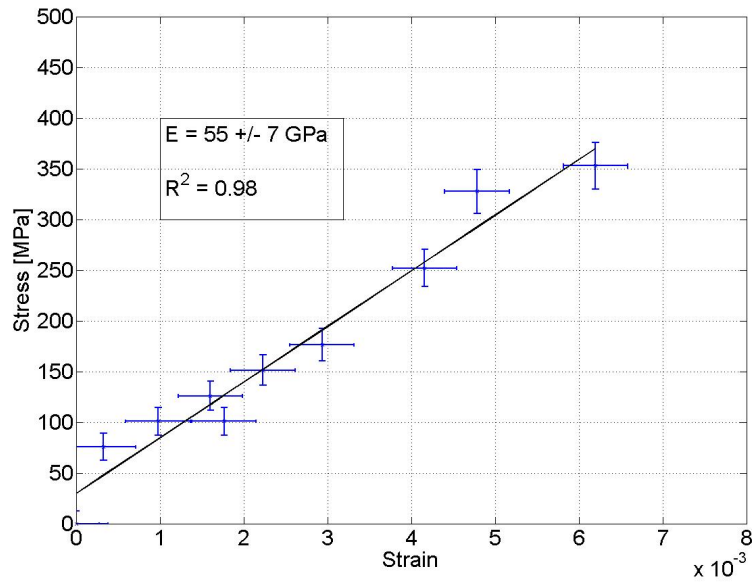
(b)

Figure 5.17: Results of tensile experiments from the same nanowire without (a) and with (b) a 20 Oe dc magnetic bias field applied. The data is within the uncertainty range and considered unaffected by field.

149
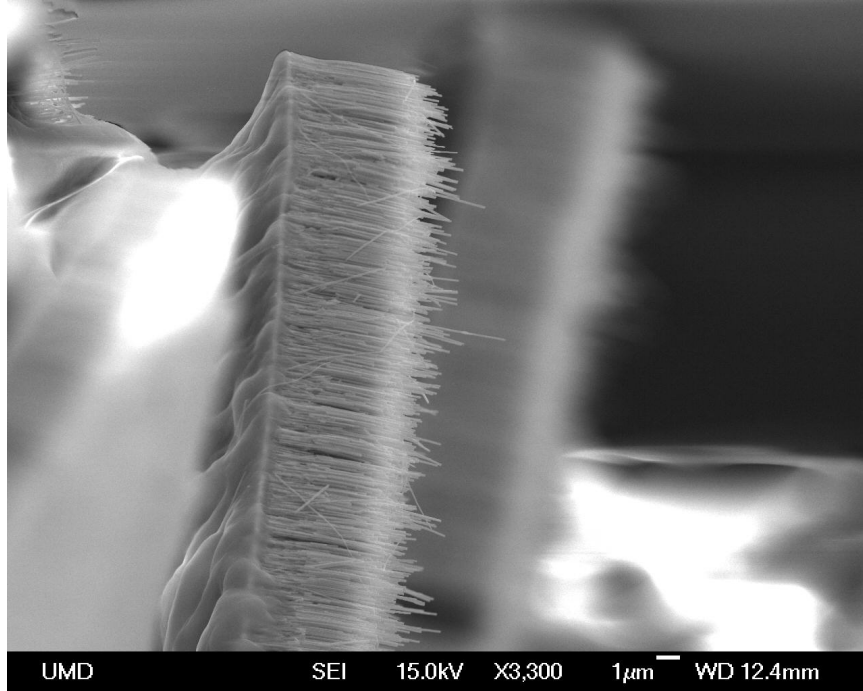
Figure 5.18: Close packed nanowire arrays positioned perpendicular to the AFM cantilever for potential resonance sample extraction.

As with the tensile experiments, the starting nanowire configurations can range from the well oriented arrays in Figure 5.18 to the loose tangle of wires in Figure 5.19. The same challenges exist here as well, as the wires frequently clump together and/or break at the tips, as presented in Figure 5.20. In one amusing example, the extracted nanowire remained attached to a section of the array and successfully suspended it. Figures 5.21 and 5.22 show the undesirable array and the attempts to remove it, including dragging it along the remainder of the array and shaking it with the piezoelectric actuator.

The result typically is a cantilevered nanowire of sufficient length to have a first mode resonance that is attainable with a conventional function generator.
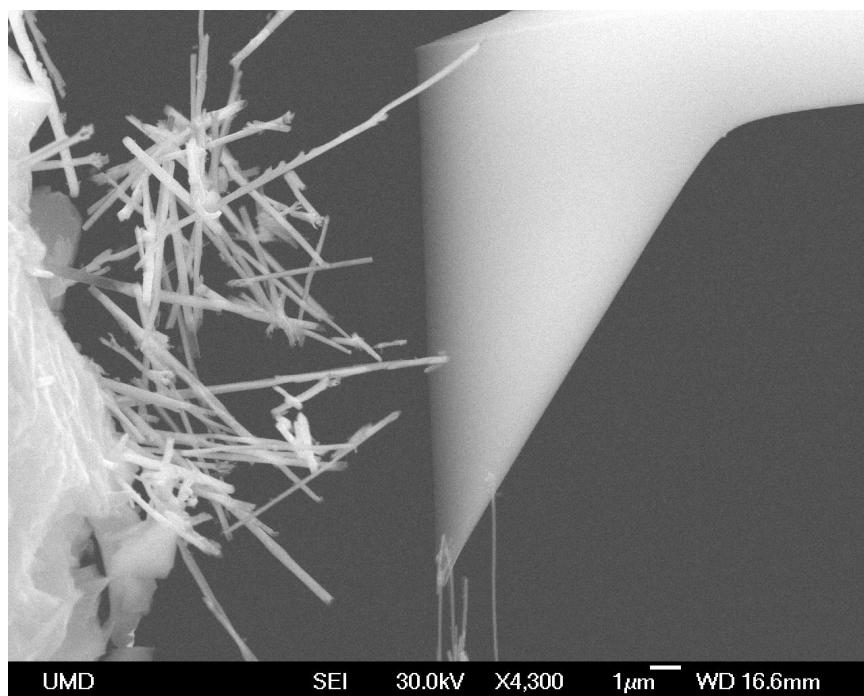
Figure 5.19: Tangle of loose nanowires from which a well oriented one can be welded onto the AFM tip and pulled out.
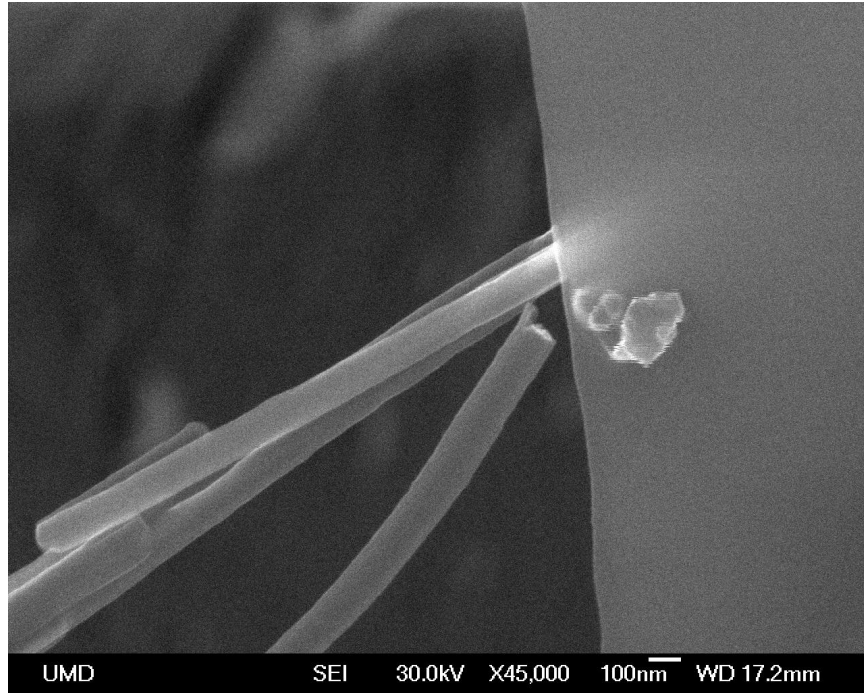
(a)
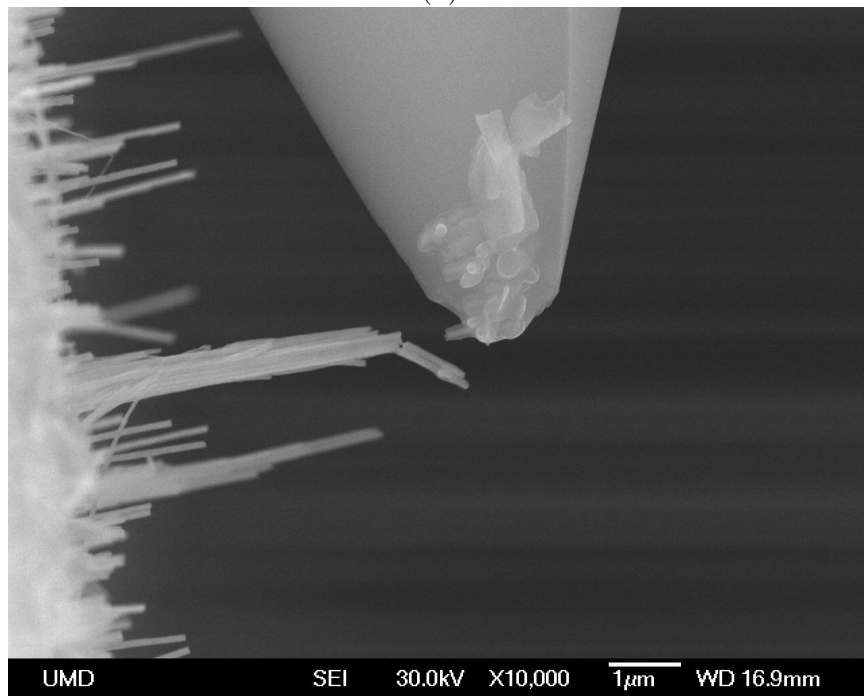
(b)

Figure 5.20: Typical challenges faced when extracting resonance samples. In many cases the wires simply clump together and do not break free from their nearest neighbors (a), and in others the tips of the wires fracture if they are overly constrained in the array (b).
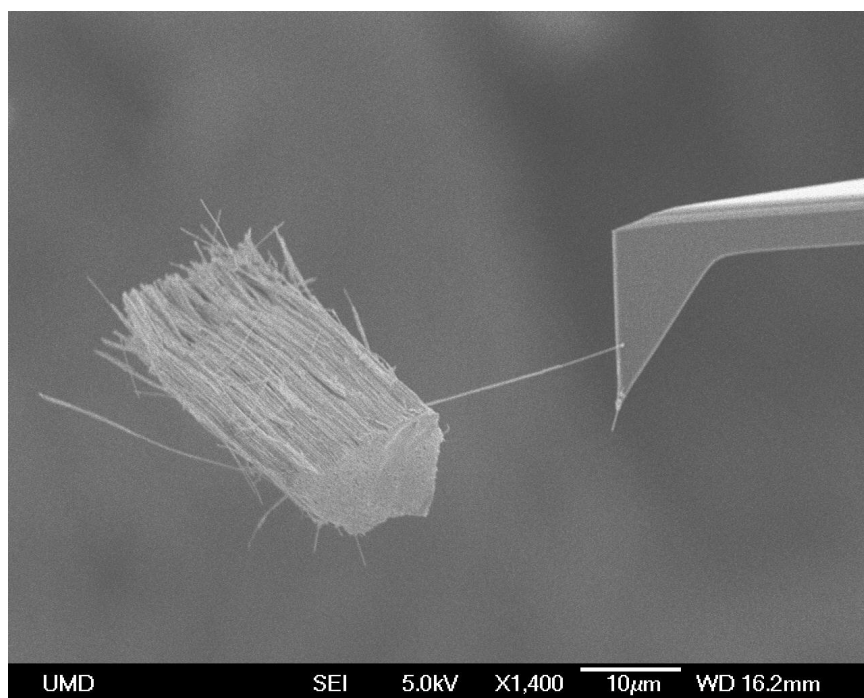
Figure 5.21: Upon removal of a cantilevered nanowire, it brought along an entire section of array and suspended it. Note that there is a second nanowire adhered to the side over the outer half of the sample.
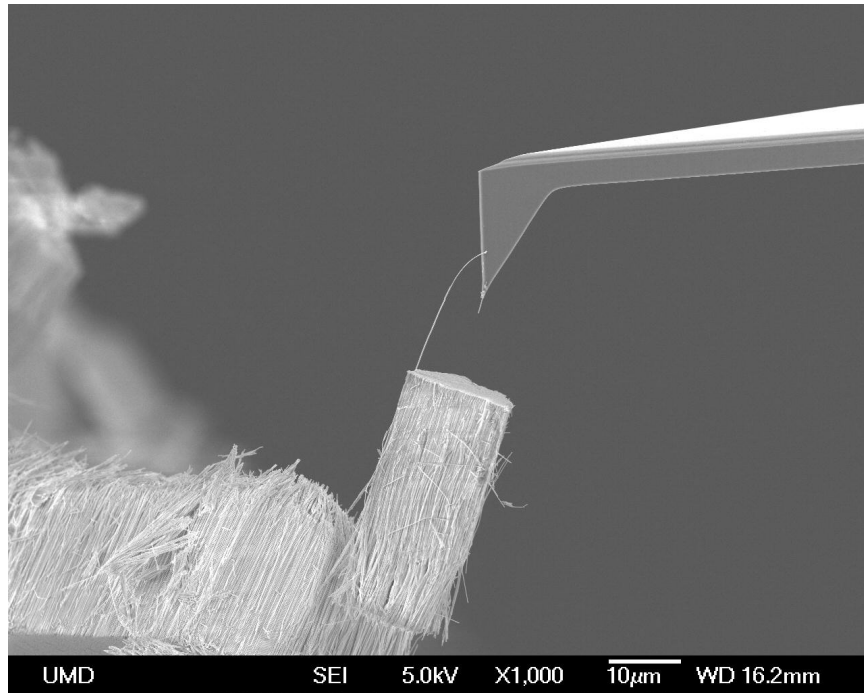
(a)
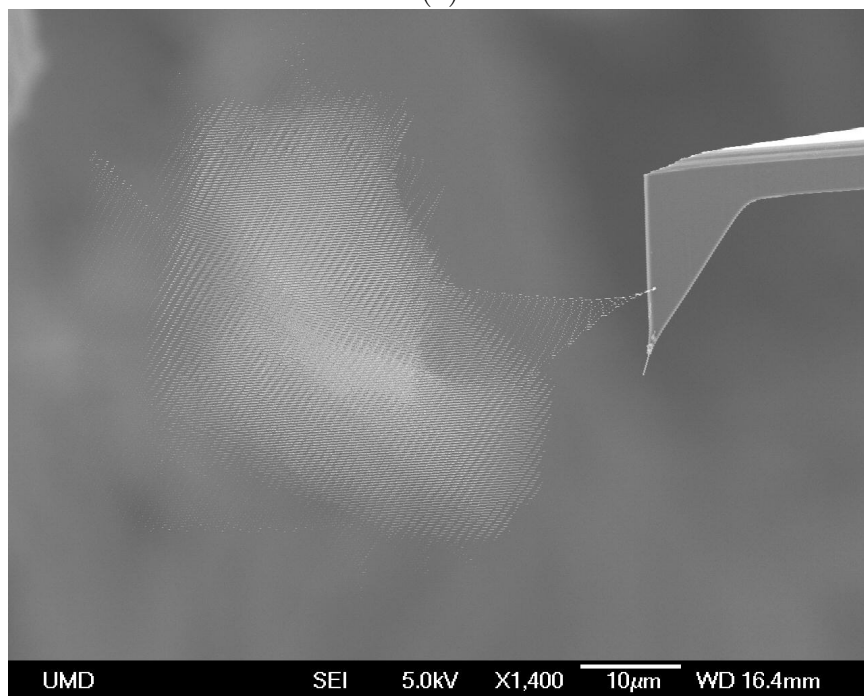
(b)

Figure 5.22: Attempts to remove the unwanted section of array: dragging it along the remainder of the array (a) and trying to shake it off with the piezoelectric bimorph (b). Eventually success was reached by smashing the entire structure into the larger array.

The experiment itself simply consists of driving the piezoelectric bimorph with a low voltage (typically up to 500 mV) swept sine signal and observing the nanowire vibration. When the beam is excited near its fundamental resonance, the nanowire appears as a blurred cone bounded by its maximum amplitude of vibration while the rest of the micrograph is still, due to the frequency of oscillation being much higher than the raster scan rate of the electron beam. Figure 5.23 demonstrates this concept. In order to reduce the chance of a spurious mode being detected, the resonance of the nanowire is always far away from that of the AFM cantilever and image oscillations induced by electrical interference can be deduced by watching the motion of the fixed background structure.

The preliminary experiments were conducted by watching the SEM display and making note of the resonance by eye. In order to make this process less tedious, a technique was developed that could detect resonances automatically by taking advantage of the voltage signal output from the microscope to the monitor. This signal is proportional to the image brightness, and is typically transmitted line by line as the image is scanned. When the beam is placed in spot mode however, the voltage is a constant relating to the intensity of the image at that fixed point. For resonance testing, the beam spot is placed at the free end of the cantilevered nanowire, corresponding to a rather bright voltage. During the frequency sweep, this point will be unchanging except for the region across which the beam is strongly vibrating, which due to the blurred cone effect will be naturally darker than the stationary wire. As a result, the measured brightness will decrease, and when inverted this recorded voltage will clearly show peaks corresponding to each frequency at which the beam
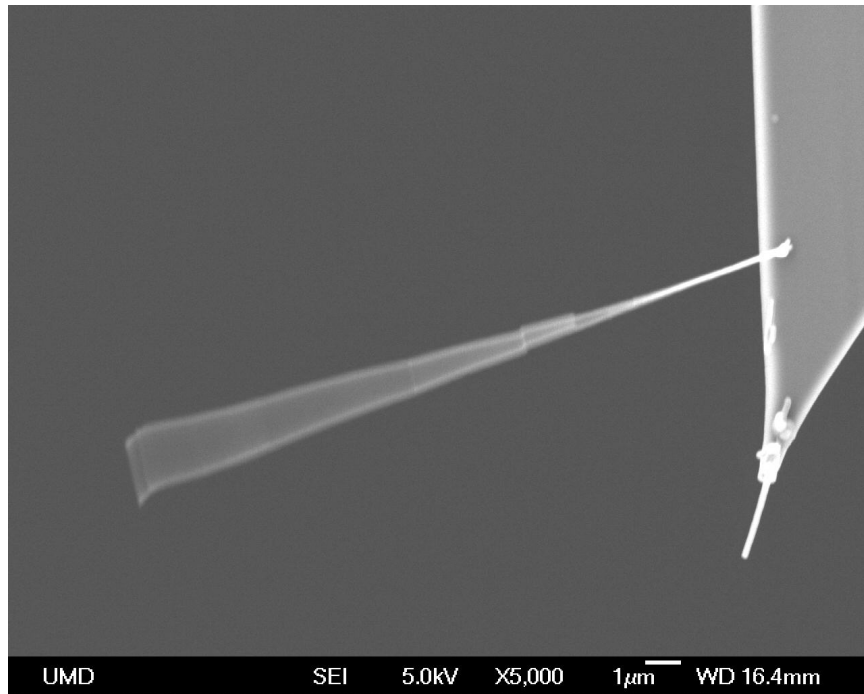
Figure 5.23: Cantilevered Galfenol nanowire excited by the piezoelectric bimorph at its resonance frequency. The image is stationary except for the wire itself, which appears blurry due to the vibration being much faster than the scanning rate of the SEM.
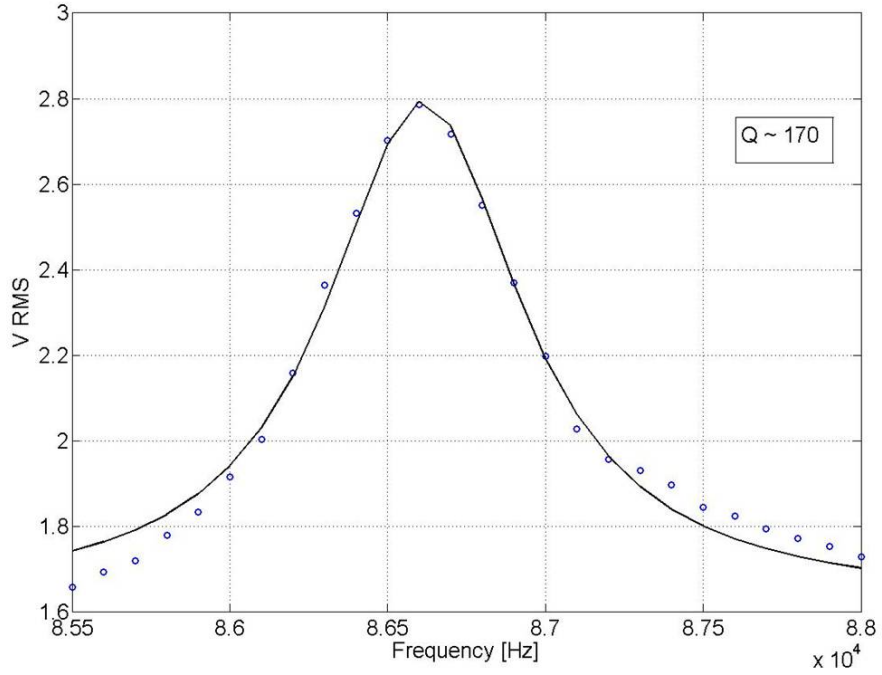
Figure 5.24: Plot of the inverted voltage signal from the SEM to the output monitor during a resonance test. With the electron beam in spot mode at the end of the cantilevered nanowire, the brightness of the image will only vary when the nanowire is in motion, such as at its fundamental resonance frequency. This technique allows for resonances to be identified during large automated sweeps.

was oscillating. Figure 5.24 displays one such voltage peak, where the resonance occurred at 86.6 kHz. Although the data represents the image brightness rather than the traditional amplitude or power spectrum, calculation of the half-power points and the bandwidth still provides a useful means of obtaining information on the damping, which can reflect the quality of the 'fixed' EBID boundary condition.

Once the resonance frequency has been accurately identified, it needs to be related to the Young's modulus of the material. This formulation once again starts with the Euler-Bernoulli beam equation, now including the unit mass m and accel-

157

eration $\ddot{w}$:

$$EI\, w'''' + m\, \ddot{w} = 0, \tag{5.24}$$

which can be solved with a separation of variables such that

$$w(x,t) = W(x)\, Y(t). \tag{5.25}$$

Substitution gives

$$EI\, Y\, W'''' = -m\, W\, \ddot{Y} \tag{5.26}$$

$$\frac{EI}{m}\, \frac{W''''}{W} = \frac{-\ddot{Y}}{Y} = \lambda, \tag{5.27}$$

where the temporal portion can be solved by assuming a harmonic response $Y(t) = Ae^{j\omega t}$, which results in

$$\ddot{Y} + \lambda Y = 0 \tag{5.28}$$

$$(-\omega^2 + \lambda)\, Ae^{j\omega t} = 0 \tag{5.29}$$

$$\lambda = \omega^2. \tag{5.30}$$

Returning to and rearranging the spatial equation for $W(x)$,

$$\frac{EI}{m}\, \frac{W''''}{W} = \lambda \tag{5.31}$$

$$W'''' - \frac{m\lambda}{EI}\, W = 0, \tag{5.32}$$

let $m\lambda/EI = p^4$, which allows the arbitrary solution to have the form

$$W(x) = C_1\, \sin(px) + C_2\, \cos(px) + C_3\, \sinh(px) + C_4\, \cosh(px). \tag{5.33}$$

The fixed-free boundary conditions

$$W(0) = 0 \tag{5.34}$$

158

$$W'(0) = 0 \tag{5.35}$$

$$W''(L) = 0 \tag{5.36}$$

$$W'''(L) = 0 \tag{5.37}$$

are used to identify that

$$C_3 = -C_1 \tag{5.38}$$

$$C_4 = -C_2 \tag{5.39}$$

$$C_2 = -C_1 \frac{\sin(pL) + \sinh(pL)}{\cos(pL) + \cosh(pL)}, \tag{5.40}$$

which leads to the characteristic equation of

$$\cos(pL)\cosh(pL) + 1 = 0 \tag{5.41}$$

that can be solved numerically for the eigenvalues

$$pL = [1.8751, 4.6941, 7.8548, 10.9955, \ldots]. \tag{5.42}$$

Looking only at the lowest eigenvalue that corresponds to the first mode, p can be solved for as $p = 1.8751/L$ which gives both the mode shape when substituted into equation (5.33) and the natural frequency f_0 via

$$\frac{m\lambda}{EI} = p^4 = (\frac{1.8751}{L})^4 \tag{5.43}$$

$$\lambda = \omega^2 = \frac{EI}{m}(\frac{1.8751}{L})^4 \tag{5.44}$$

$$f_0 = \frac{\omega}{2\pi} = \frac{1.8751^2}{2\pi}\sqrt{\frac{EI}{mL^4}}. \tag{5.45}$$

Therefore, once the resonance frequency of a nanowire has been found, equation (5.45) is solved for the modulus E with knowledge of the geometry and the mass per length m that is calculated from the material density.

159

As previously with the tensile testing, the uncertainty in this data due to measurement error can be calculated by first rearranging

$$E = \frac{4\pi^2 \, f_0^2 \, m \, L^4}{1.8751^4 \, I}, \tag{5.46}$$

then accounting for error on the measured values of L, f_0, and $I = \pi \, d^4/64$:

$$err_E = \sqrt{(\frac{\partial E}{\partial L} \, err_L)^2 + (\frac{\partial E}{\partial f_0} \, err_f)^2 + (\frac{\partial E}{\partial d} \, err_d)^2}, \tag{5.47}$$

where $err_L = 100$ nm, $err_f = 50$ Hz, and $err_d = 10$ nm.

A final note is that in at least one instance, the extracted nanowire had several large fragments of adjacent wires adhered to the side. The result can be added mass and stiffness that reduces the accuracy of the uniform bending beam model. To account for particularly large pieces, the beam is broken up into a discrete system with different mass and stiffness values over each section. Using a very basic approximation of an assumed mode $\gamma(x)$ equal to the exact solution for a cantilevered beam known from equation (5.33), Rayleigh's quotient can provide an estimate of the desired value. Starting with equation (5.26),

$$EI \, W'''' = m \, \lambda \, W, \tag{5.48}$$

Rayleigh's method with a single trial function $W = \gamma$ takes the form

$$\int_0^L EI(x) \, (\gamma(x)'')^2 \, dx = \lambda \int_0^L m(x) \, \gamma(x)^2 \, dx \tag{5.49}$$

$$\lambda = \omega^2 = (\int_0^L EI(x) \, (\gamma(x)'')^2 \, dx) \, / \, (\int_0^L m(x) \, \gamma(x)^2 \, dx) \tag{5.50}$$

$$E = ((2\pi f_0)^2 \int_0^L m(x) \, \gamma(x)^2 \, dx) \, / \, (\int_0^L I(x) \, (\gamma(x)'')^2 \, dx), \tag{5.51}$$

where each integral is split up over as many discrete regions as necessary where $I(x)$ and $m(x)$ vary. In the instance of the wire from Figure 5.21 that has an entire

160

second wire attached from $L/2$ outward, over $0 \leq x \leq L/2$ the mass and moment of inertia have the form $m(x) = m$ and $I(x) = I = \pi\, d^4/64$, while from $L/2 < x \leq L$ they are $m(x) = 2m$ and $I(x) = I + \pi d^4/4$. Fortunately this approximate method was not needed for the primary results introduced below.

5.3.2   Initial Results

Using the resonance technique, the elastic moduli of several Galfenol nanowires were characterized. The results presented in Table 5.3 show that there appear to be two distinct stiffness values of approximately 45 and 97 GPa, strongly suggesting a difference in composition, texture, or other fundamental property between wires 5-6 and 7-8. It is also important to note that the former pair were from the same batch of wires as those tested with the tensile method, meaning that the 45 GPa value needs to be reconciled with the ≈ 60 GPa number obtained previously.

The explanation for this variation is that it is known that the resonance method produces only a lower bound of the elastic modulus due to two primary sources of error. The first is that the EBID weld cantilevering the nanowire is not a perfect fixed condition, and any allowable deflection or rotation at the base will significantly lower the resonance frequency. As with the tensile specimen attachment, previous work [39] suggests that this imperfect boundary condition can lead to an underestimation of f_0 by as much as 25%, so long weld times are alloted to minimize this problem. Nonetheless, if the true resonance frequency is just 10% higher than listed in Table 5.3, it results in an increase of E of nearly 20%. The second factor in pro-

Table 5.3: Resonance testing results from nanowire samples.

Wire No.	Diameter [nm]	Length [μm]	Resonance Frequency [kHz]	Young's Modulus [GPa]
5	100±5	19.4±0.1	86.6±0.05	44±9
6	120±5	11.6±0.1	304.3±0.05	46±8
7	225±5	7.88±0.1	1781.1±0.05	96±10
8	125±5	4.43±0.1	3143.0±0.05	97±17

ducing a lower bound estimate is that the observed wire length is only a projection within the SEM. Any tilt in the z direction into or out of the plane will cause the measured value to be less than the true length. This can be exacerbated by the AFM probes having wedge shaped tips with slanted faces onto which the nanowires are attached. In the worst case, the 15° tilt on the OTESPA tip will underestimate L by 3.5%, which translates into E being potentially 15% greater. Together, these two issues can easily add up to 38% to the values of E listed in the results in addition to the natural measurement uncertainty still present.

Looking again at the results from wires 5-6, the added effects can potentially bump the moduli up to 62 GPa, much closer to the tensile values which themselves are still lower bounds as well. This certainly does nothing to explain the data from wires 7-8, however. The large discrepancy between these numbers prompted additional characterization of the nanowire samples, starting with an analysis of the chemical composition as the properties of bulk Galfenol are known to vary significantly with gallium content.
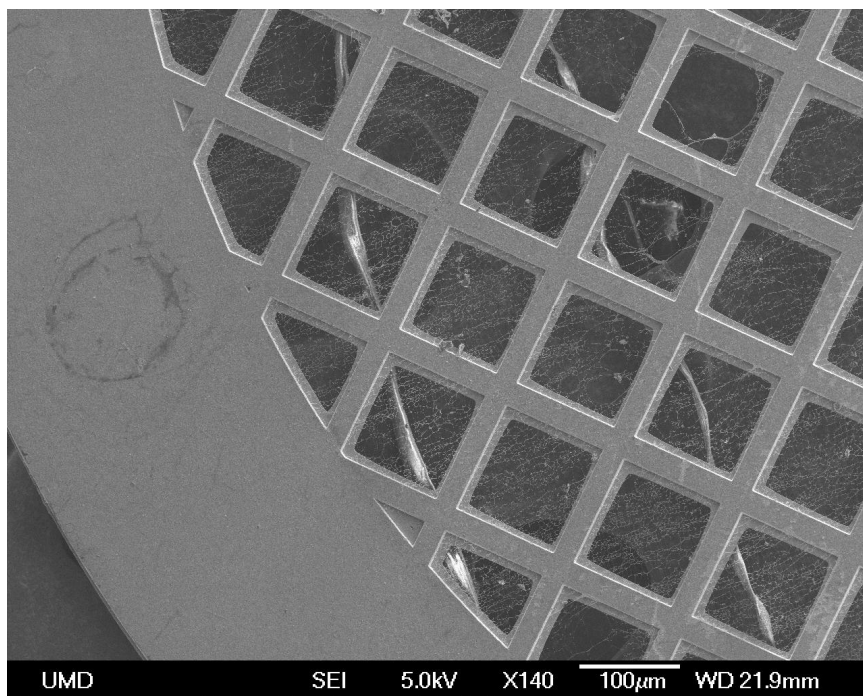
Figure 5.25: Image of a copper TEM sample grid with fine carbon mesh upon which the nanowires are placed.

5.4 Composition Analysis

The composition experiments were carried out using the JEOL 2100F transmitting electron microscope (TEM) in the Nanoscale Imaging Spectroscopy and Properties (NISP) Lab. Dr. Cumings and his student Xi Qi kindly provided assistance in accessing and using the machine. In order to prepare the sample, nanowires were scraped from their original arrays onto copper TEM grids that have a fine carbon mesh as shown in Figure 5.25. After loading the sample grid a few high resolution images were taken, revealing nanowires with a very non-uniform contrast and an apparent oxide coating (see Figures 5.26 and 5.27).

The actual chemical analysis was performed with energy dispersive x-ray spec-

163
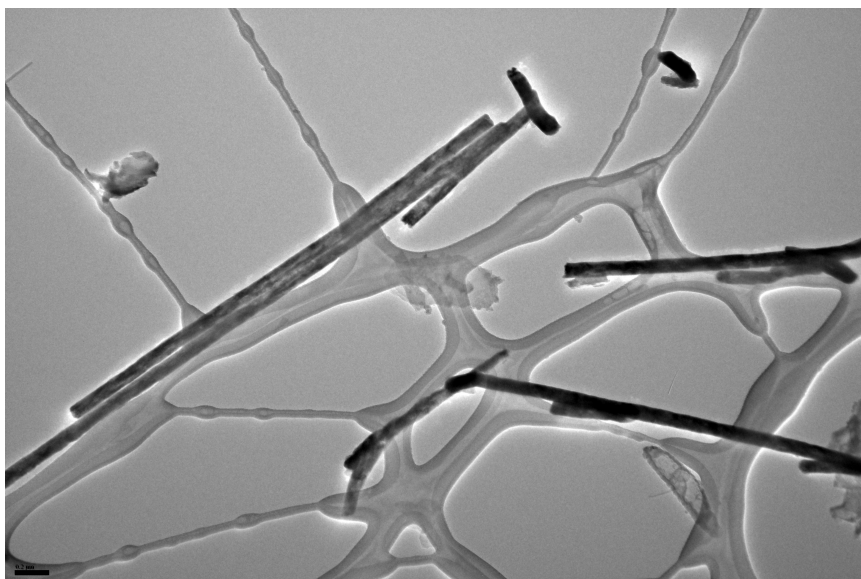
Figure 5.26: TEM micrograph revealing very rough nanowires with a large contrast non-uniformity across the surface. The lighter, randomly sized structures in the background are the carbon mesh of the TEM grid.
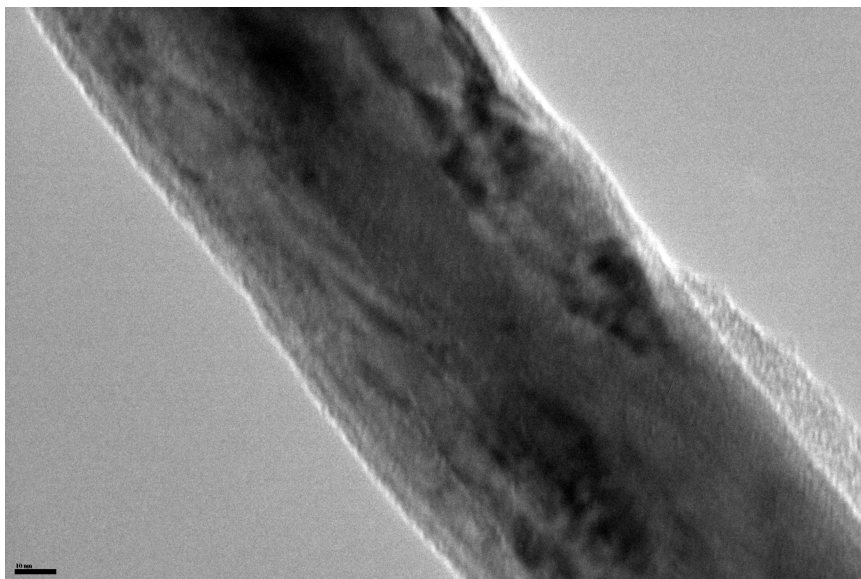
Figure 5.27: High resolution image of a Galfenol nanowire, showing both the spotted appearance and the potential presence of an oxide layer on the surface to the right.

troscopy (EDS, alternatively EDX), a technique that examines the characteristic x-rays emitted by matter that has been excited with a beam of high energy electrons [55]. By measuring the quantity of the emitted x-rays as well as their energy, the elemental composition of the sample can be determined. While there are alternate methods that provide greater chemical resolution, they often can only look for one element at a time, whereas EDS allows an entire spectrum to be collected at once. The specific EDS equipment attached to the TEM is an Oxford Instruments INCAx-sight detector system.

EDS was performed on several different nanowire configurations, including both single wires and larger clusters, from multiple points on the TEM grid. Due to the makeup of the sample grid itself, copper and carbon peaks were ignored in the analysis. The results were found to be very consistent, and an example output from one such scan is displayed in Table 5.4 and Figure 5.28, revealing a large number of contaminant elements and a very low gallium content. While the presence of each element other than iron and gallium is undesirable, they are at least understandable considering that the nanowires are fabricated in alumina templates (Al and O), etched with phosphoric and chromic acids (P and Cr), placed on silicon wafers (Si), and exposed to the air environment (O). Fortunately the relative strength of these signals are low enough to be ignored, with the exception of course of the oxygen. It is known that EDS has difficulties accurately measuring elements such as oxygen with very low energy x-ray emissions, but experience with the bulk Galfenol alloys suggests that there is some truth to the 17 at. % O, as it is highly likely that an iron-oxide layer forms on the nanowire surface. Even so, the primary cause for concern

Table 5.4: EDS composition results.

Element	Weight %	Atomic %
O	5.77	17.51
Al	0.63	1.13
Si	0.18	0.31
P	0.72	1.13
Cr	0.64	0.60
Fe	88.19	76.63
Ga	3.87	2.70
Total	100.00	-

in this data is that when looking only at the iron-gallium ratio, the results were always on the order of $Fe_{96}Ga_4$, far below the expected 15-20 at. % Ga range for optimum magnetostriction. This information was rather surprising to Dr. Stadler's nanowire fabrication group, and modifications were made to their procedure that alleviated this issue.

Another interesting observation arose from the nanowire presented in Figure 5.29, where there is an apparent change from a highly non-uniform appearance near the top to a much smoother surface over the bottom half. A moving EDS scan performed along the length of this wire discovered that while the upper section is iron-gallium, the lower end is pure copper. As previous scans implicitly ignored Cu peaks due to the TEM grid, this information was missed even when analyzing a zoomed out cluster of several wires. It is known that copper is briefly sputtered onto the backside of the AAO template in order to create an electrode for the electrochemical deposition process, but it turns out that this results in every nanowire
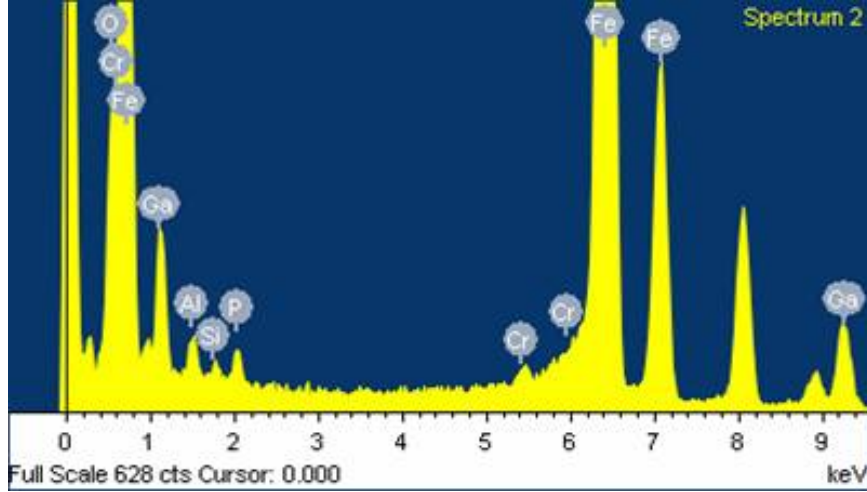
Figure 5.28: An example EDS spectrum collected from the early samples of Galfenol nanowires.

having a copper stub at the end that can be up to 5 μm long. In mechanical experiments where the nanowire is forcibly extracted from the array, it is likely that the Cu fragment breaks off from the Galfenol section and does not interfere with the data, but any test utilizing loose wires could potentially still have the copper piece attached to one end. This revelation might help explain the apparently anomalous 97 GPa elastic modulus value measured for wires 7-8 during the previous resonance testing, as it is quite possible that the wrong end was fixed to the AFM tip and therefore copper's 110 GPa modulus would dominate the resonant behavior.

5.5   Final Results and Discussion

In response to the poor composition found in the early batches of Galfenol nanowires, the deposition procedure was improved and a new sample was made.
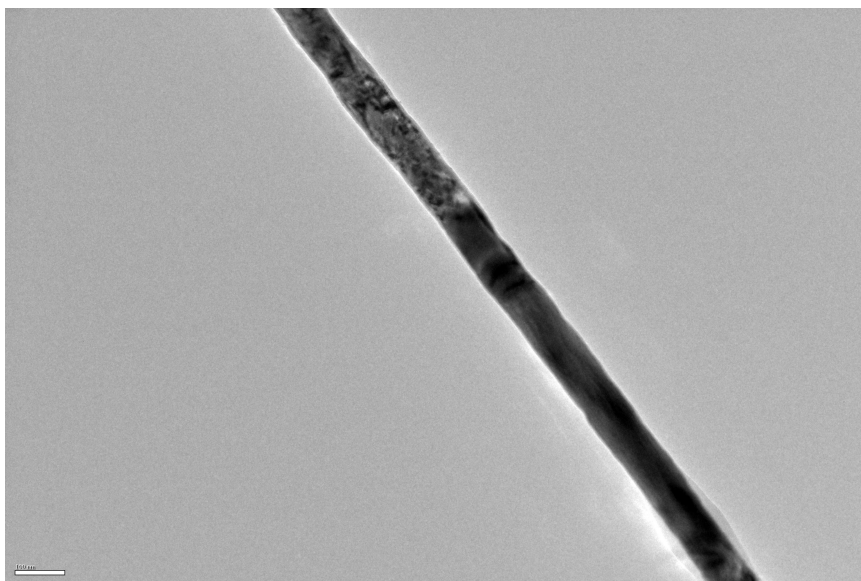
Figure 5.29: TEM image revealing a noticeable transition in appearance from the rough texture observed previously to a smoother, more uniform, surface over the lower half of the wire. EDS scans discovered that this an interface between iron-gallium and copper segments.

Immediately after fabrication at the University of Minnesota, the array was cleaved in two and the composition was tested via an SEM w/ EDS instrument along one of the exposed sides of the matrix. The measured gallium content was 16.2 ± 1.2 at. %. After shipping the sample, it was tested again on the TEM in the NISP Lab for the sake of comparison. Fortunately, four consecutive measurements of different wires produced gallium ratios of 16.52, 18.84, 19.20, and 17.49 at. %, well within the desired range. Experience has shown that the variability in these numbers is caused by a lingering composition gradient along the length of the wires that persists even in ideal conditions, but it is still much better than having next to no gallium at all.

A TEM micrograph of one of these new wires is displayed in Figure 5.30, and shows a fair amount of variation in diameter but is on average slightly thinner than previous specimens. This array of wires was placed back into the nanomanipulator, and now being aware of the copper, one Galfenol wire was successfully clamped onto an AFM tip for resonance testing. The result shown in Figure 5.31 was that the wire resonated at 4.73 MHz, producing a calculated Young's modulus bounded between 158 and 181 GPa. This number bears no resemblance to the prior experiments, but does agree quite well with the 160 GPa value for bulk Galfenol with a [110] crystal texture [71]. Recently, Dr. James at the University of Minnesota theoretically predicted that the nanowires would grow with a [110] orientation based on the results of his micromagnetic modeling. Due to the confirmation that this sample has the desired composition for Galfenol, it is concluded that these results complement one another and that the measured modulus does represent the [110] texture. The exact source of the 60 GPa values obtained from the preliminary samples is assumed
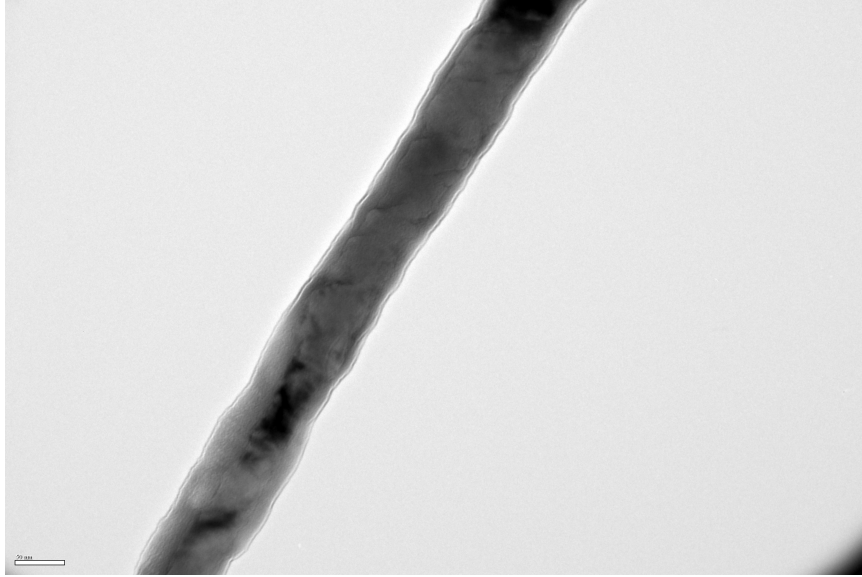
Figure 5.30: TEM image of a nanowire from the new batch with high gallium content, showing that the diameter varies along the length.

to be the various oxides and contaminants that can alter the stoichiometry, form load-bearing oxide layers, and introduce stress concentrations.

The overall conclusion from the mechanical testing is that despite a variety of challenges including large experimental errors and samples of unknown structure, it is clear that the nanowires exhibit properties that facilitate their implementation as artificial cilia sensors. Every nanowire displayed linear elastic deformations with large strain potential due to the greatly increased tensile strength, and failure always occurred as a brittle fracture. The elastic moduli initially showed a strong variation with testing method and sample batch, but once a nanowire sample of confirmed composition was manufactured the results agree well with expectations. The methodology for characterizing nanowires has been developed and improved, and the desired mechanical properties have been sufficiently identified.
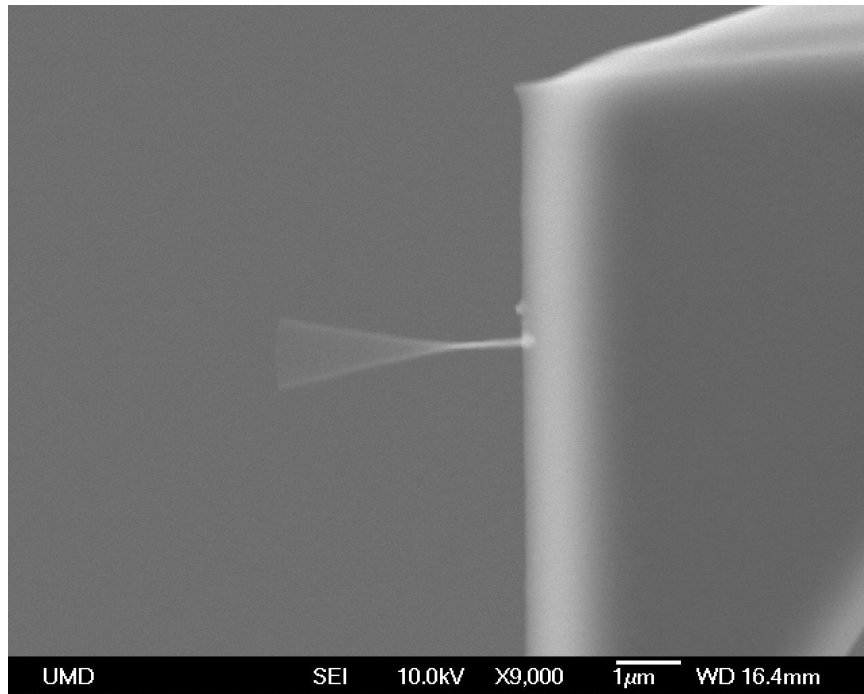
Figure 5.31: A nanowire from the high gallium sample resonating at 4.73 MHz, which corresponds to a modulus of approximately 160 GPa, in excellent agreement with the predicted [110] texture along the axis of the wire.

Chapter 6

Characterization of Nanowire Magnetic Structure

6.1   Objectives

In order to complement the mechanical testing and fully understand the magnetoelastic behavior of iron-gallium nanowires, the magnetic domain structure must be characterized. The first goal of this chapter is to modify the free energy model detailed in Chapter 3 to predict the equilibrium magnetic state of Galfenol nanowires. Fundamental differences from the bulk material will be noted and their implications for the artificial cilia sensor design will be discussed.

The other paramount objective is to verify the prediction with direct observation of the nanowire domain structure. The experimental validation will be performed primarily with magnetic force microscopy (MFM), and the specific methods and techniques used in this research will be outlined. Once the magnetic structure of the nanowires is confirmed, this work will directly lead into studying the magneto-mechanical coupling detailed in Chapter 7.

6.2 Theoretical Prediction

6.2.1 Micromagnetic Considerations

The Armstrong free energy model that was constructed for macroscale simulations provides a solid framework for investigating magnetic nanowires. As discussed at the end of Chapter 3, only cosmetic changes to the energy terms are needed to make them applicable to the Galfenol nanowires. The most significant of these is that the magnetocrystalline anisotropy needs to account for easy axes at 45° due to the [110] texture in the electrochemically deposited wires. The magnetic energy will be zero because no field is applied during experiments, and the magnetoelastic term is unchanged.

In micromagnetic modeling, the exchange coupling plays a greater role than it did at the macroscale and therefore needs to be integrated into the total energy. As a quantum mechanical construct, the origin and derivation [152] of the exchange coupling is not typically presented, as explained by Kittel:

> The relevant result... may be summarized by saying that there is a term of electrostatic origin, which does not enter on strictly classical dynamics, in the energy of interaction between neighboring atoms, and this term tends to orient the electron spins of the atoms either parallel or antiparallel to each other...

> In this review we are taking for granted the existence of an exchange interaction with the specified properties, as it is not possible in this

space to develop the necessary background of quantum theory. [75]

The exchange energy equation rewritten here

$$E_{ex} = A\left((\nabla\alpha_1)^2 + (\nabla\alpha_2)^2 + (\nabla\alpha_3)^2\right), \tag{6.1}$$

is traditionally the starting point for including the exchange coupling in magnetic domain models. In the bulk material this energy contribution was negligible because the volume fraction of domain walls in the sample is incredibly small, but at some length scale this term will become significant.

The other contribution that must be added is the magnetostatic energy that leads to shape anisotropy. This term originates when a magnetized material forms poles at different locations within the body of the sample, and as such is directly dependent on the sample geometry. A spherical body, for example, can be magnetized equally easily in any direction of applied field, but other shapes are generally easier to magnetize along their longer axis. As such, they tend to form north and south poles at opposite ends of the material, the presence of which contributes a magnetic field directed from the north to the south. This field is directly opposed to the original sample magnetization that formed the poles, and as a result acts to demagnetize the material. The strength of this demagnetizing field $\boldsymbol{H}_d$ is directly related to the magnetization $\boldsymbol{M}$ that creates it,

$$\boldsymbol{H}_d = -N_d\,\boldsymbol{M}, \tag{6.2}$$

where N_d represents the demagnetization factor in a given direction. The demagnetization factors are dimensionless and sum to unity in the SI system,

$$N_x + N_y + N_z = 1. \tag{6.3}$$

174
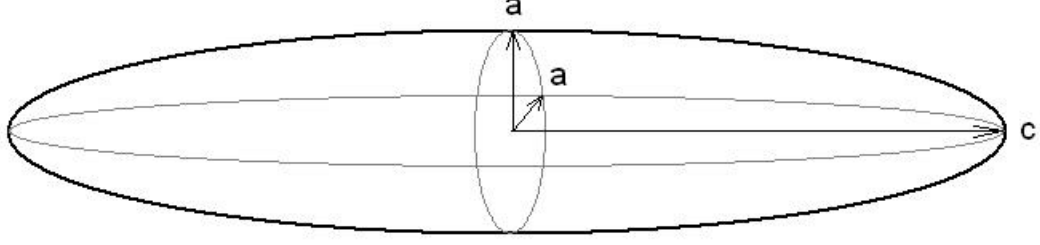
Figure 6.1: Illustration of the prolate spheroid geometry used to approx-imate the Galfenol nanowires.

The value of N varies with the geometry of the sample and the direction of interest, but analytical solutions have only been derived for ellipsoids [105, 18, 76]. While numerical estimations are possible for alternate geometries, magnetic nanowire modeling approximates the long cylinder as a prolate spheroid where $c > a = b$, as shown in Figure 6.1. The aspect ratio of the nanowire c/a determines the exact demagnetization factors (see Figure 6.2), but they range from $N_x = N_y = N_z = 1/3$ in a sphere to $N_x = 0, N_y = N_z = 1/2$ in an infinitely long cylinder.

Analogous to the magnetic energy associated with a magnetized sample in an external field, there is a magnetostatic self energy associated with the demagnetizing field that has the form

$$E_d = -\frac{1}{2} \mu_0 \, \boldsymbol{M} \cdot \boldsymbol{H_d} = \frac{1}{2} \mu_0 \, N_d \, M_s^2, \tag{6.4}$$

which for the infinite cylinder ranges from zero along the wire axis ($N_x = 0$) to a maximum value when magnetized perpendicularly ($N_y = N_z = 1/2$). The difference in energy cost between these two configurations is known as the shape anisotropy, which in the case of the prolate spheroid is a uniaxial anisotropy term favoring the
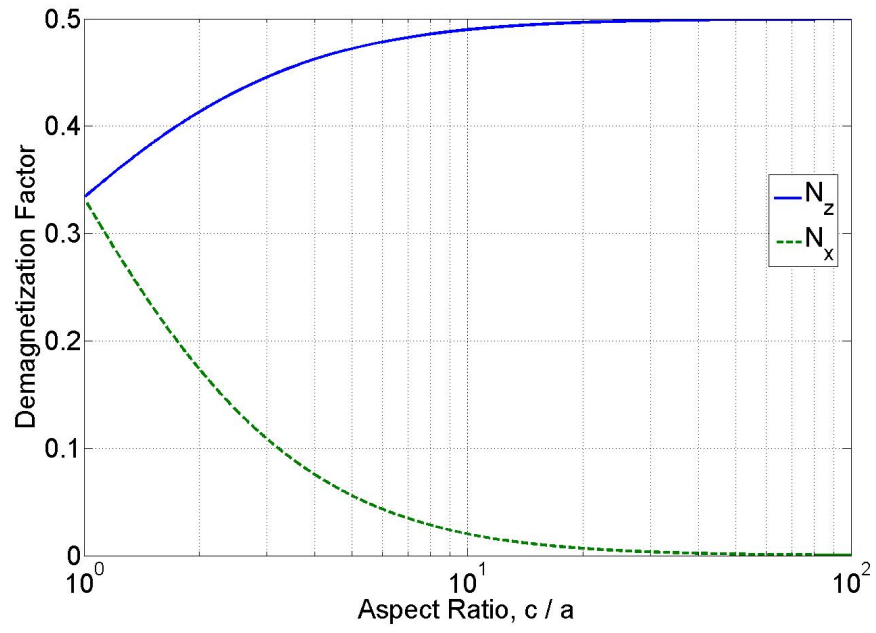
Figure 6.2: Calculated demagnetization factors for a prolate spheroid of varying aspect ratio. The infinite cylinder limit has $N_x = 0$ along the nanowire axis and $N_z = \frac{1}{2}$ along the radial dimension.

long axis of the nanowire. For modeling purposes this is expressed in terms of the $[\alpha_1, \alpha_2, \alpha_3]$ direction of magnetization using $N_d = 1/2$:

$$E_d = \frac{1}{4} \mu_0 M_s^2 \alpha_3^2. \tag{6.5}$$

The formation of magnetic domains results from a balance between the exchange and magnetostatic energies. Figure 6.3 displays a ferromagnetic material with different domain structures. When the sample is uniformly magnetized in a single domain, poles form at the ends and the demagnetization energy is quite large (a). It is therefore favorable to have the crystal split into two oppositely oriented domains (b), which effectively cuts the magnetostatic energy in half due to the reduction in demagnetizing field. Of course, there is now an exchange energy cost as the moments in each domain are not parallel. This process will continue (c) until the exchange energy cost of adding an additional domain wall is higher than the reduction in demagnetization energy. In some materials, it is possible for closure domains to form near the ends of a crystal that are oriented perpendicular to the bulk magnetization. The advantage of this formation, shown in Figure 6.4, is that the magnetic path is a complete circuit and no poles form on the surface. The formation of closure domains oriented 90° from the bulk magnetization generally requires a favorable magnetocrystalline anisotropy, such as the family of $< 100 >$ directions in cubic iron-based alloys. In materials with a uniaxial magnetocrystalline energy, such as hexagonal cobalt, these closure domains have their own high energy costs and the structure in Figure 6.3(c) would actually be preferred.

From the competition between the exchange and magnetostatic energies, there
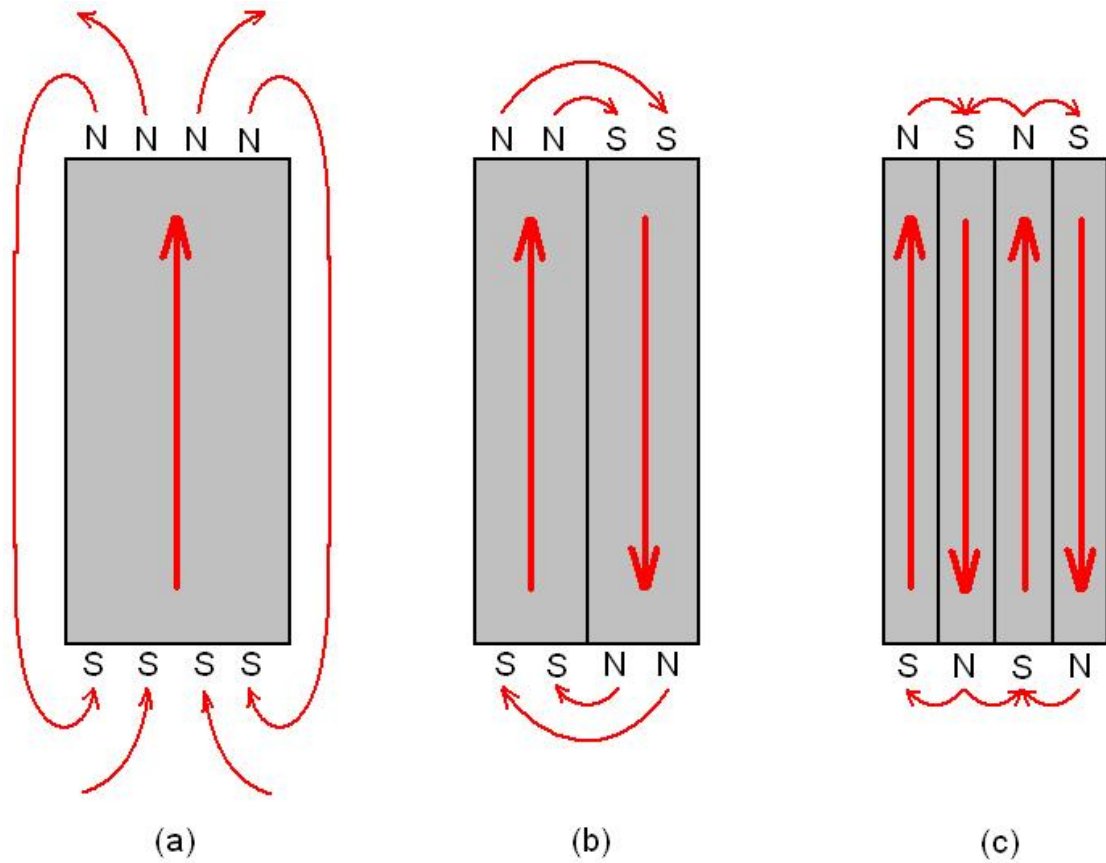
Figure 6.3: Diagram of the formation of magnetic domains. A single domain sample has zero exchange coupling expense but a large magnetostatic energy (a). Dividing the sample into two domains decreases the demagnetizing field but adds exchange energy (b). This process will continue until an energy equilibrium is reached (c).
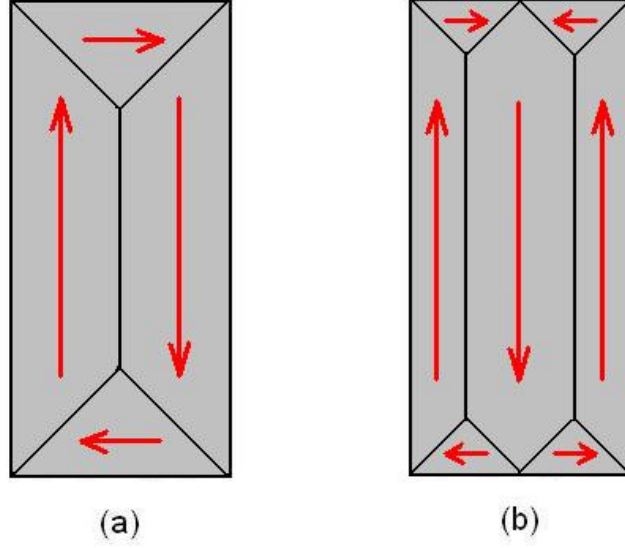
Figure 6.4: Possible configurations for the closure domains that often form in cubic ferromagnetic materials, creating a complete magnetic flux path and eliminating magnetostatic energy.

is a critical size below which a particle will remain single domain, as any domain wall formation would prove too costly with respect to the exchange coupling. This parameter is known as the exchange length, and can be written [124] as

$$l_{ex} = \sqrt{\frac{2A}{\mu_0\,M_s^2}}, \qquad (6.6)$$

which assuming a nominal $A = 1 \times 10^{-11}$ J/m yields an exchange length of $l_{ex} = 2.7$ nm. While this value is significantly smaller than the nanowire structures of interest in this work, it only represents the length scale below which the particle must be single domain; other factors make it easily possible for samples an order of magnitude or two larger to also maintain a single magnetic domain state.

The estimation of the critical radius below which a prolate spheroid will remain single domain is borrowed from Frei et al. [49], where the exchange energy of equation

179

(6.1) is calculated using the direction cosines $\alpha_1 = \cos\theta, \alpha_2 = 0, \alpha_3 = \sin\theta$. This gives the exchange energy density as

$$E_{ex} = A\,\frac{1}{r^2}\sin^2\theta, \tag{6.7}$$

and the maximum is taken when $\theta = \pi/2$ to be $E_{ex} = A/r^2$, where r is the radial coordinate in the ellipsoid. From [49], the mean total energy can then be determined with a volume integral,

$$\bar{E}_{ex} = \frac{1}{Vol}\int_{a_0/2}^{a}\int_{0}^{2c(1-r^2/a^2)^{1/2}}\int_{0}^{2\pi}\frac{A}{r^2}\,r\,d\phi\,dx\,dr \tag{6.8}$$

$$\bar{E}_{ex} = \frac{1}{4/3\pi a^2 c}\cdot 4\pi A c\left|\frac{(a^2-r^2)^{1/2}}{a} - \ln\left(\frac{(a^2-r^2)^{1/2}+a}{r}\right)\right|_{a_0/2}^{a} \tag{6.9}$$

$$\bar{E}_{ex} = \frac{3A}{a^2}\left(\ln\left(\frac{4a}{a_0}\right) - 1\right), \tag{6.10}$$

where a_0 is again the lattice parameter and from Figure 6.1 a and c are the lengths of the short and long ellipsoid radii, respectively. This energy $\bar{E}_{ex}$ is set equal to the magnetostatic energy $E_d = \frac{1}{2}\mu_0 N_d M_s^2$ from equation (6.4) to yield the implicit expression for the critical radius $a = R_c$,

$$R_c^2 = \frac{6A}{\mu_0 N_d M_s^2}\left(\ln\left(\frac{4R_c}{a_0}\right) - 1\right), \tag{6.11}$$

that needs to be solved iteratively. Figure 6.5 graphs the change in critical radius with the demagnetization factor $N_d = N_x$ along the axis, revealing that as the aspect ratio increases, the greater shape anisotropy enables larger width nanowires to remain in a single domain state. As most of the nanowires studied in this research have diameters of approximately 100 nm, those at least 500 nm long should fall just within the single domain range predicted by the theory.
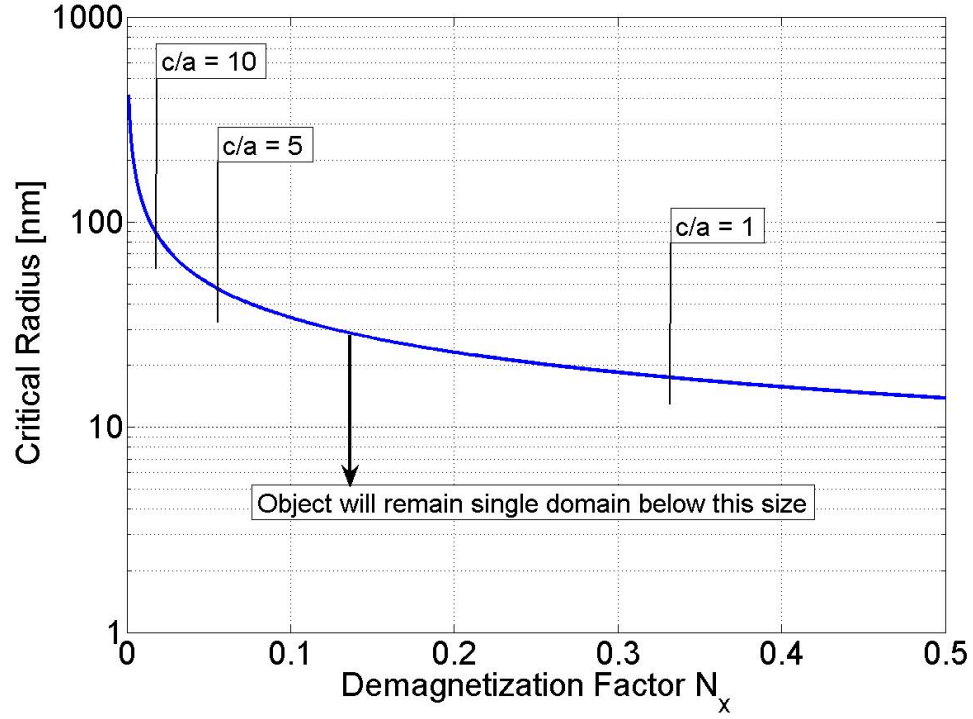
Figure 6.5: Graph of the critical radius below which a Galfenol nanowire ($M_s = 1456 \times 10^3$ A/m, $a_0 = 0.286$ nm, and $A = 1 \times 10^{-11}$ J/m) should remain single domain vs. the demagnetization factor along the axis. As this factor is based solely on geometry, the location of a few common aspect ratios (10, 5, and 1) are flagged. Adapted from [133].

Table 6.1: Maximum cost of each energy term for an unfavorable orientation.

Energy Term	Maximum Cost [erg/cm^3]
Exchange Coupling	3×10^4
Magnetocrystalline Anisotropy	3×10^5
Magnetoelastic	2.5×10^3 / MPa
Shape Anisotropy	7×10^6

6.2.2   Expected Domain Structure

Including the shape anisotropy into the total energy significantly alters the costs of unfavorable magnetization directions. Figure 6.6 shows an example of the energy cost associated with every possible angle of the magnetization, with 0° representing along the nanowire axis. Despite having a 500 MPa compressive load applied in the simulation, the shape anisotropy dominates the response and enforces the nanowires to maintain a 0° or 180° orientation, a single axial domain that should flip only between these two stable states in agreement with the prior critical radius approximation. Table 6.1 lists the maximum energy cost of each term, confirming that the demagnetization is an order of magnitude higher than the rest.

This result was further validated with Magpar v0.8, a micromagnetics FEM package solving the Landau-Lifshitz equation [79] that was configured for Galfenol by Chaitanya Mudivarthi [2]. A cylinder was created and meshed by extruding a 100 nm diameter circle 10 μm in the x direction. Using the standard Galfenol magnetic modeling coefficients, the M-H curve was simulated as presented in Figure 6.7. This prediction of a very rectangular magnetization profile agrees with the previous
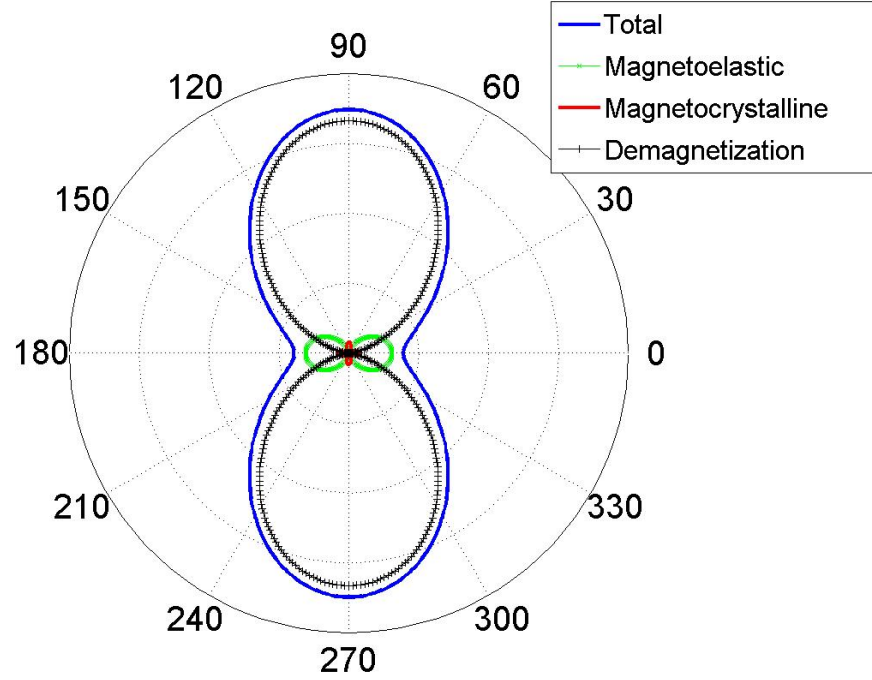
Figure 6.6: Energy cost associated with each possible angle for the magnetization vector in a typical Galfenol nanowire 100 nm in diameter and 10 μm long. Despite a simulated 500 MPa of compression applied to the wire axis, the demagnetization energy imparts a huge shape anisotropy that tends to strongly prefer only axial orientations (0° and 180°).
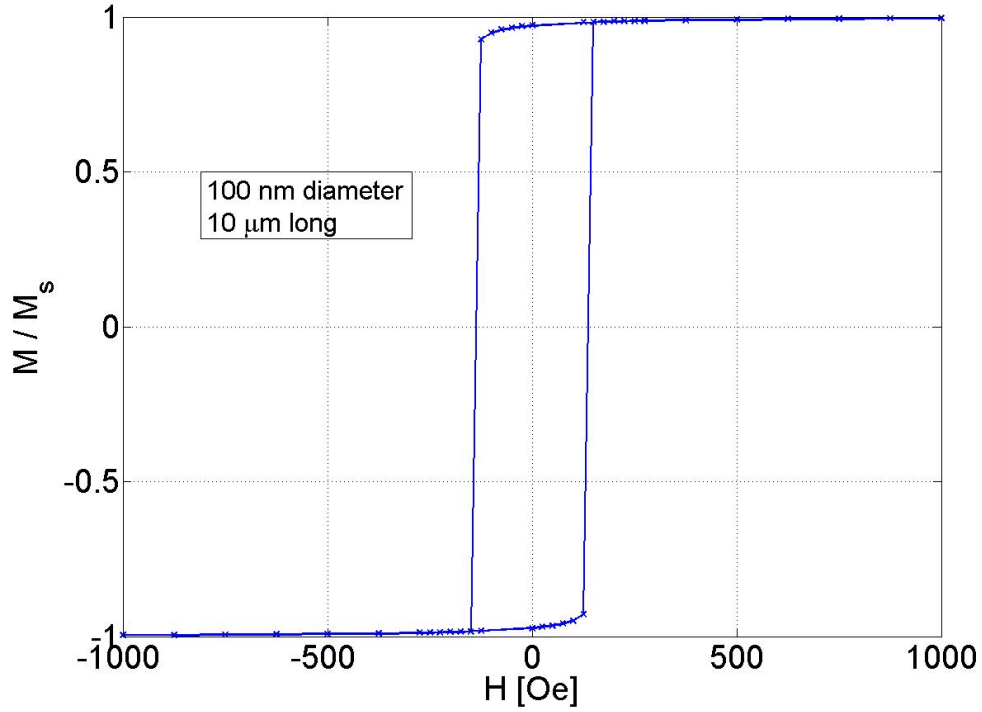
Figure 6.7: Micromagnetics FEM analysis of the magnetization curve for a 100 nm diameter, 10 μm long Galfenol nanowire.

theory that the nanowire will have only the two axial magnetization states, and will flip suddenly between them at the coercive field of 138 Oe.

A final consideration is the interaction between adjacent nanowires within the close packed array. The magnetostatic field emanating from the poled wires will act as a source of external magnetic field energy on near neighbors. The strength of this field H can be calculated [117] as

$$H = \frac{\pi}{4}\, d^2\, L\, M_s \left(y^2 + \frac{L^2}{4} \right)^{-3/2}, \tag{6.12}$$

where y is the distance away from the dipole created by a nanowire of length L and diameter d. This term is found to weaken significantly with increasing length, such
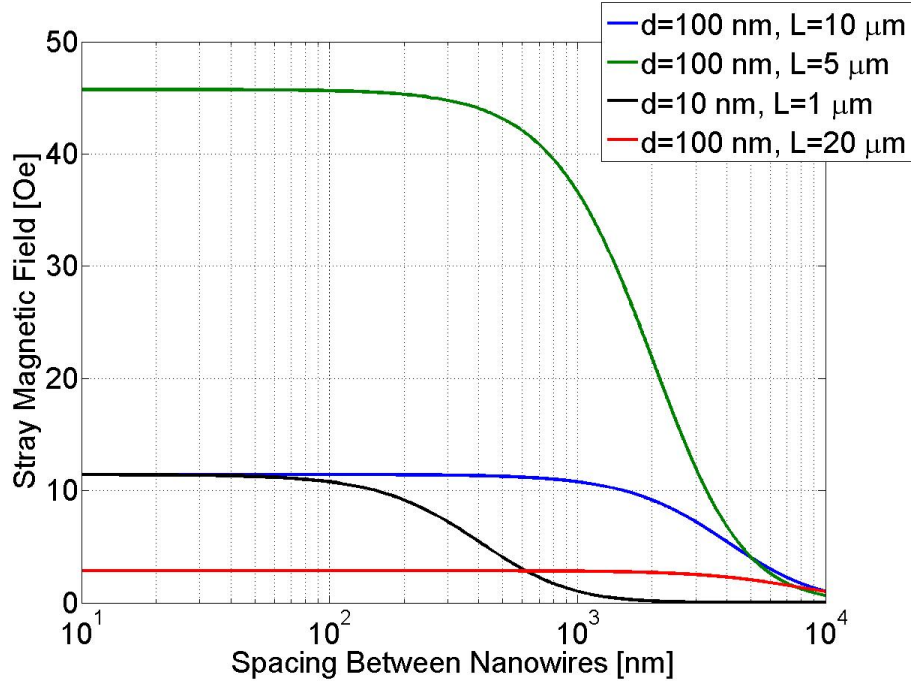
Figure 6.8: Plot of magnetic field strength versus radial distance from the nanowire dipole for several geometries. In all cases the field of interaction between adjacent wires is quite low and is ignored in calculations of the domain structure, but this magnitude increases sharply as aspect ratio decreases. As such, it should be possible to create antiferromagnetic ordering in a packed array of short nanowires [64].

that typical wires 10 μm long and 100 nm in diameter generate an axial field of only 11 Oe at a spacing of 100 nm indicative of fully packed nanowire arrays. Figure 6.8 graphs the variation in field with distance for a few nominal nanowire geometries. These results suggest that in the vast majority of cases this effect will be negligible to the demagnetization and magnetoelastic energies, but in the right circumstances could be used to create an antiferromagnetic arrangement of nanowires within the array [64].

6.3 Experimental Observation

6.3.1 Magnetic Force Microscopy

MFM is a powerful tool for imaging the micromagnetic structure of various materials [90, 118]. Numerous experimental approaches to this challenge have been developed in recent years, including electron holography [141], polarized SEM [122], Lorentz TEM [134, 110], and magneto-optical Kerr effect (MOKE) microscopy [121]. MFM provides some distinct advantages for this research, such as a convenient experimental setup that has no environmental constraints, requiring little sample preparation, being relatively insensitive to surface contaminants, and a high spatial resolution that can distinguish key features of the nanowires.

The MFM technique is an advanced operating mode of the Dimension 3100 AFM from Veeco Instruments, Inc. The general AFM procedure involves scanning a vibrating AFM cantilever along a sample, where the atomic forces between the surface and the sharp probe tip interact to damp out the oscillations. A laser is reflected off of the back of the cantilever onto a photodetector, the voltage amplitude of which is tracked with a PID controller. The height profile followed by the AFM probe that keeps the photodetector voltage uniform is a direct measure of the surface features, and by scanning over an arbitrary area the entire topography of the sample can be imaged. There are many variations upon this theme [131, 37, 169, 120] that have uses in material science, microbiology, and other fields of research.

The same instrument and setup are used for MFM scans, with the only difference in preparation being that the chosen probe is coated with a sputtered thin

film of magnetic material. As a result, the tip has its own magnetic moment and now the amplitude and frequency of the cantilever vibrations will be affected by not only the surface atomic forces but also any stray magnetic field emanating from the sample. The scan is conducted in the original manner by first acquiring the height data, but then a second interleave scan is initiated during which the MFM tip is lifted a set distance above the surface. In order to subtract out the influences of the surface, the raised tip traces out the known topographical profile while feeling only the effects of magnetic force as a shift in the cantilever resonance frequency, amplitude, and phase. The equations governing this interaction [51, 14, 17, 1] are typically reduced to

$$\Delta f \approx \frac{-f_0}{2k} \frac{\partial F}{\partial z} \tag{6.13}$$

$$\Delta\varphi \approx \frac{-Q}{k} \frac{\partial F}{\partial z}, \tag{6.14}$$

where f_0 is the nominal resonance frequency shifted by Δf, k is the cantilever spring stiffness, Q is the mechanical quality factor, $\Delta\varphi$ is the phase shift, and F is the magnetic force on the tip in the surface normal direction z. A schematic of the MFM procedure is presented in Figure 6.9, and an example result of the difference between the topography and the magnetic phase observed on a strip of recording tape is shown in Figure 6.10.

This method of observation does have some inherent limitations, however. The geometry of the tip constrains the sensitivity to stray fields that are primarily normal to the sample surface, which means that in plane magnetization vectors are very difficult to image. In many cases only the boundaries between domains are
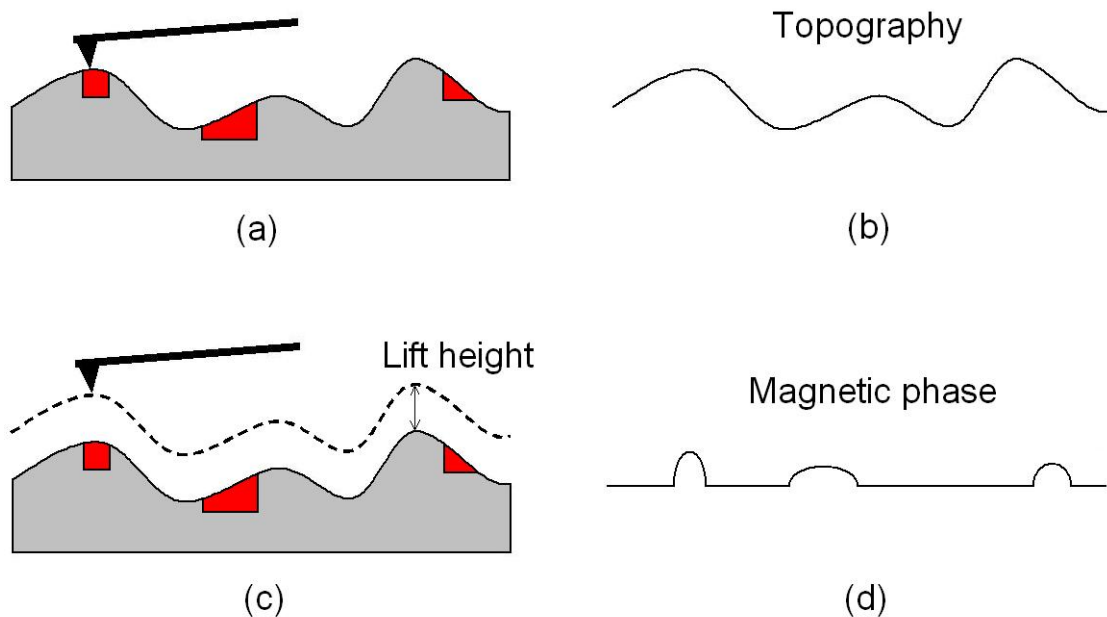
Figure 6.9: Diagram of the MFM procedure on a sample with magnetic domains displayed in red. The probe tip first scans the surface (a) to produce the topographic information (b). The tip is then raised above the surface to the prescribed lift height and traces out the known topography in order to maintain a constant separation from the surface (c). Now the magnetic probe feels only the effects of the magnetic domains, resulting in the phase data (d).
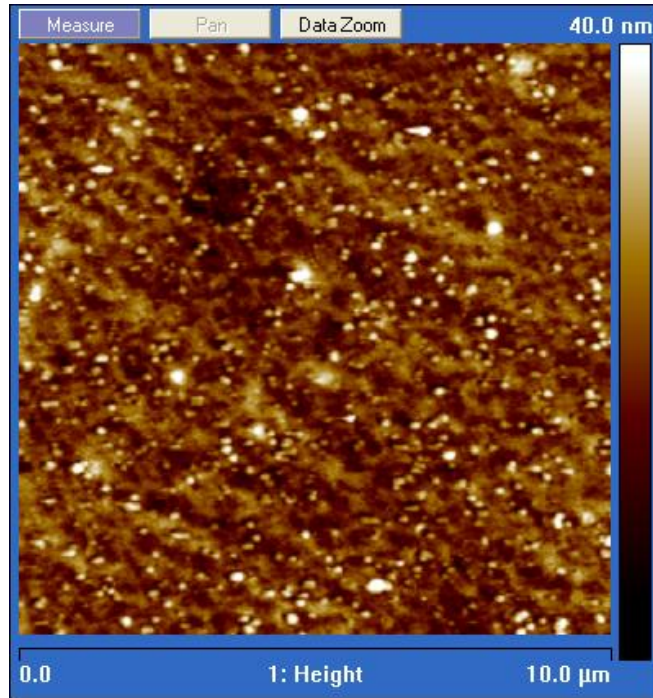
(a)
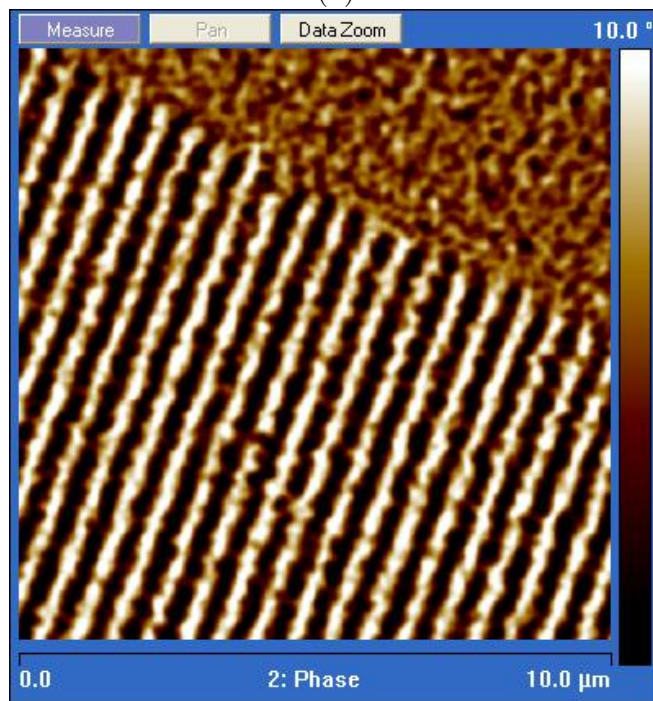
(b)

Figure 6.10: Result of MFM scan on a piece of magnetic recording tape. The height data (a) shows a rather uniform surface while the phase plot (b) easily picks out the underlying magnetic bits written on the sample.

observable, which is complicated by the fact that the measured MFM images do not map to a unique sample domain structure [151]. For example, a series of magnetization vectors oriented into and out of the material surface would appear as a set of alternating bright and dark regions as depicted in Figure 6.11(a). However, the same stray field pattern, and hence MFM result, would be generated by the configuration of in plane domains shown in Figure 6.11(b). In most applications the proper interpretation of MFM data requires a human estimation of the highest likelihood domain structure. A final criticism of MFM is that converting the raw phase or frequency shift data into quantifiable magnetic units requires detailed knowledge of the tip's magnetic moment, information that must be characterized independently for each probe. While there are a few accepted methods [113, 54] for this process, it is not generally carried out for normal MFM operation.

6.3.2   Scanning Procedure

The experimental procedure begins by depositing loose nanowires that have been suspended in isopropanol onto a silicon wafer. The sample is typically loaded first into the SEM in order to visualize the surface and locate promising regions that have numerous scattered wires lying about. Dense clusters of wires are generally avoided because they make the interpretation of the MFM images more difficult and can have relatively tall vertical features that are potentially problematic. The coordinates of various landmarks in the SEM observations are noted in order to use them as references for positioning the MFM and locating ideal wires. As Figure
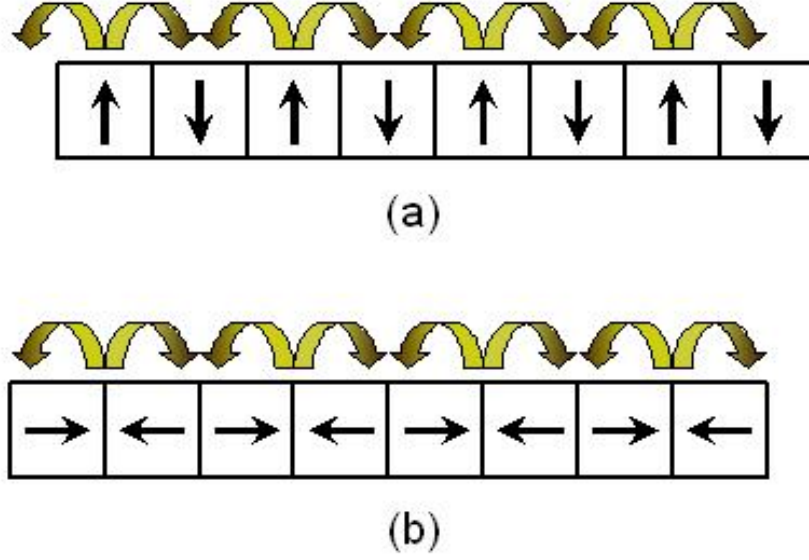
Figure 6.11: Diagram of two distinct magnetic domain structures producing the same stray field, demonstrating that exact determination of the sample magnetization is not possible with the MFM technique.

6.12 demonstrates, the resolution of the optical camera attached to the Dimension 3100 is inadequate for identifying all but the largest nanowire structures.

For the bulk of the results presented in this work, MESP-HM probes from Veeco were used. These are structurally equivalent to the FESP models used for mechanical testing, but have a 10 - 150 nm layer of Co/Cr coating the surface. The magnetic moment of the tip dipole approximation is rated as $> 3 \times 10^{-13}$ emu, with a coercivity of 400 Oe. In comparison with the standard MESP MFM probe, the high moment model offers increased sensitivity at the cost of a higher tip stray field that can potentially change the magnetization of soft samples, but this concern is minimal for Galfenol nanowires based upon the results of the theory.

Area scans were typically performed to image several scattered nanowires at

Figure 6.12: Image taken with the optical camera incorporated into the AFM/MFM instrument, showing that larger clusters of nanowires can be vaguely made out but identifying ideal single wires for scanning requires better resolution.

once, as the lateral resolution of the MFM technique is not high enough to typically warrant zooming in much further. The interleave scan used a lift height of 50 nm for the majority of experiments, although there appeared to be little variation in the result up to at least 100 nm of lift. Scanning the nanowires proved to have some unique challenges due to the sharp height changes between the flat silicon wafer and the wires. In order to have the MFM tip properly follow a retreating edge and yield accurate height data, the cantilever amplitude setpoint needed to be lower than normally suggested and the scan rate was limited to the order of 0.1 Hz, far slower than is possible with samples with a flat polished surface.

6.3.3   MFM Results and Discussion

Relating the phase images that result from MFM scans to the magnetic domain structure of the material can often be challenging and nonintuitive, but fortunately single domain nanowires are one of the most straightforward samples to interpret. Each wire should behave essentially as a bar magnet, with field lines flowing out of the positive end and curling around into the negative end. Recalling that the MFM probe tip responds to the out of plane field component, this implies that the resonating tip will be phase shifted in one direction near the positive end of the nanowire as the field lines curve upwards, have very little response over the length of the wire where the field is parallel to the surface, and then be strongly shifted in the opposite direction when passing over the negative wire end. Figure 6.13 diagrams this concept, and shows that the resultant MFM phase plot should therefore reveal
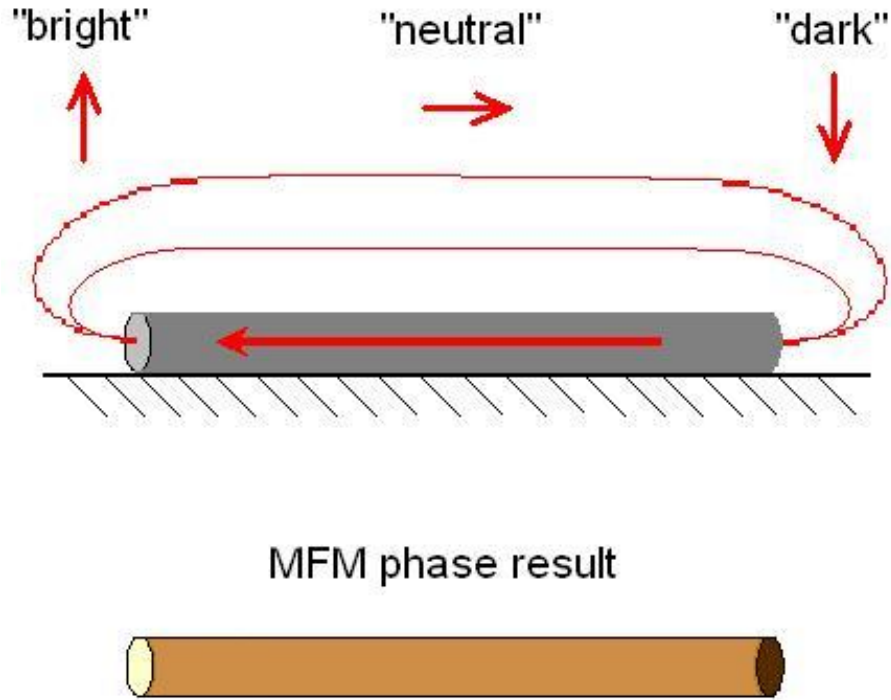
Figure 6.13: As the magnetic field lines curve around the sample, the out of plane component is non-trivial only at the ends of the nanowires. The opposite directions result in bright and dark points in the resultant MFM phase plot.

opposite bright and dark spots near the tips of the wire and little contrast variation along the length.

The phase plots measured from various nanowire samples agree strongly with this expectation. Figure 6.14 compares the height and phase diagrams of an isolated Galfenol nanowire, revealing the bright and dark end points. The exact sign of each is dependent upon the arbitrary magnetization direction of the MFM tip, so for convenience bright is labeled as positive and dark as negative. The magnitudes of these points are plotted in the degrees of phase shift induced on the MFM cantilever, as the calibration required to obtain magnetically quantitative data is beyond the
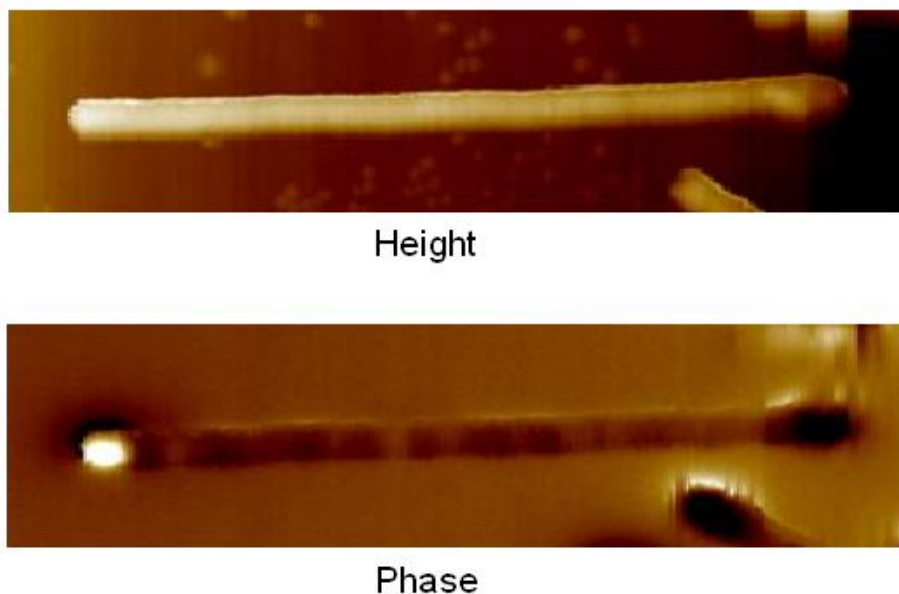
Height

Phase

Figure 6.14: Height and phase results from an MFM scan on an isolated Galfenol nanowire, revealing the anticipated bright and dark spots at opposite ends of the wire.

scope of this work. As a result, all analysis presented here relies only on the level of color contrast in the MFM images.

Several other results show good agreement between the MFM scans and the predicted single domain state. Figure 6.15 shows Galfenol wires of several different lengths all displaying the anticipated bright and dark spots. Scans of pure nickel wires were taken for comparison and Figure 6.16 reveals that there is little to distinguish them from the Galfenol, reaffirming that even with material coefficients of different magnitude the theoretical single domain state still strongly holds.

In addition to the bright and dark ends, an interesting feature is that many nanowires display a bamboo-like band structure along the length, exemplified by multiple wires in Figure 6.17. There are several possible magnetization profiles that

195
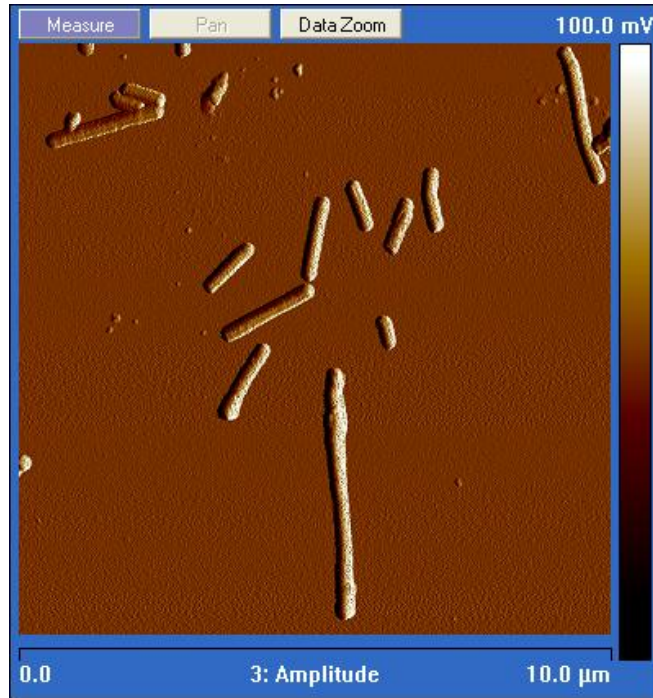
(a)
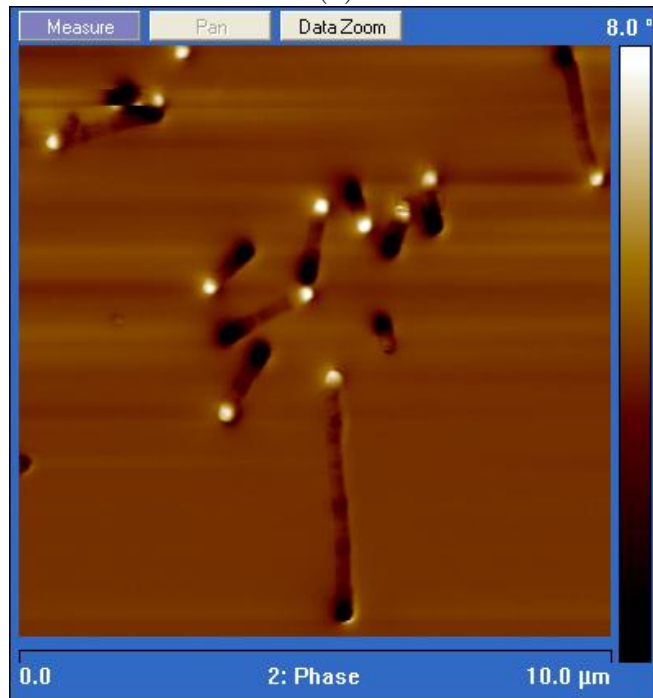
(b)

Figure 6.15: MFM amplitude (a) and phase (b) images showing several Galfenol nanowires of varying length, all of which maintain the single domain state.
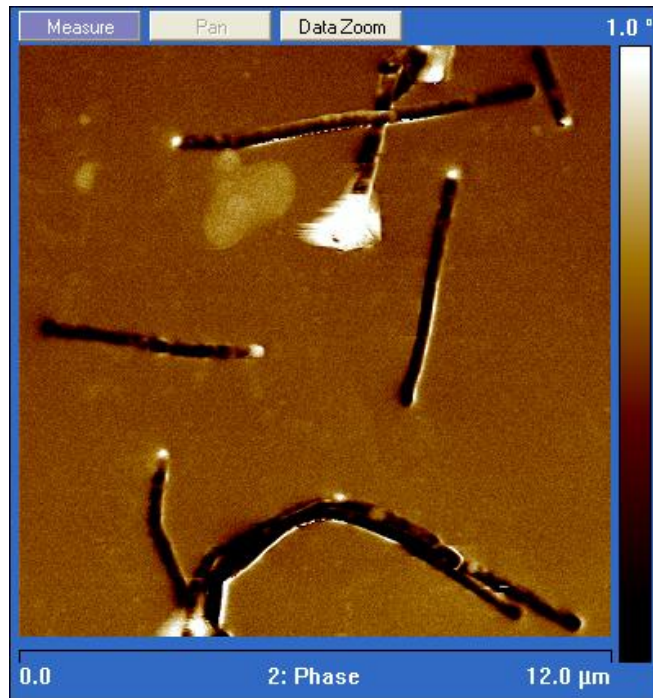
Figure 6.16: MFM phase result from scattered nickel nanowires that also are predominantly single domain.

could yield this MFM result, three of which are sketched in Figure 6.18. The top domain structure would require axially oriented ends to maintain the bright and dark extremities, but then allow perpendicular moments along the rest of the wire length. The problem with this configuration is that the perpendicular moments violate both the exchange coupling and the shape anisotropy, strongly suggesting that this is an unlikely scenario. In addition, the MFM contrast from a perpendicular domain would be expected to be far greater than the weak levels observed. An alternate possible domain structure is to have magnetically reversed segments alternating down the length, but the stray field resulting from head-to-head or tail-to-tail interfaces should be twice as strong as that originating from the wire ends. As the end contrast is clearly dominant in the MFM phase plots, this scenario is also considered unlikely. The presumed structure therefore takes the form of Figure 6.18(c), where the wire is still globally behaving as a dipole but is broken up into multiple sections with a slight misalignment. Each skew in the magnetization angle occurs at either a defect in the lattice or possibly a complete grain boundary, but the gradient of the stray field resulting from each interface will be far less than that exhibited by the two nanowire ends.

Similar conclusions have been reached from MFM analysis of other magnetic nanowires in the limited amount of literature available. A study of Ni wires [104] found exclusively single domain structures in wires with diameters up to 1 μm, with validation via SQUID magnetometry. The light band structure noticeable in the Galfenol nanowires was also observed in Co wires [50, 45, 109] and believed to have a similar root cause by interpreting the MFM images as charge mapping [60]. Ad-
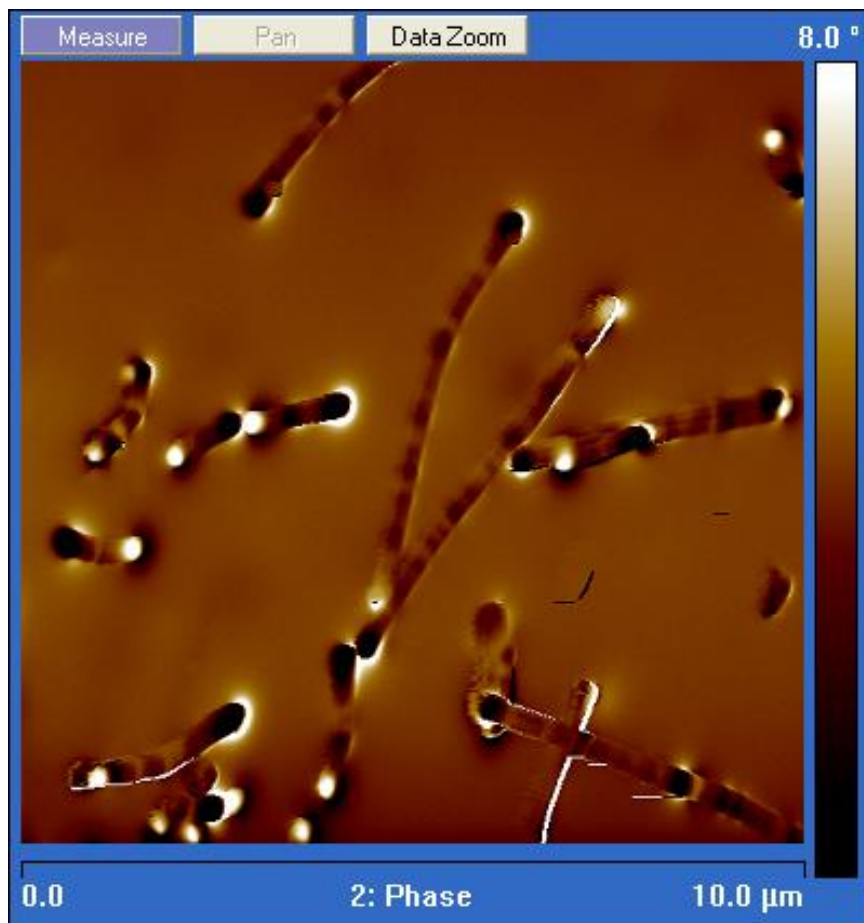
Figure 6.17: MFM phase result from scattered Galfenol nanowires. There is a distinct bamboo-like band structure along most the wire lengths.
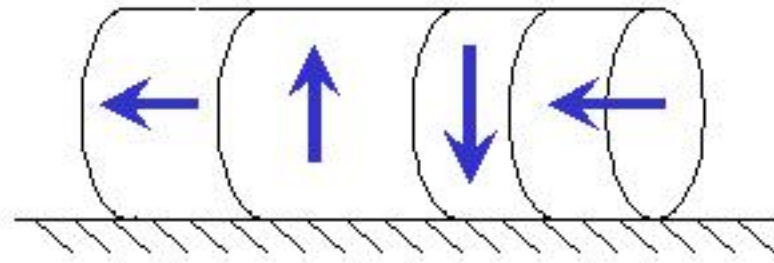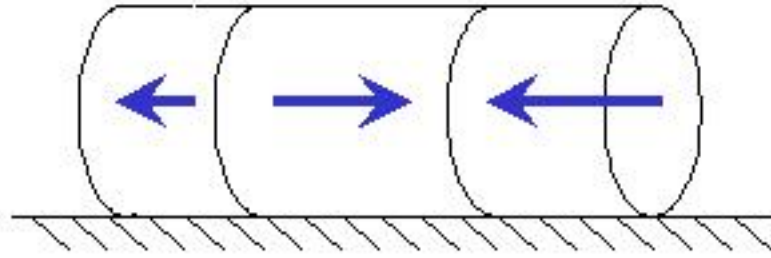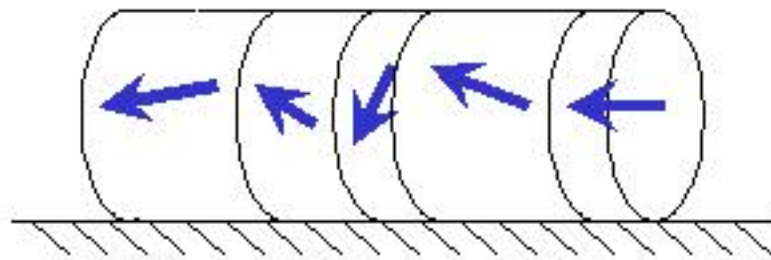
Figure 6.18: Possible domain configurations for the observed nanowires with bands of contrast along the length. The structures in (a) and (b) are less likely than (c), where the magnetization remains primarily axial. Adapted from [14].

ditional results have identified segments of alternating magnetization in multilayer Ni/Cu and Co/Cu wires [94, 126, 84, 136], and in one instance even located a Co/Cu wire exhibiting both axial and perpendicular magnetic domains due to the unique balance of magnetocrystalline and shape anisotropies [14].

There are a few sources of error that can corrupt the accuracy of the MFM phase images. In some instances features of the height data creep into the phase plot, particularly in cases where the lift height is low or the topography is especially hard to trace. More commonly however, there are bumps or branches along the surface of the nanowires that emit stray magnetic field contributions that belie the actual magnetization directions of those regions. Figure 6.19 reveals that these outcroppings from the wire surface have corresponding bright spots in the phase data as any field lines that deviate into this region will partially jump into the air rather than curve back into the core of the wire. Many of the nanowires displayed in the SEM pictures presented in Chapter 5 were relatively free of these problems, but some nanowire batches like those in Figure 6.20 are plagued by them. A final error that can arise during any general AFM operation is when a probe tip has multiple points of contact that each interact with the surface, usually as the result of fracture or particle adhesion. The results can range from simply a blurry image to the false doubling of every structure as shown in Figure 6.21.

The last interesting result of the MFM studies is the further validation of there often being a purely copper segment at the end of Galfenol nanowires. Figure 6.22 shows a sample that has the bright spot at one end but the corresponding dark point near the center of the wire, and no phase contrast over the remainder of the
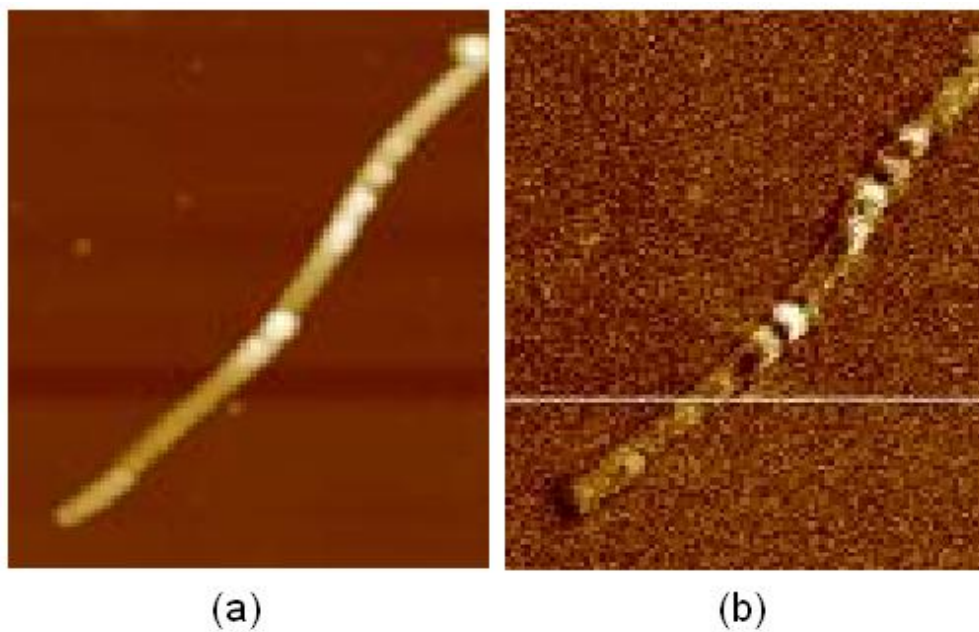
Figure 6.19: MFM data revealing that bumps on the surface of the nanowire height data (a) manifest as bright spots in the corresponding phase image (b). These false spots greatly increase the difficulty in interpreting the MFM results.
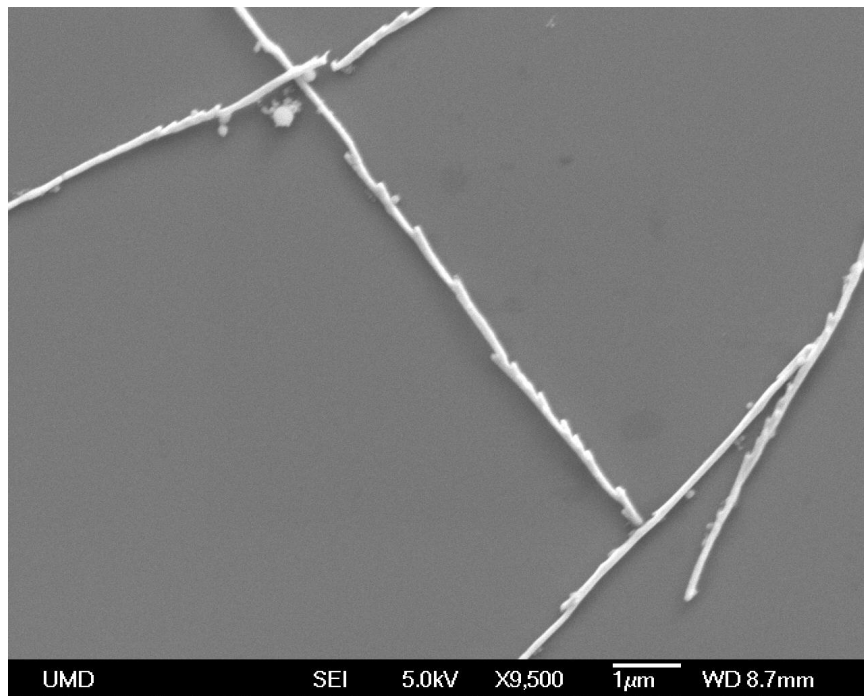
Figure 6.20: SEM image of a nanowire sample that has a significant number of branching defects on the surface, each of which can corrupt the true magnetization profile measured by MFM.
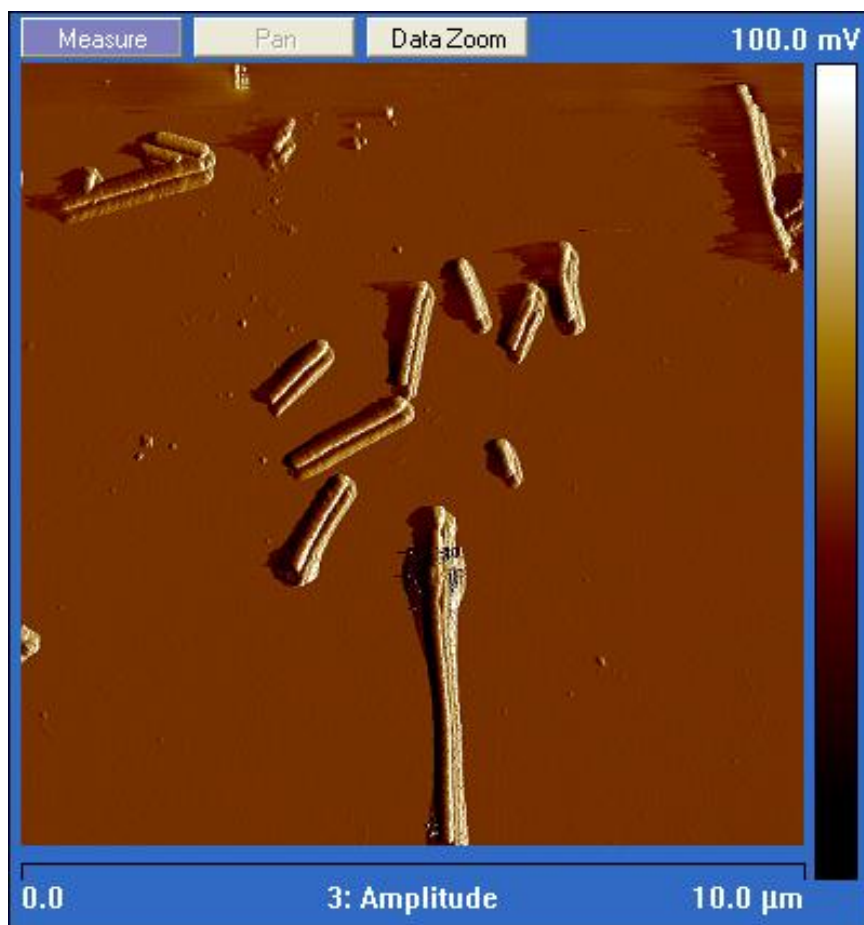
Figure 6.21: MFM amplitude image scanned with a faulty probe tip that has multiple points. Each nanowire is doubled as compared with Figure 6.15(a), although in many cases the result is simply a loss of clarity in the images.
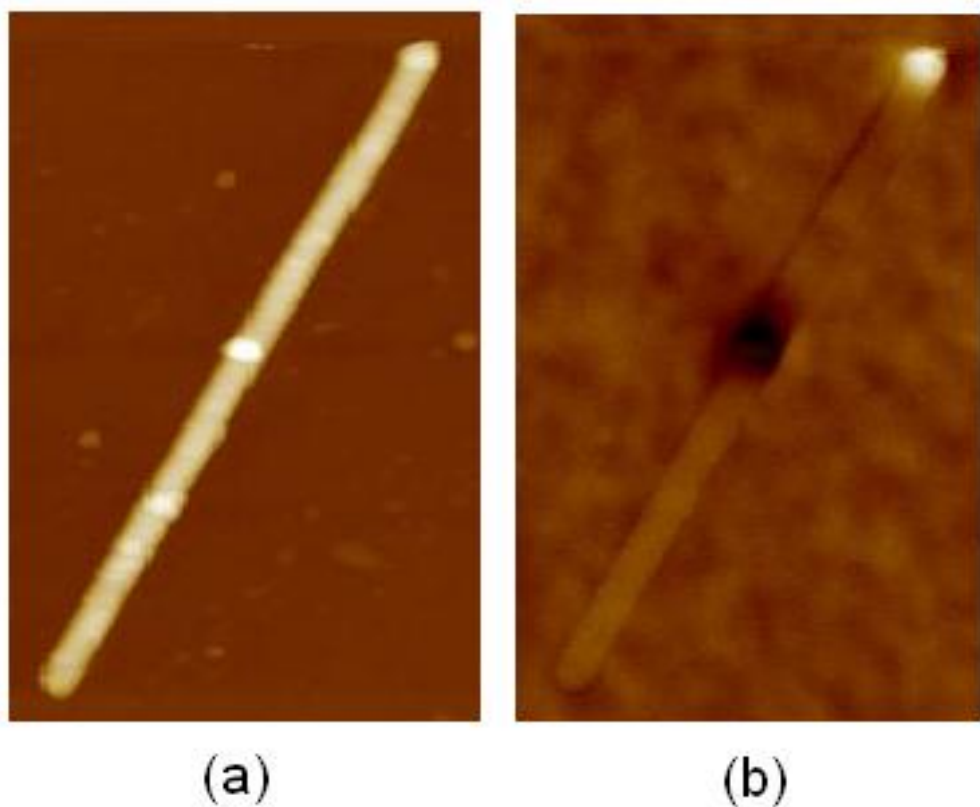
Figure 6.22: Height (a) and phase (b) results showing a distinct magnetic Galfenol upper section and a nonmagnetic segment at the lower end expected to be copper based on the results of composition analysis.

length. The simplest explanation for this result is that Galfenol makes up the upper portion of the wire while the rest consists of copper. One of the reasons that this is not observed more universally is that the wires tend to break off at this junction due to a lattice parameter mismatch, as Figure 6.23 demonstrates.

Figure 6.23: SEM image of an array that apparently consists of long Galfenol nanowires grown atop short copper stubs. The entire forward portion of the array has nothing left but these copper segments, implying that the material interface is a weak point prone to breakage.

6.3.4   Lorentz TEM Verification

An alternate means of viewing the magnetic domain structure is with Lorentz TEM [16, 40, 168, 6] utilizing the JEOL 2100F instrument that was used for the EDS analysis. In this technique, when high energy electrons penetrate a sample with a magnetic domain structure, they are deflected from their normal course due to the action of the Lorentz force, which follows the equation

$$F = q \, \boldsymbol{v} \times \boldsymbol{B}, \tag{6.15}$$

where F is the force, q is the particle charge, $\boldsymbol{v}$ is the velocity vector of the particle, and $\boldsymbol{B}$ is the magnetic induction vector. When the TEM image is intentionally defocused, the shift in image intensity due to this electron deflection can be observed as a bright or dark line along the domain boundary. In the case of an axially magnetized nanowire, the vector cross product in equation (6.15) will push the electrons uniformly to one side of the wire diameter, highlighting one continuous edge.

In practice, this is exactly what is observed. Figure 6.24 shows an isolated Galfenol nanowire lying on the carbon mesh of the TEM grid, with a white line running down the length that is slightly off-center favoring the bottom side. Based upon the Lorentz force, this implies a uniform axial magnetization pointing to the left. In every nanowire imaged in this manner, no instances of a white stripe jumping from one side to another along the length were found, which would have indicated alternating segments of inverse magnetization. With the assistance of Dr. Cumings, a wire domain was observed to flip between its up and down axial states by rotating it
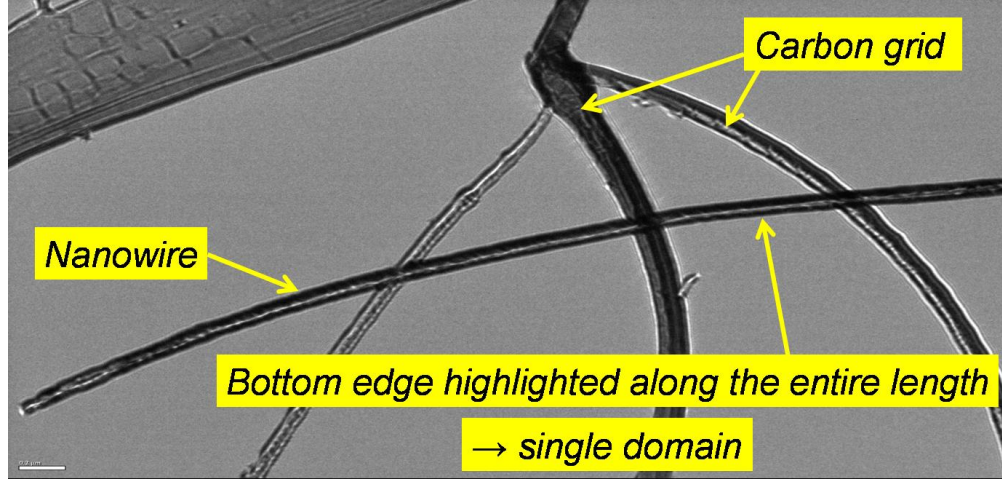
Figure 6.24: Lorentz TEM images of Galfenol nanowires on the carbon mesh. The bright stripe running along the length is slightly closer to the bottom, which implies a single axial domain oriented to the left. If multiple domain segments were present, the line would jump to the other side of the nanowire at each boundary.

within the field. Figure 6.25 shows two consecutive images of the highlight changing sides, and the field at which this switching occurred was estimated to be 110 Oe. Referring to Figure 6.7, the FEM simulation supports this by having no intermediate state between the $+M_s$ and $-M_s$ configurations and having a predicted coercivity of 138 Oe.

The primary result of this chapter is that the strong nanowire anisotropy promotes axial magnetization without the need for externally applied fields. The implication of this with regard to artificial cilia devices is that it removes a possible design challenge of accurately applying a field to these structures that does not interfere with the remainder of the sensor. With the nanowires naturally at saturation, it is also expected that the change in induction due to compressive stress
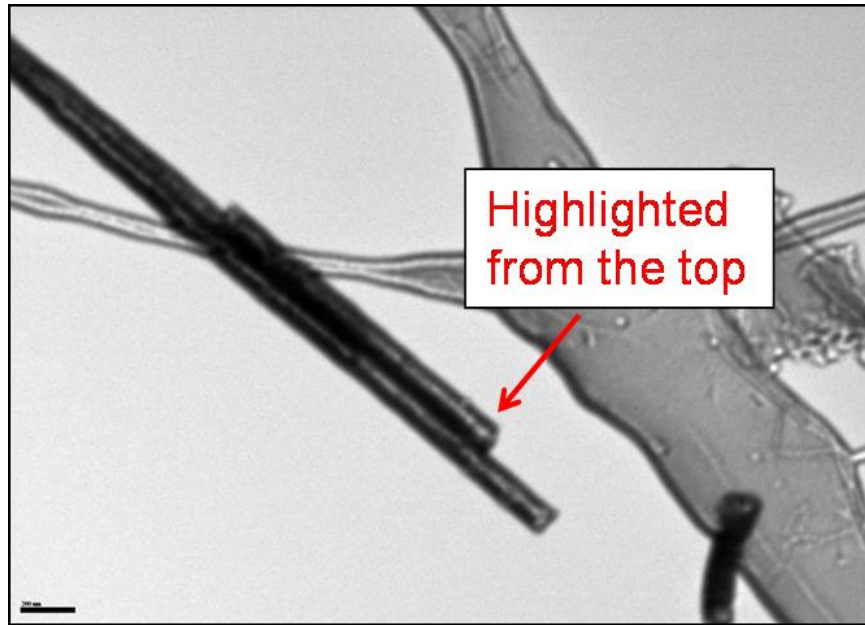
(a)
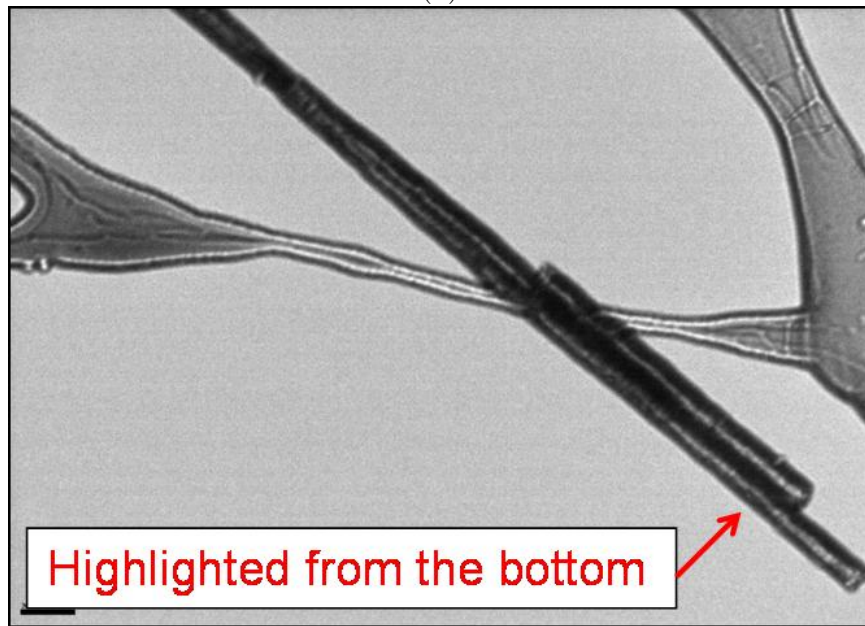
(b)

Figure 6.25: Rotating the nanowire in the field caused the magnetization to flip from the initial state oriented to the right (a) to the opposite direction (b). There was a distinct lack of an intermediate state in agreement with the very square magnetization curve predicted for these nanowires.

will be maximized. These properties should also have value in numerous other applications [56, 160, 57, 117] including biomagnetics, data storage, and microfluidics where there is a clear advantage to having ferromagnetic materials with only two stable and clearly defined states.

Chapter 7

Magneto-mechanical Coupling in Galfenol Nanowires

7.1   Challenges

Knowledge of the mechanical and magnetic properties of Galfenol nanowires segues into studying the magnetostrictive transduction on which sensor and actuator applications rely. Characterizing this coupling has proved to be a difficult task, and in many cases the results suggest that the samples require structural modification or improved integration before the desired transduction can be practically realized. Despite these conclusions, this chapter details the novel methodology used to investigate the magneto-mechanical coupling in Galfenol nanowires, taking advantage of the different experimental techniques described previously.

Experimentally characterizing the sensing magnetostriction in macroscale Galfenol samples requires measuring the change in magnetic induction with applied stress. This approach immediately highlights two potential challenges of reprising this data from the nanowire samples. First there is the matter of applying stress to individual nanowires in a controllable manner, specifically in pure bending to accurately simulate the loading in artificial cilia. In addition, measuring any magnetic data from a nanowire poses a significant obstacle. The traditional pickup coil cannot be wound around each wire, leaving Hall effect and GMR devices as the primary options, but there are still issues with the size mismatch of bonding nanowire arrays onto even

microscale sensors due to the rapid decay in magnetic field strength with distance.

The other primary concern stems from the results of Chapter 6, namely that the equilibrium state for essentially every nanowire is a single axial domain. From Table 6.1 it is clear that in wires with typical geometry, a stress on the order of GPa's may need to be applied before a legitimate competition arises between the magnetoelastic and demagnetization energies. The wire diameter falling just under the critical value of a single domain state prohibits the formation of multiple domains that could potentially rotate with stress and directly decrease the wire magnetization. With these concerns in mind, attempts have been made to observe the effect of bending stress on the magnetic domain structure of individual Galfenol nanowires.

7.2   Static Bending Experiments

7.2.1   Nanowire Bending Procedure

The nanomanipulator device can be used to bend nanowires both within and freed from the array, but the SEM imaging offers no means of observing magnetic domains. The MFM instrument provides the most straightforward means of examining the magnetic structure of the nanowires, but the scanning probe nature of the technique presents other limitations. While the nanomanipulator can be placed onto the MFM sample stage, there is no means of visualization outside of the inadequate optical camera. Thought was given to finding and bending a wire within the SEM as normal and then transferring the entire setup to the MFM, but not only is it

incredibly unlikely that the nanowire will remain in place during the move, but the MFM does not work well when trying to scan something suspended above a surface. When the probe tip is over the nanowire and the manipulator AFM tip bending it, the MFM process should behave as expected, but once the probe moves over the empty space on either side of the nanowire the controller will fully extend 6.34 μm downward in an attempt to locate the surface again, during which time it will likely crash into the nanowire or its attachments.

As a result, conducting static bending experiments requires first bending the nanowires within the SEM, holding them in the bent position while attached to a flat surface, and then observing the resultant domain structure in the MFM. This begins by depositing the nanowires onto a silicon wafer that is placed flat in the nanomanipulator. The goal is to have the AFM tip attached to the manipulator drag along the silicon surface, bending any nanowires that are in its path. The typical setup used for mechanical testing called for the AFM probes to be mounted vertically, such that the full profile can be seen in the SEM field of view. In order for the sharp tip to access the silicon wafer, the probe needs to be rotated 90° so that it points downward as in normal AFM operation. When in this position however, the width of the cantilever itself blocks observation of the tip actually impacting the surface and interacting with the nanowires. Therefore, for this procedure the AFM probe is mounted on the manipulator at approximately 45° from vertical, sufficient to make the point of the tip be the lowest feature and contact the surface first, but not enough to prevent observation. Figure 7.1 shows an SEM image of a probe tilted in this manner above the nanowires scattered on the silicon below.
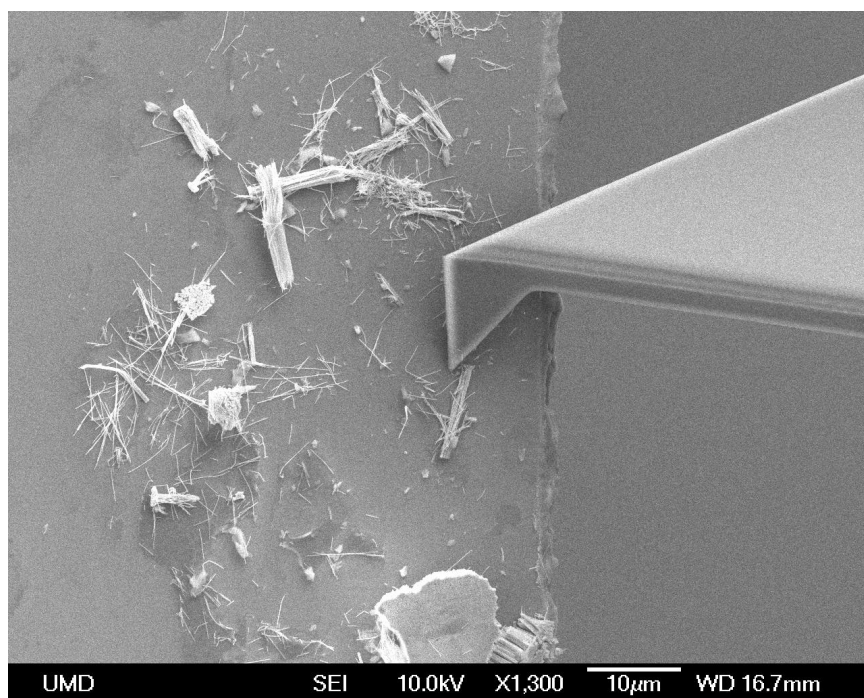
Figure 7.1: Micrograph of an OTESPA model AFM probe tilted within the manipulator stage to allow the tip to access the Galfenol nanowires scattered on the silicon surface.
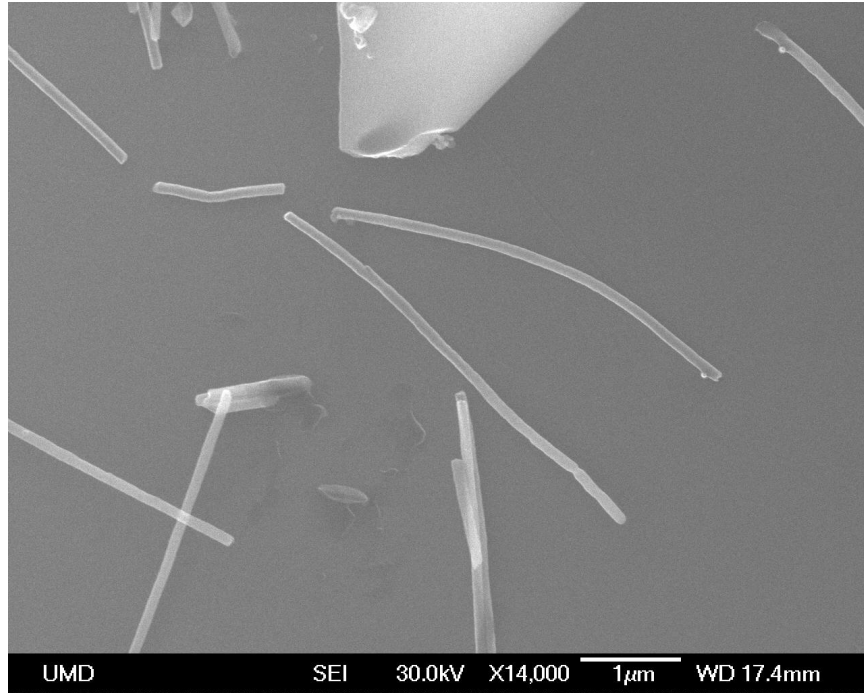
Figure 7.2: SEM image of nanowires bent with the manipulator and held in place with EBID welds. The central wire has a bright weld point at the lower right fixed end, and two less sharp weld points long the length. Another example can be seen in the upper right corner of the image.

In order to force the nanowires to bend as if they were cantilevered, once a select wire is identified an EBID weld is applied to one end in order to firmly attach it to the silicon. The AFM tip is them moved perpendicular to the wire axis out near the free end in order to bend the nanowire into the desired deformed shape. Another set of welds are performed at this end to statically hold the wire in the bent position as shown in Figure 7.2, allowing the MFM to be performed on samples with substantial bending stresses.

As usual, there are some interesting scenarios that arise during this process. The most problematic is that in many cases the wires strongly resisted being bent,

where the AFM tip would simply move over the top of the wire and continue on its way. Assuming that there was simply minor attractive forces between the nanowire and the silicon holding it in place, the AFM tip was moved further downward to increase the force applied, but in some cases this resulted in the nanowire literally being crushed rather than deflecting. Figure 7.3 reveals one extreme example, where the tail end of the sample is smashed into the silicon. Based upon earlier experiences, it was thought that perhaps the wires were oxidizing and becoming rigidly attached to the silicon surface, as there is some evidence of remnant oxide in the original position of the nanowires in Figure 7.3. A test was done by transferring a new batch of nanowires directly from the alcohol they were suspended in to the vacuum of the SEM chamber, limiting the air exposure and potential oxidation time. This resulted in the first usable bent nanowires, and although the success rate was still no greater than 50% it made a substantial difference. In several cases the wires still broke rather than bend, but it was a much cleaner brittle fracture like depicted in Figure 7.4 rather than the previous smashing. There were very few observations of wires actually rolling along on the surface, but in those select cases welding the one end adequately served its purpose.

Figure 7.5 is a sequence of images showing the position of a Galfenol nanowire before and after bending, and Figure 7.6 reveals a wire that bent into a shape resembling the second mode of a cantilevered beam. Once a handful of nanowires in a particular area were bent and welded in place, the silicon wafer was removed from the manipulator and loaded into the MFM instrument. The bent wires were located using known distances and landmarks as usual, and the magnetic phase images were
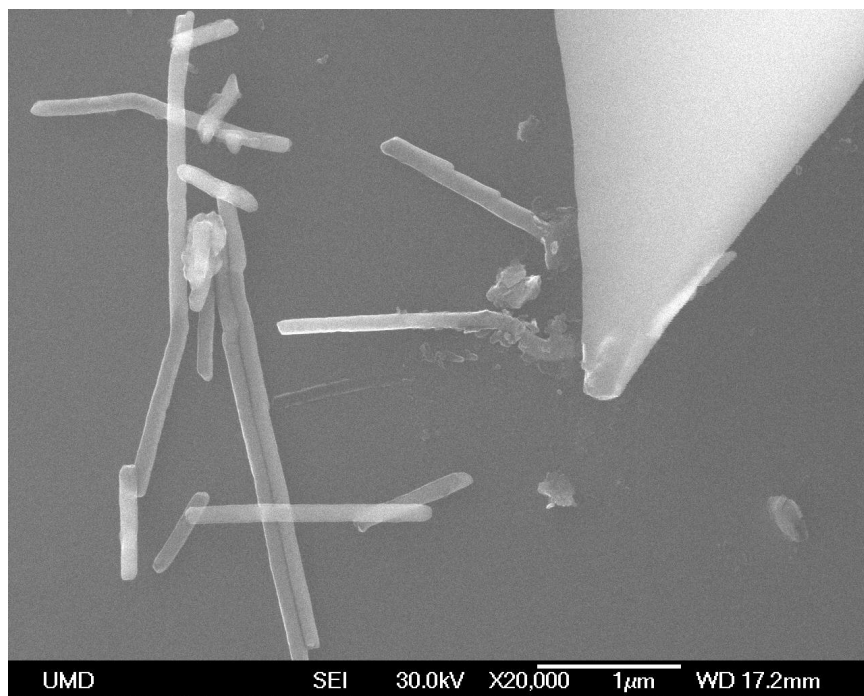
Figure 7.3: Micrograph of nanowires literally crushed by the AFM tip due to significant attractive forces between the nanowire and the silicon. In the center of the image there is an outline revealing the original position of the smashed wire, possibly residual oxide that adhered to the silicon.
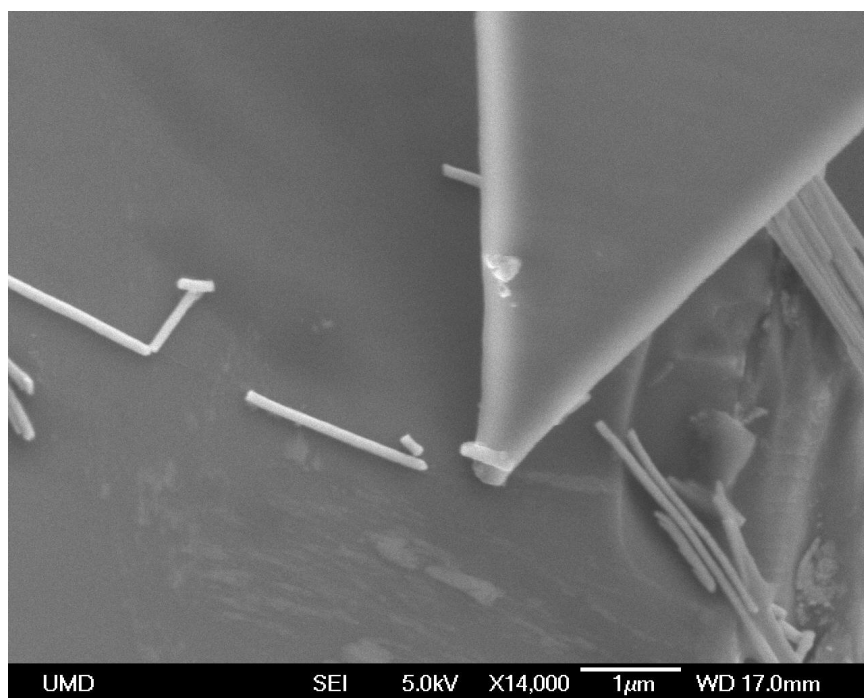
Figure 7.4: Nanowires with limited exposure to the ambient air environment often still stuck on the silicon but demonstrated the expected brittle fracture.

scanned as normal.

7.2.2   Magnetic Results and Discussion

An example of MFM data collected from a bent nanowire is presented in Figure 7.7. Despite the sharp kink in the sample there is no real contrast other than the bright and dark ends of the still single domain wire. There is a slight darkening near the bend that would result as the magnetization curls around, but it is still predominantly axial. Another example is plotted in Figure 7.8, where the upper wire exhibits a strong band structure but still has the bright and dark opposite ends. It appears that the stress applied is inadequate to cause domain rotation, although there is some interaction with the adjacent wire fragment that further clouds the image on the left end of the wire.

Figure 7.9 is the lone example of a bright spot away from the ends of the wire near the position of maximum bending stress, but unfortunately there are several characteristics that suggest this is not representative of the magnetoelastic coupling. First of all, if a magnetic domain was aligned along the short axis of the wire, the phase image should be bright on one side and dark on the other, whereas this point is uniformly bright spanning the entire diameter. In addition, if the nanowire did contain a perpendicular domain near the midsection, the unstressed length of wire from there to the bottom fixed end would still be magnetized axially and thus there would likely be another dark spot to complete the flux path of this segment. Finally, close examination of the SEM image reveals that there is a bump on the surface
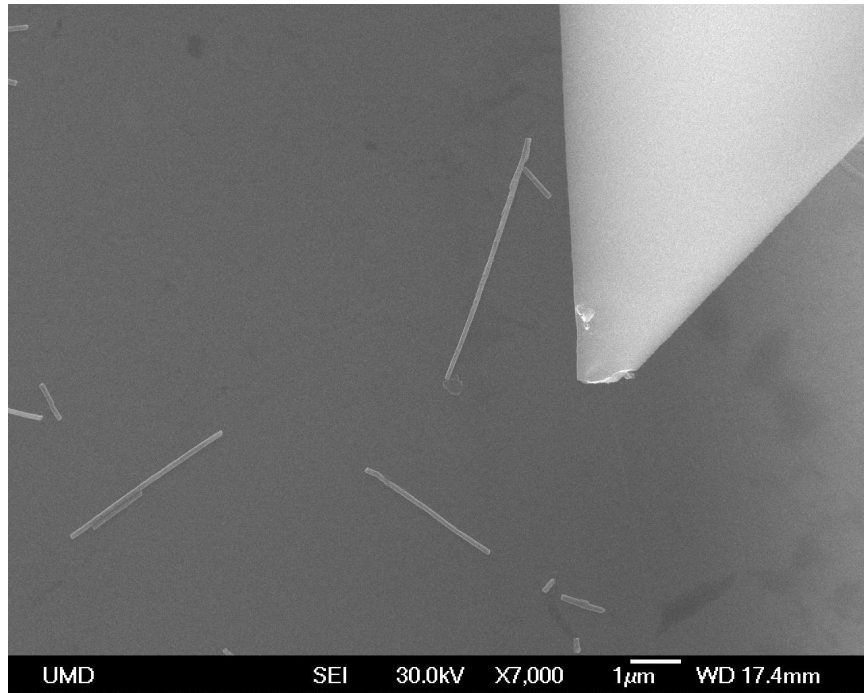
(a)
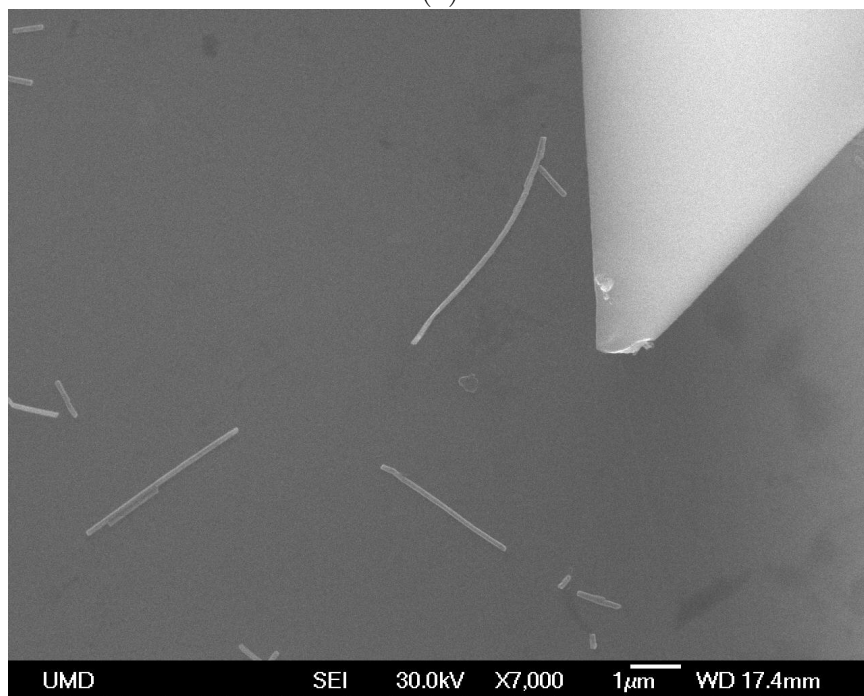
(b)

Figure 7.5: An isolated Galfenol nanowire that has been selected for bending and had an EBID weld placed near the top end (a). After moving the AFM tip to the left and deflecting the wire (b), it is ready for MFM imaging with bending stress applied.
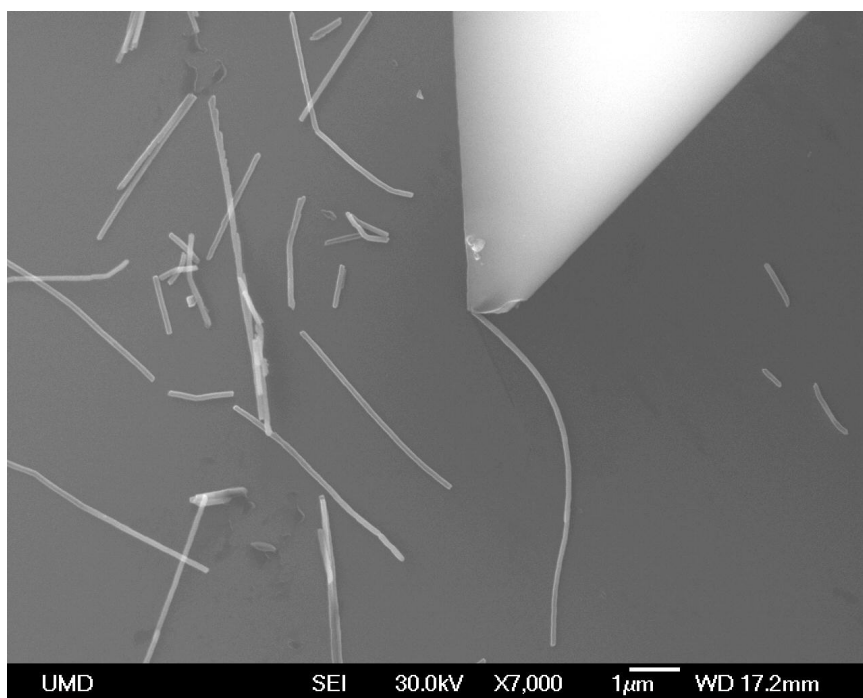
Figure 7.6: SEM image of a successfully bent Galfenol nanowire that actually deformed into a shape resembling the second mode of a cantilevered beam.
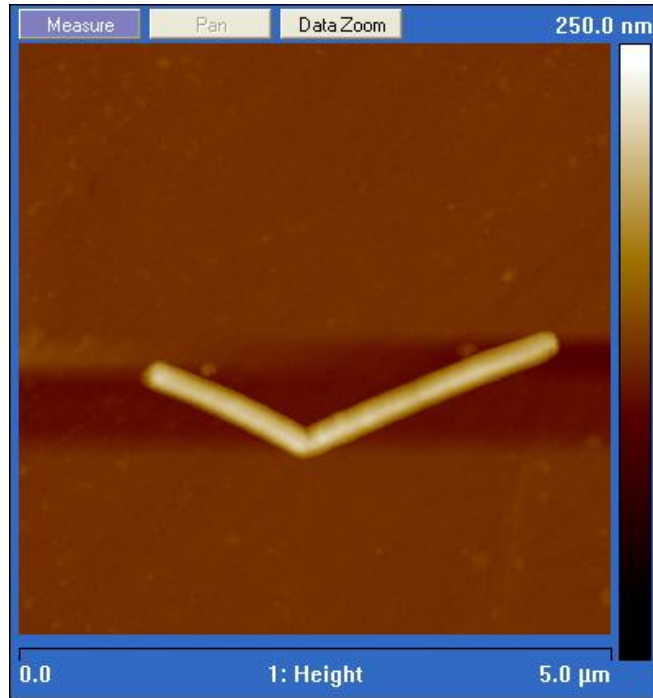
(a)
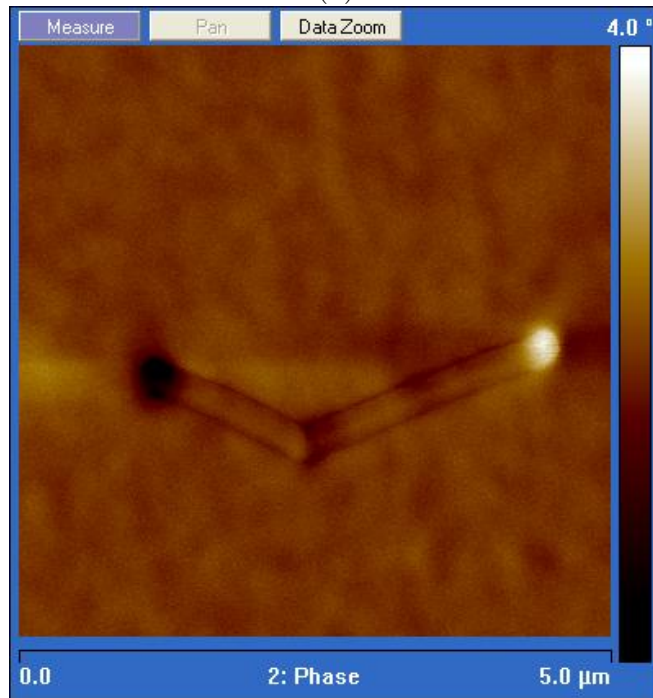
(b)

Figure 7.7: MFM results showing the height (a) and magnetic phase (b) of a nanowire bent into a sharp kink. The phase contrast reveals that the magnetization still points along the axis even around the bend.
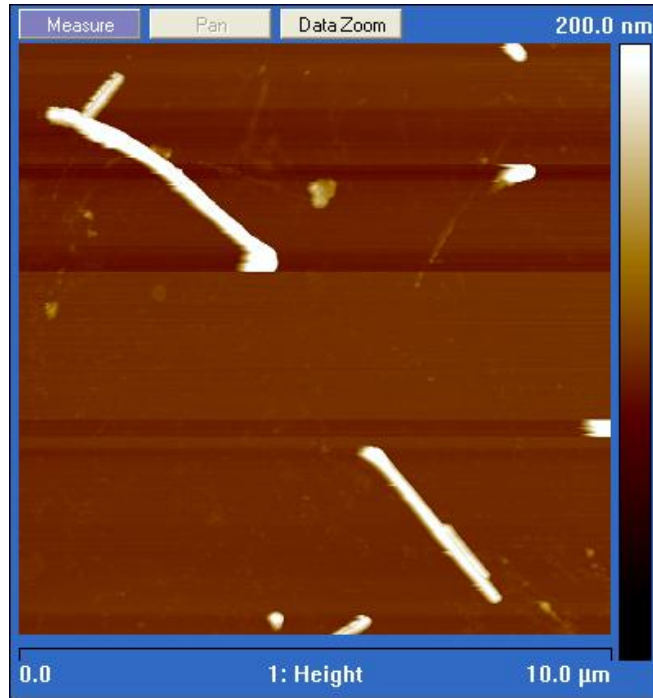
(a)
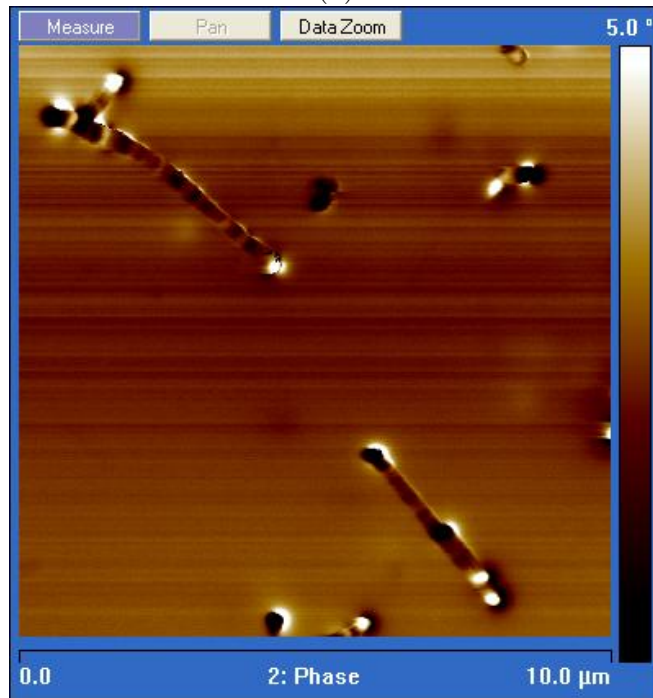
(b)

Figure 7.8: MFM data from a bent nanowire showing a very strong band structure. Some of the phase contrast (b) at the left end of the upper wire is likely caused by field interaction with the adjacent fragment in the height scan (a).
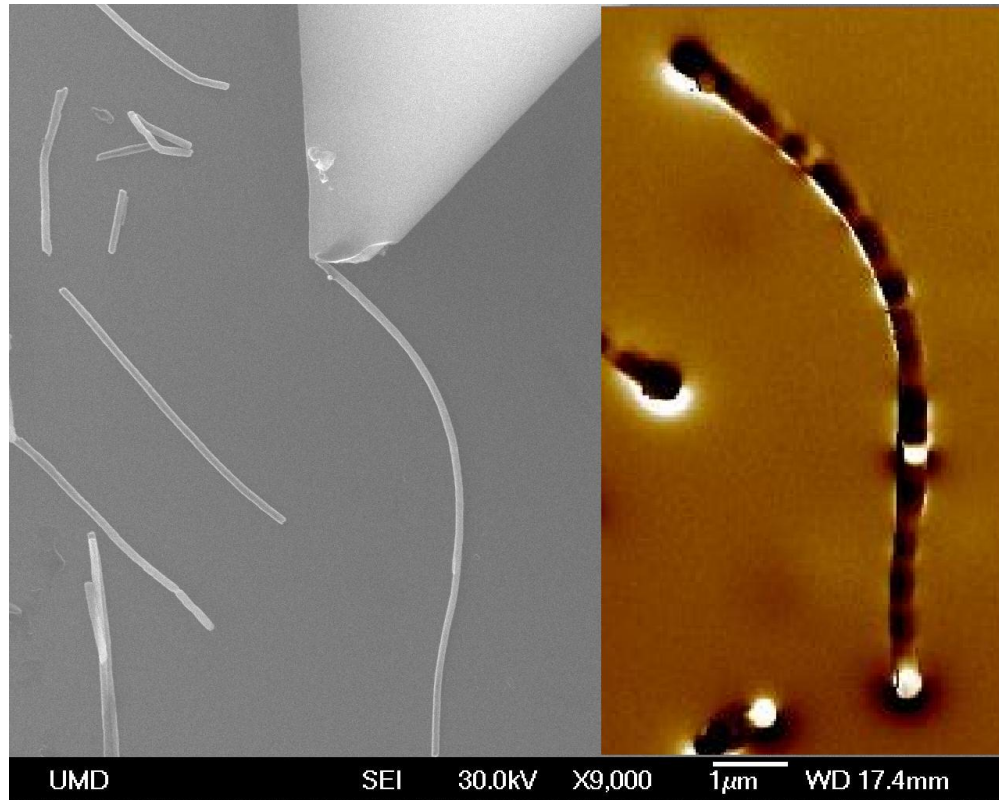
Figure 7.9: MFM phase result overlaid on the SEM image of the bent nanowire from Figure 7.6. This wire actually has a bright spot away from the ends, but it cannot be stated with any certainty that this is due to stress induced domain rotation. A possible scenario is that the bright and dark ends represent the usual axial magnetization and the middle spot is due to the topographic defect on the surface.

right at this spot, which was shown in Chapter 6 to contribute false bright spots in the MFM results. While these concepts do not entirely disprove the idea that there is stress induced domain rotation in this nanowire, it remains unlikely.

A final noteworthy result is presented in Figure 7.10, which reveals that a very sharp bend placed in one wire occurred at the interface between a length of Galfenol and the copper end segment. This further highlights the potentially weak structural connection between the two materials, and lessens the odds of finding a

224
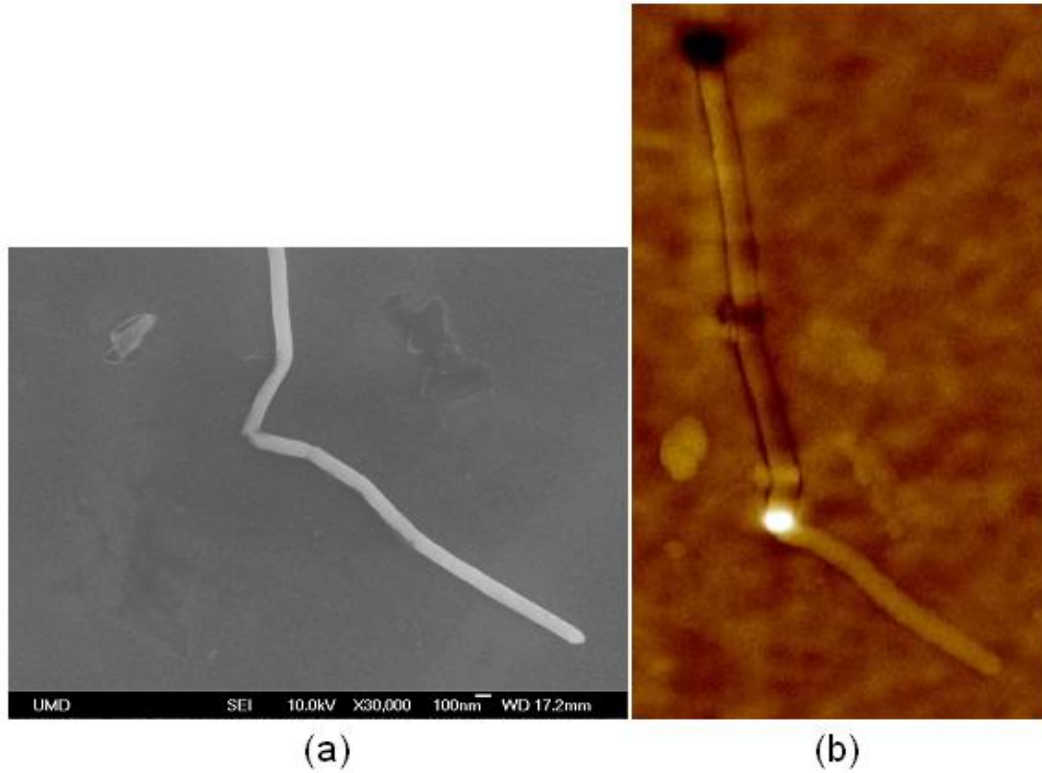
Figure 7.10: SEM image (a) and MFM phase plot (b) of a nanowire with a very distinct bend. It is apparent from the magnetic data that the bend occurred directly at the interface between the Galfenol and the copper segment, which is entirely nonmagnetic from the bend down. The top end of the wire (not shown in the SEM image) has the Galfenol's dark spot opposing the bright point at the bend.

strongly bent wire displaying magnetization rotation. Overall, it can be concluded from these results that the bending stress applied to the nanowires is insufficient to overcome the anisotropy and produce any substantial change in magnetization, producing no usable sensing transduction.

7.3 Dynamic Testing

7.3.1 Sensor Attachment

Characterizing the magneto-mechanical coupling via dynamic excitation was actually the earliest experiment conceived for this research, originating from the conceptual designs for artificial cilia devices in Chapter 1. This testing would simply consist of attaching a nanowire array on top of a magnetic field sensor, exciting the structures by either forcibly bending them at the tip or shaking the entire base, and then measuring the change in magnetic field. This operating mode would directly identify the feasibility of deploying Galfenol nanowire cilia not only in complex acoustic devices, but also in more structurally fundamental sensors such as those for fluid flow or tactile detection.

The single biggest challenge in obtaining this data was the incorporation of the nanowires with the external magnetic sensor element. Initial attempts were made to bond the copper foil attached to the backside of the array onto a Hall effect sensor using thin layers of epoxy and other adhesives. In all cases the bond layer that formed was found to be enormous compared to the feature size of the nanowires, usually several μm's thick, which prevents detecting any magnetic field from the nanowire dipoles due to the strength falling off at a rate proportional to the distance cubed. In addition, most of the thinnest bonds were too rigid to allow undamaged removal of the array for additional attempts. Vacuum compatible grease was tried, as the adhesion was just enough to ward off gravity, but the substance ended up spreading everywhere and burying the nanowires themselves as shown in
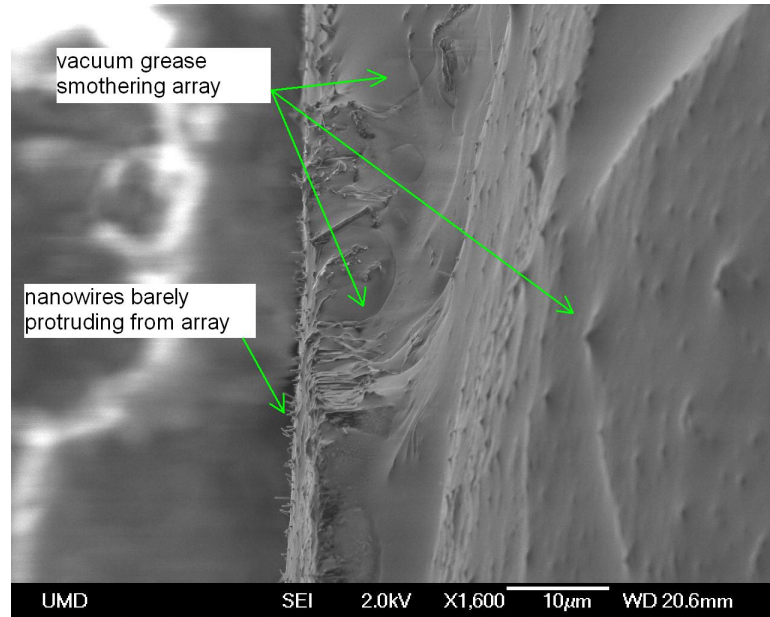
Figure 7.11: Micrograph revealing a nanowire array that became completely buried in vacuum compatible grease when attempting to use the compound as an adhesive. The manner in which the grease spread onto the top side of the sample in unknown.

Figure 7.11.

Eventually an array was affixed to a Hall probe that potentially could have detected the deflection of the nanowires, but when placed inside of the SEM chamber some combination of electrical charge and/or vacuum outgassing caused a catastrophic failure where some residual plastic coating on the Hall probe exploded. The result was a strong magnetic field originating from the Hall sensor as shown in Figure 7.12, which prevented all observation and fried an external instrument connected via the SEM feedthroughs. Subsequently, most of the nanomanipulator and SEM chamber components required cleaning as Figure 7.13 displays how there was a distinct residue of burnt plastic.
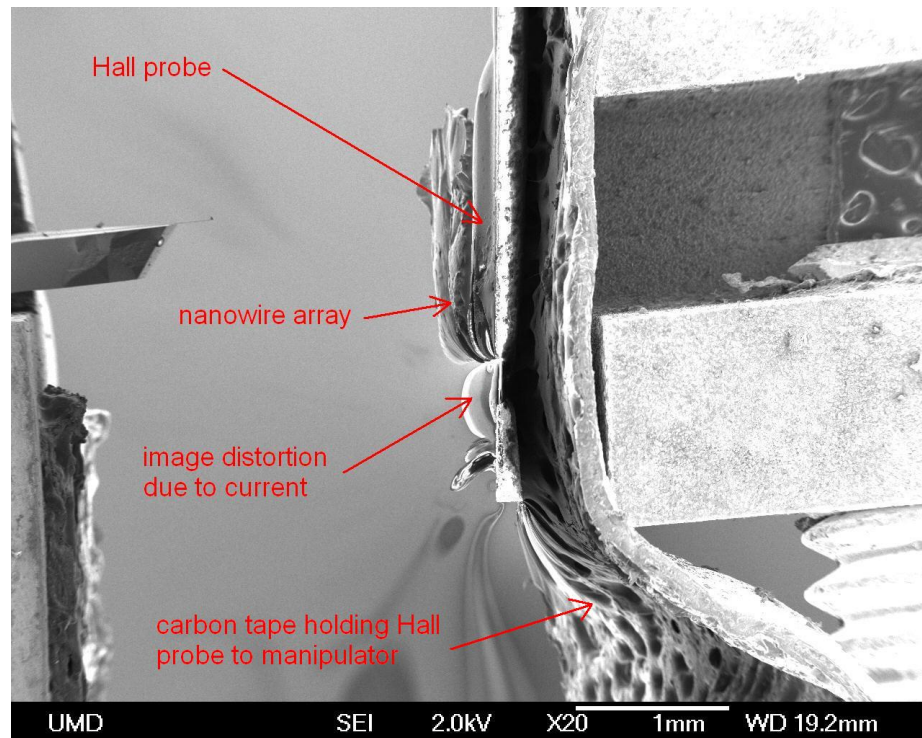
Figure 7.12: A Hall effect probe attached to the manipulator that burnt out within the SEM chamber. The resultant short circuit allowed for a strong current to flow within the sensor, generating a magnetic field that warped the electron image.
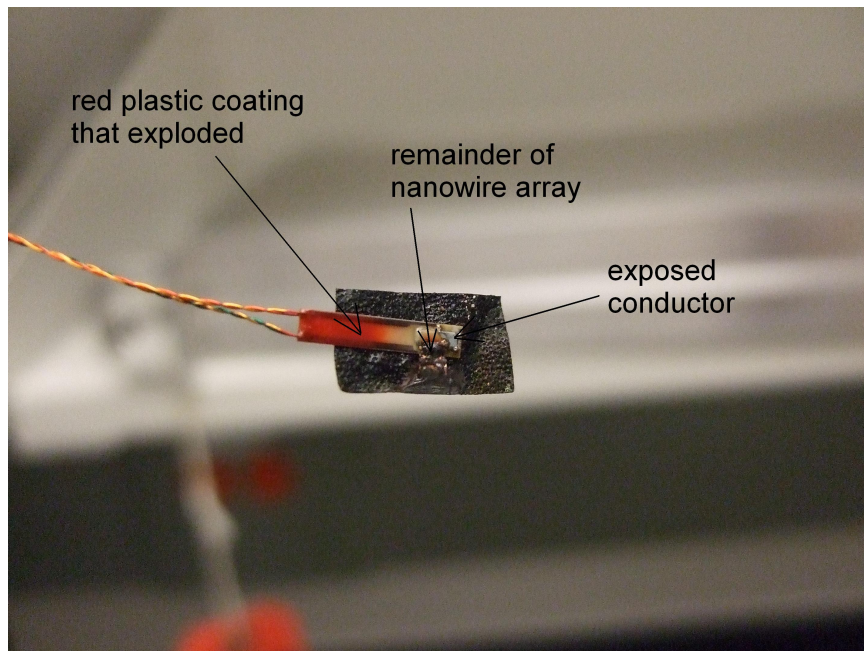
(a)
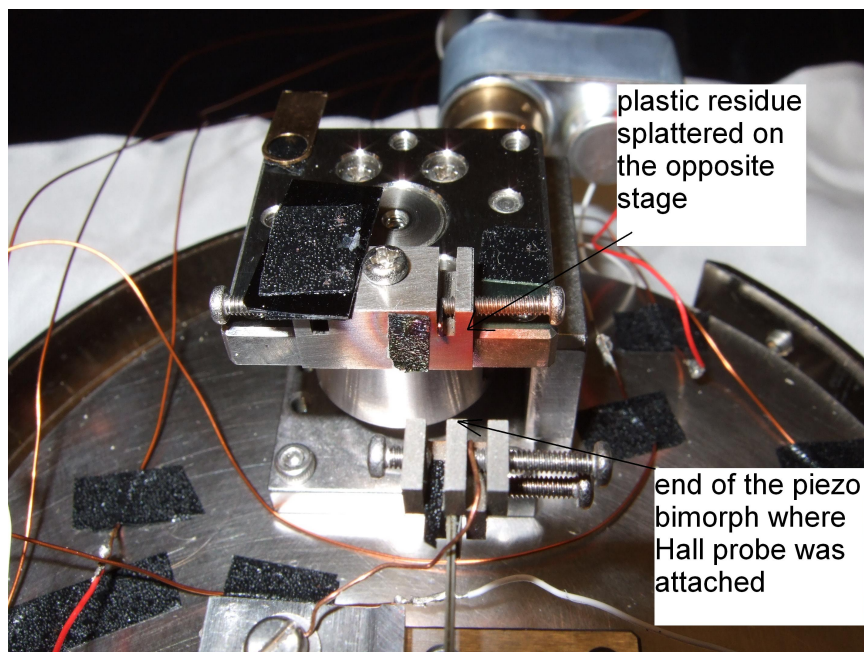
(b)

Figure 7.13: Photograph of the fried Hall probe (a) showing the burnt remnants of the nanowire array and the red polymer coating that left a residual coating on all nearby manipulator components (b).

It quickly became apparent that the approach of mounting an array onto a macroscale sensor was rather futile, and that proper execution would require the integration of magnetic sensors earlier in the fabrication process. Considering that this would require a significant shift in the allocation of time and resources, a final attempt was made to get some results from the existing samples for the purposes of proving that the nanowire fields can at least be detected. The GMR sensor included in the nanomanipulator that was discussed in Chapter 4 had exposed sensing resistors that allowed direct contact with the active elements (see Figure 4.6). If individual sections of a nanowire array could be placed onto these regions directly, without the mm-sized piece of copper foil backing, the attractive and frictional forces should be enough to hold them in place without the need for bonding agents. Using the nanomanipulator capabilities and a healthy dose of patience, a few clusters of wires were eventually moved into position on top of the GMR resistor elements. Figures 7.14 and 7.15 demonstrate a few steps during this process. The end result is the desired configuration of cantilevered nanowire protruding from the surface of a microscale GMR sensor.

7.3.2   Preliminary Results

The AFM tip attached to the nanomanipulator was used to push a large swath of the array into bending, and unsurprisingly the GMR output voltage was a resounding zero during the entire process. The GMR operation was confirmed by testing the dummy GMR resistor in the Wheatstone bridge that was wired outside
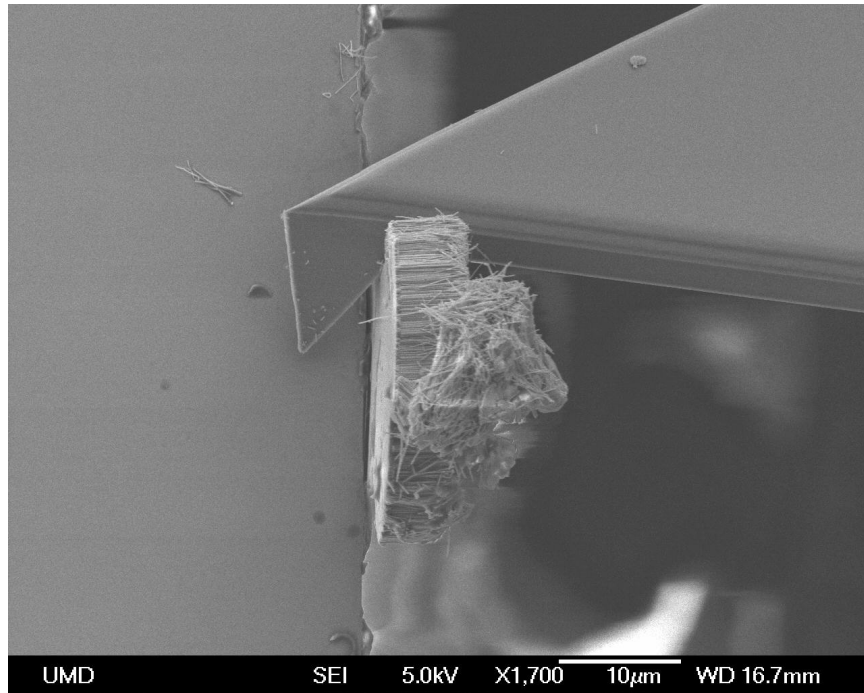
(a)
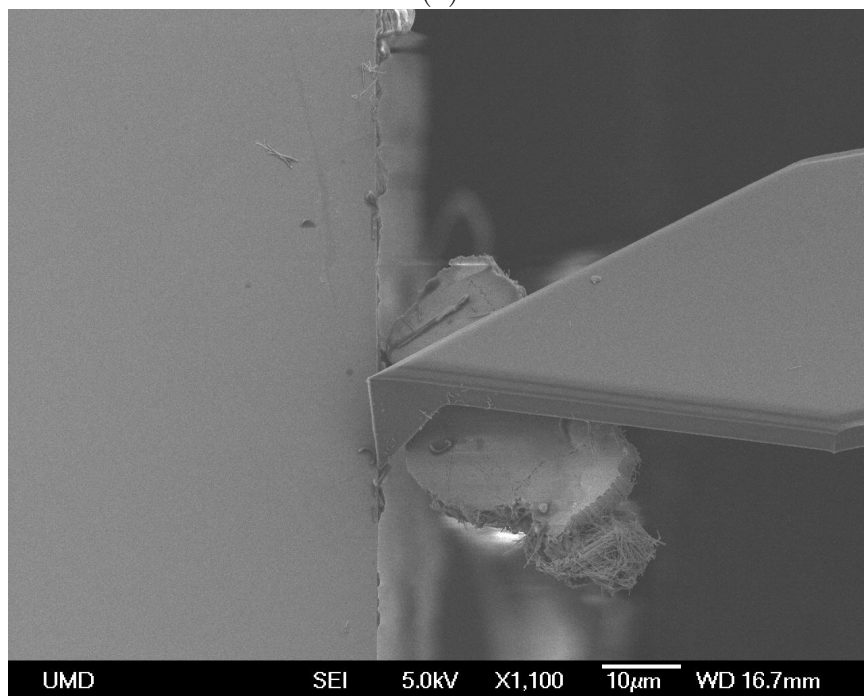
(b)

Figure 7.14: A nanowire array along the edge of a silicon wafer can be placed onto the AFM probe by simply knocking it away from its original position (a) and allowing it to stick to the probe via electrostatic, friction, and other forces (b).

231
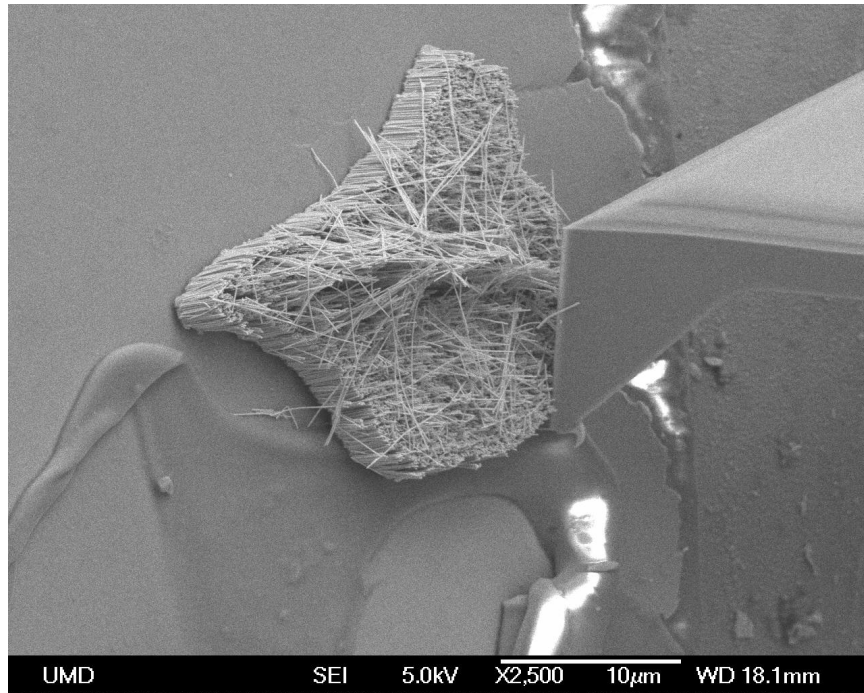
(a)
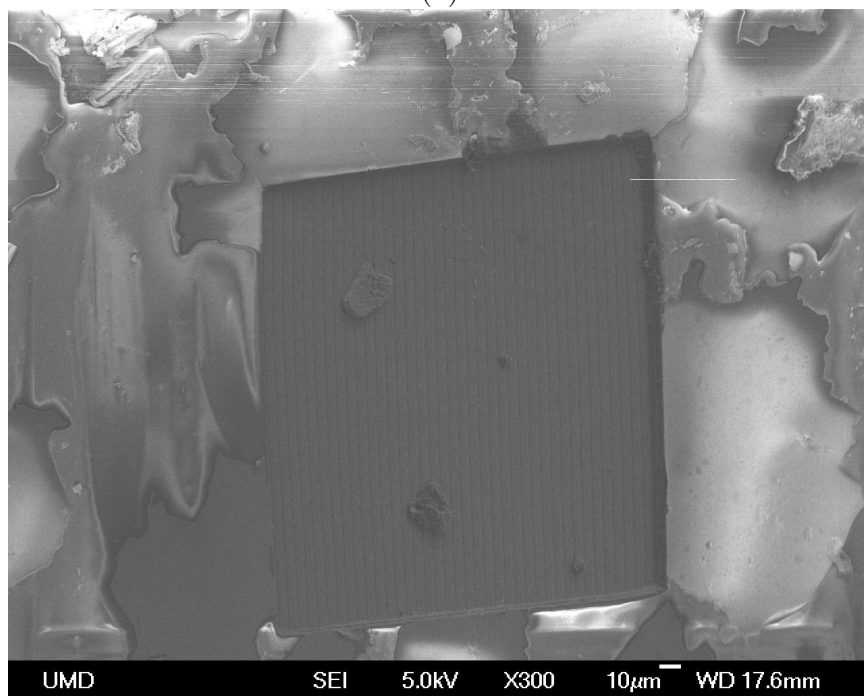
(b)

Figure 7.15: Nanowire array placed onto the GMR sensor by the same principle, namely pushing it into contact and letting attractive forces take over (a). The relative size of the placed arrays is still quite small compared to the area of GMR resistor (b).
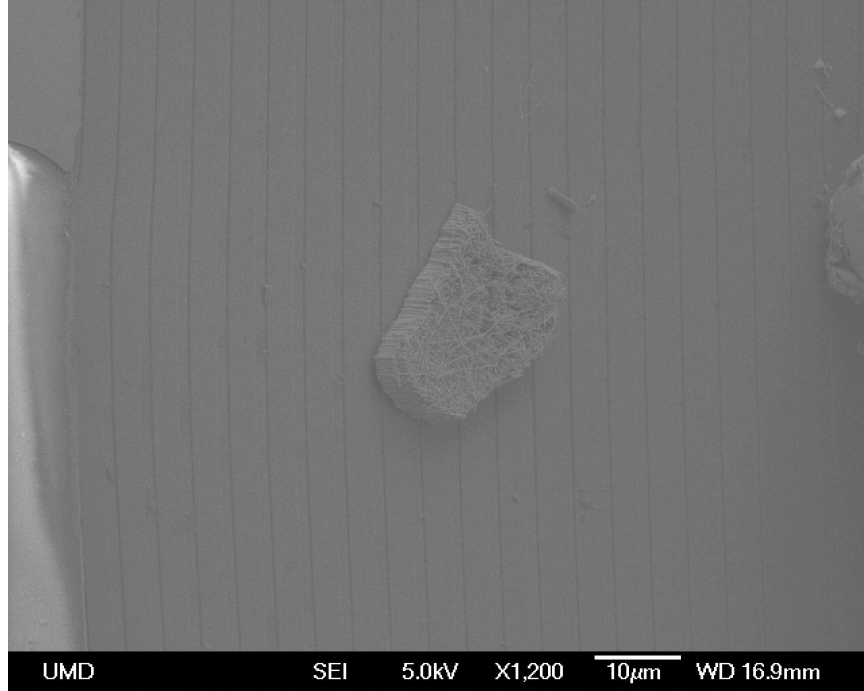
Figure 7.16: A close examination of the cantilevered nanowire array attached to the GMR sensor reveals that there is a strong possibility that it consists entirely of copper stubs.

of the SEM vacuum chamber, ensuring that the circuit was completed and that the bridge response was being properly recorded. In addition to all of the reasons previously discussed, a key factor in the lack of output from this experiment could be that the cantilevered arrays actually placed on the resistors were composed of nothing but the short copper segments. Figure 7.16 shows that most of the Galfenol appears to have broken off, most likely either in the original alcohol solution or during the deposition onto the silicon. Even if a fraction of the array has full length Galfenol wires, the extra 1 to 5 μm of spacing that the copper introduces would be enough to prohibit field measurement on its own.

Another consideration is that it is possible that the size of the arrays used

were simply too small. Specifically, if the local magnetic field changes affect only the resistance of the region directly beneath the array, the total change in resistance of that element could at best be proportional to the fraction of area covered. In order to test this hypothesis, a cluster of long wires known to be Galfenol were dropped onto another resistor. They could not be placed in the ideal cantilevered configuration due to not having a fixed backing, but Figure 7.17(a) shows that instead they actually are laying on their side in the corner. Using the manipulator, a group of these nanowires were smashed into and subsequently pushed across the face of the resistor. Figure 7.17(b) displays the translation of the nanowires stuck to the AFM tip and Figure 7.18 plots the measured voltage change from the GMR sensor. At the very minimum, it appears that the GMR resistor is capable of detecting magnetic field changes from a small group of Galfenol nanowires that are in very close proximity. It is hoped that this will hold true as well once the configuration is optimized to include a large array of cantilevered nanowires with Galfenol directly adjacent to the resistor.

Despite the lack of concrete evidence of bending transduction in Galfenol nanowires, the approach taken in this work is a novel combination of mechanical manipulation and magnetic characterization. The methodology is flexible enough to be adapted to the different nanowire samples and provides a convenient means of dynamically exciting the arrays, but accurate magnetic field measurement is still a significant challenge. It is again noted that the efficiency of this work would be greatly improved going forward by focusing on better integration of the GMR elements, either by using more traditional MEMS bonding techniques or patterning
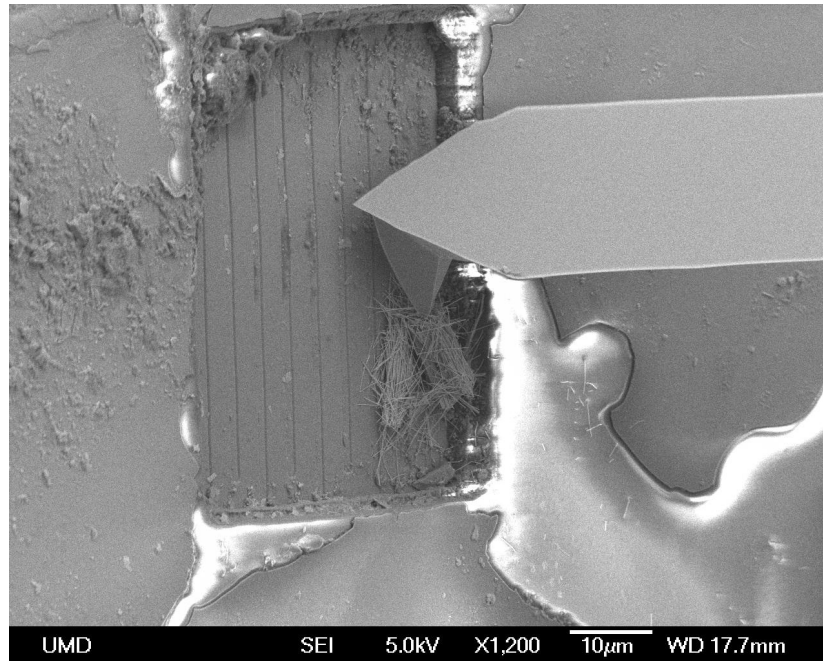
(a)
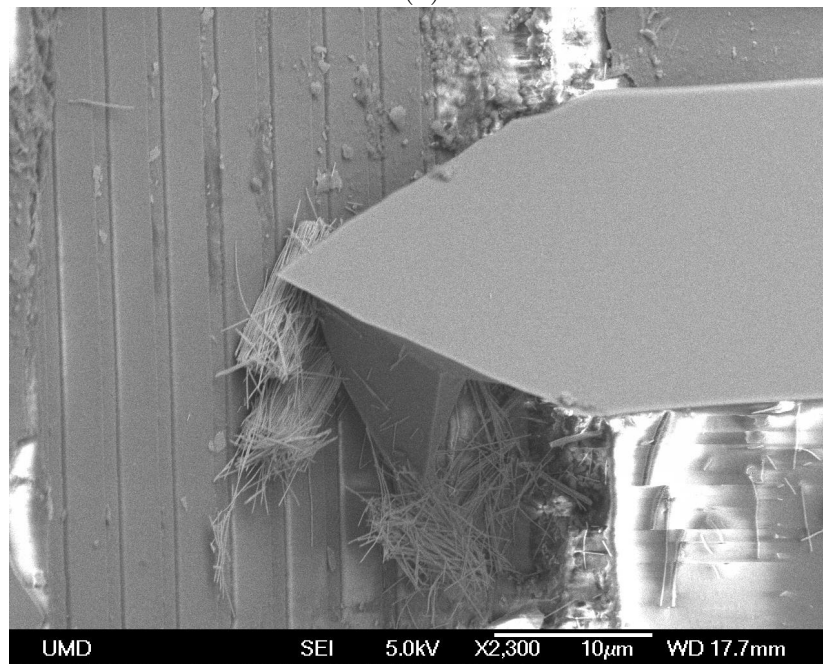
(b)

Figure 7.17: A cluster of known Galfenol nanowires were dropped onto a GMR resistor (a), and because they are broken off from the copper there is no backing to cantilever them and they simply lay as is. The AFM tip was used to push them to the left in one large step to the final translated position (b).
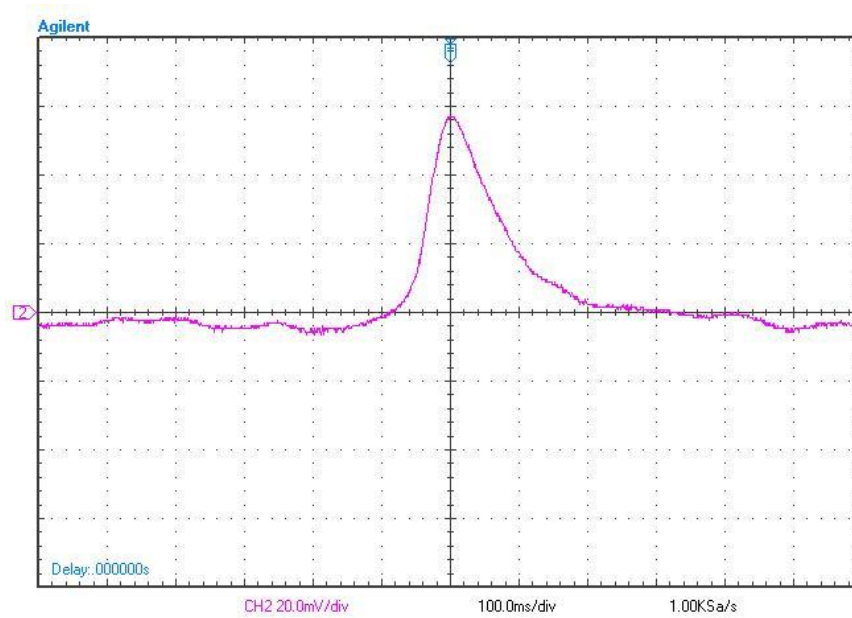
Figure 7.18: Voltage signal from the GMR Wheatstone bridge when the cluster of nanowires was pushed across the face of the resistor as shown in Figure 7.17, demonstrating that at the minimum the sensor is at least capable of detecting the magnetic field from a small group of wires.

the arrays directly onto the resistors at the start of fabrication.

7.4   Improving Transduction

Even if the experimental procedure becomes more refined, the data is still likely to be poor due to the overbearing shape anisotropy in the Galfenol nanowires. There are a few ways to change the relative strength of the competing energy terms and increase the probability of having the magnetization lie off of the wire axis. The most direct approach is to reduce the aspect ratio, greatly smoothing the M-H curve shown in Figure 7.19 and allowing for domain structures other than axial. The FEM model in Figure 7.20, generated using Magpar, shows that at equilibrium with zero applied field, a nanowire with aspect ratio of only five actually forms two opposite vortex domains at each end separated by a domain wall near the center. While this structure certainly provides more options for magnetization rotation, the short aspect ratio eliminates the mechanical flexibility needed for robust artificial cilia. Another idea is to increase the diameter of the wires to somewhere substantially above the critical single domain value, but doing so causes similar issues with stiffening the overall structure and requiring additional excitation to get the desired deflections and stresses. There also is a maximum pore size that can self-assemble in the anodized alumina templates, and thus increasing the nanowire diameter by an order of magnitude would call for an entirely different fabrication method.
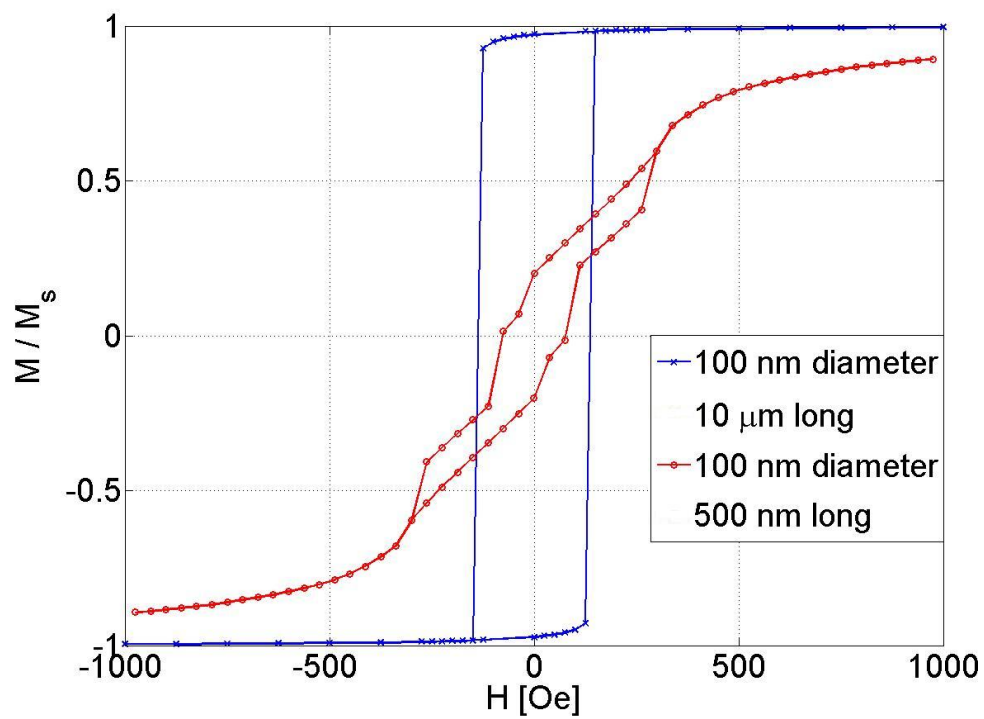
Figure 7.19: Micromagnetic FEM analysis of the magnetization curve for a 100 nm diameter, 500 nm long Galfenol nanowire overlaid with the previous simulation of a wire with large aspect ratio.
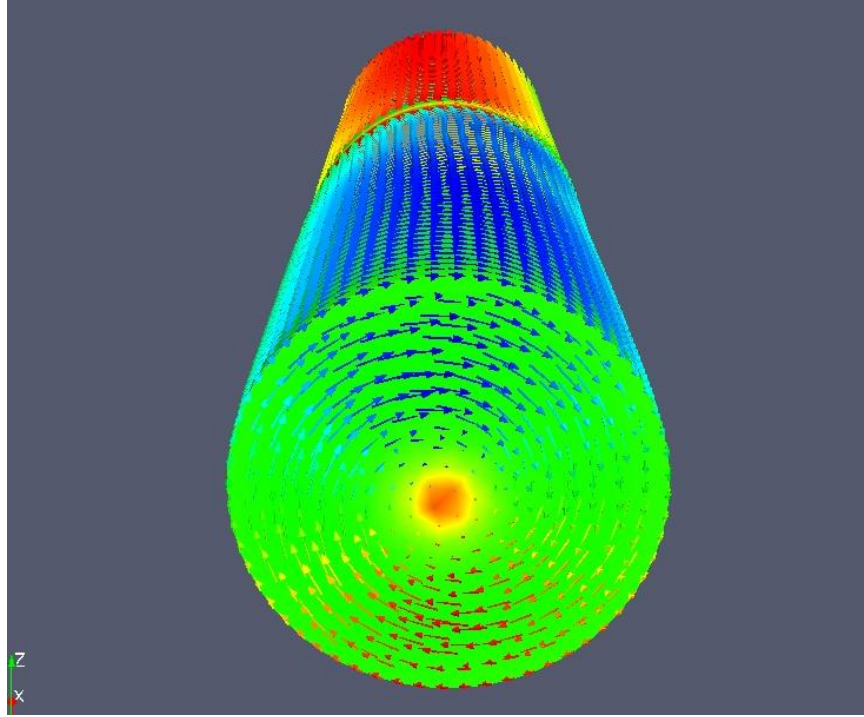
(a)
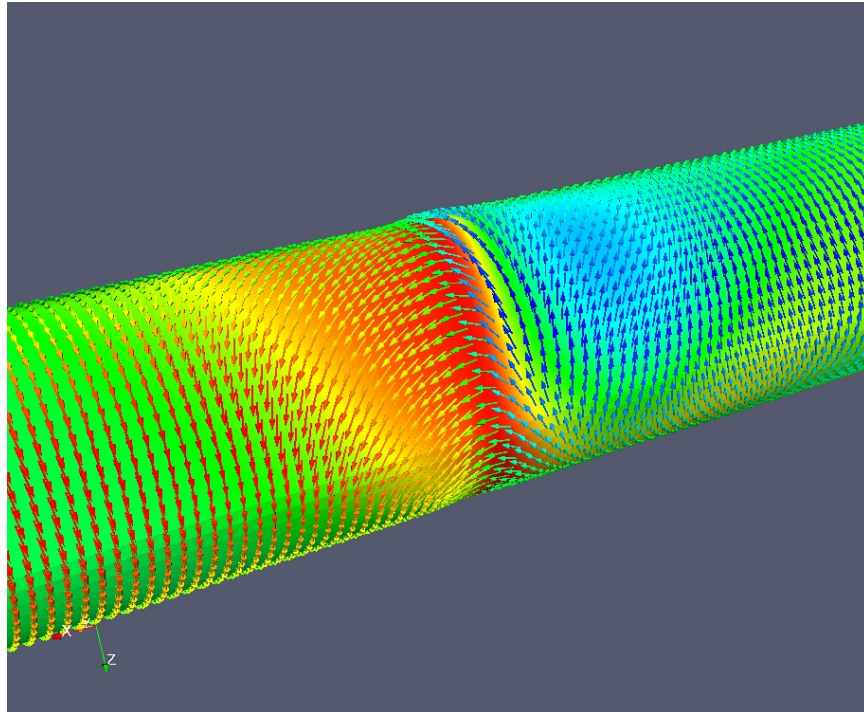
(b)

Figure 7.20: Micromagnetic FEM prediction of a short Galfenol nanowire with no applied field. A vortex domain forms at each end of the wire (a) with an apparent Néel wall separating them (b).

7.4.1 Multilayer Nanowires

The most feasible solution to this problem is believed to be multilayer nanowires, composed of alternating segments of Galfenol and a nonmagnetic material. These wires can be grown in the usual templates to have the same overall dimensions and mechanical performance, but should have a reduced anisotropy in each magnetostrictive segment. In theory, the effect these structures have on the magnetization profile should be equivalent to the shearing that results from the reduced aspect ratio of the Galfenol from Figure 7.19. This increases the probability of measuring a net magnetization change from the wire, as each small layer can potentially be rotated by stress away from the uniaxial condition. There are numerous studies [135, 12, 114, 86, 94, 84] looking to take advantage of multilayer magnetic nanowires due to the large variety of shapes that can be configured, ranging from thin in plane discs [43, 112, 136] to complex vortex states [124, 99]. In all of these examples however, the activation mechanism is externally applied field rather than the unique magnetoelastic coupling investigated in this work.

In the interests of the artificial cilia sensors, some shape anisotropy is desirable because it allows the wires to be close to saturation to maximize the rotation ability of compressive stress without requiring an external magnetic bias field, the application of which is still unwieldy in these devices. Based upon the modeling results, an aspect ratio between 5 and 10 is initially targeted. Another key consideration is that the maximum stress in a bending cantilever occurs at the base, so in reality only the first segment needs to be Galfenol [64] and the rest of the wire can be chosen

from whatever material best interfaces structurally and has the desired mechanical properties. Ironically, this is essentially the exact inverse of the current samples that have a copper segment of moderate aspect ratio at the base and Galfenol from there outward.

With these ideas in mind, one batch of multilayer FeGa/Cu nanowires was received from Minnesota. The intent was to place them in the MFM and identify the alternating segments of the two materials, similar to how the copper end segment was found in Figure 6.22. However, initial inspection in the SEM found that the wire clusters were predominantly covered in an insulator layer believed to be rubber cement, so the sample was baked at 200°C for 20 minutes to try and remove this material after conventional solvents such as acetone failed to. Figure 7.21 reveals that some of the wires turned out to be free enough to scan with the MFM, although the nanowires themselves appear particularly non-uniform.

7.4.2 MFM Results

The magnetic phase images generated with MFM appear rather different than anticipated. The expectation was that there would be Galfenol segments with opposing bright and dark spots that alternate with sections of copper showing no phase response. Figure 7.22 shows that the vast majority of the nanowires appear to be nonmagnetic, with only a scattering of points with phase contrast. Interestingly, every spot identified appears dark with no corresponding bright point to represent flux closure, suggesting that each dark spot is a small piece of Galfenol

241
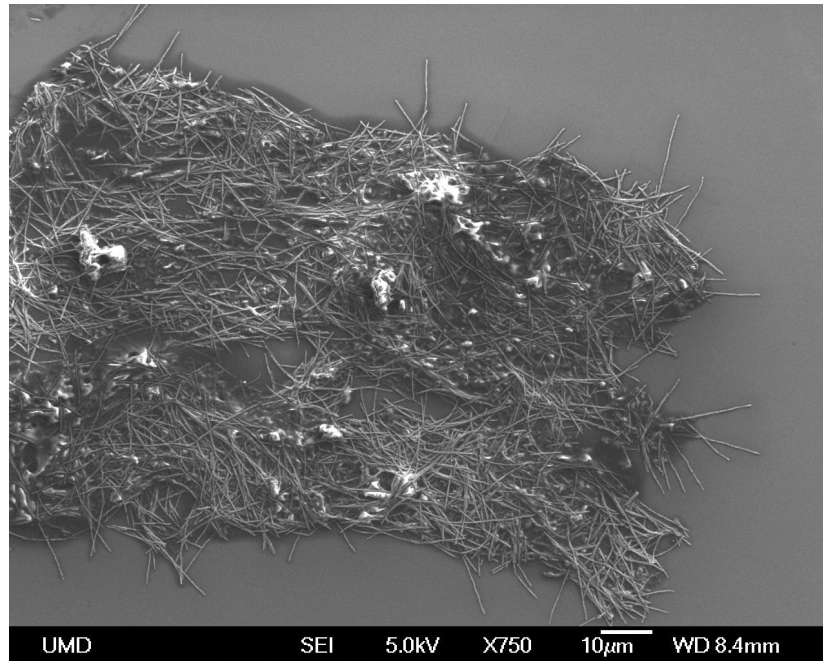
(a)
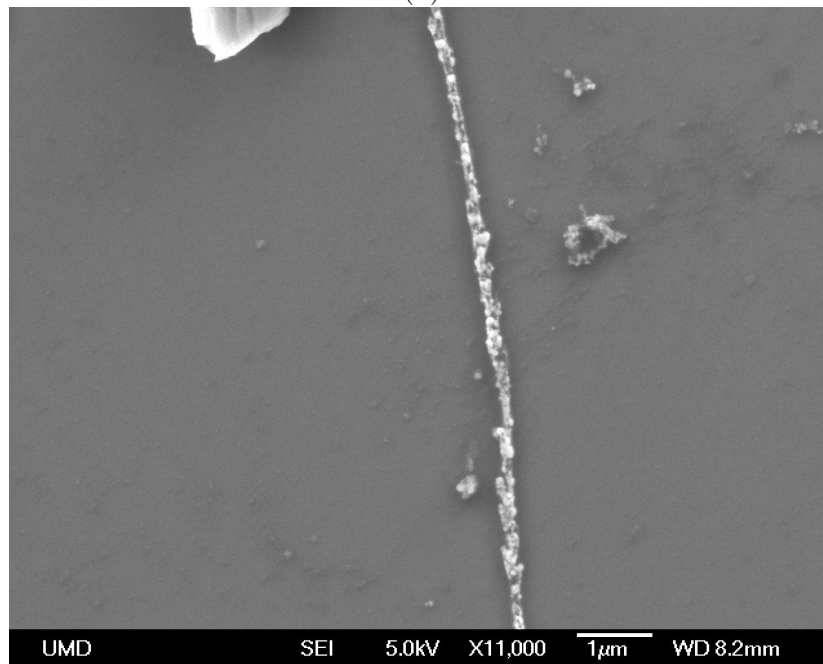
(b)

Figure 7.21: Images of the multilayer nanowires after baking the sample to remove the insulating compound used during fabrication. Some wires still appear to be covered (a) but those protruding from the edge are accessible. In some other areas the wires have a terrible surface finish thought to be excessive oxidation within the furnace (b).

that is magnetized downward into the silicon wafer. As the aspect ratios of these magnetic segments are ≈ 1 rather than the sought after ≈ 5, this configuration has the advantage of very little shape anisotropy which allows for the magnetization to be non-axial. Due to this combination of low shape anisotropy and uniformly dark spots in the MFM results, it is believed that the stray field of the MFM probe itself is perturbing the magnetization of the Galfenol pieces to align parallel to the tip [149, 138], downward into the page in agreement with the phase image.

In order to investigate this further, MFM scans were performed with a dc magnetic field applied to rotate the magnetization as desired. If the small Galfenol sections along the nanowire behave as expected, they should each align with the applied field even if it is oriented perpendicular to the nanowire axis. The application of field during MFM operation was made possible by incorporating a magnetic flux path driven by a wound wire solenoid. This apparatus was borrowed from Supratik Datta who originally constructed it from low carbon steel for applying field during four-point bending tests [36]. New pole pieces were machined to better concentrate the field across the MFM samples, allowing for up to 600 Oe to be applied in the air gap, limited only by thermal concerns. Figure 7.23 displays a picture of this configuration.

Figure 7.24 shows the MFM phase images from two multilayer FeGa/Cu nanowires with the magnetic field directed perpendicular to their axes. In each result, there is a distinct bright and dark pair oriented with the field at each small Galfenol piece and no contrast elsewhere. For the results presented in Figure 7.25, the field was directed axially and flipped between the positive and negative direc-
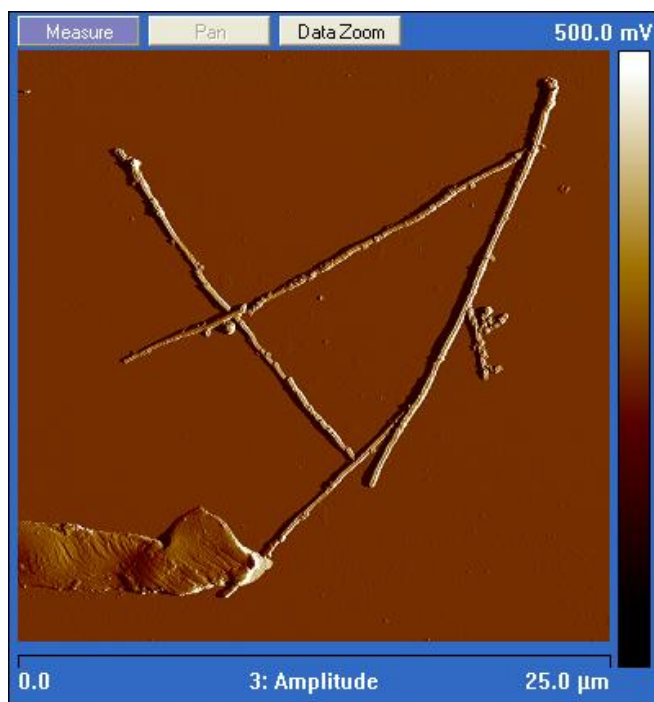
(a)
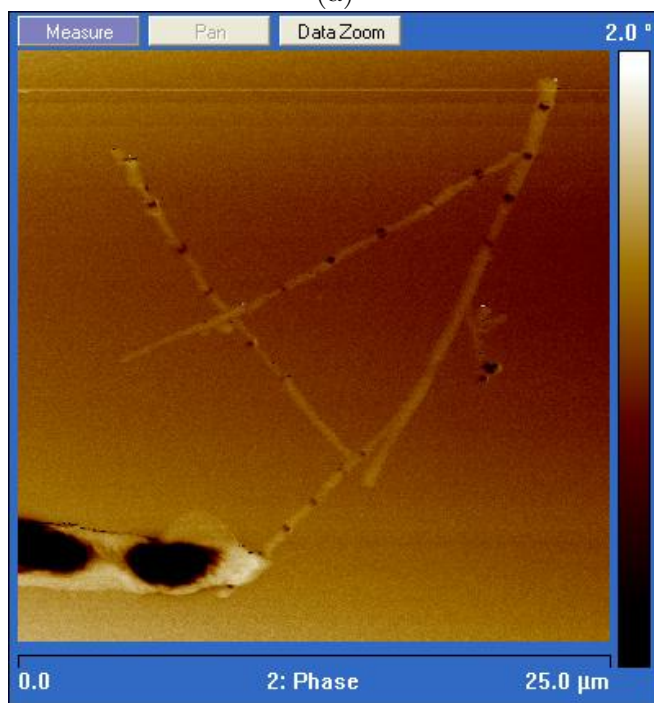
(b)

Figure 7.22: MFM amplitude (a) and phase (b) scans from a group of multilayer FeGa/Cu nanowires. The dark points each likely represent a small Galfenol segment magnetized into the page.

244
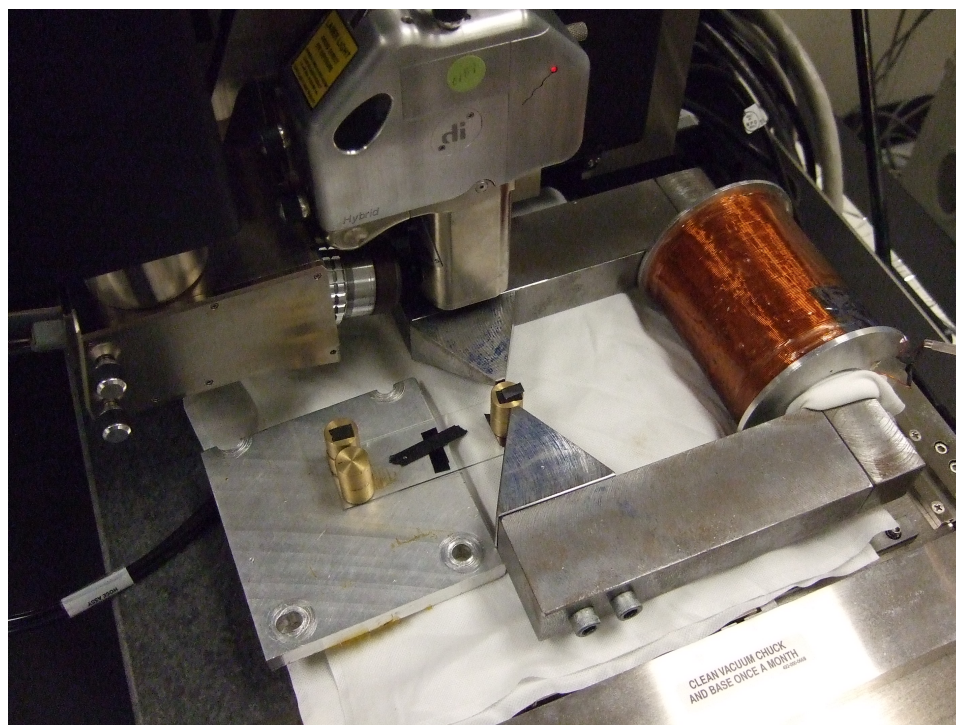
Figure 7.23: Photograph of the magnetic flux path apparatus used to apply directional magnetic fields to MFM samples during operation. The nanowires are deposited on the silicon wafer atop the central brass cylinders, where the field in the air gap between the pole pieces can easily reach 600 Oe. During operation the MFM scanner head has just enough clearance to contact the sample surface prior to bumping the flux path.

tions. While the first plot is not as visually sharp as the second, it is established that the domain structure flips in response to the change in field. These images verify that by reducing the shape anisotropy with multilayer wires, the magnetization is capable of rotating in any direction and thus providing transduction for cilia sensor applications.

7.5   Actuator Performance

An interesting prospect based upon the Galfenol segments successfully aligning with an external magnetic field is making use of the direct magnetostriction effect where the sample strains as the magnetization changes from the perpendicular to parallel states. While the nanowires are predominantly copper, the magnetization processes in the each small Galfenol layer should still result in an overall change in length. Unfortunately the magnitude of this strain is dependent on the nominal length of magnetostrictive material, which based upon the previous MFM results is likely to be around 5 μm at best. Assuming that the magnetostriction follows the same $\approx$ 300 ppm measured in bulk single crystals, the maximum length change of these multilayer nanowires should only be approximately $\delta l = \lambda_{100}\, l = 1.5$ nm.

In future work the composition of the multilayer nanowires can be improved upon to have a much larger presence of Galfenol and therefore a greater expected strain response. For the interests of this work however, it was still deemed worthwhile to attempt measuring the magnetostrictive strain in order to present the relevant experimental details that might be of interest in further studies of these
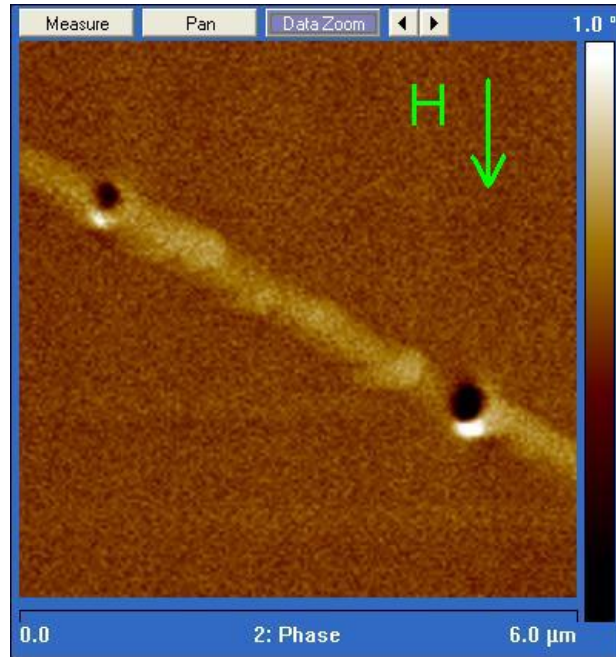
(a)
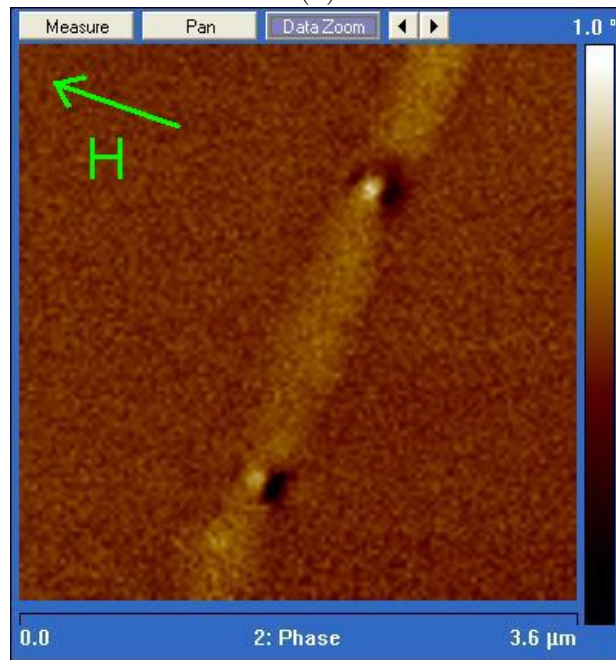
(b)

Figure 7.24: MFM phase plots from two multilayer nanowires with 600 Oe applied perpendicular to the wire axes. In each case, there is a clear bright and dark pair aligned with the field, verifying that with the reduced shape anisotropy the Galfenol magnetization is able to rotate away from the axial state.
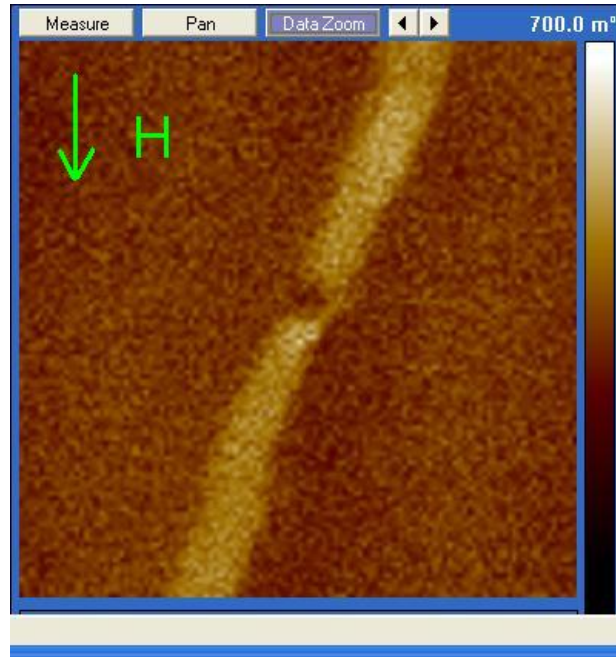
(a)
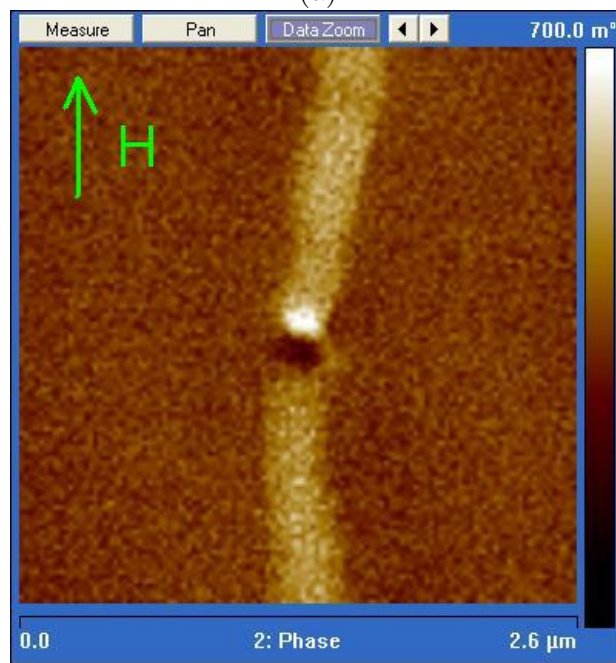
(b)

Figure 7.25: MFM phase plots from a multilayer nanowire with 600 Oe of field applied along in its axis in both directions. Although the data is not as sharp in (a), the domain does flip between these two extremes due to external field. These results combined with the possibility for perpendicular magnetization bode well for the nanowire transduction.

nanostructures.

There are a number of constraints that limit the available means of observing this length change. The most obvious is that features on this scale are quite difficult to capture even with the AFM or SEM. In order to have adequate resolution the image must be zoomed in substantially, but in doing so there is no fixed frame of reference and any apparent motion could be attributed to simple image drift. It also has been firmly established that applying large magnetic fields within the SEM chamber is itself a difficult problem, and this eliminates that instrument as a means of strain measurement. In the AFM, field application can be carried out using the above apparatus, but capturing any length change is problematic due to the slow scan rate, potential shift from field-scanner interactions, and noise.

In the end, the following procedure was used to scan for any actuation strain caused by nanowire magnetostriction. A long isolated nanowire was found in the SEM and an EBID weld was performed at one end to firmly attach it to the silicon [52]. The sample was then placed within the AFM with the external magnetic field apparatus. The 600 Oe dc field was applied perpendicular to the desired nanowire in order to magnetize the Galfenol segments normal to the wire axis for the initial condition. The field was shut off and the sample was rotated 90° so that when the field is again switched on it will be aligned along the nanowire axis. Once prepared, the AFM was engaged onto the desired nanowire using a nonmagnetic FESP model cantilever. After locating the free end of the wire, the scan size was reduced to the order of 100 nm so the trace lines clearly reveal the large jump in height as the tip scans from the silicon wafer onto the end of the wire. At this

scale, if the wire were to strain due to magnetostriction, the point at which this jump occurs should shift slightly outward due to the fixed weld constraint at the opposite wire end. Therefore, after scanning a portion of the wire edge without the field applied, the current amplifier is turned on to magnetize the wire axially and any changes in the AFM profile should be apparent.

This experiment was conducted on a multilayer wire that had a few Galfenol segments along the length. Imaging the abrupt ≈ 100 nm step from the silicon onto the nanowire was not as clear as hoped, likely the result of oxidation forming all around the base of the wire. Figure 7.26 shows that the large amounts of copper in these samples prompted substantial growth after days of air exposure. While the nanowire used in this test did not appear to have this problem, at the scale of interest it is quite likely that corrosion made some contribution toward not seeing a perfectly vertical wall in the AFM traces. The other contributor would be the geometry of the AFM tip and the inherent inability to resolve purely vertical structures at all but a select few scan angles. Figure 7.27 plots the height scan lines taken before and after the magnetic field was turned on, and it is clear that the data appears unchanged. This result was expected considering the very small amount of length change that the little amount of Galfenol would provide, but it still reveals other causes for concern. The noise in the AFM data is substantially larger than is normally observed, and there appears to be some periodicity. Analysis has revealed that 60 Hz noise in the current amplifier, and thus magnetic field, is likely to blame. Although great care was taken to ensure that the AFM probe and sample mounting components were nonmagnetic, even small motions of the magnetic flux path could

induce base vibrations that corrupt the AFM signal quality. Even with this error however, this experimental approach should be adequate for the observation of the 10 nm of nanowire magnetostriction that could easily be produced from advanced nanowire samples. It is intended that this method be used in conjunction with other characterization techniques to formally identify the first instances of Galfenol nanowire magnetostriction.
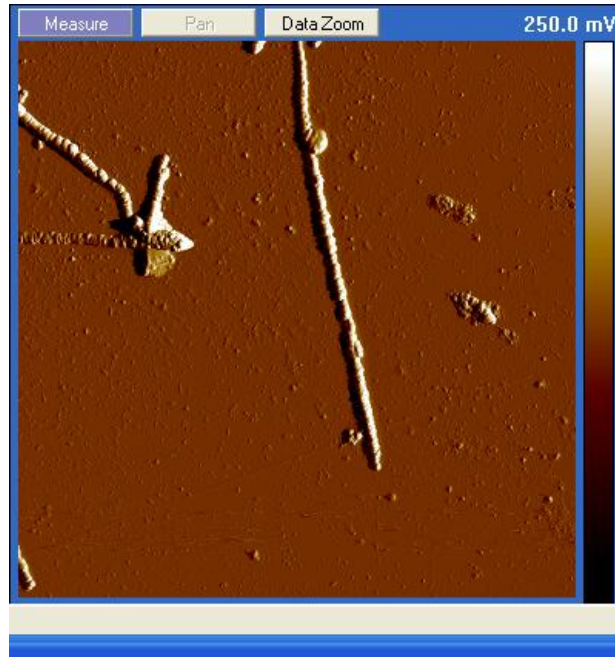
(a)
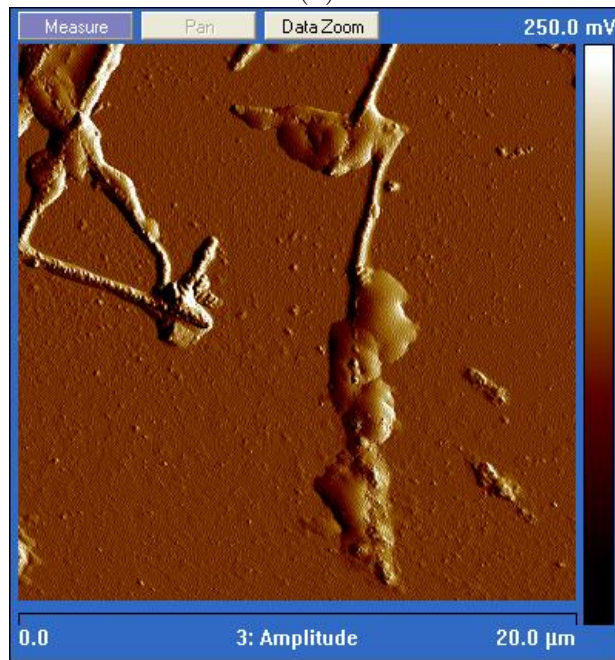
(b)

Figure 7.26: MFM amplitude scans of a multilayer FeGa/Cu nanowire, with (b) captured a week after (a). Due to the prolonged air exposure, it is believed that the copper oxidized rapidly and formed a substantial growth around the sample, limiting the effectiveness of the MFM procedure.
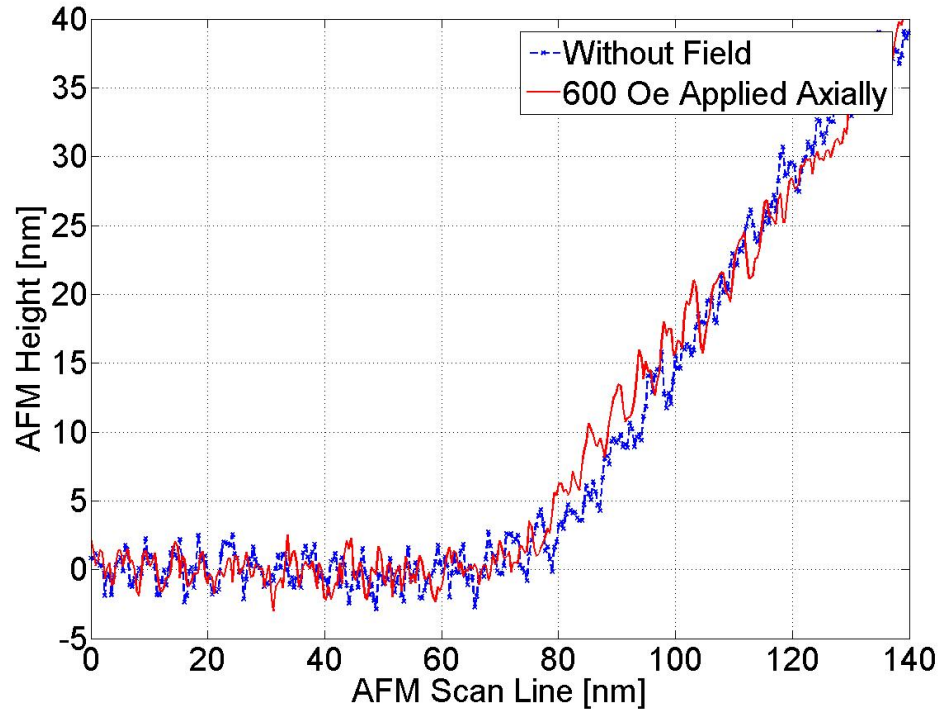
Figure 7.27: Plot of successive AFM scan lines at the free end of a multi-layer wire, recorded before and after the 600 Oe axial field was switched on. If there was an appreciable change in length due to magnetostriction, the red trace should appear shifted to the left. This data is inconclusive due to the very small strain expected and the presence of noise likely caused by the amplifier driving the magnetic field, but the methodology should prove more useful as improvements are made to the system.

Chapter 8

Conclusions

8.1 Summary of Research

This project was motivated by the prospect of using magnetostrictive Galfenol nanowires to mimic the sensing capabilities and mechanical robustness of biological cilia. This iron-gallium alloy presents a unique combination of magnetostrictive and structural properties that should allow for large deflections in cantilevered nanowires that create stress induced changes in magnetization. Considering the lack of research into this specific topic, the problem was approached in several distinct steps that each contributed to greater understanding. The overall objectives of this research were to: investigate sensing magnetostriction in bending Galfenol beams both experimentally and analytically, develop an experimental methodology to enable the study of these properties at the nanowire scale, and perform characterization experiments that prove the feasibility of implementing Galfenol nanowires in the artificial cilia role. The key results of how each chapter worked toward these goals are summarized below.

Chapter 2 detailed the proof-of-concept experiments intended to verify the existence of an appreciable magnetostrictive response in bending Galfenol beams despite the presence of equal and opposite stresses within the sample. The tests were conducted on several samples of varying composition and dimension, with the

greatest response being measured from a single crystal beam of $Fe_{84}Ga_{16}$ that was 32.7 mm long and 1.58 mm in diameter. A significant contribution from these experiments was the demonstration that the magnetostrictive response manifests as a rectified version of the beam vibration due to the dominance of the compressive side of the sample. In addition, this magnetic output can be successfully and equivalently measured with both the traditional pickup coil as well as commercial GMR sensors that are intended for use in the nanowire devices.

In Chapter 3, the origin of the asymmetry in the beam response was investigated analytically. Beginning with the mechanical deflections and stresses derived from Euler-Bernoulli beam theory, these results were input into the constitutive magnetostriction model using non-constant coefficients. In order to properly simulate the effect of tensile stress in these beams, a set of experiments were conducted to fill out the data that had previously been collected only in compression. The result of this method was solid agreement between the model and the data, and an understanding of how despite the point of optimum sensitivity shifting during loading, the average magnetic induction is surprisingly consistent. In order to have an analytical framework that was more flexible for studying nanowires as well as bulk samples, the constitutive magnetostriction model was replaced with a more robust formulation from the literature. After reviewing some of the existing magneto-mechanical models, the Armstrong approach based upon a free energy summation was deemed the best starting point for this work. The implementation was greatly improved and the results once again agree very well with the measured data.

Chapter 4 begins the transition to studying Galfenol nanowires. In order for it

to be conducted in a familiar and straightforward manner, this research required a means of interacting with samples ranging from dense nanowire arrays surrounded by alumina to individual wires suspended in alcohol solution. Based heavily off of a design made by Dr. Ruoff's group, a nanomanipulator stage was constructed that consists of two fine positioning stages each capable of mounting nanowires, AFM probes, and GMR sensors. A piezoelectric bimorph provides dynamic excitation, while the individual stepper motors allow for a positional resolution of 12 nm in all three directions. By sitting entirely within the sample chamber of the SEM, some important capabilities were able to be visualized, such as attaching wires with EBID nano-welding, exciting cantilevered specimens at resonance, and bending isolated samples with large deflections.

The mechanical behavior of Galfenol nanowires was presented in Chapter 5. The primary results were found to include great nanowire flexibility, wholly elastic behavior, significant improvement in ultimate strength, no change due to applied magnetic field, and estimates of the Young's modulus for modeling purposes. Most of these traits were measured with quasi-static tensile testing, where nanowires were suspended between two opposing AFM tips that were slowly pulled apart, with stress and strain data compiled directly from micrograph analysis. In addition to the mechanical data itself, some of the most important results of this work were the numerous troubleshooting steps taken to confirm the accuracy of this technique. Various sources of error including the AFM stiffness, misalignment, and EBID weld effects were identified and improved upon, and this tensile procedure was further validated by obtaining data from MWCNT's as a benchmark. Resonance testing

256

was also performed, which directly prompted a full analysis of the composition of the nanowire samples using EDS. These results provided substantial feedback to the University of Minnesota and allowed them to improve upon their fabrication process. The final result is that in nanowires with a desired gallium content of near 16%, there is a [110] texture with a 160 GPa modulus, in agreement with expectations.

Chapter 6 focused on the magnetic domain structure of the Galfenol nanowires. The theory introduced previously is augmented with micromagnetic considerations such as the exchange coupling and the demagnetization energy. An energy balance between these terms provides an estimation of the critical radius below which the nanowires will remain a single axial domain, the results of which suggest that this configuration will be present in all but a few nanowires with extreme geometries. An FEM simulation corroborates this assumption. The experimental observation of the nanowire domain structures was conducted primarily with MFM, and the phase image results agree well with the predictions that each wire is a single magnetic domain with magnetization oriented along the axis. This technique also provided some interesting results that suggest a series of crystallographic defects or grain boundaries along the length of many nanowires, but not enough to cause deviation from the single axial domain. Lorentz TEM was employed as a secondary experimental method to corroborate the MFM results.

In Chapter 7, many of the various experimental tools described previously are combined to investigate the coupling between the mechanical and magnetic states of the nanowires. Novel experiments were carried out that statically bent Galfenol nanowires throughout an MFM scan in order to observe any stress induced changes

to the magnetic domain structure. Mechanically, these tests identified several more sources of oxidation and fracture, and the magnetic images appeared unchanged due to the overbearing shape anisotropy in the pure Galfenol wires. Dynamic testing was initiated that consisted of attaching a dense array of cantilevered nanowires onto a magnetic field sensor and exciting the entire structure at high frequency with the nanomanipulator. Due to the numerous known obstacles the results of these tests were inconclusive, but it was verified that the GMR sensor is capable of detecting nanowire fields. The final sections of this chapter outlined the best approach toward improving the transduction capabilities of the nanowires. Samples with multilayers of Galfenol and copper were found to have a sufficiently reduced shape anisotropy to allow for complete magnetization rotation in each magnetic segment. An experiment was presented that will provide a means of measuring actuation strain from a magnetostrictive sample as the nanowire fabrication and integration continue to advance.

8.2   Key Contributions

- Experimentally demonstrated that Galfenol can be used as an active sensing material when loaded in static and dynamic bending, in spite of the anti-symmetric stress distribution. This result promotes the idea of incorporating Galfenol alloys in smart structures without the need for a thin film, substrate layer, or prestress mechanism.

- Established that GMR sensors make a reliable alternative for measuring the

magnetic response of conventional magnetostrictive devices. In bending beam samples where the magnetization varies spatially, it has been shown that these sensors detect the volume average of magnetic induction with little sensitivity to GMR placement.

- Made the first measurements of sensing magnetostriction from hot-rolled sheets of polycrystalline Galfenol. This result holds a lot of promise for using thin patches of Galfenol in numerous smart structures applications as the deformation processing becomes more refined.

- Combined beam theory with existing magneto-mechanical transduction models to analytically confirm the source of the large rectified magnetic induction response within a bending magnetostrictive beam. Demonstrated the flexibility of using this modeling approach for simulating both bulk samples and individual nanowires.

- Designed and constructed a platform that allows for the characterization of nanostructures using traditional mechanical testing techniques. The demonstrated functionality of this nanomanipulator includes high spatial resolution, dynamic actuation, nano-welding capabilities, and magnetic sensor attachment.

- Developed an experimental process to study the relevant mechanical properties of Galfenol nanowires, and provided an estimation of these values from various samples. Uncovered challenges that were unforeseen from the macroscale

research, and substantially improved the level of interaction with the nanowire arrays and the accuracy of the measurement techniques.

- Showed an agreement between micromagnetic theory, FEM modeling, and experimental observation that Galfenol nanowires form a single axial domain in their equilibrium state. Presented scenarios strongly suggesting that there are a multitude of crystallographic defects and compositional errors along the length of the wires, results that greatly aided the fabrication research at the University of Minnesota.

- Conducted a novel experiment that made use of both nanomanipulation and MFM to investigate the coupling between the magnetic domain structure and the bending stress in individual Galfenol nanowires. Confirmed suspicions that the shape anisotropy dominates the energy and prohibits transduction in wires composed entirely of magnetic material. Proved that despite this issue, the GMR sensors are capable of detecting stray field from translating nanowires in close proximity.

- Improved upon the original configuration with multilayer wires of Galfenol and copper. Demonstrated the reduced anisotropy by observing magnetization rotation due to an externally applied directional magnetic field. Segued this result into an experiment to measure actuation strain in an attempt to capture the first evidence of nanowire magnetostriction.

8.3 Future Work Suggestions

Overall, the results of this research have substantially advanced the knowledge base of bending magnetostriction and the properties of Galfenol nanowires. There have also been significant gains in the understanding of microscopy and manipulation techniques and the inherent challenges of nanoscale experimentation. It is hoped that this work leaves future researchers much better prepared for the continuing study of magnetic nanostructures or branching off on other related projects. That said, there are a number of areas covered in this dissertation that merit further investigation to improve the potential for using Galfenol nanowires as artificial cilia.

The design and capabilities of the nanomanipulator can be enhanced with some additional focus. Incorporating a rotational degree-of-freedom should improve the ease with which nanowires can be accessed and extracted from arrays, not to mention alleviating the concerns of seeing only a projection of a nanowire's true length. The wiring can be improved in order to minimize charging issues. While the EBID technique easily allows for all manner of objects to become attached to one another, the manipulator currently lacks a means of cutting or separating nanowires other than forcibly breaking them. Developing a technique for precisely cutting nanostructures would be a substantial boost to the capabilities of the device. In the long term, it would be ideal to have the manipulator become a permanent fixture within the SEM that did not impede normal loading and operation.

In the interests of more rigorously measuring the nanowire mechanical properties, a full statistical study could be conducted of the Young's modulus and ultimate

tensile strength across samples of varying size and composition. In conjunction with more regular chemical analysis, these results would provide an excellent basis for identifying the optimum nanowire configuration for any targeted application.

One of the most substantial improvements would be integrating the nanowire arrays and the GMR magnetic field sensors prior to fabrication. The attachment of the nanowires onto the various sensors employed in this work was the single biggest cause of frustration and the source of the largest errors. The attachment of the aluminum template onto the GMR resistor prior to anodization and electrochemical deposition should be limited only by the reactivity of the GMR element to the various chemicals used later in the sequence. Once a sensor is made with cantilevered Galfenol nanowires directly on it, the first experiment to conduct should be exciting the entire structure with the piezoelectric bimorph and comparing the magnetic response to the amplitude of vibration. This type of test can directly correlate to sensing flow, vibration, etc., and the lack of successful implementation of this in this dissertation is most regrettable.

The results from the multilayer wires also suggest some immediate future work. With evidence that the shorter Galfenol segments can rotate into arbitrary orientations, repeating the static bending experiments outlined in Section 7.2 on these samples should allow for the direct observation of the stress-induced effect on the magnetic domain structure. This task may require the acquisition of a new batch of nanowires however, as the current multilayer samples are known to heavily oxidize in a manner that greatly limits the application of bending loads.

The experiment designed to measure actuation magnetostriction could also be

improved. From the initial results it is apparent that better isolation of the sample and magnetic flux path might reduce vibration and noise, while generating a cleaner dc current for the solenoid would also help in this regard. There also is room for acquiring AFM probes with special tip geometry in order to allow for proper imaging of the vertical face of the nanowire end.

In parallel to all of this, there is room for modification in the fabrication and handling of the nanowires themselves. Continuing with multilayer samples might be a good course of action, but the challenges of growing segments of specific aspect ratio while maintaining the desirable composition need to be further investigated. In addition, the results of this work suggest that copper is perhaps not the ideal nonmagnetic material to combine with Galfenol. It may be worth researching if there is a better alternative with a matching lattice parameter that improves the strength at the material interface. One promising idea is to sandwich a thin (5 - 10 nm) layer of nickel between the Galfenol and copper segments, as it interfaces quite well with both materials and would have a negligible contribution to the magnetization. This would also be very easy to implement as nickel is a commonly used element in electrochemical deposition. In summary, it is concluded that the nanowire structure that optimizes sensing performance will consist of a Galfenol segment with aspect ratio of close to 5, with a thin nickel layer strengthening the transition to copper, which can extend from there outward to achieve the desired flexibility. Due to the customization available, it is believed that the specific geometry will vary based upon the different applications of the artificial cilia sensors.

Corresponding to the multilayer fabrication, there are still general concerns

with regards to excessive nanowire oxidation. While it might be possible to avoid all air exposure when manufacturing completely packaged cilia sensors, it is not practical at the current characterization level. It is believed that a combination of minor changes will sum up to alleviate this problem in most instances. By better integrating the nanowires with the GMR sensors, there will be far less need for fiddling with them and exposing them to air and other adhesives. Replacing the copper with a material that does not oxidize as rapidly would help, as would adding trace elements that promote corrosion resistance. Using the Lorentz TEM rather than the MFM for magnetically imaging critical samples might also be worthwhile.

Bibliography

[1] Characterization and calibration of MFM tip. Quantitative measurements in magnetic force microscopy. Available online at MikroMasch Library, http://www.spmtips.com/main/.

[2] Magpar v0.8. Available online at http://magnet.atp.tuwien.ac.at/scholz/magpar/. Installed and configured by Chaitanya Mudivarthi based upon the lecture "Device modeling and design: Micromagnetic Modeling of Nanomagnetics" given by Werner Scholz of Seagate.

[3] Zyvex S100. Available online at http://www.zyvex.com.

[4] J. T. Albert, O. C. Friedrich, H.-E. Denchant, and F. G. Barth. Arthropod touch reception: Spider hair sensilla as rapid touch detectors. *Journal of Comparative Physiology A*, 187:303–312, 2001.

[5] William D. Armstrong. Magnetization and magnetostriction processes in Tb(0.27-0.30)Dy(0.73-0.70)Fe(1.9-2.0). *J. Appl. Phys.*, 81(5):2321–2326, March 1997.

[6] T. Asaka, Y. Anan, T. Nagai, S. Tsutsumi, H. Kuwahara, K. Kimoto, Y. Tokura, and Y. Matsui. Ferromagnetic domain structures and nanoclusters in $Nd_{1/2}Sr_{1/2}MnO_3$. *Phys. Rev. Lett.*, 89(20):207203, November 2002.

[7] Jayasimha Atulasimha. *Characterization and Modeling of the Magnetomechanical Behavior of Iron-Gallium Alloys*. PhD thesis, University of Maryland, 2006.

[8] Jayasimha Atulasimha, Alison B. Flatau, Inderjit Chopra, and Rick A. Kellogg. Effect of stoichiometry on sensing behavior of iron-gallium. *Proc. SPIE Smart Structures*, 5387, 2004.

[9] L. Ba and W. S. Li. Influence of anodizing conditions on the ordered pore formation in anodic alumina. *J. Phys. D: Appl. Phys.*, 33:2527–2531, 2000.

[10] F. G. Barth. Spider mechanoreceptors. *Current Opinion in Neurobiology*, 14:415–422, 2004.

[11] F. G. Barth, U. Wastl, J. A. C. Humphrey, and R. Devarakonda. Dynamics of arthropod filiform hairs II. Mechanical properties of spider trichobothria. *Philosophical Transactions: Biological Sciences*, 340:445–461, 1993.

[12] G. Beck, K. Petrikowski, and H. R. Khan. Magnetism in magnetic nanowire arrays. Microstructure Analysis in Materials Science Conference, June 2005. Freiberg.

[13] E. Belcher. Hand-held sonar displays, near photographic images. *Sea Technology*, 39:19–23, 1998.

[14] L. Belliard, J. Miltat, A. Thiaville, S. Dubois, J. L. Duvail, and L. Piraux. Observing magnetic nanowires by means of magnetic force microscopy. *J. Magn. Mag. Mater.*, 190:1–16, 1998.

[15] Joseph D. Bronzino. *The Biomedical Engineering Handbook*. CRC Press, Inc., 2006.

[16] W. Bruckner, J. Thomasa, R. Hertel, R. Schafer, and C. M. Schneider. Magnetic domains in a textured Co nanowire. *J. Magn. Mag. Mater.*, 283:82–88, 2004.

[17] A. A. Bukharaev, D. V. Ovchinnikov, N. I. Nurgazizov, E. F. Kukovitskiand M. Klaber, and R. Wiesendanger. Investigation of micromagnetism and magnetic reversal of Ni nanoparticles using a magnetic force microscope. *Physics of the Solid State*, 40(7):1163–1168, 1998.

[18] Du-Xing Chen, James A. Brug, and Ronald B. Goldfarb. Demagnetizing factors for cylinders. *IEEE Trans. Magn.*, 27(4):3601–3619, 1991.

[19] Jack Chen, Jonathan Engel, Nannan Chen, Saunvit Pandya, Sheryl Coombs, and Chang Liu. Artificial lateral line and hydrodynamic object tracking. MEMS Conference, January 2006. Istanbul, Turkey.

[20] Nannan Chen, Jack Chen, Jonathan Engel, Saunvit Pandya, Craig Tucker, and Chang Liu. Development and characterization of high sensitivity bioinspired artificial haircell sensor. The 12th Solid State Sensors, Actuator, and Microsystems Workshop, June 2006. Hilton Head, SC, USA.

[21] A. E. Clark, B. F. DeSavage, and R. M. Bozorth. Anomalous thermal expansion and magnetostriction of single crystal dysprosium. *Phys. Rev.*, 138:A216–A224, 1965.

[22] A. E. Clark, K. B. Hathaway, M. Wun-Fogle, J. B. Restorff, T. A. Lograsso, V. M. Keppens, G. Petculescu, and R. A. Taylor. Extraordinary magnetoelasticity and lattice softening in bcc Fe-Ga alloys. *J. Appl. Phys.*, 93(10):8621–8623, May 2003.

[23] A. E. Clark, J. B. Restorff, M. Wun-Fogle, K. B. Hathaway, T. A. Lograsso, M. Huang, and E. Summers. Magnetostriction of ternary FeGaX (X=C,V,Cr,Mn,Co,Rh) alloys. *J. Appl. Phys.*, 101:09C507, 2007.

[24] A. E. Clark, J. B. Restorff, M. Wun-Fogle, and J. F. Lindberg. Magnetoelastic coupling and ΔE effect in Tb_xDy_{1-x} single crystals. *J. Appl. Phys.*, 73(10):6150–6152, May 1993.

[25] A. E. Clark, J. B. Restorff, M. Wun-Fogle, T. A. Lograsso, and D. L. Schlagel. Magnetostrictive properties of body-centered cubic Fe-Ga and Fe-Ga-Al alloys. *IEEE Transactions on Magnetics*, 36(5):3238–3240, September 2000.

[26] A. E. Clark and M. Wun-Fogle. Modern magnetostrictive materials - classical and non-classical alloys. *Proc. SPIE Smart Structures and Materials*, 4699, 2002.

[27] A. E. Clark, M. Wun-Fogle, J. B. Restorff, and T. A. Lograsso. Magnetostrictive properties of Galfenol alloys under compressive stress. *Materials Transactions*, 43(5):881–886, 2002.

[28] S. Coombs. Smart skins: Information processing by lateral line flow sensors. *Autonomous Robots*, 11:255–261, 2001.

[29] S. Coombs and J. C. Montgomery. Enigmatic lateral line system. In A. N. Popper, editor, *Comparative Hearing. Fish and Amphibians*. Springer, New York, 1999.

[30] J. R. Cullen, A. E. Clark, M. Wun-Fogle, J. B. Restorff, and T. A. Lograsso. Magnetoelasticity of Fe-Ga and Fe-Al alloys. *J. Magn. Mag. Mat.*, 226-230:948–949, 2001.

[31] B. D. Cullity. *Introduction to Magnetic Materials*. Addison-Wesley, Reading, MA, 1972.

[32] Marcelo J. Dapino, Ralph C. Smith, and Alison B. Flatau. An active and structural strain model for magnetostrictive transducers. *Proc. SPIE Smart Structures and Materials*, 3329, 1998.

[33] Marcelo J. Dapino, Ralph C. Smith, and Alison B. Flatau. Structural magnetic strain model for magnetostrictive transducers. *IEEE Trans. Magn.*, 36(3):545–556, May 2000.

[34] S. Datta, J. Atulasimha, C. Mudivarthi, and A. B. Flatau. The modeling of magnetomechanical sensors in laminated structures. *Smart Mater. Struct.*, 17:025010, 2008.

[35] S. Datta, M. Huang, J. Raim, T. A. Lograsso, and A. B. Flatau. Effect of thermal history and gallium content on magnetomechanical properties of iron gallium alloys. *Materials Science and Engineering A*, 435-436:221–227, November 2006.

[36] Supratik Datta, Jayasimha Atulasimha, and Alison B. Flatau. Modeling of magnetostrictive Galfenol sensor and validation using four point bending test. *J. Appl. Phys.*, 101:09C521, 2007.

[37] P. DeWolf, E. Brazel, N. Pangon, and M. Lefevre. Tunneling AFM and conductive AFM with NanoScope AFMs. 2005. Veeco Application Note 42.

[38] D. A. Dikin, X. Chen, W. Ding, G. Wagner, and R. S. Ruoff. Resonance vibration of amorphous SiO_2 nanowires driven by mechanical or electrical field excitation. *J. Appl. Phys.*, 93(1):226–230, 2003.

[39] Weiqiang Ding, Lorenzo Calabri, Xinqi Chen, Kevin M. Kohlhaas, and Rodney S. Ruoff. Mechanics of crystalline boron nanowires. *Composites Science and Technology*, 66:1109–1121, 2006.

[40] Jennifer Dooley, Marc De Graef, and Michael E. McHenry. Induction mapping of magnetostrictive materials. *J. Appl. Phys.*, 83(11):6837–6839, 1998.

[41] Patrick R. Downey, Alison B. Flatau, Patrick D. McGary, and Bethanie J. H. Stadler. Effect of magnetic field on the mechanical properties of magnetostrictive iron-gallium nanowires. *J. Appl. Phys.*, 103:07D305, 2008.

[42] E. du Tremolet de Lacheisserie. *Magnetostriction Theory and Applications of Magnetoelasticity*. CRC Press, Inc., Boca Raton, 1993.

[43] S. Dubois, C. Marchal, J. M. Beuken, L. Piraux, J. L. Duvail, A. Fert, J. M. George, and J. L. Maurice. Perpendicular giant magnetoresistance of NiFe/Cu multilayered nanowires. *Appl. Phys. Lett.*, 70(3):396–398, January 1997.

[44] T. W. Ebbesen and P. M. Ajayan. Large-scale synthesis of carbon nanotubes. *Nature*, 358:220, 1992.

[45] U. Ebels, A. Radulescu, Y. Henry, L. Piraux, and K. Ounadjela. Spin accumulation and domain wall magnetoresistance in 35 nm Co wires. *Phys. Rev. Lett.*, 84(5):983–986, 2000.

[46] Jonathan Engel, Jack Chen, Chang Liu, and David Bullen. Polyurethane rubber all-polymer artificial hair cell sensor. *J. MEMS*, 15(4):729–736, August 2006.

[47] Phillip Evans and Marcelo Dapino. Fully-coupled model for 3-d induction and strain of Galfenol with geometry effects and applied currents. *Proc. ASME Conference on Smart Materials, Adaptive Structures and Intelligent Systems*, SMASIS 2008-328, October 2008. Ellicot City, MD.

[48] Alison Flatau. *Galfenol-NanoSensors for Underwater Applications*, 2003. ONR Technical Proposal.

[49] E. H. Frei, S. Shtrikman, and D. Treves. Critical size and nucleation field of ideal ferromagnetic particles. *Phys. Rev.*, 106(3):446–455, May 1957.

[50] J. M. Garcia, A. Asenjo, M. Vazquez, P. Aranda, and E. Ruiz-Hitzky. Characterization of cobalt nanowires by means of force microscopy. *IEEE Trans. Magn.*, 36(5):2981–2983, September 2000.

[51] J. M. Garcia, A. Thiaville, and J. Miltat. MFM imaging of nanowires and elongated patterned elements. *J. Magn. Mag. Mater.*, 249:163–169, 2002.

[52] R. G. Gatiyatov, P. A. Borodin, A. A. Bukharaev, and D. A. Bizyaev. High-precision measurements of magnetostriction in nickel structures for magnetoresistive nanocontacts. *Tech. Phys. Lett.*, 32(10):857–859, 2006.

[53] Victor Giurgiutiu, Florin Jichi, Justin B. Berman, and Jason M. Kamphaus. Theoretical and experimental investigation of magnetostrictive composite beams. *Smart Materials and Structures*, 10:934–945, 2001.

[54] T. Goddenhenrich, H. Lemke, M. Muck, U. Hartmann, and C. Heiden. Probe calibration in magnetic force microscopy. *Appl. Phys. Lett.*, 57(24):2612–2614, December 1990.

[55] Joseph Goldstein, Dale E. Newbury, Patrick Echlin, Charles E. Lyman, David C. Joy, Eric Lifshin, L. C. Sawyer, and Joseph R. Michael. *Scanning Electron Microscopy and X-ray Microanalysis*. Springer, New York, 2003.

[56] C. Haber and D. Wirtz. Magnetic tweezers for DNA micromanipulation. *Rev. Sci. Instrum.*, 71:4561–4570, 2000.

[57] U. Hafeli, W. Schutt, J. Teller, and M. Zborowshi, editors. *Scientific and Clinical Applications of Magnetic Carriers*. Plenum, New York, 1997.

[58] R. C. Hall. Single-crystal magnetic anisotropy and magnetostriction studies in iron-based alloys. *J. Appl. Phys.*, 32:1037–1038, 1960.

[59] M. Huang, T. A. Lograsso, A. E. Clark, J. B. Restorff, and M. Wun-Fogle. Effect of interstitial additions on magnetostriction in FeGa alloys. *J. Appl. Phys.*, 103:07B314, 2008.

[60] A. Hubert, W. Rave, and S. L. Tomlinson. Imaging magnetic charges with magnetic force microscopy. *Phys. Stat. Sol. B*, 204:817, 1997.

[61] A. Hubert and R. Schafer. *Magnetic Domains. The Analysis of Magnetic Microstructures*. Springer-Verlag, New York, 1998.

[62] F. V. Hunt. *Electroacoustics: The Analysis of Transduction and its Historical Background*. AIP Press for the Acoustical Society of America, 1982.

[63] Rupal Jain, F. Patrick McCluskey, and Alison B. Flatau. Development and packaging of Galfenol nanowire acoustic sensor for under-water applications. ASME InterPACK'07, July 2007. Vancouver, BC.

[64] R. D. James and K. S. Narayan. Galfenol nanowires: magnetomechanical modeling for artificial cilia, tactile and acoustic sensors. Presented at the Structural Magnetostrictive Alloys MURI Year 1 Review, May 2007.

[65] O. Jessensky, F. Mller, and U. Gsele. Self-organized formation of hexagonal pore arrays in anodic alumina. *Appl. Phys. Lett.*, 72:1173–1175, 1998.

[66] D. C. Jiles. *Introduction to Magnetism and Magnetic Materials.* Chapman and Hall, New York, 1991.

[67] D. C. Jiles and D. L. Atherton. Theory of the magnetisation process in ferromagnets and its application to the magnetomechanical effect. *J. Phys. D: Appl. Phys., 17 (1984) 1265-128*, 17:1265–1281, 1984.

[68] D. C. Jiles and J. B. Thoelke. Theory of ferromagnetic hysteresis: Determination ofmodel parameters from experimental hysteresis loops. *IEEE Trans. Magn.*, 25(5):3928–3930, September 1989.

[69] J. P. Joule. *(Sturgeon's) Annals of Electricity, Magnetism, and Chemistry*, 8:219, 1842.

[70] C. Journet, W. K. Maser, P. Bernier, A. Loiseau, M. L. Delachapelle, S. Lefrant, P. Deniard, R. Lee, and J. E. Fischer. Large-scale production of single-walled carbon nanotubes by the electric-arc technique. *Nature*, 388:756, 1997.

[71] R. A. Kellogg, A. M. Russell, T. A. Lograsso, A. B. Flatau, A. E. Clark, and M. Wun-Fogle. Tensile properties of magnetostrictive iron-gallium alloys. *Acta Materialia*, 52:5043–5050, 2004.

[72] Rick Allen Kellogg. *Development and modeling of iron-gallium alloys.* PhD thesis, Iowa State University, 2003.

[73] A. G. Khachaturyan and D. Viehland. Structurally heterogeneous model of extrinsic magnetostriction for Fe-Ga and similar magnetic alloys: Part I. decomposition and confined displacive transformation. *Metal. Mater. Trans. A*, 38A:2308–2316, 2007.

[74] A. G. Khachaturyan and D. Viehland. Structurally heterogeneous model of extrinsic magnetostriction for Fe-Ga and similar magnetic alloys: Part II. giant magnetostriction and elastic softening. *Metal. Mater. Trans. A*, 38A:2317–2328, 2007.

[75] Charles Kittel. Physical theory of ferromagnetic domains. *Rev. Mod. Phys.*, 21(4):541–583, October 1949.

[76] Osamu Kohmoto. Effective demagnetizing factors of second-order magnetocrystalline anisotropies in ferromagnetic resonance kittel formula. *Jpn. J. Appl. Phys.*, 43(4A):1334–1338, 2004.

[77] Hans W. P. Koops, Johannes Kretz, Michael Rudolph, Markus Weber, Gerold Dahm, and Kam L. Lee. Characterization and applications of materials grown by electron-beam-induced deposition. *Jpn. J. Appl. Phys.*, 33:7099–7107, 1994.

[78] O. Kubaschewski. *Iron-Binary Phase Diagrams*. Springer-Verlag, 1982.

[79] L. D. Landau and E. M. Lifshitz. *Course of Theoretical Physics*, volume 1. Pergamon Press, England, 3 edition, 1991. Translated from Russian by J. B. Sykes and J. S. Bell.

[80] E. Lee. Magnetostriction and magnetomechanical effects. *Reports on Prog. in Phys.*, 18:184–229, 1955.

[81] B. Lewis and R. Street. The interpretation of magnetic susceptibility and the ΔE effect in terms of domain processes. *Proc. Phys. Soc.*, LXXII(4):604–617, May 1958.

[82] A.-P. Li, F. Mller, A. Birner, K. Nielsch, , and U. Gsele. Fabrication and microstructuring of hexagonally ordered two-dimensional nanopore arrays in anodic alumina. *Adv. Mater.*, 11:483–487, 1999.

[83] Z. Li, S. Li, and Z.-Y. Cheng. Micro-biosensor based on magnetostrictive microcantilever. *J. Int. Mat. Sys. Struc.*, 2004. submitted.

[84] R. S. Liu, S. C. Chang, S. F. Hu, and C. Y. Huang. Highly ordered magnetic multilayer Ni/Cu nanowires. *Phys. Stat. Sol. C*, 3(5):1339–1342, 2006.

[85] T. A. Lograsso and E. M. Summers. Detection and quantification of D03 chemical order in Fe-Ga alloys using high resolution x-ray diffraction. *Materials Science and Engineering A*, 416(1-2):240–245, January 2006.

[86] N. Lupu, H. Chiriac, and P. Pascariu. Electrochemical deposition of FeGa/NiFe magnetic multilayered films and nanowire arrays. *J. Appl. Phys.*, 103:07B511, 2008.

[87] Atsushi Maeda, Minoru Kume, Takashi Ogura, Kazuhiko Kuroki, Takashi Yamada, Madoka Nishikawa, and Yasoo Harada. Magnetic wire and box arrays. *J. Appl. Phys.*, 76(10):6667–6670, November 1994.

[88] G. A. Manley. *Peripheral Hearing Mechanisms in Reptiles and Birds*. Zoophysiology Vol. 26. Springer-Verlag, 1982.

[89] U. Marschner, B. Adolphi, U. Merkel, C. Wenzel, E. Starke, G. Pfeifer, H. Neubert, and W. J. Fischer. Transducer properties of a transversal beam with sputtered Galfenol top layer. U.S. Navy Workshop on Acoustic Transduction Materials and Devices, May 2008. Penn State University.

[90] Y. Martin and H. K. Wickramasinghe. Magnetic imaging by "force microscopy" with 1000 a resolution. *Appl. Phys. Lett.*, 50(20):1455, 1987.

[91] T. Massalaski, editor. *Binary Alloy Phase Diagrams 2nd Ed.* ASM International, Materials Park, OH, 2002.

[92] H. Masuda and K. Fakuda. Ordered metal nanohole arrays made by a two-step replication of honeycomb structures of anodic alumina. *Science*, 268:466–468, 1995.

[93] H. Masuda, F. Hasegawa, and S. Ono. Self-ordering of cell arrangement of anodic porous alumina formed in sulfuric acid solution. *J. Electrochem. Soc.*, 144:L127–L130, 1997.

[94] J.-L. Maurice, D. Imhoff, P. Etienne, O. Durand, S. Dubois, L. Piraux, J.-M. George, P. Galtier, and A. Fert. Microstructure of magnetic metallic superlattices grown by electrodeposition in membrane nanopores. *J. Magn. Mag. Mater.*, 184:1–18, 1998.

[95] D. Al Mawlawi, N. Coombs, and M. Moskovits. Magnetic properties of Fe deposited into anodic aluminum oxide pores as a function of particle size. *J. Appl. Phys.*, 70:4421–4425, 1991.

[96] Patrick D. McGary, Liwen Tan, Jia Zou, Bethanie J. H. Stadler, Patrick R. Downey, and Alison B. Flatau. Magnetic nanowires for acoustic sensors. *J. Appl. Phys.*, 99:08B310, 2006.

[97] Patrick David McGary. *Electrochemically Synthesized Magnetic Nanowire Heterostructures and Arrays for Acoustic Sensing.* PhD thesis, University of Minnesota, 2008.

[98] Leonard Meirovitch. *Fundamentals of Vibrations.* McGraw-Hill, 2001.

[99] J. Mejía-López, D. Altbir, A. H. Romero, X. Batlle, Igor V. Roshchin, Chang-Peng Li, and Ivan K. Schuller. Vortex state and effect of anisotropy in sub-100-nm magnetic nanodots. *J. Appl. Phys.*, 100:104319, 2006.

[100] Naruhisa Miura, Hideaki Ishii, Jun ichi Shirakashi, Akira Yamada, and Makoto Konagai. Electron-beam-induced deposition of carbonaceous microstructures using scanning electron microscopy. *Applied Surface Science*, 113/114:269–273, 1997.

[101] C. Mudivarthi, S. Datta, J. Atulasimha, and A. B. Flatau. A bidirectionally coupled magnetoelastic model and its validation using a Galfenol unimorph sensor. *Smart Materials and Structures*, 17:035005, 2008.

[102] Suok-Min Na and Alison B. Flatau. Deformation behavior and magnetostriction of polycrystalline FeGaX (X=B,C,Mn,Mo,Nb,NbC) alloys. *J. Appl. Phys.*, 103:07D304, 2008.

[103] K. Nielsch, F. Mller, A.-P. Li, and U. Gsele. Uniform nickel deposition into ordered alumina pores by pulsed electrodeposition. *Adv. Mater.*, 12:582–586, 2000.

[104] R. O'Barr, M. Lederman, S. Schultz, Weihua Xu, A. Scherer, and R. J. Tonucci. Preparation and quantitative magnetic studies of single-domain nickel cylinders. *J. Appl. Phys.*, 79(8):5303–5305, April 1996.

[105] J. A. Osborn. Demagnetizing factors of the general ellipsoid. *Phys. Rev.*, 67(11/12):351–357, June 1945.

[106] Y. Ozaki, T. Ohyama, T. Yasuda, and I. Shimoyama. Air flow sensor modeled on wind receptor hairs of insects. IEEE International Conference on MEMS, 2000.

[107] Matthew J. Parsons, Supratik Datta, Chaitanya Mudivarthi, Suok Min Na, and Alison Flatau. Torque sensing using rolled Galfenol patches. *Proc. SPIE Smart Structures*, 6933, 2008.

[108] J. O. Pickles. *Introduction to the Physiology of Hearing.* Academic Press, 1982.

[109] L. Piraux, S. Dubois, E. Ferain, R. Legras, K. Ounadjela, J.M. George, J.L. Maurice, and A. Fert. Anisotropic transport and magnetic properties of arrays of sub-micron wires. *J. Magn. Mag. Mat.*, 165:352–355, 1997.

[110] R. Ploessl, J. N. Chapman, A. M. Thompson, J. Zweck, and H. Hoffmann. *J. Appl. Phys.*, 73:2447, 1993.

[111] E. P. Popov. *Mechanics of Materials.* Prentice Hall, 1964.

[112] C. Prados, I. Panagiotopoulus, G. C. Hadjipanayis, J. J. Freijo, and A. Wemando. High magnetostriction in low applied magnetic fields in amorphous Tb-Fe (hard) / Fe-B (soft) multilayers. *IEEE Trans. Magn.*, 33(5):3712–3714, September 1997.

[113] Roger Proksch, George D. Skidmore, E. Dan Dahlberg, Sheryl Foss, J. J. Schmidt, Chris Merton, Brian Walsh, and Matt Dugas. Quantitative magnetic field measurements with the magnetic force microscope. *Appl. Phys. Lett.*, 69(17):2599–2601, October 1996.

[114] E. Quandt, A. Ludwig, J. Betz, K. Mackay, and D. Givord. Giant magnetostrictive spring magnet type multilayers. *J. Appl. Phys.*, 81(8):5420–5422, April 1997.

[115] J. B. Restorff, M. Wun-Fogle, A. E. Clark, and K. B. Hathaway. Induced magnetic anisotropy in stress-annealed Galfenol alloys. *IEEE Trans. Magn.*, 42(10):3087–3089, 2006.

[116] J. J. Rhyne and S. Legvold. Magnetostriction of Tb single crystals. *Phys. Rev.*, 138:A507–A514, 1965.

[117] Ronald E. Rosensweig. *Ferrohydrodynamics.* Courier Dover, 1997.

[118] J. J. Sáenz, N. García, P. Grtter, E. Meyer, H. Heinzelmann, R. Wiesendanger, L. Rosenthaler, H. R. Hidber, , and H.-J. Gntherodt. Observation of magnetic forces by the atomic force microscope. *J. Appl. Phys.*, 62(10):4293–4295, 1987.

[119] D. Sander, A. Enders, and J. Kirschner. Magnetization, magnetostriction and film stress of Fe monolayers on W(100). *IEEE Trans. Magn.*, 34(4):2015–2017, 1998.

[120] D. M. Schafer, A. Patil, R. P. Andres, and R. Reifenberger. Elastic properties of individual nanometer-size supported gold clusters. *Phys. Rev. B*, 51(8):5322–5332, 1995.

[121] R. Schafer, B. E. Argyle, S. Takayama, and D. Dingley. *IEEE Trans. Magn.*, 29:3876, 1993.

[122] R. Scheifein, J. Unguris, R. J. Celotta, and D. T. Pierce. *Phys. Rev. Lett.*, 63:668, 1989.

[123] Robert W. Schneider and Carl H. Smith. Low magnetic field sensing with GMR sensors, Part I: The theory of solid-state magnetic sensing. *Sensors*, 1999.

[124] W. Scholz, K. Y. Guslienko, V. Novosad, D. Suess, T. Schrefl, R. W. Chantrell, and J. Fidler. Transition from single-domain to vortex state in soft magnetic cylindrical nanodots. *J. Magn. Mag. Mat.*, 266:155–163, 2003.

[125] D. J. Sellmyer, M. Zheng, and R. Skomski. Magnetism of Fe, Co and Ni nanowires in self-assembled arrays. *J. Phys. Condens. Matter*, 13:R433–R460, 2001.

[126] Kwanyong Seo, K. S. K. Varadwaj, Paritosh Mohanty, Sunghun Lee, Younghun Jo, Myung-Hwa Jung, Jinhee Kim, and Bongsoo Kim. Magnetic properties of single-crystalline CoSi nanowires. *Nano Letters*, 7(5):1240–1245, 2007.

[127] Ho-Mun Si and Chongdu Cho. Finite element modeling of magnetostriction for multilayered MEMS devices. *Journal of Magnetism and Magnetic Materials*, 270:167–173, 2004.

[128] Ralph C. Smith, Marcelo J. Dapino, and Stefan Seelecke. Free energy model for hysteresis in magnetostrictive transducers. *J. Appl. Phys.*, 93(1):458–466, January 2003.

[129] Ralph C. Smith, Stefan Seelecke, Marcelo J. Dapino, and Zoubeida Ounaies. A unified framework for modeling hysteresis in ferroic materials. *Journal of the Mechanics and Physics of Solids*, 54(1):46–85, 2005.

[130] B. J. H. Stadler, P. McGary, L. Tan, and N. Basantkumar. Galfenol nanowire formation. Presented at the Structural Magnetostrictive Alloys MURI Year 1 Review, May 2007.

[131] C. Su, L. Huang, P. Neilson, and V. Kelley. In-situ measurement of in-plane and out-of-plane force gradient with a torsional resonance mode AFM. *Proc. Scanning Tunneling Microscopy/Spectroscopy and Related Techniques: 12th International Conference*, page CP696, 2003.

[132] E. Summers, T. A. Lograsso, J. D. Snodgrass, and J. Slaughter. Magnetic and mechanical properties of polycrystalline Galfenol. *Proc. SPIE Smart Structures*, 5387:448–459, 2004.

[133] L. Sun, Y. Hao, C.-L. Chien, and P. C. Searson. Tuning the properties of magnetic nanowires. *IBM J. Res. & Dev.*, 49(1):79–102, January 2005.

[134] T. Suzuki and K. Suziki. *IEEE Trans. Magn.*, 13:1505, 1977.

[135] Liwen Tan, Patrick D. McGary, and Bethanie J. H. Stadler. Controlling the angular response of magnetoresistance in Co/Cu multilayered nanowires using Co crystallographic orientation. *J. Appl. Phys.*, 103:07B504, 2008.

[136] Xue-Ti Tang, Gwo-Ching Wang, and Mutsuhiro Shima. Magnetic layer thickness dependence of magnetization reversal in electrodeposited CoNi/Cu multilayer nanowires. *J. Magn. Mag. Mater.*, 309:188–196, 2007.

[137] G. E. Thompson. Porous anodic alumina: Fabrication characterization and applications. *Thin Solid Films*, 297:192–201, 1997.

[138] S. L. Tomlinson, A. N. Farley, S. R. Hoon, and M. S. Valera. Interactions between soft magnetic samples and mfm tips. *J. Magn. Mag. Mater.*, 157/158:557–558, 1996.

[139] Mark Tondra. *NVE Application Notes for GMR Sensors*, 2004. www.nve.com.

[140] Mark Tondra, Peter Eames, Robert Schneider, Marc Porter, Nikolas Pekas, Rachel Millen, and John Nordling. BioMagnetICs program review. February 2006.

[141] A. Tonomura, T. Matsuda, H. Tanabe, N. Osakabe, J. Endo, A. Fukuhare, K. Shinagawa, and H. Fujiwara. *Phys. Rev. B*, 25:6799, 1982.

[142] M. Tortonese and M. Kirk. Characterization of application specific probes for SPMs. *Proc. SPIE Micromachining and Imaging*, 3009:53–60, 1997.

[143] Ching Tsang, Robert E. Fontana, Tsann Lin, D. E. Heim, Virgil S. Speriosu, Bruce A. Gurney, and Mason L. Williams. Design, fabrication & testing of spin-valve read heads for high density recording. *IEEE Trans. Magn.*, 30(6):3801–3806, November 1994.

[144] Craig Tucker, Nannan Chen, Jonathan Engel, Yingchen Yang, Saunvit Pandya, and Chang Liu. High-sensitivity bi-directional flow sensor based on biological inspiration of animal haircell sensors. IEEE Sensors Conference, October 2006. Korea.

[145] Luke M. Twarek and Alison B. Flatau. Dynamic property determination of magnetostrictive iron-gallium alloys. *Proc. SPIE Smart Structures*, 5761, 2005.

[146] T. Ueno, E. Summers, and T. Higuchi. *Proc. ACTUATOR2006*, 1:410–413, 2006.

[147] T. Ueno, E. Summers, and T. Higuchi. Machining of iron-gallium for microactuator. *Proc. SPIE Smart Structures*, 6170, 2006.

[148] J. v. Baar, M. Dijkstra, R. Wiegerink, T. Lammerink, R. d. Boer, and G. Krijnen. Arrays of cricket-inspired sensory hairs with capacitive motion detection. IEEE International Conference on MEMS, 2005. Miami, FL.

[149] M. S. Valera, S. L. Tomlinson, G.P. Heydon, A. N. Farley, S. R. Hoon, L. Zhou, S. McVitie, and J. N. Chapman. Magnetic force microscopy of soft magnetic materials. *J. Magn. Mag. Mater.*, 157/158:555–556, 1996.

[150] M. Vázquez, M. Hernández-Vélez, A. Asenjo, D. Navas, K. Pirota, V. Prida, O. Sánchez, and J. L. Baldonedo. Preparation and properties of novel magnetic composite nanostructures: Arrays of nanowires in porous membranes. *Physica B*, 384:36–40, 2006.

[151] Bas Vellekoop, Leon Abelmann, Steffen Porthun, and Cock Lodder. On the determination of the internal magnetic structure by magnetic force microscopy. *J. Magn. Mag. Mater.*, 190:148–151, 1998.

[152] J. H. Van Vleck. A survey of the theory of ferromagnetism. *Rev. Mod. Phys.*, 17:27–47, 1945.

[153] G. von Békésy. *Experiments in Hearing.* Acoustical Society of America, reprinted by arrangement with McGraw-Hill Book Company, 1960.

[154] P. Weiss. L'hypothése du champ moléculaire et la propriété ferromagnétique. *J. de Phys.*, 6:661–690, 1907.

[155] N. M. Wereley and A. Chadhuri. Underwater explosion shock isolation. Presented at the Structural Magnetostrictive Alloys MURI Year 2 Review, June 2008.

[156] Robert C. Wetherhold and Harsh Deep Chopra. Beam model for calculating magnetostriction strains in thin films and multilayers. *Appl. Phys. Lett.*, 79(23):3818–3820, December 2001.

[157] Robert D. White and Karl Grosh. Design and characterization of a MEMS piezoresistive cochlear-like acoustic sensor. *Proc. IMECE'02 ASME International Mechanical Engineering Congress and Exposition*, 33309, November 2002. New Orleans, LA, USA.

[158] T. M. Whitney, J. S. Jiang, P. C. Searson, and C. L. Chien. Fabrication and magnetic properties of arrays of metallic nanowires. *Science*, 261(5126):1316–1319, September 1993.

[159] R. Wu. Origin of large magnetostriction in FeGa alloys. *J. Appl. Phys.*, 91:7358, 2002.

[160] X. W. Wu, H. Zhou, R. J. M. van de Veerdonk, T. J. Klemmer, C. Liu, N. Shukla, D. Weller, M. Tanase, and D. E. Laughlin. Studies of switching field and thermal energy barrier distributions in a FePt nanoparticle system. *J. Appl. Phys.*, 93:7181–7183, 2003.

[161] Manfred Wuttig, Liyang Dai, and James Cullen. Elasticity and magnetoelasticity of FeGa solid solutions. *Applied Physics Letters*, 80(7):1135–1137, February 2002.

[162] Yingchen Yang, Nannan Chen, Jonathan Engel, Craig Tucker, Saunvit Pandya, and Chang Liu. From artificial haircell sensor to artificial lateral line system: Development and application. MEMS 2007 - 20th IEEE International Conference on Micro Electro Mechanical Systems, January 2007. Kobe, Japan.

[163] J.-H. Yoo, J. B. Restorff, M. Wun-Fogle, and A. B. Flatau. The effect of magnetic field annealing on single crystal iron-gallium alloy. *J. Appl. Phys.*, 103:07B325, 2008.

[164] Jin-Hyeong Yoo, Uwe Marschner, and Alison B. Flatau. Preliminary Galfenol vibratory gyro-sensor design. *Proc. SPIE Smart Structures*, 5764, 2005.

[165] W. A. Yost and D. W. Nielsen. *Fundamentals of Hearing 2nd Ed.* Holt, Rinehart and Winston, 1985.

[166] Min-Feng Yu, Mark J. Dyer, George D. Skidmore, Henry W. Rohrs, Xue-Kun Lu, Kevin D. Ausman, James R. Von Ehr, and Rodney S. Ruoff. Three-dimensional manipulation of carbon nanotubes under a scanning electron microscope. *Nanotechnology*, 10:244–252, 1999.

[167] Min-Feng Yu, Oleg Lourie, Mark J. Dyer, Katerina Moloni, Thomas F. Kelly, and Rodney S. Ruoff. Strength and breaking mechanism of multiwalled carbon nanotubes under tensile load. *Science*, 287:637, 2000.

[168] X. Z. Yua, M. Uchida, Y. Onose, J. P. He, Y. Kaneko, T. Asaka, K. Kimoto, Y. Matsui, T. Arima, and Y. Tokura. Observation of spin reorientation in

layered manganites $La_{1.2}Sr_{1.8}(Mn_{1-y}Ru_y)_2O_7$ (0.0≤y≤0.2) by Lorentz transmission electron microscopy. *J. Magn. Mag. Mater.*, 302:391–396, 2006.

[169] J. Zhang, D. Le Roux, C. E. Madden-Smith, S. Luk, A. Parker, N. Patel, and C. J. Roberts. Nano thermal analysis. 2004. Anasys Instruments Application Note 6.